

Annual Modulation Measurement of  
the Low Energy Solar Neutrino Flux with the Borexino Detector

Szymon Maria Manecki

Dissertation submitted to the Faculty of the  
Virginia Polytechnic Institute and State University  
in partial fulfillment of the requirements for the degree of

Doctor of Philosophy

in

Physics

Robert Bruce Vogelaar, Chair

Ramaswamy S. Raghavan<sup>†</sup>

Jonathan M. Link

Patrick Huber

Mark L. Pitt

May 9, 2013

Blacksburg, Virginia

Keywords: Neutrino Physics, Annual Modulation

Copyright 2013, Szymon M. Manecki



# Annual Modulation Measurement of the Low Energy Solar Neutrino Flux with the Borexino Detector

Szymon M. Manecki

(ABSTRACT)

This work reports a first attempt to measure the solar neutrino annual flux modulation due to Earth's elliptical orbit with the Borexino detector. Borexino is a real-time calorimetric detector for low energy neutrino spectroscopy located in the underground laboratory of Gran Sasso, Italy. The experiment's main focus is the direct measurement of the  ${}^7\text{Be}$  solar neutrino flux of all flavors via neutrino-electron scattering in an ultra-pure scintillation liquid. The original goal of this work was to quantify sensitivity of the Borexino detector to a 7% peak-to-peak signal variation over the course of a year and study background stability. A Monte-Carlo simulated sample of the expected variation was prepared in two phases of data acquisition, Phase I that spans from May-2007 to May-2010 and Phase II from October-2011 to September-2012. The data was then fitted in the time domain with a sinusoidal function and analyzed with the Lomb-Scargle fast Fourier transformation in the search for significant periodicities between periods of 0.5 and 1.5 years. The search was performed in the energy window dominated by  ${}^7\text{Be}$ , [210; 760] keV, and 60-day bins in the case of the fit and 10-bins for the Lomb-Scargle scan. This work also contains study of the post-purification data of Phase II beyond September-2012 with a prediction for the future sensitivity and justification of the achieved background levels. Results from an innovative method of signal's periodicity search, the *Empirical Mode Decomposition*, will be shown in the work of Francesco Lombardi of Laboratori Nazionali del Gran Sasso, and can be found in [1].

*This work was supported by NSF Grant 0802114*

# Dedication

I dedicate this work to my parents, Maria and Jacek Manecy. You are irreplaceable.

I love you.

# Acknowledgments

The work presented in this dissertation would not have been possible without the tremendous effort of a number of people.

I must begin by expressing my deep sorrow that Professor Raju Raghavan is no longer with us to see the results of my work. He was an inspiration to all of us and one of the initial reasons I wanted to join the Borexino group at Virginia Tech.

I would like underline the importance of my adviser, Professor Bruce Vogelaar, who has always believed in me, and who never failed to assist his students or to provide us with the resources that we needed to be successful researchers.

It has been such a pleasure to be a member of the Borexino collaboration. This unique group of experts has played such a significant role in my education, specifically: Marco Pallavicini, Aldo Ianni, Laszlo Papp, Andrea Ianni.

It is also worth mentioning that this work is the result of the group-effort of the *Seasonal Modulation* Working-Group, of which I was a member. I would like to thank Emanuela Meroni, Barbara Caccianiga, Livia Ludhova, Gioacchino Ranucci and Francesco Lombardi for their critical guidance.

In its initial phase, the Borexino group at Virginia Tech lead the calibration campaigns and later took on the data analysis process. I worked closely with Steve Hardy, Matt Joyce and

Derek Rountree, and furthered my understanding of this component of the field. It is thanks to them that I am now so familiar with this process.

The Princeton University group also became one of my work's most fundamental resources, and I owe Professor Frank Calaprice and Professor Cristiano Galbiati for their continued dedication. I would like to underline that if it was not for the graduate students of Princeton, Alvaro Chavarria, Richard Saldanha and Pablo Mosteiro, my graduate work and experience could not have been one of a kind.

Furthermore, it cannot go unstated that I first began my journey and career in Kraków, Poland, my birthplace. Inexperienced with the graduate school system in the United States, I am proud to say that I have come so far.

I would like to thank Dr. hab. Maciej Manecki, an alumni of Kent State University, who introduced me to the graduate application process in the United States, and who became a tremendous resource for this to become possible.

It was Dr. Tomasz Płazak who came to me one day and said: *Leave those 'engines', you were meant to do stars..* When I first began college, I entered with a specialization in Solid State Physics, and it was him, my Cosmology professor at the time, who showed me neutrinos. I thank him for his words until this day.

This story would not be complete if I did not mention the most traumatic experiences of my life, which has shaped me into the man I am today, my work at the Klezmer-Hois restaurant in the Jewish district of Kraków where I worked during my entire high school career and college. Trying to save every weekend for the big plans that I had floating around in my head, there was one (terrible as always) evening that I met a wonderful couple of tourists from Fredericksburg, VA , Joan and James Baker, who were in town for a big orchestral concert that they had been preparing for quite some time. It was this lovely couple that

hosted me the first time I came to Virginia, and they have become very dear friends to me and my family. Thank you for being such kind and generous people.

I would not be here today if it were not for my family, and my parents. They have shaped me, and helped me to build a unique set of attributes that brought me to where I am today. You make me feel so proud.

# Contents

<b>Abstract</b>	<b>ii</b>
<b>Dedication</b>	<b>iv</b>
<b>Acknowledgments</b>	<b>v</b>
<b>List of Figures</b>	<b>xi</b>
<b>List of Tables</b>	<b>xxii</b>
<b>1 Introduction</b>	<b>2</b>
<b>2 Neutrinos</b>	<b>4</b>
2.1 The Standard Model of Particle Physics . . . . .	5
2.2 Solar Neutrino Physics . . . . .	11
2.3 Neutrino Oscillations . . . . .	21
2.4 Annual Modulation . . . . .	30

2.5	Other Neutrino Sources in Nature . . . . .	34
<b>3</b>	<b>Borexino Detector</b>	<b>37</b>
3.1	Detector Design and Construction . . . . .	37
3.2	DAQ Electronics and Software . . . . .	51
3.3	CCD Positioning System . . . . .	63
3.4	Detector Calibration . . . . .	80
3.5	Physics Potential . . . . .	90
<b>4</b>	<b>Stability Conditions</b>	<b>97</b>
4.1	The Inner Vessel Shape . . . . .	98
4.2	Backgrounds Stability . . . . .	112
4.3	Spectral Fit Stability . . . . .	133
<b>5</b>	<b>Methodology and Approach</b>	<b>135</b>
5.1	Analysis Approach . . . . .	135
5.2	Event Selection . . . . .	145
<b>6</b>	<b>Results</b>	<b>156</b>
6.1	Phase I and II . . . . .	156
<b>7</b>	<b>Conclusion</b>	<b>176</b>

<b>Appendix A Table of Abbreviations</b>	<b>180</b>
<b>Appendix B List of Operations</b>	<b>182</b>
<b>Bibliography</b>	<b>182</b>

# List of Figures

2.1	Sixteen elementary particles . . . . .	6
2.2	Diagram of Standard Model of Particle Interactions. . . . .	7
2.3	Diphoton ( $\gamma\gamma$ ) invariant mass distribution from CMS. . . . .	8
2.4	Diphoton ( $\gamma\gamma$ ) invariant mass distribution from ATLAS. . . . .	8
2.5	Solar pp-chain and resulting neutrino spectrum in the SSM. . . . .	16
2.6	Prediction for the ${}^7\text{Be}$ and ${}^8\text{B}$ for different abundance models. . . . .	21
2.8	Survival probability for the solar electron neutrino. . . . .	29
2.9	Seasonal Earth-to-Sun distance oscillation . . . . .	31
2.10	Intensity loss with distance. . . . .	31
2.11	Expected seasonal modulation of 3-year ${}^7\text{Be}$ neutrino rate in Borexino. . . . .	33
2.12	Expected seasonal modulation of 3-year ${}^7\text{Be}$ neutrino rate in Borexino, based on results from [55]. . . . .	33
2.13	Total neutrino flux composition of all the natural sources available on Earth. Figure from [56]. . . . .	34

3.1	The CTF detector. . . . .	38
3.2	Deep, underground facility of the Gran Sasso National Laboratory in Italy. . . . .	40
3.3	The Borexino design. . . . .	41
3.4	The emission spectra for pure PC and PC+PPO. . . . .	42
3.5	Chart for the energy levels of a PC liquid scintillator. . . . .	43
3.6	Quenching factor for electrons and gamma particles in PC. . . . .	44
3.7	The heavy bosons exchange presented with Feynman diagrams. . . . .	45
3.8	$^{238}\text{U}$ , and $^{232}\text{Th}$ diagrams representing the decay chains of major impurities in Borexino. . . . .	48
3.9	Seasonal modulation of the measured muon flux in Borexino. . . . .	50
3.10	The Borexino DAQ electronics scheme. . . . .	52
3.11	$^{210}\text{Po}$ peak position every 10 days for various variables in $N_{pe}$ , $N_{hits}$ , and $N_{PMTs}$ . . . . .	58
3.12	Normalized Scintillation Pulse Shape. . . . .	59
3.13	The Gatti $\alpha/\beta$ discrimination parameter. . . . .	61
3.14	Gatti $\alpha/\beta$ statistical subtraction performed on three two years of data in fiducial mass of 145 tons. . . . .	63
3.15	Positions of the seven CCD cameras. . . . .	65
3.16	Images from each of the 6 cameras except for number 7. . . . .	70
3.17	An example of the measured source position using the rods. . . . .	71

3.18	A snapshot of the reconstructed source position and shortest distances to each of the rays. . . . .	72
3.19	Histogram of the radial error distribution data. . . . .	72
3.20	A 'pin-hole lights' view from each of the CCD cameras. . . . .	74
3.21	The effect of the temperature gradient and, as a result, change in the index of refraction and light-bending in the buffer. . . . .	77
3.22	Reconstructed $z$ coordinate of the laser ball source calibration data with <i>Echidna</i> c12 code. . . . .	79
3.23	The calibration source coupler. . . . .	81
3.24	A diagram of the source deployment system. . . . .	82
3.25	A map of the locations where sources were deployed. . . . .	82
3.26	$^{214}\text{Bi}^{214}\text{Po}$ coincidences count rates in 100 tons as a function of time. . . . .	85
3.27	Count rate in the energy region between (500-600) keV and (600-700) keV as a function of time. . . . .	85
3.28	SSS with indicated tubes that were used in the external calibration campaign. . . . .	86
3.29	Energy spectra of $\gamma$ -lines from eight different calibration sources. . . . .	87
3.30	Time distributions of the first photon arrival. . . . .	88
3.31	Energy resolution in $x$ , $y$ and $z$ as a function of energy. . . . .	88
3.32	Spatial cuts applied in the trigger efficiency test from $\gamma$ sources. . . . .	90
3.33	The Borexino spectrum after $\alpha/\beta$ statistical subtraction. . . . .	91
3.34	The anti-neutrino spectrum in Borexino. . . . .	92

3.35	Energy spectrum for the <i>pep</i> candidates after $^{11}\text{C}$ removal. . . . .	93
3.36	Decay scheme for the $^{51}\text{Cr}$ neutrino source. . . . .	96
3.37	Decay scheme for the $^{144}\text{Ce}$ anti-neutrino source. . . . .	96
3.38	Sterile neutrinos; 95% contour plot for the $\Delta m_{new}^2$ and $\sin^2(2\theta_{new})$ oscillation parameters. . . . .	96
4.1	The buffer events in a y-slice of [-1.5; 1.5] m. . . . .	99
4.2	The buffer events in a y-slice of [-1.5; 1.5] m after the leak. . . . .	99
4.3	Rates in different regions of the spectrum at $R < 4\text{m}$ . . . . .	99
4.4	Spatial distribution of the background. . . . .	101
4.5	Spatial distribution of the $^{210}\text{Bi}$ in the $^7\text{Be}$ -valley. . . . .	101
4.6	Correction for the leak events with a Bi-Gaussian fit to the radial distribution of $^{210}\text{Bi}$ background in a six-degree slice. . . . .	103
4.7	IV shapes obtained from a polynomial fit. . . . .	104
4.8	IV shapes obtained from an elliptical fit. . . . .	104
4.9	Time evolution of the nine fit parameters for the eighth order polynomial function. . . . .	105
4.10	Time evolution as in Fig. 4.9, but of the six fit parameters for the elliptical function. . . . .	105
4.11	Comparison of the polynomial and elliptical fit functions with the data as well as the CCD cameras in February 2009. . . . .	106

4.12	Comparison of the polynomial and elliptical fit functions with the data as well as the CCD cameras in Nov 2010. . . . .	106
4.13	The shortest distance to the vessel. . . . .	107
4.14	Zoomed view at the bottom of the detector for the shortest distance to the vessel. . . . .	107
4.15	The vessel shape function for May 17 2009 with reconstructed shortest distances to the IV for all the events. . . . .	108
4.16	The vessel shape function for May 17 2009 with reconstructed shortest distances to the IV for all the events. . . . .	108
4.17	The vessel shape function from Aug 2009 and the calculated DSV values for 15 events. . . . .	108
4.18	The vessel shape function from Aug 2009 and the calculated DSV values for all the 800k events. . . . .	108
4.19	Two-dimensional distribution of the vessel-events used for the shape fit (Red). The IV position is shown in blue. . . . .	109
4.20	In Blue, the mean value of the 2-D fit function from Fig. 4.19, and in Pink, the shortest to the IV at 0.50 m. . . . .	109
4.21	Rotational integration of the vessel profile function obtained for the DST years of 2007 through 2011. . . . .	110
4.22	Spectral shapes of $^{85}\text{Kr}$ and $^{210}\text{Bi}$ in npe. . . . .	112
4.23	$^{210}\text{Bi}$ count rate in the $^7\text{Be}$ -valley. . . . .	113
4.24	$^{210}\text{Bi}$ count rate from spectral fit. . . . .	113

4.25	$^{210}\text{Bi}$ count rate in the $^7\text{Be}$ -valley for the 145-ton fiducial mass. . . . .	114
4.26	The effect of an exponential background component on the mis-identification of the Lomb-Scargle peak. . . . .	115
4.27	$^{210}\text{Po}$ count rate in the FV used in this analysis. . . . .	116
4.28	Spectral fit results for the Borexino data after 90, 192, and 740 days from left to right. . . . .	117
4.29	$^{222}\text{Rn}$ coincidence tagged on in the whole inner vessel between May 2007 and May 2010. FM: 278 t. . . . .	119
4.30	$^7\text{Be}$ count rate without $^{214}\text{Pb}$ reduction. . . . .	119
4.31	$^{222}\text{Rn}$ events radial distribution, weighted by $1/r^2$ . . . . .	119
4.32	Weighted radial distribution of the $^{14}\text{C}$ event within the inner vessel. . . . .	119
4.33	Cross section of the external calibration source impact in [95;380] npe window. . . . .	120
4.34	Cross section of the external calibration source impact in [1000;1280] npe window. . . . .	120
4.35	2-D fit in the energy-to-Gatti space. Data divided into weekly bins and collected from the whole IV. . . . .	121
4.36	Peak positions in the Gatti parameter space obtained for each week. . . . .	121
4.37	Peak positions in the Gatti parameter space in [380;665] npe. From the fit presented in Fig. 4.35 . . . . .	121
4.38	Peak positions in the Gatti parameter space in [665;950] npe. From the fit presented in Fig. 4.35 . . . . .	121

4.39	$^{210}\text{Po}$ npe peak position distribution in weekly bins. Selected data contains events within the whole IV. . . . .	122
4.40	Absolute distance between $^{214}\text{BiPo}$ in three periods, Red: May'07, Green: Jul'09, Blue: Apr'10. . . . .	122
4.41	Temperature readings from the top and bottom regions of detector buffer. Units are degrees Celsius. . . . .	123
4.42	Lomb-Scargle periodogram for the temperature distribution in the top of the outer detector. . . . .	123
4.43	An idea of the PC mixing in the active volume due to temperature gradient.	124
4.44	Asymmetry of the $^{210}\text{Bi}$ count rate between the top and bottom hemispheres	124
4.45	Count rates in the $^7\text{Be}$ -valley for the top and bottom hemispheres. . . . .	124
4.46	Comparison of the energy scale in the top and bottom hemispheres in number of photoelectrons. FM: 145 tons. . . . .	125
4.47	Asymmetry plot of radius for the further most point in the top of the vessel, and the closest in the bottom. . . . .	126
4.48	Asymmetry plot for a fraction of the volumes between the top and bottom hemispheres. . . . .	126
4.49	Top-to-bottom comparison in the window of [1000; 1280] npe for a DSV=0.50 m cut; FM: 170 tons. . . . .	127
4.50	Top-to-bottom comparison in the window of [1280; 1450] npe for a DSV=0.50 m cut; FM: 170 tons. . . . .	127
4.51	Top-to-bottom comparison in the window of [1000; 1280] npe; FM: 145 tons. .	127

4.52	Top-to-bottom comparison in the window of [1280; 1450] npe; FM: 145 tons. .	127
4.53	Visual representation of the inner vessel division into 3 vertical and 72 horizontal regions. . . . .	129
4.54	Reconstructed position of the vessel in the 3 vertical regions: Top, Middle, Bottom. . . . .	129
4.55	RMS of the reconstructed vessel position in the three regions shows no indication of big variation in $\theta$ . . . . .	129
4.56	The inner vessel volume shells. . . . .	130
5.1	Selection of the Spectral Regions for the analysis. . . . .	137
5.2	An example of the electrical signal in a Time-domain. . . . .	137
5.3	Classic Power Spectrum after transformation from the Time-domain. . . . .	137
5.4	Lomb-Scargle Periodogram for an ideal, evenly distributed data-set with a signal variation. . . . .	140
5.5	Lomb-Scargle Periodogram after randomly removing 75% of data points. . . . .	142
5.6	A Monte-Carlo simulation for an ideal sample of $10^4$ Lomb-Scargle periodograms. . . . .	143
5.7	A Lomb-Scargle Monte-Carlo simulation for the 1-day binning. . . . .	144
5.8	A Lomb-Scargle Monte-Carlo simulation for the 60-day binning. . . . .	144
5.9	Duty cycle per day in the data taking phase of Borexino between May 13, 2007 and Feb 17, 2010. . . . .	145
5.10	Comparison of a raw ROOT-file, run 13992, with low-level cuts in a DST-file for the week of Aug_08 2010. . . . .	147

5.11 Comparison of the raw photoelectron spectrum after applying the standard analysis cuts. . . . .	150
5.12 Shapes of the inner vessel obtained from an elliptical fit to background events in the nylon during Phase I. . . . .	151
5.13 Shapes of the IV from an elliptical fit in Phase II. . . . .	151
5.14 Phase I, Fiducial Volume cuts. . . . .	152
5.15 Phase II, Fiducial Volume cut. . . . .	152
5.16 Gatti parameter vs number of p.e in 75 tons. . . . .	153
5.17 Gatti parameter vs number of p.e in 170 tons. . . . .	153
5.18 Energy spectrum of the removed $\alpha$ events in 75 tons. . . . .	154
5.19 Energy spectrum of the removed $\alpha$ events in 170 tons. . . . .	154
6.1 MC simulation of $\alpha$ rate distribution with 10-day binning. Green curve represents the simulated signal. FM: 75 t. . . . .	158
6.2 Lomb-Scargle power spectral sensitivity at 1, 2, 3 sigma with corresponding probability of 65.33, 23.42 and 3.85%. . . . .	158
6.3 MC simulation of $\alpha$ rate distribution with 10-day binning. Green curve represents the simulated signal. FM: 145 t. . . . .	158
6.4 Lomb-Scargle power spectral sensitivity at 1, 2, 3 sigma with corresponding probability of 81.62, 43.54 and 11.68%. . . . .	158
6.5 Rates distribution with 10-day binning. $^7\text{Be}$ -valley count-rate was shifted by a const. number. FM: 75 t. . . . .	159

6.6	Lomb-Scargle periodogram from Fig. 6.5. A significant peak close to 1-year period was identified at SPD of 7.411. . . . .	159
6.7	Rates distribution with 10-day binning. ${}^7\text{Be}$ -valley count-rate was shifted by a const. number. FM: 145 t. . . . .	159
6.8	Lomb-Scargle periodogram from Fig. 6.7. A similar peak close to 1-year period was identified at SPD of 7.961. . . . .	159
6.9	Count rates in the ${}^7\text{Be}$ FV for 60-day binning. . . . .	161
6.10	Sinusoidal, best fit results for the 145 t fiducial mass. . . . .	163
6.11	$\chi^2$ profile for eccentricity in 145 tons. . . . .	163
6.12	Residuals distribution for the sinusoidal fit in 145 tons. . . . .	163
6.13	Residuals normal probability distribution. . . . .	163
6.14	2 d.o.f. $\chi^2$ profile for eccentricity with respect to period. . . . .	164
6.15	2 d.o.f. $\chi^2$ profile for eccentricity with respect to $\nu$ -rate. . . . .	164
6.16	The expected annual modulation of 48.30 cpd of ${}^7\text{Be}$ $\nu$ . . . . .	165
6.17	The expected annual modulation of 47.40 cpd for the removed data. . . . .	165
6.18	Earth-Sun distance between May 13, 2007 and May 8, 2010. . . . .	166
6.19	Comparison of normalized spectra between the maximum and minimum Earth-to-Sun distance. . . . .	166
6.20	Spectral fit results for the whole data-set. . . . .	167
6.21	Spectral fit results for the whole data-set and only the minimal Earth-Sun distance. . . . .	167

6.22 Spectral fit results for the whole data-set and only the maximal Earth-Sun distance. . . . .	167
6.23 Earth-Sun distance for the periods considered in this analysis. . . . .	169
6.24 Comparison of normalized spectra between the maximum and minimum Earth-to-Sun distance. . . . .	169
6.25 Spectral fit results for the selected data-set. . . . .	170
6.26 Spectral fit results for the selected data-set and only the minimal Earth-Sun distance. . . . .	170
6.27 Spectral fit results for the selected data-set and only the maximal Earth-Sun distance. . . . .	170
6.28 History of the inner vessel shapes in Phase II. . . . .	173
6.29 Gatti parameter cut definition in Phase II. . . . .	173
6.30 ${}^7\text{Be}$ rate distribution. ${}^7\text{Be}$ -valley count-rate was scaled by a const. number. FM: 145 t. . . . .	174
6.31 Count rate in 60-day binning in comparison with the expected modulation (green curve). . . . .	174
6.32 A prediction for 28 months in Phase II with stable backgrounds. . . . .	175
6.33 Detection sensitivity in Phase II, based on Lomb-Scargle. . . . .	175
7.1 A Monte-Carlo simulation of $\sim 10^4$ events in Borexino. Phase I, FM: 145 t. . . . .	177
7.2 A Monte-Carlo simulation of $\sim 10^4$ events in LENA. . . . .	177
7.3 The evolution of the inner vessel shapes during Phase I. . . . .	178

7.4	$^{210}\text{Bi}$ background count-rates throughout Phase I, FM: 145 tons. . . . .	178
7.5	Count-rates in the energy window of interest in Phase I. . . . .	178
7.6	Count-rates in the energy window of interest in Phase II. . . . .	178

# List of Tables

2.1	The Fundamental Particles of SM, according to their flavors and electric charges	9
2.2	Solar composition given as $\log \epsilon_i = \log N_i/N_H + 12$ .	14
2.3	Reference effective neutrino fluxes at Earth calculated at $1\sigma$ , in the units of $cm^{-2} s^{-1}$ .	20
2.4	Various neutrino sources and their associated experimental sensitivities.	26
3.1	Dimensions of the SSS, as measured before filling in 2007. All values in mm.	73
3.2	Diameter of the SSS. All values in mm.	73
3.3	The reconstructed and nominal source position for the laser source calibration data.	80
3.4	The radioactive sources used in the Borexino internal calibration campaigns.	83
3.5	Comparison of $\gamma$ radioactive source count rates for Method I, as described in the text.	89
3.6	Results of the trigger efficiency test.	90

4.1	Division of the official Borexino Phase I periods into six, approximately even in terms of live time groups. . . . .	113
4.2	Major operations on the Borexino scintillator that are responsible for the increase in $^{210}\text{Po}$ count rate. . . . .	116
4.3	Table for one-year long periods, presenting comparison of the spectral fit with rates for $^7\text{Be}$ , $^{85}\text{Kr}$ , and $^{210}\text{Bi}$ . . . . .	133
4.4	Table for six-month long periods, presenting comparison of the spectral fit with rates for $^7\text{Be}$ , $^{85}\text{Kr}$ , and $^{210}\text{Bi}$ . . . . .	133
4.5	Table for one-year long periods with a comparison of the stability fit parameters. . . . .	134
4.6	Table for six-month long periods with a comparison of the stability fit parameters. . . . .	134
5.1	Spectral regions of interest (also indicated with various colored regions in Fig. 5.1). . . . .	136
5.2	Fraction of $\beta$ spectra in the $^7\text{Be}$ window according to Fig. 5.1 in the units of photoelectrons and counts/day-100t. . . . .	138
5.3	Detection efficiency with a Lomb-Scargle method for the two extreme binning cases, 1-day and 60-day. . . . .	144
5.4	Definition of the fiducial volumes used in the different solar neutrino analyses.	151
5.5	Definition of the fiducial volumes for the annual modulation study in Phase I and II. . . . .	152

5.6	Fractions of $\beta$ events in the energy regions affected by the Gatti cut (FM: 145 tons.). Species available from a Monte-Carlo simulation in Borexino. . . . .	155
5.7	List of rejected periods from the analysis in both Phase I and II. . . . .	155
6.1	Correlation matrix for the fit parameters in Fig. 6.10. . . . .	164
6.2	Collection of the spectral fit results for the whole data-set. . . . .	168
6.3	Collection of the spectral fit results for the selected data-set. . . . .	171
6.4	Summary of the spectral fit results. . . . .	171
7.1	Comparison of all the results presented in Section 6.1 for the FM of 145 tons. . . . .	179
A.1	Table of Abbreviations. . . . .	180
B.1	Table of operations and maintenance of the Borexino detector. . . . .	182

# Chapter 1

## Introduction

A precision measurement of the  ${}^7\text{Be}$   $\nu$  rate provided the first evidence for the matter-enhanced solar neutrino oscillation scenario with the Borexino detector [2]. In this case, lack of oscillations was excluded at  $5\sigma$  Confidence Level (C.L.). Further measurements of the (absence) of the Day-Night asymmetry of the  ${}^7\text{Be}$  solar neutrinos [3], disfavored a scenario of neutrino regeneration in the Earth's matter at the level of  $8.5\sigma$ . Finally, with the annual modulation search of the signal in Borexino, we can probe a possibility of vacuum oscillations of neutrinos on their way to Earth. If however, the currently favored model of oscillations in the solar mass is correct, we expect to observe a normal effect of inverse-square dependence of the rate with the varying Earth-Sun distance. The first such measurement was attempted by the Super-Kamiokande [4] and SNO [5] collaborations in 2004 and 2005, respectively. Even though these results were in agreement with the expectations, their significance was not high enough to claim a discovery. Also in Borexino, we are limited mainly by the available statistics, with the expected signal of 50 counts/(day x 100 ton), and the 7% peak-to-peak modulation, the signal we search for is already on the order of the statistical error.

A structural layout of this work is presented below with a brief description of each chapter:

- In Chapter 2 we will introduce the reader to our current understanding and state of the neutrino field with a major focus on the solar physics. We will also discuss the astronomical origins of the annual flux modulation, the topic of this thesis work.
- Chapter 3 focuses on the Borexino detector itself; it describes its conceptual design, construction and its first prototype, the Counting Test Facility. The presence of the internal as well as the external backgrounds will become critical in understanding of the signal stability, which ultimately becomes one of the most important aspects of this work.
- Chapter 4 is entirely devoted to the study of the stability conditions. Both the natural impurities with background fluctuations, but also mechanical changes of the detector's vessel shape will provide important input for the understanding of the stability. We will also discuss certain aspects of the environmental changes, such as the temperature or external operations that were difficult to monitor but could potentially affect our results.
- Chapter 5 is the framework of this work; it presents strict requirements for the selection of events used in the analysis, sophisticated tools implemented in the production of the neutrino spectra, and some critical methods developed specifically for the search of periodicities in the signal. It forms the critical arsenal for this study.
- All results are presented in Chapter 6. Starting from the background stability checks we go over the verification with Monte-Carlo simulations and an attempt to estimate the major background levels. Results of the techniques for measuring the time and frequency domains that were previously discussed are also presented.
- To conclude this document, a list of final remarks and comments has been included in the last chapter.

# Chapter 2

## Neutrinos

A new chapter in particle physics was opened in 2002, when pioneers of early neutrino discoveries, Ray Davis and Masatoshi Koshihira, became recipients of the Noble Prize in physics. Their work comprised a thirty-year-long measurement of solar neutrinos in Homestake, USA, as well as the first observation of supernovae neutrinos in 1987. But this was only the tip of the iceberg of what was to be discovered in the neutrino world. Shortly thereafter, confirmation of inter-flavor conversion of neutrinos had opened even newer questions about the Standard Model (discussed in Section 2.1), which has served as the most coherent theory in particle physics for over three decades.

The story of neutrinos started back in the days of Wolfgang Pauli, when he hypothesized the existence of a particle that could explain the continuous spectrum of radioactive  $\beta^-$  decay, previously analyzed by James Chadwick. When in 1932, Enrico Fermi proposed his theory of weak interactions that could calculate cross-sections of an inverse  $\beta^-$ -decay for the anti-neutrino [6], it was quickly discovered how difficult it would be to detect such a particle: a whole galaxy of water would be necessary for only one neutrino to interact with matter. It was Fermi who coined the term *neutrino* to describe this small and neutral particle. In

fact, there are three known light-weight and so-called, active neutrinos in physics. After the discovery of the  $\mu$  particle in 1947, Pontecorvo speculated that because muons undergo only weak interactions, similarly to the electrons, they might be decaying into a different type of neutrino. The first accelerator experiment confirmed that after the interaction of the anti-neutrino beam from  $\pi$  decays, there were mostly  $\mu$ 's created in the detector [7], as opposed to the electrons that would normally be created in the inverse  $\beta$ -decay. Then, in 1975, the third, heaviest particle of the lepton family was discovered, the  $\tau$  [8]. It was also speculated that  $\tau$  would be accompanied by its own neutrino flavor, which was not experimentally confirmed until the end of the century. The DONuT (Direct Observation of the NU Tau) collaboration chose a similar approach to SLAC (Stanford Linear Accelerator Center), and in proton-proton collisions they had been searching for rare decays of  $\tau$  into  $\nu_\tau$  and two muons. Their first results were based upon only 4 detected charged current interactions of  $\nu_\tau$ . Nevertheless, thanks to extremely low backgrounds this was sufficient to confirm the existence of a  $\nu_\tau$  neutrino [9]. Although these discoveries only pertain to light neutrinos (whose masses do not exceed half the mass of  $Z^0$  bosons) the presence of more flavors of ultra-heavy neutrinos was proposed in such models as the Grand Unified Theory. But for now, we will focus on the current situation in the neutrino and particle physics field.

## 2.1 The Standard Model of Particle Physics

The Standard Model (SM) is the most commonly used model governing the physics of particles, and it is thus important to understand its foundation. Modern versions of the SM were first established in the early 70s of the previous century, and provided a framework for explaining fundamental processes in elementary particle physics and chemistry. It includes

strong interactions through the color charges of quarks and gluons and a combined theory of electroweak interactions, with bosons W and Z as carriers of the weak force, and photons as carriers of the electromagnetic force. As it can be seen in Figure 2.1, 25 particles (12 Fermions, 8 gluons, 2 W bosons) make up for the matter generation, gauge, and the Higgs boson. Some are accompanied by pairs of anti-particles (W and Fermions), and some are their own anti-particles (Gluons, Z, the Higgs and Photons).

	Fermions			Bosons	
Quarks	$u$ up	$c$ charm	$t$ top	$\gamma$ photon	Force carriers
	$d$ down	$s$ strange	$b$ bottom	$Z$ Z boson	
Leptons	$\nu_e$ electron neutrino	$\nu_\mu$ muon neutrino	$\nu_\tau$ tau neutrino	$W$ W boson	
	$e$ electron	$\mu$ muon	$\tau$ tau	$g$ gluon	
				Higgs boson	

Source: AAAS

**Figure 2.1:** Sixteen fundamental particles of the Standard Model of Particle Physics. Fermions of spin  $-\frac{1}{2}$  plotted to the left, and the Gauge Bosons of spin 1 to the right.

These particles and their interactions can be used in the SM to create any other form of matter, and as a result, provide the theoretical and experimental layout for potential new discoveries. Fermions are usually referred to as the matter constituents and twelve elementary particles belong to this group. The fact that fermions are the only particles<sup>1</sup> that respect the Pauli exclusion principle was used by Dirac to explain negative energy states in the solutions of his relativistic wave equations, leading to the discovery of the electron's antiparticle, the positron [10]. Multiple bosons on the other hand can occupy one quantum state without

<sup>1</sup>To be precise, only the  $W^+$  and  $W^-$  bosons are the true particle-anti-particle pair, the rest, such as photons, gravitons and potentially the Higgs bosons are all their own anti-particles

violation of the Fermi principle. They are also the force carriers and, as depicted in Figure 2.2, they are responsible for the fundamental interactions via the exchange of:

- Photons: carries of the *electromagnetic* force for the charged particles even though they do not carry charge themselves,
- $W^+$ ,  $W^-$ ,  $Z$  bosons: responsible for the *weak* interaction;  $W$  and  $Z$  bosons are very massive compared to other elementary particles. At energies beyond 100 GeV, both photons and  $W$  and  $Z$  bosons are often merged into a *unified theory* of electroweak interactions. Such conditions were satisfied shortly after the Big Bang at temperatures of  $\sim 10^{15}$  K.
- Gluons: the *strong* force mediators for the color charged quarks; they are massless particles and because of their eight independent color-states they can interact between themselves.

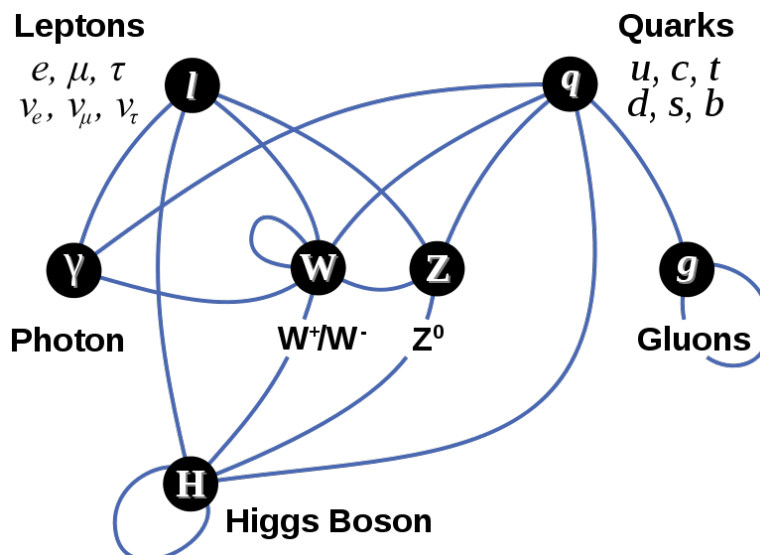


**Figure 2.2:** *Standard Model of Particle Interactions. There are four fundamental forces in nature: Strong, Electromagnetic, Weak, and Gravitational of which only the gravitation is not included in the model.*

## The God(damn) Particle

Initially proposed back in the 1960's by Peter Higgs of Edinburgh University [11], the Higgs boson remained undiscovered for a very long time, hence the original name *the Goddamn Particle* which later evolved to a more commonly used *God Particle*. At the same time, it was the only part of the SM that could explain the masses of particles and the nature of the remaining force type through the Higgs field mechanism. Over a decade of experiments using the most powerful particle accelerators in the world, such as SLAC and FermiLab had not revealed any sign of the Higgs presence, setting only limits on its mass reaching over  $80 \text{ GeV}/c^2$ . In early 2010, the Large Hadron Collider (LHC) began its operation in CERN at a center-of-mass energy of  $7 \text{ TeV}$ . The first results from the Compact Muon Solenoid experiment (CMS) were in perfect agreement with the predictions of the SM, leaving only the region below  $145 \text{ GeV}/c^2$  of the Higgs mass with hopes for its discovery. In July 2012, the two collaborations, CMS and ATLAS identified for the first time the characteristic decay products of the Higgs particle at  $5\sigma$  confidence level and announced the discovery of a new particle with a mass of  $125 \text{ GeV}/c^2$  ([12], [13]).

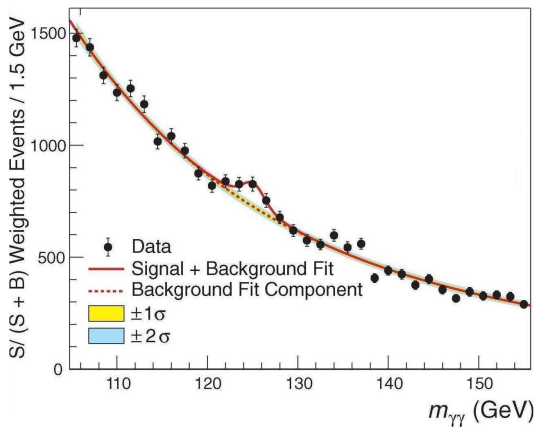


**Figure 2.3:** *Di-photon ( $\gamma\gamma$ ) invariant mass distribution for the 7- and 8-TeV data collected by CMS. Figure from [12].*

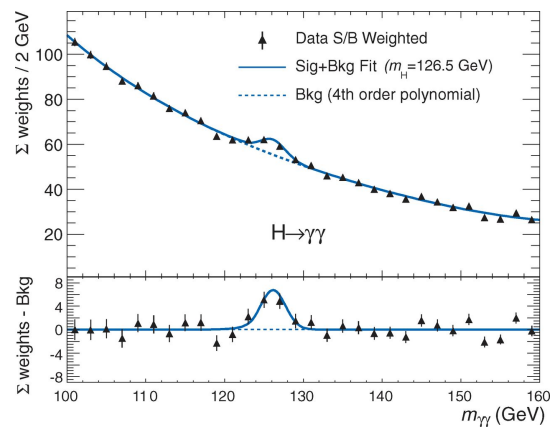


**Figure 2.4:** *Di-photon ( $\gamma\gamma$ ) invariant mass distribution for the 7- and 8-TeV data collected by ATLAS. Figure from [13].*

The principle behind the detection in both the experiments is the same; they look at the decay products of unstable particles in proton-proton collisions. In many cases it involves looking at the secondary products due to their longer decay times. The Higgs particle itself is also unstable and undergoes decay through various channels. For instance at 125 GeV the SM predicts the following possibilities:  $H \rightarrow WW$  (BR = 14%),  $H \rightarrow ZZ$  (BR = 1.6%), and  $H \rightarrow \gamma\gamma$  (BR = 0.23%). Even though the di-photon channel ( $\gamma\gamma$ ), is characterized by such a small branching ratio, it is at the same time, the easiest tag for both the CMS and ATLAS detectors. In the two di-photon plots in Figures 2.3 and 2.4, we observe a visible excess of events around the mass of 126 GeV. Assuming the absence of the Higgs boson in the given mass range, the probability for the background fluctuation that would imitate the observed signal are on the order of one in three million, which corresponds to about a  $5\sigma$  C.L.

## Other Fundamental Particles

Quarks and leptons are not only fundamental particles in physics, they are the fundamental constituents of all the matter that we observe. Both particles come in three flavors, which are then grouped into families, or generations, each accompanied by their own anti-particle respectively. Such structures result in 12 different types of particles (as well as anti-particles) as shown in Fig. 2.1 and listed in Table 2.1.

**Table 2.1:** *The Fundamental Particles of SM, according to their flavors and electric charges*

Fermions				Bosons	
Leptons	Charge	Quarks	Charge	Particle	Charge
$\nu_e$	0	$u$ :up	$+\frac{2}{3}$	$\gamma$	0
$e$	-1	$d$ :down	$-\frac{1}{3}$	$W^-$	-1
$\nu_\mu$	0	$c$ :charm	$+\frac{2}{3}$	$W^+$	+1
$\mu$	-1	$s$ :strange	$-\frac{1}{3}$	$Z^0$	0
$\nu_\tau$	0	$t$ :top	$+\frac{2}{3}$	$gluon$	0
$\tau$	-1	$b$ :bottom	$-\frac{1}{3}$	$Higgs$	0

*Hadron* is the term used for any particle composed of either quark-anti-quark pairs, or triplets, coupled using strong forces mediated by gluons (as presented in Fig. 2.2). *Baryons* are normally made up of triplets, with either pure quarks ( $qqq$ ) or anti-quarks ( $\bar{q}\bar{q}\bar{q}$ ), whereas *mesons* represent pairs of quark-anti-quark ( $q\bar{q}$ ). This rule in the SM is called *quark confinement*; regardless of the composition, the resulting *Hadron* must be colorless<sup>2</sup>.

As it has been shown, quarks can interact via more than only the two fundamental forces, strong and electromagnetic, but in fact, they can also exchange the W and Z bosons making the quarks susceptible to weak interactions leading to flavor change. Such mixing of weak eigenstates ( $d', s', b'$ ), along with the corresponding mass eigenstates ( $d, s, b$ ), is represented by the Cabibbo-Kobayashi-Maskawa (CKM) matrix, as displayed below:

$$\begin{pmatrix} |d'\rangle \\ |s'\rangle \\ |b'\rangle \end{pmatrix} = \begin{pmatrix} V_{ud} & V_{us} & V_{ub} \\ V_{cd} & V_{cs} & V_{cb} \\ V_{td} & V_{ts} & V_{tb} \end{pmatrix} \begin{pmatrix} |d\rangle \\ |s\rangle \\ |b\rangle \end{pmatrix} = V_{\text{CKM}} \begin{pmatrix} |d\rangle \\ |s\rangle \\ |b\rangle \end{pmatrix}, \quad (2.1)$$

where,

$$V_{CKM} = \begin{pmatrix} c_{12}c_{13} & s_{12}c_{13} & s_{13}e^{-i\delta} \\ -s_{12}c_{23} - c_{12}s_{23}s_{13}e^{i\delta} & c_{12}c_{23} - s_{12}s_{23}s_{13}e^{i\delta} & s_{23}c_{13} \\ s_{12}s_{23} - c_{12}c_{23}s_{13}e^{i\delta} & -c_{12}s_{23} - s_{12}c_{23}s_{13}e^{i\delta} & c_{23}c_{13} \end{pmatrix}, \quad (2.2)$$

and  $s_{ij} = \sin\theta_{ij}$ ,  $c_{ij} = \cos\theta_{ij}$  with  $\theta_{ij}$  being angles rotating in flavor space and  $\delta$  is the CP violating phase. This form of parametrization was used by Particle Data group as the default parametrization[14].

Leptons, as in the case of the quarks group of the three families, are each composed of two particles (charged  $e/\mu/\tau$  | non-charged  $\nu_e/\nu_\mu/\nu_\tau$ ) as listed in Table 2.1. As the strong in-

---

<sup>2</sup>Standard colors assigned to quarks are, *Red, Green, Blue*

interactions rule color charge, leptons do not undergo such an exchange. They can, however, interact via weak nuclear forces that transform them from one to another. According to the classic version of SM, neutrinos are assumed to be massless particles, thus forbidding any inter-flavor oscillations due to the presence of only one weak-eigenstate (which for a massive particle would mean a linear combination of energy eigenstates, allowing flavor conversions as the neutrino traverses space). There have been attempts to implement massless neutrino oscillation models (e.g. by Sheldon Glashow), but since this approach would require intricate complexity it is no longer considered.

## 2.2 Solar Neutrino Physics

Solar neutrinos are the products of nuclear fusion that powers all active stars. While there are many neutrinos available on Earth from sources other than the Sun, their overall flux, types and energies are different, giving us the unique opportunity to study stellar internal processes. In the next two sections, we will introduce to the reader our current understanding of the solar model and the thermonuclear processes in the solar core that result in the creation of the solar neutrinos.

### The Standard Solar Model

The history of The Standard Solar Model (SSM) began in the early 1960's when Ray Davis and John Bahcall started collaborating on possible neutrino experiments. Shortly after, it turned out that without a detailed model of the Sun a precise calculation of the solar neutrino flux would not be possible. John Bahcall, Dick Sears and Icko Iben, originally

involved in stellar evolution, generated the first numerical prediction of the solar production. Generally speaking, the Sun relies on a simple principle of equal and opposite forces, the gravitational contraction and the pressure caused by the thermonuclear processes in its interior (gas and radiation pressures). The hydrostatic equilibrium is achieved on a short time scale of about an hour for each volume element in the Sun. The SSM assumes that the Sun can be approximated by a spherically symmetric plasma sphere, constrained by the luminosity, radius, age and composition. The model of the Sun is based on conservation laws (mass, momentum, and energy) and energy transport equations. The equations are usually written in a differential form [15] (here,  $r$  is distance to the center,  $\rho$  is density,  $p$  is pressure):

- **Conservation of Mass:** Mass usually remains constant over the lifetime of a star while the radius changes, that's why it is better to express the equation leaving the mass as an independent parameter:

$$\frac{dm}{dr} = 4\pi r^2 \rho \quad (2.3)$$

$m$  is the stellar mass contained within radius  $r$ .

- **Conservation of Energy:** It is the net energy passing outwards through a shell at radius  $r$ , some of that energy may be absorbed or released within the shell:

$$\frac{dL}{dr} = 4\pi r^2 \left[ \rho \epsilon - \rho \frac{d}{dt} \left( \frac{u}{\rho} \right) + \frac{p}{\rho} \frac{d\rho}{dt} \right] \quad (2.4)$$

$L$  is the flow of energy per unit time through the sphere of radius  $r$ ,  $\epsilon$  is the rate of nuclear energy generation per unit mass and time, and  $u$  is the internal energy per unit volume.

- **Hydrostatic Equilibrium:** This equilibrium balances the radiative pressure against gravity; The weight in one solar shell must cancel the pressure difference felt from the other shell, thus:

$$\frac{dp}{dr} = -\frac{Gm\rho}{r^2} \quad (2.5)$$

$G$  is the gravitational constant.

- **Thermal Structure:** Through a temperature gradient ( $\nabla = d\ln T/d\ln p$ ) we can express the thermal structure for a star in hydrostatic equilibrium as:

$$\frac{dT}{dr} = \nabla \frac{T}{p} \frac{dp}{dr} \quad (2.6)$$

Provided the initial and boundary conditions, these four equations describe the time evolution of a star with a given distribution of chemical abundance for various elements,  $X_i$ , with  $i = 1, 2, 3, \dots$ . However, due to the nuclear reactions that power the stars, we need one additional equation to capture the changing chemical composition. This equation describes the evolution of  $\partial X_i/\partial t$  as a function of  $\rho$ ,  $T$  and  $X_j$ . In the case of hydrogen, the equation takes the following form:

$$\frac{\partial X}{\partial t} = R_H + \frac{1}{r^2 \rho} \frac{\partial}{\partial r} \left[ r^2 \rho \left( D_H \frac{X}{r} + V_H X \right) \right] \quad (2.7)$$

Similarly parametrized for other elements, where  $R_H$  is the rate of change in hydrogen abundance,  $D_H$  is the diffusion coefficient and  $V_H$ , the settling speed.

Variations of the SSM calculations can be achieved by using different input parameters. The initial work by Grevesse & Sauval [16] resulted in establishing some golden standards in the measurement of solar abundances, measurements that are usually performed through mass spectroscopy of meteorites or analysis of the Fraunhofer spectral lines of the photosphere

in the visible range. Table 2.2 presents solar composition for the most important models. (GS98, [16]), also known as the *High-Z* model, is the only one that agrees the most closely with helioseismology, a study of solar oscillations originating from acoustic waves in the solar interior [17], [18]. Unfortunately, the most recent corrections implemented in 2005 (AGS05, [19]) and 2009 (AGSS09, [20]; AGSS09<sub>ph</sub><sup>3</sup>, [21]) resulted in significantly lower elemental abundances, thus these models are often referred to as the *Low-Z* models.

**Table 2.2:** *Solar composition given as  $\log \epsilon_i = \log N_i/N_H + 12$ .*

Element	GS98	AGS05	AGSS09	AGSS09 <sub>ph</sub>
C	8.52	8.39	8.43	8.43
N	7.92	7.78	7.83	7.83
O	8.83	8.66	8.69	8.69

## Solar Fusion Reactions

The question of what powers the Sun was the main concern for scientists in the 19th century. It was not until Einstein's equation for the mass-energy equivalence that the mystery started to lead to new theories. Today, we already know that the reason why we receive energy on Earth in all the available forms is hidden deep in the solar core. The electrostatic forces between protons are overwhelmed by enormous pressures in the solar core which increase the probability for them to fuse. This major process, called the *proton-proton* chain, was first laid out by Hans Bethe in 1939 [22]. The conversion of protons and electrons into an  $\alpha$ -particle can be formally described in the following way:



From Equation 2.8 we can derive a simple relation between the total number of neutrinos

<sup>3</sup>It is a SSM based only on the latest estimated photospheric metal composition.

emitted by the Sun with respect to the observed photon energy on Earth, the so called luminosity constraint, further discussed in [23]. It assumes that we know all the fusion reactions that contribute to the overall neutrino flux, and that the rate of these reactions is stable in time, as it takes approximately  $10^5$  years for the energy generated in the solar core, other than neutrinos, to reach the surface. The limit on the expected solar neutrino flux can be summarized in the following form:

$$\Phi_\nu = \frac{2L_\odot}{26.7\text{MeV} \cdot 4\pi r^2} \quad (2.9)$$

Where  $L_\odot$  is the solar luminosity,  $r$  the Earth-Sun distance, and the factor of 2 in the equation above is a result of 2 neutrinos being emitted every time 26. MeV of energy is released in reaction 2.8.

The  $pp$ -chains are a dominant reaction in the Sun (or stars of  $\sim 1.3 M_\odot$ ), but for more massive stars, where the core temperatures are much higher, an additional cycle is also present. It relies on the catalytic burning of hydrogen via heavier elements such as Carbon, Nitrogen and Oxygen; hence the name, the  $CNO$ -cycle. Also present in the Sun, although contributing no more than 2% to the total energy output, the  $CNO$ -cycle is a crucial process in the study of the SSM. We will now review some of the important aspects of both cycles.

**The  $pp$  Chain** This cycle begins with the formation of a deuteron through the interaction of the protons; due to the nature of the process it is the slowest reaction in the whole chain (it is governed by the weak interaction). The energy release is given in the parentheses.



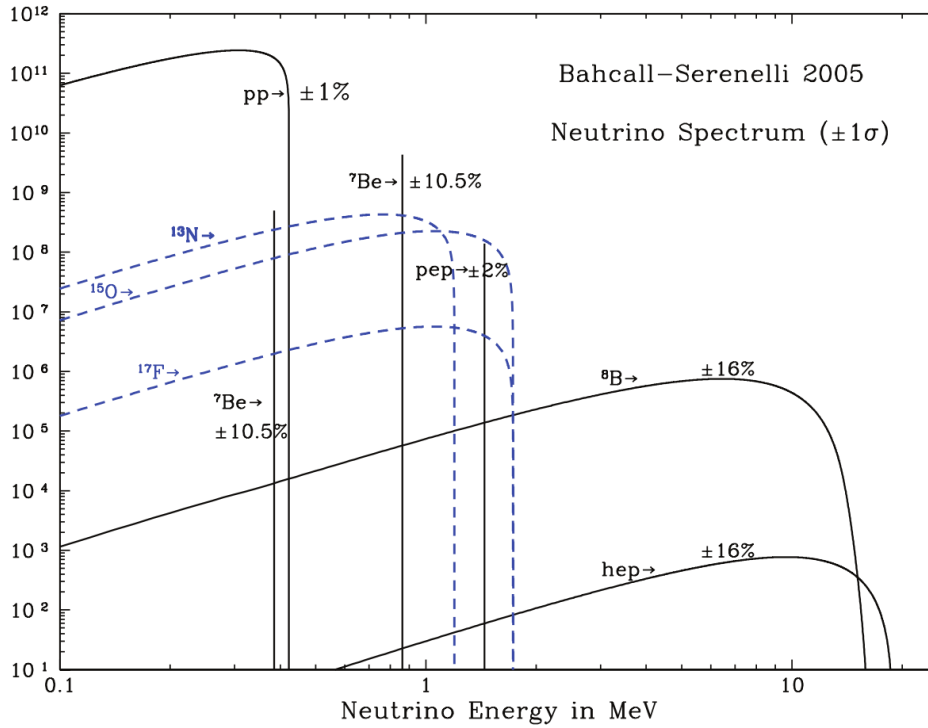


**Figure 2.5:** A complete Solar  $pp$ -chain and resulting neutrino spectrum as predicted by the Standard Solar Model (Bahcall and Pinsonneault 2004) The neutrino fluxes from continuum sources (like  $pp$  and  ${}^8\text{B}$ ) are given in the units of counts per  $\text{cm}^{-2}\text{s}^{-1}\text{MeV}^{-1}$  at one astronomical unit. The monochromatic fluxes ( $pep$  and  ${}^7\text{Be}$ ) are given in counts per  $\text{cm}^{-2}\text{s}^{-1}$ . Dashed lines represent the CNO cycle, and the yellow box depicts the energy range available in Borexino. Figure from [24].

Equation 2.11 presents the dominant reaction that generates a continuous neutrino flux with a contribution of more than 99% of the solar neutrino spectrum. This is also the best known reaction in the SSM with an uncertainty of about 1% (assuming the luminosity constraint). The second path to the deuteron generation involves three particles and its rate is, by factor of 400, smaller than the  $pp$  process. It results in a production of a monoenergetic neutrino at 1.44 MeV.

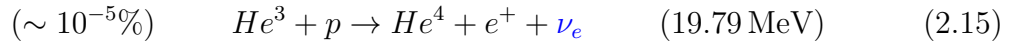
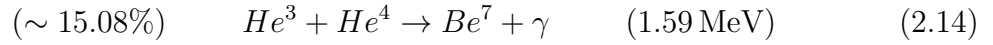
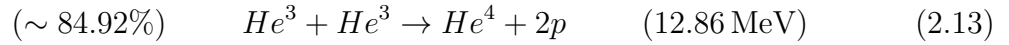


The remaining part of the  $pp$  chain can be conveniently divided into three individual sub-branches,  $pp$ -I,  $pp$ -II and  $pp$ -III.

- **PP-I** In the first step, a proton interacts with the deuteron from the initial process:

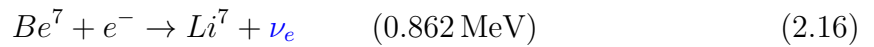


The created  $He^3$  nuclei can now take part in the following three reactions, one of which results in the emission of another neutrino, the so-called *hep* flux:



The rare *hep* weak interaction (2.15) generates the smallest neutrino flux among the three, with a contribution on the order of only  $10^{-5}\%$ , but at the same time, it gives the highest energy in the neutrino spectrum.

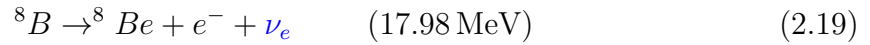
- **PP-II** In the second branch, a vast majority (more than 99%) of the  ${}^7\text{Be}$  generated via process from equation 2.14 is terminated in the electron capture in a two-stage reaction:



Neutrinos emitted in reaction 2.16 are monoenergetic and 10% of the time  $Li^7$  is created in an excited state. As a result,  ${}^7\text{Be}$   $\nu$  have two lines at 0.862 and 0.384 MeV that were the major goal of the Borexino detector flux measurement ([2], [25], [26]).

- **PP-III** The remaining 0.1% of  ${}^7\text{Be}$  from the previous processes is terminated via a

very rare process of proton absorption. It leads however, to the most energetic solar neutrinos, the  ${}^8\text{B}$   $\nu$ .



The high energy of  ${}^8\text{B}$   $\nu$ s allowed their detection in the early experiments such as Super-Kamiokande, where the spectrum below 6.5 MeV was unaccessible [27]. In the later years, it also allowed for the first time in history the detection of solar neutrino oscillations at Sudbury Neutrino Observatory (SNO) [28].  ${}^8\text{B}$   $\nu$ 's were also measured by the Borexino collaboration with a threshold of 3 MeV ([29]).

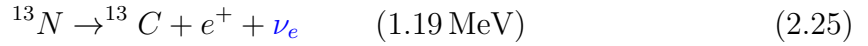
**The CNO Chain** The most significant aspect of this cycle is the fact that Carbon, Nitrogen and Oxygen were not naturally produced in the solar core, at least at this stage of solar evolution, where the temperatures are too low for the fusion of Helium-4 into heavier elements (this is also referred to as the *triple alpha* process). The elements of C, N, O are in fact impurities in the solar atmosphere and they act as catalysts. The process forms Helium-4 nucleus out of four protons via the following net process:



Neutrinos are emitted in the  $\beta^+$  decays of the cycle. There are two major sub-processes in the CNO-cycle, the so-called *CN*, and *NO* sub-cycles.

- **The CN-loop** This cycle makes 99.5% of the whole chain. The following reactions

are a part of it:



- **The NO-loop** This cycle is responsible for only 0.5% of the total *CNO* flux:



Contribution of the *CNO* neutrinos to the solar luminosity is negligible, below 1%. However, the importance of experimental confirmation of such processes in stars is critical. The measurement would not only confirm how massive stars are powered but would also help in resolving the current Sun's metallicity controversy. To date, the best experimental constraint on the *CNO* neutrino flux was established by the Borexino collaboration [30].

Finally, all the solar fluxes for the *pp*- and *CNO*-chains that were presented in this chapter for different abundance models are summarized once again in Table 2.3.

**Table 2.3:** Reference effective neutrino fluxes at Earth calculated at  $1\sigma$ , in the units of  $\text{cm}^{-2} \text{s}^{-1}$ .

Source	GS98	AGS05	AGSS09	AGSS09ph
pp ( $\times 10^{10}$ )	5.97	6.04	6.03	6.01
pep ( $\times 10^8$ )	1.41	1.44	1.44	1.43
hep ( $\times 10^3$ )	7.91	8.24	8.18	8.1
${}^7\text{Be}$ ( $\times 10^9$ )	5.08	4.54	4.64	4.79
${}^8\text{B}$ ( $\times 10^6$ )	5.88	4.66	4.85	5.22
${}^{13}\text{N}$ ( $\times 10^8$ )	2.82	1.85	2.07	2.15
${}^{15}\text{O}$ ( $\times 10^8$ )	2.09	1.29	1.47	1.55
${}^{17}\text{F}$ ( $\times 10^6$ )	5.65	3.14	3.48	3.7

**Problems with the SSM** The decrease in abundances results in a change of the core temperature of the Sun, and as a result a drastic drop in the fluxes of  ${}^7\text{Be}$  and  ${}^8\text{B}$  neutrinos that are strongly correlated with the core temperature (a decrease in one flux brought an increase in the production of the  $pp$  neutrinos). (see Table 2.3 for reference). Unfortunately, the predictions from models (AGS05, AGSS09, AGSS09ph) do not agree with the helioseismology measurements based on the speed of sound related to a change in the temperature gradient- the discrepancy is by about a factor of five worse than in the (GS98) models. Certain solutions to this so-called second order neutrino problem have been already proposed: they assume higher opacities in the solar interior thus increasing the fusion rates. However, this would require the abundance levels of Helium to be in disagreement with prediction and also enforce a non-uniform distribution of the *High*- and *Low* -  $Z$  zones. This in turn, would conflict with the seismic measurements of the speed of sound.

As a consequence, it becomes critical for the solar experiments to be able to determine the neutrino flux with a very high precision. We can also try to draw a prediction whether with these abundances we would have a chance to determine the correct model using Borexino or SNO data however, as it can be seen in Figure 2.6, with  $1\sigma$  error bars it is impossible to distinguish the two.

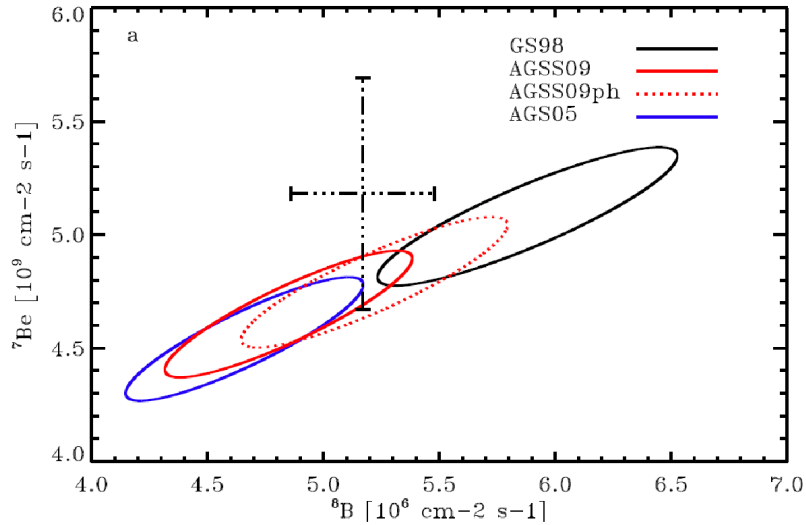


**Figure 2.6:** Prediction for the  ${}^7\text{Be}$  and  ${}^8\text{B}$  for different abundance models as listed in Table 2.2. The dashed-black line indicates central values from Borexino and SNO (at  $1\sigma$ ). Figure from [31].

## 2.3 Neutrino Oscillations

In the originally formulated Standard Model, neutrinos were considered to be massless particles. As a result, individual flavors cannot freely convert into one another. In principle, it would be against the conservation of the lepton number (the number of leptons minus the number of anti-leptons) individually for the three families. In this case, because the helicity of neutrinos is always left-handed, whereas anti-neutrinos are right-handed, a mirror image of a neutrino would correspond to the right-handed particle that does not, in fact, exist in nature.

For example, even at the time when the SM was being formulated, Bruno Pontecorvo had already proposed (1958) the possibility of flavor conversion in the neutrino sector, as this model assumed zero-neutrino mass, [32], [33]. In 1962, Maki's collaboration postulated that even if only one neutrino mass was non-zero, the mass eigenstates  $|\nu_1\rangle$ ,  $|\nu_2\rangle$ ,  $|\nu_3\rangle$  would not necessarily have to be equivalent to their weak eigenstates  $|\nu_e\rangle$ ,  $|\nu_\mu\rangle$ ,  $|\nu_\tau\rangle$ , with a mixing matrix  $\hat{U}_{\alpha i}$ , also known as a  $\hat{U}_{PMNS}$ , an analogue to the CKM matrix for quarks (as shown in

Equation 2.32 and 2.35), [34]. That would fundamentally allow for the neutrinos to oscillate between the flavors. In this scenario, in order to find what mass a certain neutrino carries, we could either specify a dominant mass, or if such mass does not exist, then we could calculate the average masses.

$$\begin{aligned}
|\nu_e\rangle &= u_{e1}|\nu_1\rangle + u_{e2}|\nu_2\rangle + u_{e3}|\nu_3\rangle \\
|\nu_\mu\rangle &= u_{\mu1}|\nu_1\rangle + u_{\mu2}|\nu_2\rangle + u_{\mu3}|\nu_3\rangle \\
|\nu_\tau\rangle &= u_{\tau1}|\nu_1\rangle + u_{\tau2}|\nu_2\rangle + u_{\tau3}|\nu_3\rangle
\end{aligned} \tag{2.32}$$

$$\begin{aligned}
\langle m_{\nu_e} \rangle &= |u_{e1}|^2 m_1 + |u_{e2}|^2 m_2 + |u_{e3}|^2 m_3 \\
\langle m_{\nu_\mu} \rangle &= |u_{\mu1}|^2 m_1 + |u_{\mu2}|^2 m_2 + |u_{\mu3}|^2 m_3 \\
\langle m_{\nu_\tau} \rangle &= |u_{\tau1}|^2 m_1 + |u_{\tau2}|^2 m_2 + |u_{\tau3}|^2 m_3
\end{aligned} \tag{2.33}$$

The orthogonal basis of mass eigenstates from 2.32 is sometimes simply abbreviated through an introduction of a unitary mixing matrix  $U^*$ , and written in the following form:

$$|\nu_\alpha\rangle = \sum_i U_{\alpha i}^* |\nu_i\rangle \tag{2.34}$$

Where in the case of the three-flavor neutrino oscillation scenario,  $\alpha = e, \mu, \tau$  for the flavor and  $m_i = m_1, m_2, m_3$  for the mass eigenstates. In such case, the mixing matrix was constructed by Pontecorvo, Maki, Nakagawa, Sakata and it is referred to as the PMNS matrix:

$$\hat{U}_{\text{PMNS}} = \begin{pmatrix} c_{12}c_{13} & s_{12}c_{13} & s_{13}e^{-i\delta} \\ -s_{12}c_{23} - c_{12}s_{23}s_{13}e^{i\delta} & c_{12}c_{23} - s_{12}s_{23}s_{13}e^{i\delta} & s_{23}c_{13} \\ s_{12}s_{23} - c_{12}c_{23}s_{13}e^{i\delta} & -c_{12}s_{23} - s_{12}c_{23}s_{13}e^{i\delta} & c_{23}c_{13} \end{pmatrix} \tag{2.35}$$

where  $c_{ij} = \cos(\theta_{ij})$ ,  $s_{ij} = \sin(\theta_{ij})$ , and  $\delta$  is the CP violating phase parameter. Currently best

known values for the oscillation parameters from global fit ([35], [36], [37]) are as following:

$$\begin{aligned}\Delta m_{21}^2 &= 7.64 \times 10^{-5} \text{eV}^2, & \Delta m_{31}^2 &= 2.45 \times 10^{-3} \text{eV}^2; \\ \theta_{21} &= 34.2^\circ, & \theta_{23} &= 45^\circ, & \theta_{13} &= 9.2^\circ.\end{aligned}$$

Since the very first measurements in Davis' radiochemical experiment, the number of expected neutrinos was not in agreement with the collaboration's results. According to an evaluation conducted by J. Bahcall, the number of electron neutrinos detected by the experiment was lower by a factor of three with respect to what was predicted by the SSM. Additional confirmation provided by other experiments, such as Sage and Gallex/GNO, also identified energy dependence on the amount of the "missing" neutrinos. These observations, later referred to as the *solar neutrino problem*, were the first steps to the confirmation of Pontecorvo's predictions. As it was later discovered in the case of solar neutrinos, there were also other mechanisms involved in the process of their oscillations before reaching detectors on Earth. A more complete illustration will be presented in the following two chapters.

## Oscillations in Vacuum

As previously mentioned, neutrinos naturally oscillate due to their quantum nature. In a simplified scenario, if only two neutrino flavors were to be assumed, such as:  $|\nu_e\rangle \rightarrow |\nu_\mu\rangle$ , or  $|\nu_\mu\rangle \rightarrow |\nu_\tau\rangle$ , then the mixing matrix could be defined as:

$$\begin{pmatrix} |\nu_e\rangle \\ |\nu_\mu\rangle \end{pmatrix} = \begin{pmatrix} \cos\theta & \sin\theta \\ -\sin\theta & \cos\theta \end{pmatrix} \cdot \begin{pmatrix} |\nu_1\rangle \\ |\nu_2\rangle \end{pmatrix} \quad (2.36)$$

where  $\theta$  is the mixing angle. We are justified to use this approximation since it has been

shown by various experiments that  $\sin\theta_{13} \ll 1$  (T2K, [38]; Daya-Bay, [39]). As a result, there are two mixing angles remaining,  $\theta_{12}$  (often referred to as  $\theta_{sol}$ ), and  $\theta_{23}$  (referred to as  $\theta_{atm}$ ) with their associated mass square differences,  $\Delta m_{ij}^2 = (m_j^2 - m_i^2)$ ,  $\Delta m_{21}^2$  and  $\Delta m_{32}^2$ .

We begin our derivation by switching to a Schrödinger framework and rewriting  $|\nu(t)\rangle$  as the two-flavor state vector where  $|\nu_e\rangle = f_e(t)$ ,  $|\nu_\mu\rangle = f_\mu(t)$ ,  $f_\alpha(t)$  being the amplitude for the neutrino in state  $\alpha$ , and  $\mathcal{H}$  is a matrix of the interaction Hamiltonian:

$$i\frac{\partial}{\partial t}|\nu(t)\rangle = \mathcal{H}|\nu(t)\rangle \quad (2.37)$$

We will refer to this Hamiltonian in vacuum as  $\mathcal{H}_{Vac}$ , and using equation 2.32 we can rewrite its elements as:

$$\begin{aligned} \langle\nu_\alpha|\mathcal{H}_{Vac}|\nu_\beta\rangle &= \langle\sum_i U_{\alpha i}^* \nu_i|\mathcal{H}_{Vac}|\sum_j U_{\beta j}^* \nu_j\rangle \\ &= \sum_j U_j U_{\beta j}^* \sqrt{p^2 + m_j^2} \end{aligned} \quad (2.38)$$

where  $\mathcal{H}_{Vac}|\nu_j\rangle = E_j|\nu_j\rangle$ . Now, with their tiny masses neutrinos can be treated as relativistic particles and this allows us to rewrite their energies and momenta as  $E_j = \sqrt{p^2 + m_j^2} \approx p + \frac{m_j^2}{2p}$  and  $p \cong E$ . Using the two-neutrino matrix from Equation 2.36, we transform the vacuum Hamiltonian for Eq. 2.38 into:

$$\mathcal{H}_{Vac} = \frac{\Delta m_{12}^2}{4E} \begin{pmatrix} -\cos 2\theta & \sin 2\theta \\ \sin 2\theta & \cos 2\theta \end{pmatrix} \quad (2.39)$$

In order to derive the oscillation probability, we now take Equation 2.32 for  $|\nu_e\rangle$  and  $|\nu_\mu\rangle$

and so eigenvalues for  $\mathcal{H}_{Vac}$  become:

$$\lambda_1 = -\frac{\Delta m_{12}^2}{4E}, \quad \lambda_2 = +\frac{\Delta m_{12}^2}{4E}. \quad (2.40)$$

In the case of the Sun we can think of the  $|\nu_e\rangle$  (electron neutrino) created at time  $t = 0$ , and its propagation through space will result in evolution after time  $t$  into:

$$|\nu(t)\rangle = |\nu_1\rangle e^{i\lambda_1 t} \cos\theta + |\nu_2\rangle e^{-i\lambda_2 t} \sin\theta \quad (2.41)$$

This leads us to a general formulation of probability  $P$  that a neutrino of energy  $E$ , generated in a given flavor  $\alpha$  will oscillate into a another flavor  $\beta$  after traveling distance  $L$ . We can express it as:

$$\begin{aligned} P(\nu_e \rightarrow \nu_\mu) &= |\langle \nu_\mu | \nu(t) \rangle|^2, \\ &= |\sin\theta \cos\theta (-e^{i\frac{\Delta m_{12}^2}{4E}t} + e^{-i\frac{\Delta m_{12}^2}{4E}t})|^2, \\ &= \sin^2 2\theta \cdot \sin^2 \left( \frac{\pi x}{L} \right). \end{aligned} \quad (2.42)$$

The model has been written in this form in order to emphasize the  $L$  parameter, or the oscillation length defined as  $L = \frac{4\pi E}{\Delta m^2}$ . That is to say that for a maximum mixing angle  $\theta = 45^\circ$ , the probability for an electron neutrino to be detected as  $\nu_\mu$  at distance  $L/2$  from the source equals 1. Different experiments are sensitive to various values of the characteristic oscillation length  $L$  as well as the neutrino energy  $E$ . For this reason we list in Table 2.4 the scale for these parameters and various neutrino sources.

**Table 2.4:** *Various neutrino sources and their associated experimental sensitivities.*

Source	$\nu$ type	E[MeV]	L[km]	$\Delta m_{min}^2$ [eV <sup>2</sup> ]
Sun	$\nu_e$	$\sim 1$	$1.5 \times 10^8$	$\sim 10^{11}$
Reactor	$\bar{\nu}_e$	$\sim 1$	100	$\sim 10^{-5}$
Reactor	$\bar{\nu}_e$	$\sim 1$	1	$\sim 10^{-3}$
Atmospheric	$\nu_e, \bar{\nu}_e, \nu_\mu, \bar{\nu}_\mu$	$\sim 10^3$	$\sim 10^4$	$\sim 10^{-4}$
Accelerator	$\nu_\mu, \bar{\nu}_\mu$	$\sim 10^3$	$\sim 10^3$	$\sim 10^{-3}$

## The MSW Effect in Matter

Another interesting effect is related to the enhanced oscillatory pattern when neutrinos traverse very dense matter. Perhaps this is coincidence, but there are a couple of factors contributing to such behavior of solar neutrinos. Firstly, they will interact with other particles through forward coherent scattering with an exchange of the W or Z bosons. For the electron neutrinos (exchange of the  $W^\pm$  boson with the electrons in matter) this gives rise to an additional potential that is proportional to the Fermi coupling constant,  $G_f$  ( $8.96 \times 10^{-32}$  MeVcm<sup>3</sup>) and of course the electron density in matter,  $n_e$ :

$$V_W = +\sqrt{2}G_f n_e \quad (2.43)$$

This oscillation enhancement for electron-neutrinos is known as the Mikheyev-Smirnov-Wolfenstein effect, or simply MSW [40], [41]. At the same time, all neutrino flavors will interact with electrons, protons and neutrons in matter via exchange of the Z boson. For this reason we define their interaction potential as:

$$V_Z = -\frac{\sqrt{2}}{2}G_f n_n \quad (2.44)$$

Since we assume solar matter as electrically neutral, which will result in canceling potentials

$V_Z$  for electrons and protons, we can write it as proportional to the number of neutrons in matter,  $n_n$ . In order to start considering matter enhanced effects on neutrinos, we go back to the definition of the Hamiltonian in vacuum and according to the introduced potentials  $V_W$  and  $V_Z$ , we write a new Hamiltonian as:

$$\mathcal{H}_{\mathcal{M}} = \mathcal{H}_{Vac} + V_W + V_Z \quad (2.45)$$

Since the contribution of the  $V_Z$  potential is expressed through the identity matrix as mentioned before, we can drop this term because it does not impose any change. Additionally, we eliminate the term of the  $V_W$  that is proportional to identity, and as a result, we can rewrite  $\mathcal{H}_{\mathcal{M}}$  similarly to Equation 2.39

$$\mathcal{H}_{\mathcal{M}} = \frac{\Delta m_{12}^2}{4E} \begin{pmatrix} -(\cos 2\theta - x) & \sin 2\theta \\ \sin 2\theta & (\cos 2\theta - x) \end{pmatrix} \quad (2.46)$$

where we abbreviated  $x = \frac{V_W/2}{\Delta m_{12}^2} 4E$ . We can now define:

$$\Delta m_{\mathcal{M}}^2 = \Delta m_{12}^2 \sqrt{\sin^2 2\theta + (\cos 2\theta - x)^2} \quad (2.47)$$

and,

$$\sin^2 2\theta_{\mathcal{M}} = \frac{\sin^2 2\theta}{\sin^2 2\theta + (\cos 2\theta - x)^2} \quad (2.48)$$

then the  $\mathcal{H}_{\mathcal{M}}$  becomes identical to its vacuum representation with the mass-square  $\Delta m_{\mathcal{M}}^2$  and  $\theta_{\mathcal{M}}$  parameters being their matter equivalent:

$$\mathcal{H}_{\mathcal{M}} = \frac{\Delta m_{\mathcal{M}}^2}{4E} \begin{pmatrix} -\cos 2\theta_{\mathcal{M}} & \sin 2\theta_{\mathcal{M}} \\ \sin 2\theta_{\mathcal{M}} & \cos 2\theta_{\mathcal{M}} \end{pmatrix} \quad (2.49)$$

The oscillation probability for an electron neutrino to oscillate into  $\nu_\mu$  takes the exact same form, and the mixing-angle becomes the matter mixing-angle as shown:

$$P_{\mathcal{M}}(\nu_e \rightarrow \nu_\mu) = \sin^2 2\theta_{\mathcal{M}} \cdot \sin^2 \left( \frac{\pi x}{L} \right). \quad (2.50)$$

However, this time  $L = \frac{4\pi E}{\Delta m_{\mathcal{M}}^2}$  represents the matter parameters. It should be underlined that when  $n_e \approx 0$  the matter mixing angle is equal to the vacuum one,  $\theta_m \approx \theta$ .

## The MSW Effect for Solar Neutrinos

It is because the major purpose of the work presented in this thesis is the verification of the solar MSW effect and whether additional oscillations could take place in vacuum between Sun and Earth, we would like to discuss in more detail the effects that govern the solar neutrino oscillations. Some predictions to the *solar neutrino problem* were made by Bahcall, Gonzalez-Garcia, and Pena-Garay in the so-called large angle MSW solution, [42]. In this approach, the initially produced electron neutrinos in the Sun, undergo adiabatic conversion when they travel through the solar matter, from the core to the surface. The first confirmation of this effect for anti-neutrinos with energies  $>3.4$  MeV was provided by the KamLAND collaboration [43]. From Equation 2.48 we can see that the effective mixing angle  $\theta_{\mathcal{M}}$  depends on the electron density (through the substituted  $x$  parameter). As a result, at the core of the sun, where  $n_e$  is very high,  $\theta_m \approx \pi/2$ . Which means that at the center, an electron neutrino is born predominantly in the  $|\nu_{m2}\rangle$  eigenstate (top, red bar in Figure 2.7). While it propagates outwards through a decreasing electron density, it passes through an interesting region for which the mixing is maximal,  $\theta_m \approx \pi/4$ , it is the so-called *resonant effect* (indicated with  $n_e(\text{resonant})$  and a yellow bar in Figure 2.7). The adiabatic condition guarantees that the neutrino will remain in the  $|\nu_{m2}\rangle$ , and while it approaches lower electron density at the

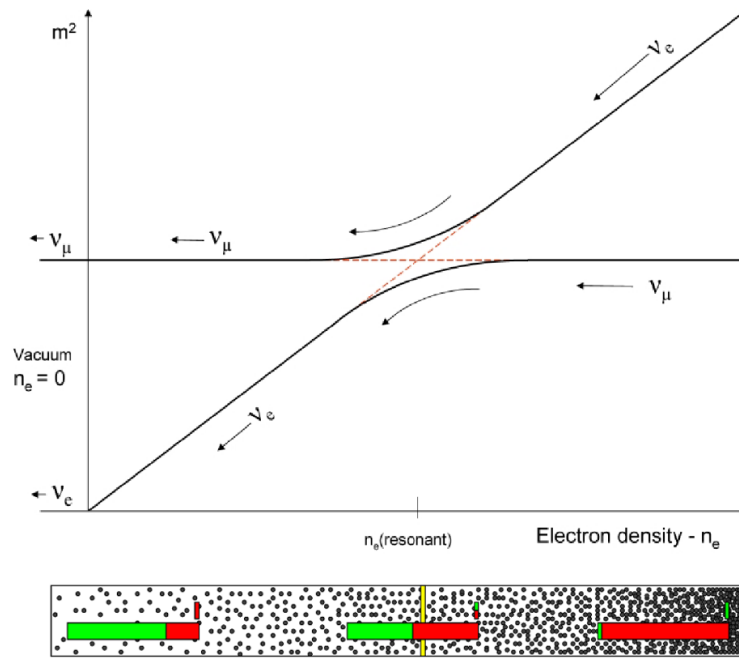


**Figure 2.7:** Adiabatic effect for solar neutrinos. Figures from [44] (top), and [45] (bottom).

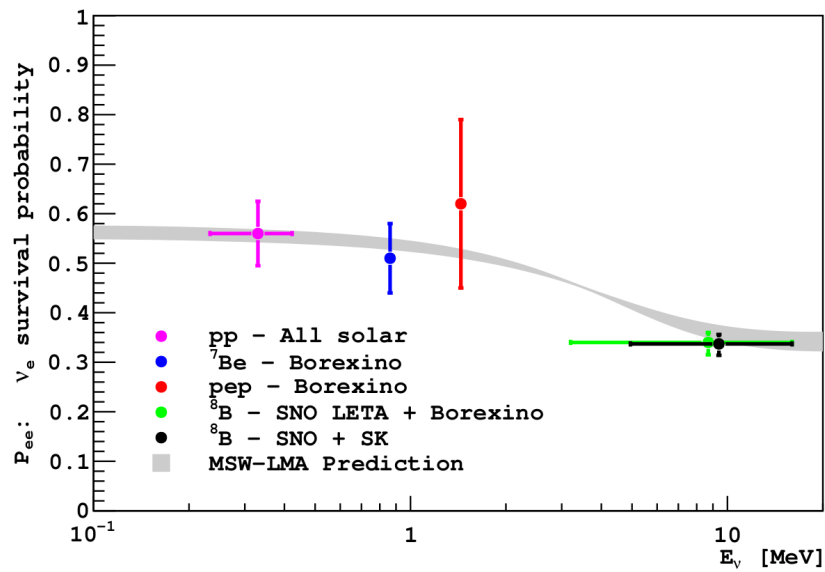


**Figure 2.8:** Survival probability for the electron neutrino. The gray band represents the  $1\sigma$  calculated uncertainty for the oscillation parameters. Figure from [30].

surface of the Sun, it exits in the  $|\nu_2\rangle$  vacuum eigenstate, which corresponds to oscillations into  $\nu_\mu$  (this level-crossing is depicted in the top of Figure 2.7).

Even though, by far the most dominant effect in the process of solar neutrino oscillations is the adiabatic effect, we should underline that in fact, there are three regions of different features in the transition (shown in Figure 2.8 as the  $\nu_e$  survival probability):

- At energies below 2 MeV, the vacuum oscillations with small matter corrections occur,
- Intermediate energy range  $E \sim (2-10)$  MeV, the interplay of the oscillations and adiabatic conversion takes place,
- At high energies,  $E > 10$  MeV, nearly non-oscillatory transition occurs.

The major conclusion of this discussion is to point out that the Large Mixing Angle MSW effect results in a gradual evolution of the  $\nu_e$  into the  $\nu_2$  eigenstate without further vacuum oscillations between Sun and Earth.

## 2.4 Annual Modulation

Kepler's three laws governing the motion of planets opened a new chapter in our understanding of the solar system. Even though it was more of an observation rather than an actual mathematical proof at the time, it solidified a fundamental feature of the earth's orbit that we can now investigate with the solar neutrinos:

*The orbit of every planet is an ellipse with the Sun at one of the two foci.*

If we look at the solar system from the astronomical scale, it is accurate to say that the Sun is a point-like source. It is a law for any kind of radiation emitted radially outward in a three-dimensional space that its intensity will be inversely proportional to a square

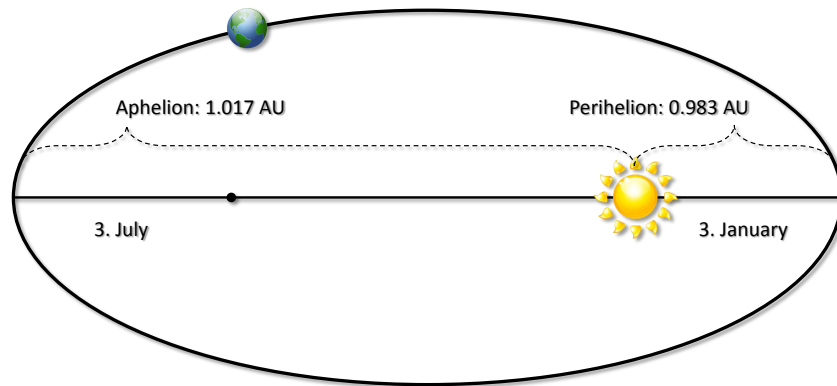


**Figure 2.9:** *Seasonal Earth-to-Sun distance oscillation*

of distance from the source. This is a result of the radiation spread over the surface of a sphere at a given radius, the surface of which is proportional to  $r^2$ . For instance, the Solar Irradiation (Luminosity measured on Earth) is related to Luminosity ( $L_{\odot} = 3.939 \times 10^{33}$  erg/s, including both the electromagnetic and neutrino radiation) in the following way (represented graphically in Fig. 2.10):

$$I_{\odot} = \frac{1}{4\pi} \frac{L_{\odot}}{r^2}; \quad (2.51)$$

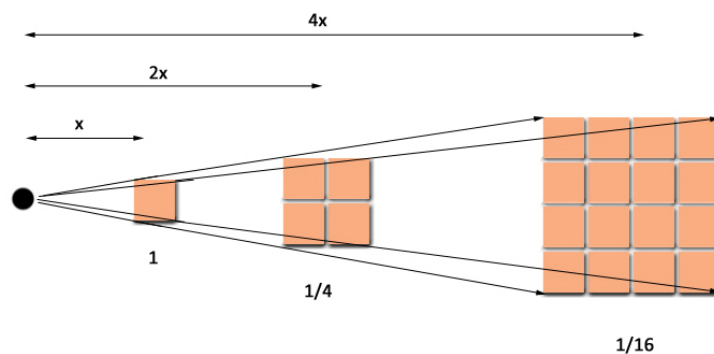


**Figure 2.10:** *Principle of the intensity loss with distance. The further away, the bigger surface the beam needs to cover.*

Early experiments allowed four physically distinguishable solutions to the *solar neutrino problem*: three MSW solutions, namely a small mixing angle solution (SMA), where a large conversion is due to the crossing of a resonance, a large mixing angle solution (LMA), where neutrinos adiabatically cross the solar density, and a low neutrino mass squared splitting solution (LOW), where non-adiabaticity and neutrino regeneration inside the Earth are relevant. Finally a vacuum oscillation solution (Just-So) is the one where the neutrino mass squared splitting matches the ratio of the energy to the path length from the Sun to the Earth. The LOW solution was solely disfavored by Borexino itself in the measurement of (absence) of the day-night rate asymmetry at more than  $8.5\sigma$  [3]. The Just-So and SMA solutions are strongly disfavored by the flatness of the  $^8\text{B}$  neutrino spectrum and the  $^8\text{B}$  rate ([46],[47],[48],[49]), ([50],[51],[52],[53]) As a result, the most favored solution is the large mixing angle MSW one, which leads us to the expected, *normal* scenario of the the annual modulation, governed by the inverse-square-law. According to MSW-LMA, Borexino is expected to see an average of  $46 \pm 1.5$  counts/(day x 100 ton) in the window of 250-800 keV [2]. For the elliptic orbit, the distance between Earth and the Sun will vary as:

$$r(t) = r_0 \left[ 1 - \epsilon \cos \left( \frac{2\pi t}{T} \right) \right] + O(\epsilon^2); \quad (2.52)$$

Where Earth's eccentricity  $\epsilon = 0.0167$ , and  $r_0 = 1.496 \times 10^8$  km at the semi-major axis, i.e. the original definition of the Astronomical Unit (1 AU) [54]. Combined with the inverse-square-law and a known background function  $B$  (see Section 4.2), the rate becomes:

$$R(t) = B + \left( \frac{\bar{r}_0}{r(t)} \right)^2 = B + \bar{R} \left[ 1 + 2\epsilon \cos \left( \frac{2\pi t}{T} - \phi \right) \right]; \quad (2.53)$$

neglecting higher order terms due to small  $\epsilon$ . This in turn results in a variation on the order of 7% annually, simulated in Fig. 2.11 for the theoretical values of the parameters.

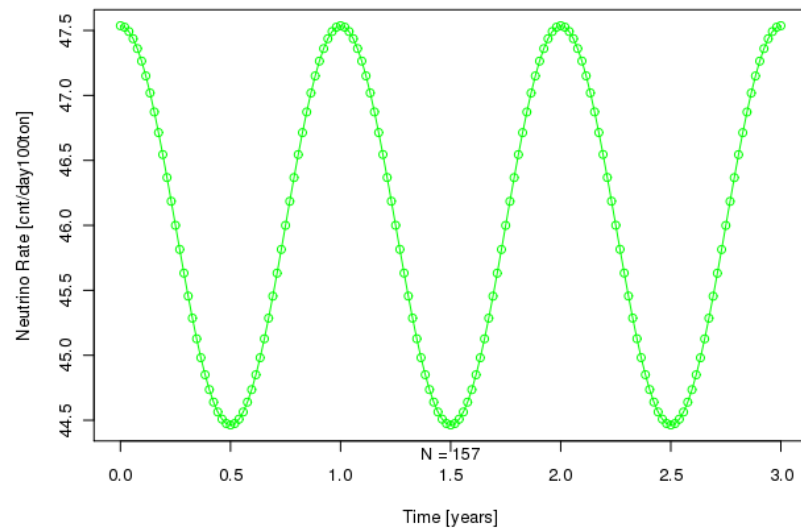


**Figure 2.11:** Expected seasonal modulation of 3-year  ${}^7\text{Be}$  neutrino rate in Borexino from Eq. 6.1 assuming no backgrounds. Period  $T = 1$  year, starting at Earth's perigee on January 3rd.

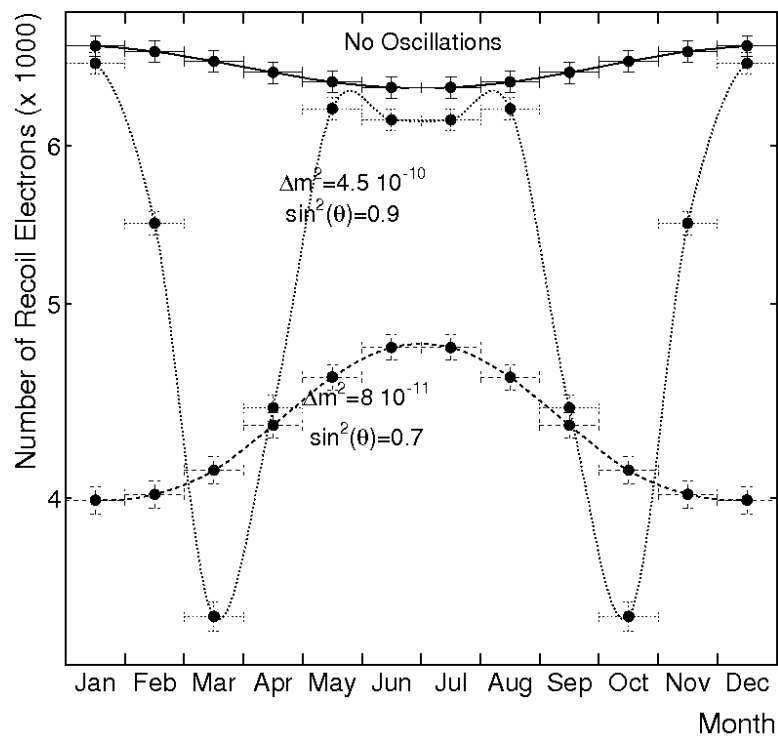


**Figure 2.12:** Expected seasonal modulation of 3-year of data for  ${}^7\text{Be}$  neutrino rate in Borexino. The plot presents the “normal” (No Oscillations) and “anomalous” (“low point” and “high point” configurations of the oscillation parameters) annual modulation patterns. Figure from [55].

If however, the disfavored scenario of *anomalous* modulation was allowed, the neutrinos would additionally oscillate in vacuum on their way from Sun to Earth. In such a situation, a distinct pattern could be easily extracted if for instance, the two oscillation parameters,  $\sin^2 2\theta_{12}$  and  $\Delta m^2$ , would take the following values: 1)  $\sin^2 2\theta_{12} = 0.7$ ,  $\Delta m^2 = 8 \times 10^{-11} \text{ eV}^2$  (*low point*) or 2)  $\sin^2 2\theta_{12} = 0.9$ ,  $\Delta m^2 = 4.5 \times 10^{-10} \text{ eV}^2$  (*high point*). Figure 2.12 presents a simulation performed by A. de Gouvea, A. Friedland, H. Murayama in [55], for the Borexino signal, in the case of the *normal* (No Oscillations) and *anomalous* (*low point* and *high point* configurations of the oscillation parameters) annual modulation effects.

## 2.5 Other Neutrino Sources in Nature

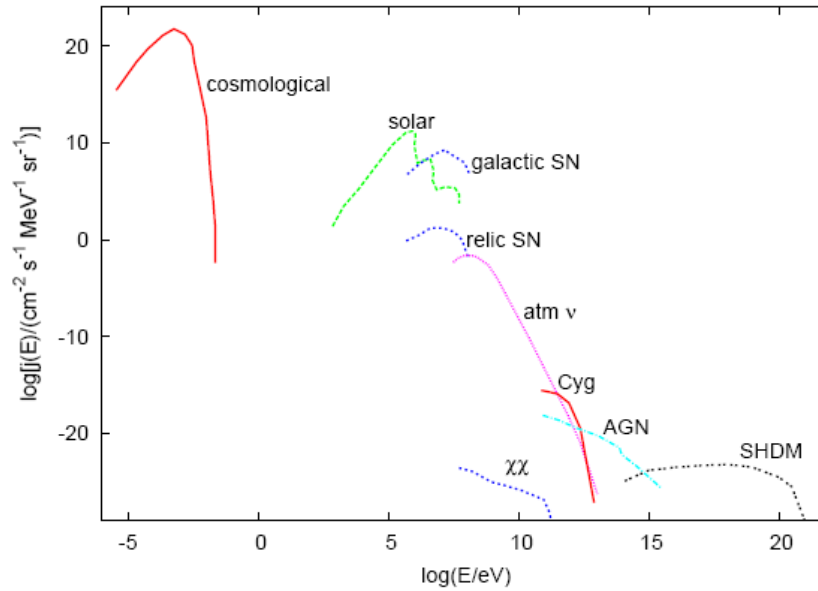


**Figure 2.13:** Total neutrino flux composition of all the natural sources available on Earth. Figure from [56].

Neutrinos are the most common particles in the universe, after photons. Initially, many speculated that since they were discovered to carry mass, they could explain the origins of *dark matter*, the 84% of all the matter in the universe. Later however, it was shown that

the active neutrinos were in fact not massive enough to account for measured dark matter component from cosmology [57]. Nonetheless, there are many sources of neutrinos in nature, and we will now try to introduce some of the most important ones.

First of all, the energy spectrum of neutrinos detected on Earth is really broad, ranging from meV to over 20 orders of magnitude higher as shown in Figure 2.13. The least energetic are also the oldest neutrinos in the universe, those that were created in the Big Bang, called *relic* neutrinos. Even though their energies at creation were significant, billions of years of universal expansion lowered it a little over  $10^{-4}$  eV, making them practically invisible, even for today's hypothetical experiments. Right above the already presented, solar neutrinos, we have the family of neutrinos originated in Supernovae, with average energies in the 10-20 MeV range. The process in which these particles are created is rather specific, and could be referred to as the last neutrinos of a star. Very rare Supernova explosions, with predicted probability for a given galaxy of only one per half a century, require the detectors on Earth to operate at their highest possible duty cycles; considering also the fact that a burst from such Supernovae as SN1987A ([58]) lasts only a few seconds, the detection becomes a really difficult task. Originating from just above our heads are the atmospheric neutrinos whose spectrum spans throughout the broad range of energies, reaching even the highest energetic TeV neutrinos from rare point-like sources or other galaxies. The term *atmospheric* indicates directly that in fact, these neutrinos are of Earth-like origin. As a result of the cosmic ray interactions in the upper parts of our atmosphere, mesons  $\pi$  and K decay into leptons  $\mu$  and  $\nu_\mu$ . The muon then cascades further into  $\nu_\mu$  and  $\nu_e$ , providing the final flux detectable from the ground. One of the first experiments to study these neutrinos and confirm the ambiguity in the  $\nu_\mu/\nu_e$  ratio due to flavor conversion was Super-Kamiokande ([59]).

The *geo-neutrinos*, as they are referred to, are nothing else than an answer to the oldest question in neutrino physics that Pauli was once posing. They originate in Earth's crust and mantle as part of the natural radioactive decay of  $^{238}\text{U}$ ,  $^{232}\text{Th}$  and  $^{40}\text{K}$  chains. Even though

their energies are on average 2-3 MeV, their flux is estimated to be at the level of  $6 \times 10^6 / \text{cm}^2\text{-sec}$  and contributes to about 20 TW of heat generated in the Earth's core. The hypothesis of a uranium-fuelled nuclear geo-reactor in the core was, however, ruled out by the most recent measurements of Borexino ([60]). There are also multiple options for generating neutrinos artificially. Worth mentioning, is the accelerator source where a beam of energetic protons produce  $\pi$  mesons that later decay into  $\nu_\mu$ , a mechanism similar to the cosmic interactions in the atmosphere. An important difference is that such a configuration provides a precise control over the energy, timing, direction, and collimation of the resulting neutrino beam. This in turn allows the detection in a so-called off-axis mode, which is found to reveal the  $\nu_\mu$  to  $\nu_e$  oscillation at its maximum. This becomes critical in the determination of the  $\theta_{13}$  parameter in the PMNS matrix that gives access to the CP violating phase  $\delta$ . Currently, experiments such as T2K and NO $\nu$ A are preparing for this task. Unfortunately the J-PARC accelerator had to be shutdown as a result of the earthquake that struck the shores of Japan in April, 2011, leaving T2K with only 2% of the originally planned measurement. NO $\nu$ A, on the other hand, is planned to begin service in 2014. The best to date result on the value of  $\theta_{13}$  is held by the Daya-Bay collaboration,  $\sin^2 2\theta_{13} = 0.092 \pm 0.016_{stat} \pm 0.005_{syst}$  ([61]).

# Chapter 3

## Borexino Detector

### 3.1 Detector Design and Construction

The Borexino experiment incorporates a calorimetric detector whose signal is a measure of the recoil electron energy from the elastic electron-neutrino scattering, as it will be described in detail in one of the paragraphs of this section. This rare interaction is indistinguishable, based on event-by-event basis, from many other radioactive decay tracks, including both the internal as well as the external backgrounds (dominated by  $\beta$  and  $\gamma$  events). This points us to the first requirement on the Borexino's design: the concept of graded shielding, whose main goal is to effectively address and block sources of contamination from the outer regions of the detector and products of cosmic radiation. On the other hand, the internal impurities of the detector can be significantly suppressed by proper selection of low-radioactive components, most importantly at the heart of the detector where purity of the active scintillator plays a crucial role.

## Counting Test Facility

The concept of the Borexino design was first tested on a small-scale prototype called the Counting Test Facility (CTF) as shown in Figure 3.1 ([62]). It was built in the early 90's and remained operational until 2010 when the construction of the first DarkSide low-radioactivity underground argon (UAr) detector (DS-50) began ([63]). The CTF prototype was constructed with mainly one goal: to prove that the scintillator's radioactive contaminants in the  $^{238}\text{U}$  and  $^{232}\text{Th}$  chains, the neutrino-scattered electrons' major background, could be reduced to acceptable levels. In this section we will present also how unprecedented low background levels were achieved in the Borexino design.

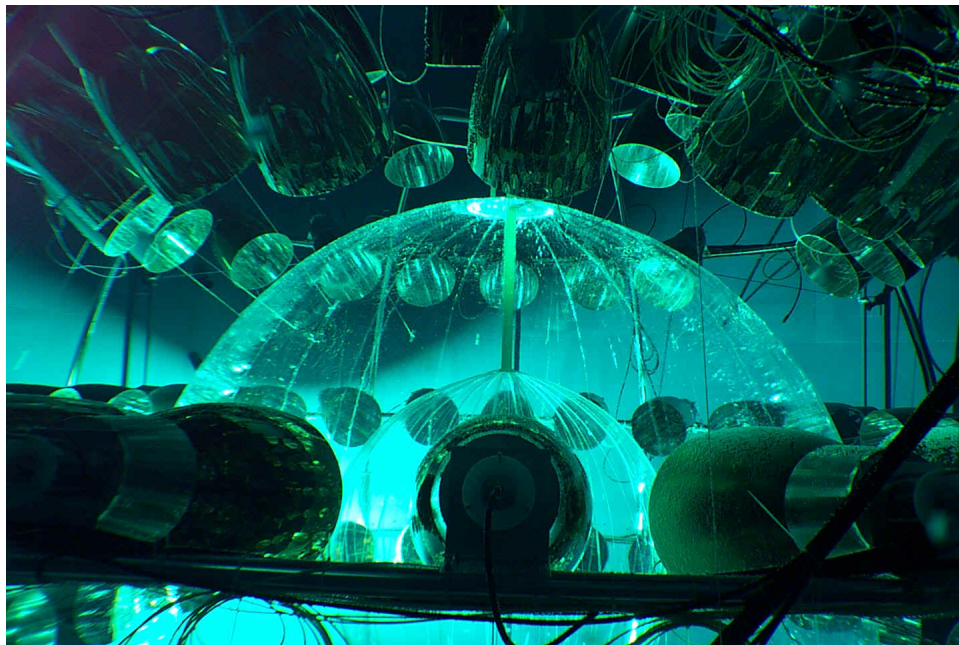


**Figure 3.1:** *CTF detector at its initial filling stage. The nylon vessel, thicker than in Borexino, can be seen inside. It is surrounded by about 100 PMTs (Photomultiplier-Tubes).*

The CTF detector was significantly smaller in comparison to Borexino. The inner vessel was only 2 m in diameter, containing about 4 tons of liquid scintillator. Nevertheless, the capacity was sufficient to tag the coincident events and prove the effectiveness of purification plants. It left enough margin to hope that the remaining impurities could be eliminated by software

cuts in Borexino. Assuming secular equilibrium, the internal background determination was:

- $^{14}\text{C}/^{12}\text{C} = (1.94 \pm 0.09) \times 10^{-18} \text{ g/g}$
- $^{232}\text{Th} = (4.4 + 1.5 - 1.2) \times 10^{-16} \text{ g/g}$
- $^{238}\text{U} = (3.5 \pm 1.3) \times 10^{-16} \text{ g/g}$

During its campaign, the CTF provided the information essential for the construction of the Borexino detector. It served as a mature test-bed for such aspects of the design as the purification technique, hardware, electronics and data acquisition. Over the course of almost 20 years of its operation, the CTF underwent three stages of development, contributing independent results on the emission of solar axions, and electron anti-neutrinos ([62]).

## The Borexino Design

Even though the graded shielding physically separates individual compartments of the Borexino detector, in the end, it is a 100 ton software defined<sup>1</sup> sphere of liquid scintillator that serves as an active target, called the standard fiducial volume (FV). In order to provide proper conditions of radio-purity, the detector first has to satisfy certain construction requirements. As previously mentioned, Borexino relies on a graded shielding concept which has its origins beyond the walls of the detector. Hall C of Gran Sasso (3.2) is an underground cavern that provides the first shielding requirement for a low-energy, stellar neutrino physics detector. Located around one mile underground, with 3600 m.w.e. of rock, Borexino is guaranteed necessary shielding from the bombardment of cosmic ray muons at a rate of about  $1 \mu / \text{hr} / \text{m}^2$ , a few orders of magnitude lower with respect<sup>1</sup> to the surface at sea level ( $1 \mu / \text{min} / \text{cm}^2$  [64]). Details of the muon flux measurement with the Borexino detector can be found in one of the recent publications [65].

---

<sup>1</sup> It relies on the timing of the PMTs

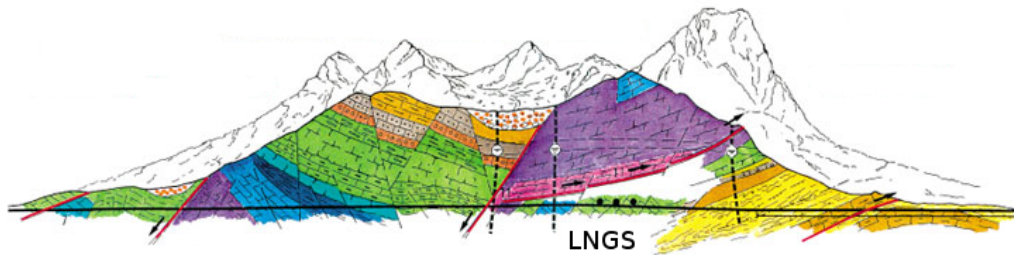


**Figure 3.2:** Deep, underground facility of the Gran Sasso National Laboratory in Italy. Experiments, Opera, Borexino and its prototype, CTF, are located in Hall C.

In Borexino’s original proposal from 1991, two basic concepts for the design of the detector were considered (referred to as *A* and *B* in [66]). Both designs address graded shielding, while also taking into consideration the operational inconveniences, cost and safety. The major difference between designs (*A*) and (*B*) was in the placement of the support frame for the Photo-Multiplier-Tubes (PMTs). In the first concept, the scintillation vessel as well as the PMTs would be completely submerged in water. Such a design, although economically feasible and simple would not allow for a future maintenance team to access the PMTs in the case of failure. From past experience, we have learned that on average about twenty five channels per year would have to be disconnected due to a short circuit or a leak. The second concept, on the other hand, would prevent such incidents, with a smaller containment tank the PMTs would be mounted on the outside of the stainless-steel sphere (SSS), and operated in air. The decrease in active volume and lack of water buffer would require additional shielding that was planned to be achieved by installing a concrete wall surrounding the detector. Finally, a merged version of the two concepts was brought to life, which contained the best of both. Two nylon vessels filled with scintillator in a 13.5 m Stainless-Steel-Sphere (SSS) serving also as a support for the PMTs and submerged in water tank turned out to be the optimal solution. Final concept of the Borexino detector is presented in Fig. 3.3.

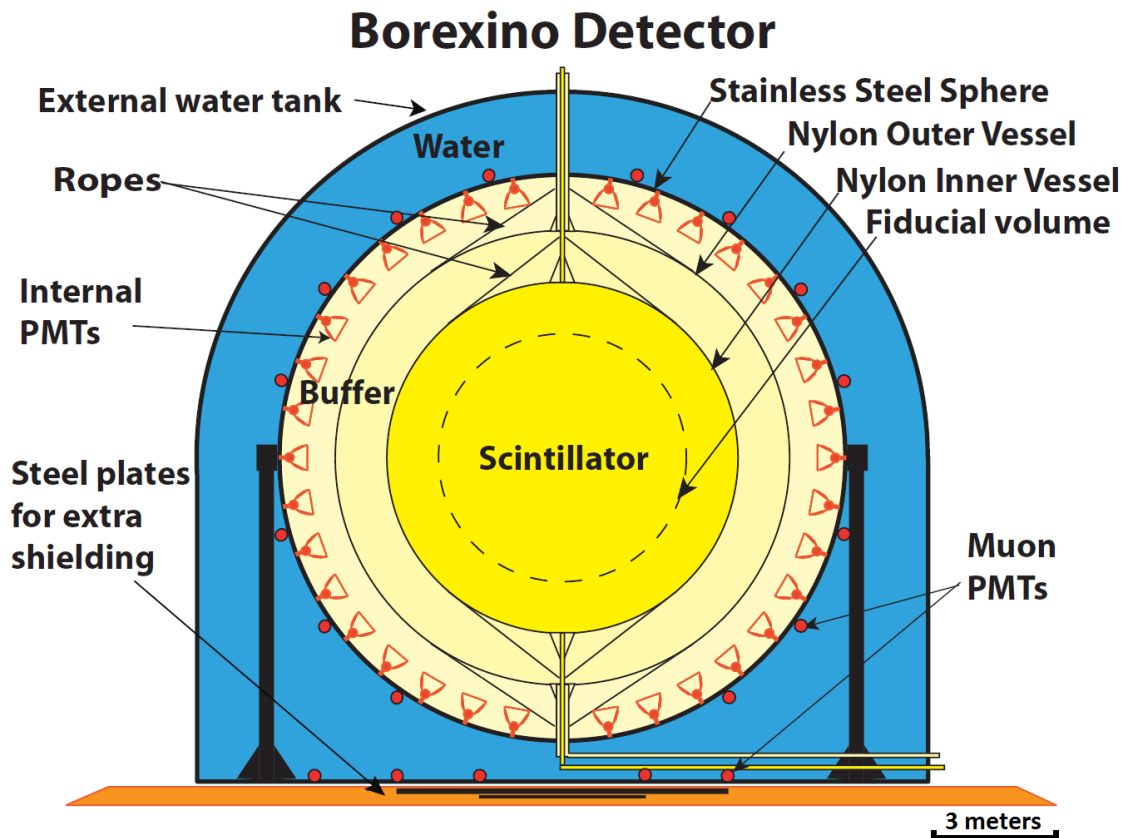


**Figure 3.3:** *Borexino design, 1kton stainless-steel sphere of scintillator holding 2212 8" ETL 9351 PMTs (1800 of which have additional light concentrators) provide efficient light collection on the inside with 200 outward-mounted tubes collecting muon Čerenkov cones in the ultra-pure water buffer. Figure from [67].*

## Borexino Scintillator

The Borexino detector has 300 tons of liquid scintillator that plays critical role of translating the neutrino signal into bursts of photons that will be collected by the PMTs. Thus the Light Yield (LY), attenuation length and timing response become the three major factors in the selection of the final scintillation cocktail. Again, a number of candidates were considered, leaving pseudocumene (PC) and trimethylborate (TMB) as the final options. As an anecdote, the name BOREX was in fact derived from the TMB, and as for the detector, later on fiscal

reality and focus on  ${}^7\text{Be}$  which did not require boron, had to be shrunk together with the name to BOREXino (it.). In principle, after the interaction of an incoming particle the scintillator becomes transparent to its re-emitted light and in order to achieve that, a so called wave-length shifter was added in small amounts to the mixture. That could be PPO in case of PC or butyl-PBD for TMB with concentrations usually on the order of  $<10\%$ . This provides an additional improvement in the light collection since quantum efficiency of the PMTs is highest only at certain wave-length, usually its peak is at around 375 nm. In normal conditions this miss-matches the peak emission light length of a pure scintillator. Addition of PPO into PC makes the perfect alignment of the two curves which is presented in 3.4, maximizing the LY.

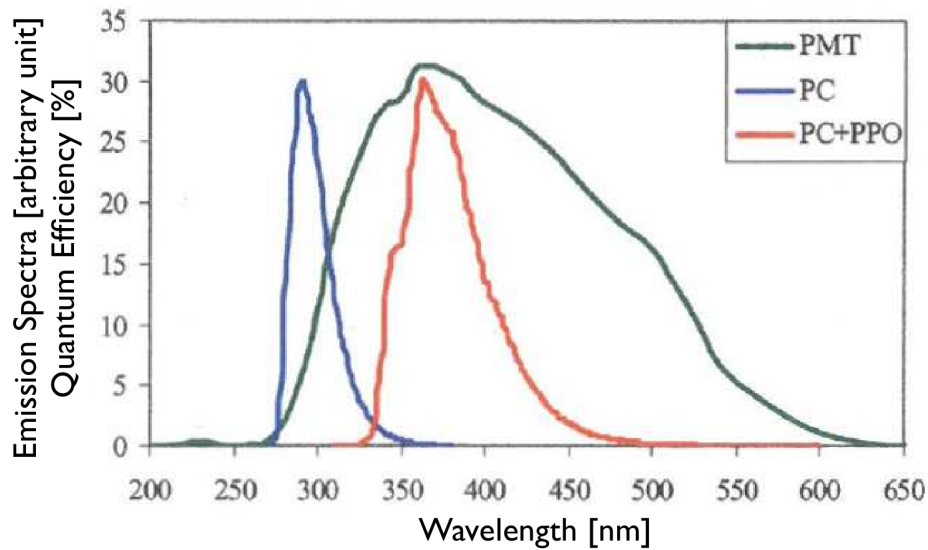


**Figure 3.4:** Example of the emission spectra for the pure PC and PC+PPO compound compared with a quantum efficiency of the Borexino Photo-Tubes (custom Thorn-EMI brand). Figure from [68].

Organic and inorganic scintillators (liquid/crystal) rely on the same excitation principle of its molecules in detecting radioactive particles such as  $\alpha$ ,  $\beta$ , or  $\gamma$ . The process shown in 3.5 illustrates how the scintillation light is being emitted during the deexcitation  $\pi$  -

electron from a Singlet-state. Rare for  $\beta$ , however somewhat common in the case of the  $\alpha$  particles, is a process called phosphorescence, i.e. emission of light from a decaying Triplet-state having a longer decay time. The effect is ionization-density dependent and results in very characteristic time response for heavy  $\alpha$  particles. The first phenomenon is called the quenching, a reduction in the fluorescent light independently of the particle's initial energy. In some cases the consequences are significant, effectively reducing the energy by even an order of magnitude; in Borexino for instance, the dominant  $^{210}\text{Po}$   $\alpha$  peak of 5.307 MeV occurs at 0.417 MeV. The second effect is related to the lifetime of a Triplet-state which, due intercrossing back to Singlet-state, increases to some  $100 \mu\text{s}$  leaving distinct pulse-shape of  $\alpha$ 's. In many applications this serves as an efficient tool in distinguishing between the two types of particles, method is being further discussed in 3.2, further application in the study of the annual flux modulation search is presented in Section 5.2.

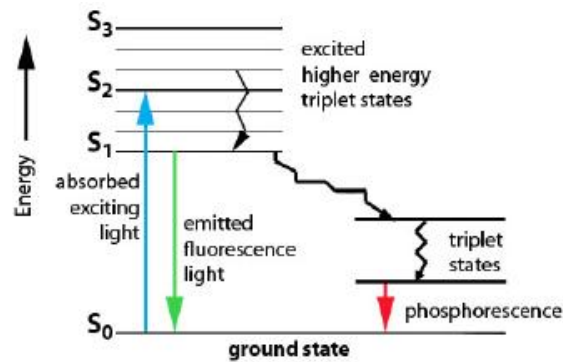


**Figure 3.5:** Chart for the energy levels of a PC liquid scintillator.

Quenching effects play significant role in reduction of the output light of the scintillator. It is not only the chemical properties or impurities of the liquid, such as Oxygen, that contributes to the overall result. After excitation there is a finite probability that emission of light will not happen when the molecule de-excites to the ground-state and the energy is transformed into pure heat. Low energy  $\beta$ 's, for which the ionization density is high due to large stopping power, will be most affected. In normal conditions the relation between specific fluorescence

$(dL/dx)$  and stopping power  $(dE/dx)$  is linear, but when the energy of a particle drops below 1 MeV, it starts to follow the Birks model [69]:

$$\frac{dL}{dx} = Y \frac{\frac{dE}{dx}}{1 + k_B \frac{dE}{dx}} \quad (3.1)$$

where,  $k_B$  is the Birks parameter,  $Y$ , the Photon Yield and  $x$  the travelled distance by a particle. Monte-Carlo simulations for Borexino favor  $Y = 11250$  ph/MeV, and  $k_B = 0.0120$  cm/MeV. The ionization quenching effect  $\gamma$  spectrum, in which case it is the multiplicity of Compton-scattered electrons that constitute to the overall drop in the detected energy. Figure 3.6 shows an example of the quenching factor dependence,  $q$ , with respect to the incoming particle kinetic energy [70].

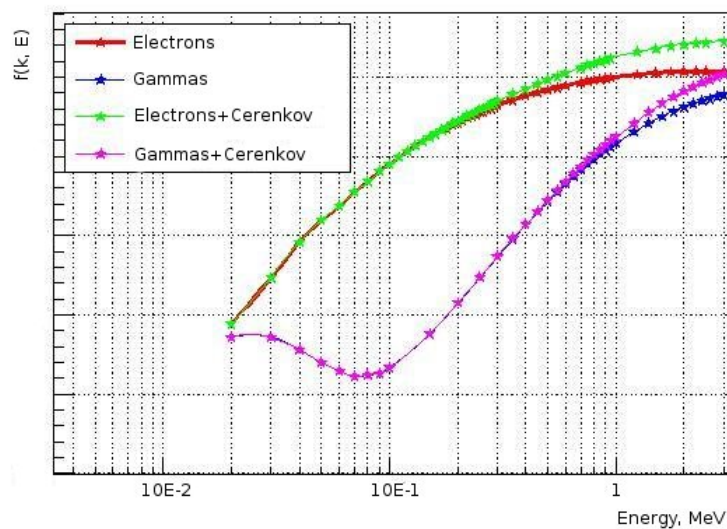


**Figure 3.6:** Quenching factor  $q = 1 / (1 + k_B dE/dx)$  for electrons and gamma particles. It's simulation for PC reveals significant energy loss in the sub-MeV range. This behavior shows how critical it is to understand this effect in the search for ultra-low-energy neutrinos with liquid scintillators. Figure from [70].

## Neutrino Detection in Borexino

Neutrinos can only interact via a charged-current (CC) or neutral-current (NC) exchange of heavy bosons  $W^\pm$  and  $Z^0$  as it is presented in Figure 3.7 using the first-order Feynman-diagram notation.

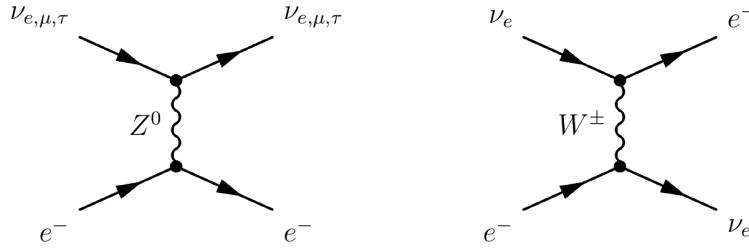


**Figure 3.7:** Feynman diagrams presenting the exchange of heavy bosons  $W^\pm$ ,  $Z^0$  in the process of neutrino-electro elastic scattering. Any neutrino flavor can undergo the  $Z$  exchange in the Neutral-current interaction whereas only the electron-neutrinos can exchange the  $W$  boson in the Charged-current process.

It is important for this discussion to mention the concentration of electrons in the Borexino scintillator which becomes critical in the final determination of the neutrino rate calculation. First, the density of PC is temperature dependent according to ([71] and [72]):

$$\rho_{PC}[\text{g}/\text{cm}^3] = (0.89179 \pm 0.00003) - (8.015 \pm 0.009) \times 10^{-4} \cdot T[^\circ\text{C}] \quad (3.2)$$

for pure pseudocumene, and with the addition of the PPO shifter it becomes:

$$\rho_{PC+PPO}[\text{g}/\text{cm}^3] = \rho_{PC} \cdot (1 + (3.16 \pm 0.01) \times 10^{-1} \cdot \eta_{PPO}) \cdot T[^\circ\text{C}] \quad (3.3)$$

With the concentration of PPO ( $\eta_{PPO}$ ) in Borexino on the order of  $(1.45 \pm 0.05) \times 10^{-3} \text{ g}/\text{cm}^3$  and an average scintillator temperature in the FV of  $15.0 \pm 0.5 \text{ }^\circ\text{C}$ , we calculate the density to be  $0.8802 \pm 0.0004 \text{ g}/\text{cm}^3$ . This gives us  $n = (3.307 \pm 0.003) \times 10^{29} \text{ e}^-/\text{ton}$  in Borexino.

The leptonic process of neutrino (of energy  $E_\nu$ ) scattering off of an electron (resulting in its kinetic energy  $T$ ) can be written as  $\nu_x + e^- \rightarrow \nu_x + e^-$ . The differential cross sections for  $\nu_\mu$  scattering on electrons can be written as ([73]):

$$\frac{d\sigma^{\nu_\mu}}{dT} = \sigma_0 \left[ g_L^2 + g_R^2 \left( 1 - \frac{T}{E_\nu} \right)^2 - g_L g_R \frac{T}{E_\nu} \frac{m_e c^2}{E_\nu} \right] \quad (3.4)$$

where  $\sigma_0 = G_F^2 s / 4\pi$ ,  $s = 2m_e E_\nu$ ,  $g_L = \sin^2 \theta_W \pm \frac{1}{2}$  and  $g_R = \sin^2 \theta_W \sim 0.2312$ . For scattering of  $\nu_e$  on electrons the presence of the CC diagram results in a differential cross section of

$$\frac{d\sigma^{\nu_e}}{dT} = \sigma_0 \left[ (g_L + 2)^2 + g_R^2 \left( 1 - \frac{T}{E_\nu} \right)^2 - g_L g_R \frac{T}{E_\nu} \frac{m_e c^2}{E_\nu} \right] \quad (3.5)$$

We now use the equation for the angular dependence of the recoil electron kinetic energy:

$$T = \frac{2E_\nu^2 \cos^2 \theta}{(1 + E_\nu)^2 - E_\nu^2 \cos^2 \theta} \quad (3.6)$$

Which results in total cross section for back-scattered neutrinos ( $T = T_{max}$ ) of:

$$\sigma(E_\nu) = \sigma_0 T_{max} \left[ (g_L + g_R)^2 - (g_R^2 + g_L g_R) \frac{T}{E_\nu} + g_R^3 \frac{T_{max}^2 m_e c^2}{3E_\nu^2} \right] \quad (3.7)$$

Keep in mind that what we measure is in fact the average interaction rate  $\bar{R}$ , i.e. a number of  $\nu_e e^-$  scatterings per volume per day. Assuming known flavor composition of solar neutrinos this gives:  $\bar{R} = \Phi (P \sigma_{\nu_e e^-} + (1 - P) \sigma_{\nu_{\mu,\tau} e^-}) N_e = 74 \pm 5.2$ . Where  $\sigma_{\nu_x e^-}$  is the total cross section for  $\nu_x e^-$  interactions,  $N_e$ , the number of target electrons,  $3.31 \times 10^{31}$ , and the SSM predicted flux  $\Phi$  for  ${}^7\text{Be}$  of  $4.48 \pm 0.31 \times 10^9 \text{ cm}^{-2} \text{ s}^{-1}$ . Assuming the survival probability  $P = 0.55$  with  $\nu_e$  conversion into  $\nu_\mu$ ,  $\nu_\tau$  (detectable in Borexino but with a cross section 4.5 times lower) Borexino is expected to see average of  $47.5 \pm 3.4$  counts/(day x 100 ton).

## Internal Backgrounds

The background contributing to the internal radioactivity is a result of natural contamination of the materials and hardware used in the construction of the Borexino detector. It is tempting to assume that the future background suppression in the region of interest would be determined only by purification and material selection. Even with the unprecedented low levels of  $^{238}\text{U}$ ,  $^{232}\text{Th}$  concentrations achieved in Borexino the background count rate still exceeds the signal by a factor of two or three. Thus, in final selection of the events it was necessary to apply both spacial and timing cuts in the analysis. Another difficulty in preparation for the experiment arises from the fact that the presence of certain isotopes (e.g. 210-mass) will be design dependent, and as a result they will be hard to determine in the CTF purification tests. The issue is mainly related to  $^{210}\text{Pb}$  whose long half-life (22 years) and tendency to adsorb on to surfaces, often causes its daughters ( $^{210}\text{Bi}$ ,  $^{210}\text{Po}$ ) to be found out of secular equilibrium with the  $^{222}\text{Rn}$  section of the chain above it.

We can categorize the most important internal backgrounds for Borexino into three independent groups. The first includes long-lived isotopes dating far back to the era of Solar System formation,  $^{232}\text{Th}$ ,  $^{238}\text{U}$ , and  $^{40}\text{K}$ . While potassium is a  $\beta^-$  emitter with an end-point of 1.312 MeV, extending in energies over our neutrino signal, it is fairly easy to estimate its contamination in the scintillator due to the other, 10% electron-capture branch into  $^{40}\text{Ar}$  that immediately decays away with a gamma. Contribution of  $^{238}\text{U}$ , and  $^{232}\text{Th}$  daughters on the other hand, tremendously exceed that of  $^{40}\text{K}$ . Fortunately, most of its spectra are composed of easily distinguishable particles, 95% of which can be rejected via statistical subtraction. Worth mentioning are the two most problematic daughters of the chains:  $^{222}\text{Rn}$ , and  $^{208}\text{Tl}$ . As a noble gas,  $^{222}\text{Rn}$  tends to diffuse through the materials of the detector. Such spatial relocation disturbs the secondary equilibrium with other daughters making it difficult to estimate the original concentration of  $^{208}\text{Tl}$ . Its count rate on the other hand, is particularly

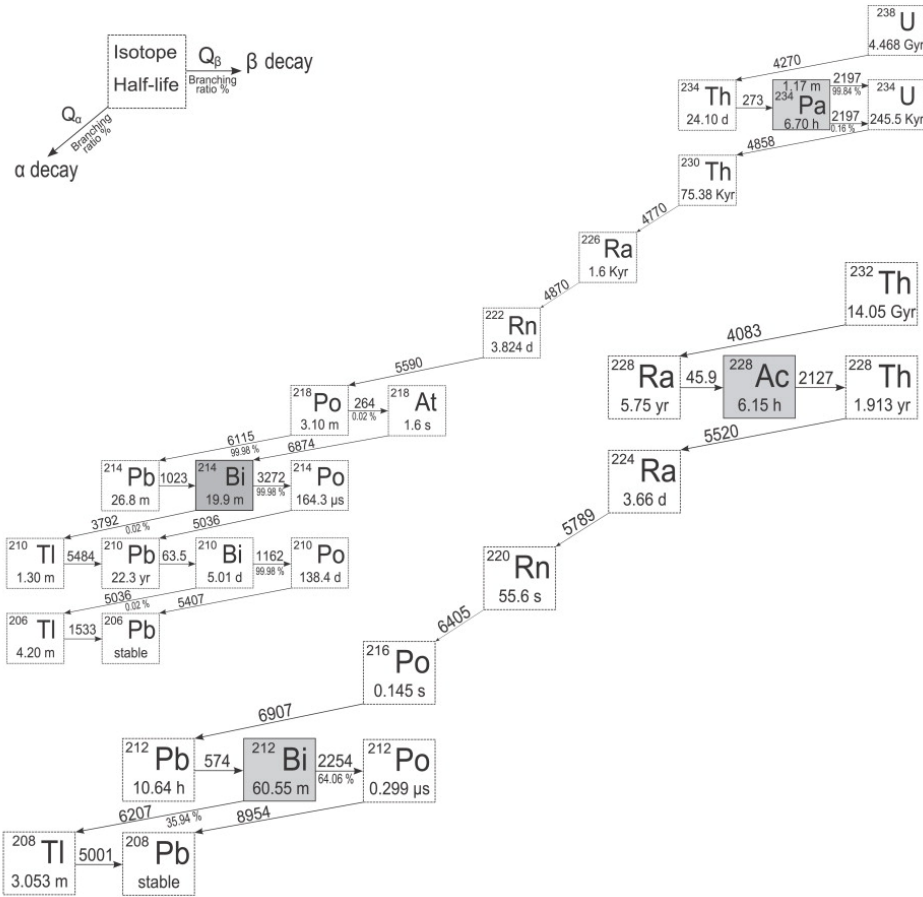


**Figure 3.8:**  $^{238}\text{U}$ , and  $^{232}\text{Th}$  cascade diagrams representing the decay chains of major impurities in Borexino. Their typical activities are 30 mBq/kg, and 40 mBq/kg respectively, which for the entire chain is equivalent to over 120 cnt/day in a 100ton Fiducial Volume.

easy to determine in the scintillator, however its penetrating 2.615 MeV  $\gamma$ -ray from the outer regions of the detector makes this isotope a major difficulty in low-energy neutrino detection.

The second origin of the backgrounds, of particular danger to the experiment, comes from  $^{39}\text{Ar}$ ,  $^{85}\text{Kr}$ , and  $^{222}\text{Rn}$  noble gases that can enter the scintillator when in contact with un-purified air at the time of filling or sparging. The  $\beta^-$  end-point of  $^{85}\text{Kr}$  is at 0.687 MeV, making it indistinguishable from neutrino-scattered electrons. With a half-life of 10.8 years, 0.45% of the time  $^{85}\text{Kr}$  fortunately decays into an excited state of  $^{85}\text{Rb}$ , whose decay provides another coincidence tag cut. Similarly, fast  $\alpha$ -decaying  $^{222}\text{Rn}$  contamination can be

efficiently inferred by a subsequent  $^{214}\text{BiPo}$  double coincidence. The situation however, does not present itself as positively in case of  $^{39}\text{Ar}$ , it is only the initial radio-purity that can save the detector from its indistinguishable  $\beta^-$ 's.

Lastly, it is worth mentioning the contribution of Carbon, the most common isotopes in the organic scintillator of Borexino. Natural  $^{12}\text{C}$ , through interaction with cosmic rays, can convert into radioactive  $^{14}\text{C}$  that  $\beta^-$  decays with a Q-value of 0.156 MeV. Even though the energy of events is much lower than the desired  $^7\text{Be}$   $\nu$  window, the rate is high enough to significantly contribute to a so-called pile-up effect. A coincident decay in two spatially distant parts of the detector. Fortunately PC used in Borexino was extracted from crude oil that was trapped underground for billions of years, well protected from the cosmic rays.

## External Backgrounds

Even though the term *external backgrounds* may refer to various sources, including even the components of the detector itself, we would like to focus the attention now on muons, which can drastically suppress the overall performance of any detector. Even with orders of magnitude reduction due the overburden, those can still lead in the number of background events throughout the spectrum. At the depths of Borexino about one muon crosses a square meter every hour, which for this size of a detector means over 4000 events per day. They are highly energetic ( $> \text{GeV}$ ) and likely to interact with the active mass, generating long- and short-lived radio-isotopes ( $^{14}\text{C}$ ,  $^{10}\text{C}$ ,  $^{11}\text{C}$ ,  $^9\text{C}$ ,  $^{12}\text{B}$ ,  $^{11}\text{Be}$ ,  $^8\text{He}$ ,  $^8\text{B}$ ,  $^6\text{He}$ ,  $^9\text{Li}$ ,  $^6\text{Li}$ ). As a result, the efficiency of muon detection must be high in order to provide satisfactory rejection conditions. In Borexino, it is achieved by combining two detectors: Inner and Outer, in the following tags

- Muon Trigger Flag (MTF): A hardware flag out the Outer Detector (OD)
- Muon Clustering Flag (MCF): A combination of OD PMTs hits.
- Inner Detector Flag (IDF): A software, Pulse-Shape-determined flag.

These tools give the Borexino incredible sensitivity to muons traversing walls of the detector resulting in identification of over 99.99% of all the muon tracks. The short-lived cosmogenics are removed by a blank, two-second veto after each muon. Identification of a long-lived  $^{11}\text{C}$  (20 min half-life) is performed by a triple coincidence cut (i. muon track, ii. neutron capture, iii.  $^{11}\text{C}$  decay).

Before the Borexino era, the effect of muon flux seasonal modulation has been studied with various experiments ([74], [75], [76]). Since the origin of cosmic muons is in the decaying  $\pi$ , and K mesons in the atmosphere it is clear that the production rate will depend on the density of air at a given point in time of the year, and as a result on the temperature and seasons 3.9.

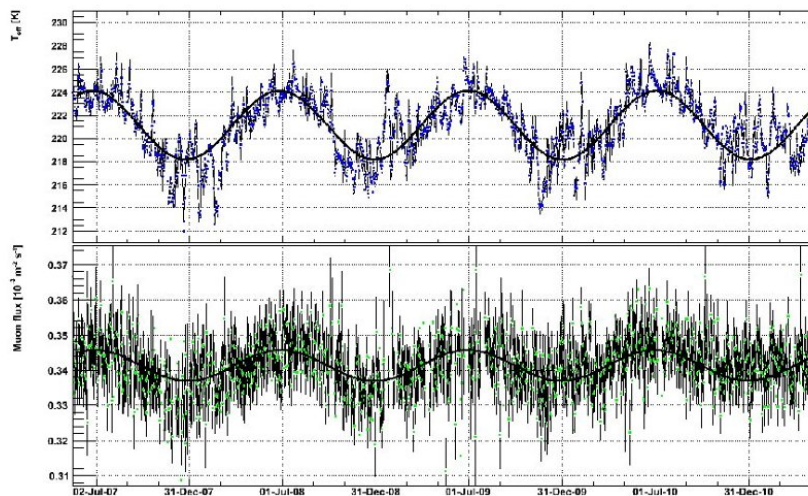


**Figure 3.9:** Seasonal modulation of the measured muon flux in the Borexino detector (top blue), and the effective temperature  $T_{eff}$  variations (bottom green) in time. The correlation between the two is clear. Figure from [74].

The muons interact within the inner vessel with a  $^{12}\text{C}$  nucleus, resulting in a radioactive  $^{11}\text{C}$  whose rate we can analyze searching for any correlation with the  $^7\text{Be}$  fluctuations.  $^{12}\text{C}$  is present in the region of spectrum where most of the natural backgrounds are stable or negligible, thus giving us a decent probe of the signal variation.

## 3.2 DAQ Electronics and Software

In order to collect and analyze the physics events from over 2000 Borexino PMTs, the detector was equipped with a dedicated Data Acquisition electronics comprised of 14 identical racks of High-Voltage, Scalers, Laben-, Front-End-Boards, and Patch Panels handling 160 PMTs each. Over 100 MB, or 100,000 events of data is collected every hour which must be filtered and organized properly for further analysis with a custom reconstruction software. In these sections, both aspects of the DAQ will be described.

### Electronics and Low Level Software

The first of the two major detection systems in Borexino, presented in Figure 3.10 and is responsible for the inner detector. The photomultipliers are controlled by the analog Front-End boards which provide and decouple the high-voltage from the signal that is being amplified and later used for the timing of events. The integrated signal from all channels will be used to determine the total charge. The performance of the system has been tested with a signal to noise ratio on the order of  $10^{-4}$  ([77]). Physics events are being recorded when a trigger fires, that is, when a certain number of PMT hits happen within a 50 ns window. The Borexino Trigger Board (BTB) is re-configurable (on a user level) and in normal mode is set to 25 channels, an equivalent of about 50 keV. For quality reasons it is important to

begin recording the events slightly before the trigger start until a few  $\mu\text{s}$  after its end. The signal is then transferred to the digital boards where functions responsible for calculation of the position and energy of events have been implemented into the read-out cards governing 8 channels at a time. A number of work-stations was also established to control the process of data acquisition: *bxbuild*, where processing of the data takes place; *bxdb*, computer running the database, *bxweb*, server holding the web-GUI for the user; *bxslow*, controlling the power supplies; and finally *bxmon*, a firewall machine.

Each channel will be collecting and saving the information for each event with its:

- Position, determined based on either the PMTs-hit-times or charge collected by individual PMTs
- Energy, being a sum of hits or collected charge from all the PMTs
- Timing (also relative timing for determination of coincident events)
- Pulse shape, for future  $\alpha/\beta$  discrimination see Section 3.2

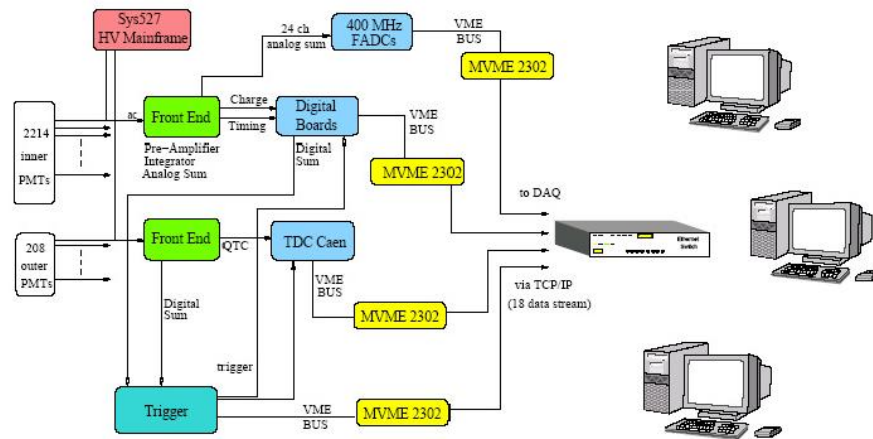


**Figure 3.10:** Cartoon representing the Borexino DAQ electronics scheme. Inner and outer detector PMTs are shown on the left-hand-side, with the work-stations to the right. Figure from [78].

The ID electronics was designed from the very beginning with a goal of sub-MeV performance. Thus, such events as energetic muons traversing the scintillator could easily blind

all the PMTs. In order to avoid such situation, an additional, and independent system was designed. Composed of 208 photomultiplier tubes facing the Water Tank (WT) the Outer-Detector will search for Čerenkov light. For the most part the functioning of the OD is performed in the same way as that of the ID with an exception of decoupling of the high-voltage which is not done in the front-end part anymore. As a consequence of muons crossing the inner detector, about 70 times a day a spallation neutron will be created. Neutrons emit a characteristic gamma of 2.26 MeV after a mean capture time of about 250  $\mu$ s on the hydrogen nuclei, which makes them easy to correlate with a muon event. Within a few months after the beginning of Borexino operation in 2007 a new neutron triggering system was implemented in place of the old and inefficient one. Detailed information regarding spallation neutrons is crucial for removal of  $^{10}\text{C}$  background [79].

## High Level Software

The offline reconstruction of events provides a further conversion of the raw-data information into more tractable variables. These *ntuples* will represent identification, energy, position, correlation between successive hits, timing of the events and many more properties. More details about most of the Borexino variables available in the reconstruction software can be found in [81]. At the beginning of 2004 and 2007, two independent reconstruction codes were developed, European *Echidna*, and American *Mach4* generations. Both were written in C++, with an output file into a standard **ROOT** analysis platform. Independently of the generation, the tasks for each one are composed of the following:

- Pre-calibration
  - Synchronization of the timing for each channel based on the pulser trigger from the beginning of each run
  - Calibration of each channel with respect to the laser fiber pulses pointing at individual PMTs
  - Dark rate subtraction for each cluster, revealing the pure signal

- Cluster identification (division of each *trigger* into individual, physical events)
- Position Reconstruction, a set of reconstruction algorithms searching for most accurate position of the events within the Inner Vessel (used to define a Fiducial Volume)
- Pulse Shape and  $\alpha/\beta$  discrimination (discussed in Sections 3.2 and 3.2)

In mid-2010 it was decided by the Borexino Collaboration that the two codes could be finally merged, incorporating the best features of each. Mach on Top of Echidna, also known as *Ma(ch)idna* or simply *MOE*, uses the Low Level<sup>2</sup> of *Echidna* ROOT files to process and add *Mach4* variables.

Clustering of events is important due to a known problem of the length of the gate. Every time a trigger fires, a 16  $\mu$ s gate opens, leaving enough room for multiple, fast coincidence events to happen. In order to identify them, each gate window is then re-binned into smaller, 16 ns groups of hit-times (the identical procedure is applied to 1.6 ms muon gates). With such a definition of clustering we can calculate the energy variables (details in 3.2).

Determination of the position of each event in a cluster is based on timing of individual hits ( $i$ ), and since the scintillator is not a perfect environment, a cascade of delays need to be accounted for in the final estimation, such that:

$$T_{T_i} = T_{E_i} + T_{PDF_i} + T_{TOF_{i,j}} + T_{J_{i,j}} \quad (3.8)$$

where,

$T_{E_i}$  - GPS time of the event

$T_{PDF_i}$ - the scintillators re-emission, or decay time (modeled according to a theoretical Probability Distribution Function (PDF)<sup>3</sup>)

$T_{TOF_i}$  - Time\_of\_Flight from the emission point to individual PMTs <sub>$j$</sub>

$T_{J_i}$  -  $\sim 1$  ns transit time within the PMTs (insignificant)

---

<sup>2</sup>Determination of hit times and charge

<sup>3</sup>The scintillator's Probability Distribution Function

A reconstruction algorithm was developed in *Mach4* searching for the minimization of the  $(T_{E_i} - T_{TOF_i})$  and the PDF, using a log-likelihood based fit- which turned out to be the most reliable and widely used. Similar implementations have been made within *Echidna*, and since that code had been under development for much longer, various techniques such as, center-of-mass, Landau-based-PDF, or analytical-PDF were investigated using it.

The scintillator's Light Yield (on the order of 500 photoelectrons/MeV) in the Borexino detector favors very good spatial resolution for reconstructed events of about 12 cm at 1 MeV that scales as  $N_{p.e.}^{-\frac{1}{2}}$ .

## Energy Variables

When an event occurs in Borexino, it is most probable that each PMT will be hit by a single photon. Therefore, it is natural to assume that the total energy would be proportional to the sum of all the hits. By categorizing information from the cluster of an event, we define two species of energy variables, based on a total number of hit-tubes,  $N_{hits}$ , and a total collected charge from the ADCs (number of photoelectrons),  $N_{pe}$ . Since the  $N_{hits}$  for higher values of deposited energy<sup>4</sup> tend to be underestimated due to increasing probability for multiple hits of a PMTs, we will continue this analysis using only the charge variables. Regardless,  $N_{hits}$  remains a suitable parameter for many other applications<sup>5</sup>. After the merging of the *Echidna* and *Mach4* codes, we were left with a couple of charge variables that were all very similar in definition, yet carrying certain differences. Let us have a look at the most important ones in addition to those that will be used in the work presented.

---

<sup>4</sup>Effect visible for energies as low as  $\sim 2.5 MeV$

<sup>5</sup>The stability check for instance, in the low-energetic  $^{14}C$  region will be performed using the  $N_{hits}$  variable

**Echidna's charge-short**

This is the total charge in all of the channels of short cluster windows (retriggered channels are also included). Result is normalized to the standard value of 2000 *live* PMTs, which means:

$$npe_{short} = \sum_0^{2218} npe_i \times \frac{2000}{N_{PMT}} \quad (3.9)$$

**Echidna's charge-long**

Definition is for the most part identical to the previous one, except that this variable applies to long, fixed-length types of cluster windows.

**MOE's npe\_noavg\_corrected**

Once again, the charge from all hits is collected and summed, including the retriggered channels in the cluster. Next, the expected dark-noise is subtracted from the obtained value and the result is normalized to the number of live PMTs.

**MOE's npe\_corrected**

Identical variable to the previously defined `npe_noavg_corrected`, but this time with added possibility to recover charge by collecting it from the surrounding hits within 15 ns. It is performed whenever the timing of a hit is correct but the charge is not recorded. The result is also normalized to the number of live PMTs.

**MOE's `npe_hitdist_corrected`<sup>6</sup>.**

A brand-new energy reconstruction algorithm; for the first time available in version 9.8 of *Mach4* and MOE. It has been noticed that due to the asymmetric distribution of PMTs in the top, as opposed to the bottom of the detector, the reconstructed energy of events could be different. This variable however, is expected to be position-independent. The concept relies on the fact that there is a strong correlation between the probability of hitting PMT, and its solid angle to the scintillation event. The derivation is similar to the case of equivalent PMTs with a correction for the dead ones:

$$\langle \epsilon \rangle = N \langle \epsilon_i \rangle = \sum \epsilon_i = npe; \quad (3.10)$$

$$\langle \epsilon \rangle = N_0 \langle \epsilon_i \rangle = \frac{N_0}{N} \sum \epsilon_i = npe_{corrected}; \quad (3.11)$$

It is assumed that the number of photons hitting a particular PMT is proportional to the subtended solid angle:

$$\langle \epsilon \rangle = \frac{\Omega_0}{\Omega} npe; \quad (3.12)$$

Further discussion of the top-to-bottom asymmetry in the energy scale reconstruction is presented in Section 4.2, where we introduce a geometrical correction derived from the study of the external Gamma source calibration.

From information obtained from the <sup>210</sup>Po energy peak position stability in time (shown in Figure 3.11), we determined that the most stable, and thus the most suitable variables for this analysis are *Mach4*'s charge variables:

- MOE's `npe_noavg_corrected`, and
- MOE's `npe_hitdist_corrected`;

---

<sup>6</sup>Implementation into the code, Jingke Xu of Princeton University [80]

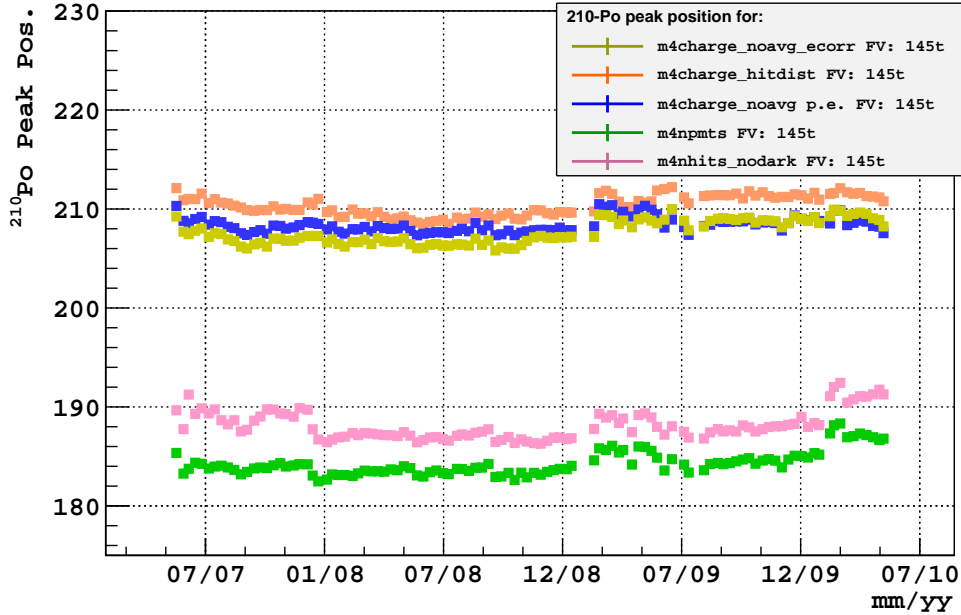


**Figure 3.11:**  $^{210}\text{Po}$  peak position every 10 days for various variables in  $N_{pe}$ ,  $N_{hits}$ , and  $N_{PMTs}$ .

## Pulse Shape Discrimination

Once the position and time variables for events are determined we can calculate the hit-time profiles. As mentioned already, due to differences in the ionization densities,  $\alpha$  and  $\beta$  particles have different characteristics of the time *emission* profiles. Unfortunately, because the  $\gamma$  interactions are indistinguishable from  $\beta$ 's, they will be corrupting the  $\beta$  shapes due to multiple Compton scatterings, slightly shifting the timing of hits.

In *Mach4*, there were originally two algorithms responsible for  $\alpha/\beta$  discrimination, Tail-To-Total, and the *Gatti* parameter, further discussed in the next section. Other methods were also developed and tested in the initial, or even pre-initial stages of the *Echidna* sister, such as: Maximum Likelihood, Kolmogorov distance, Primary SVM<sup>7</sup>, and Global SVM, none of which ever implemented in the final versions of the reconstruction codes.

<sup>7</sup>Support Vector Machines

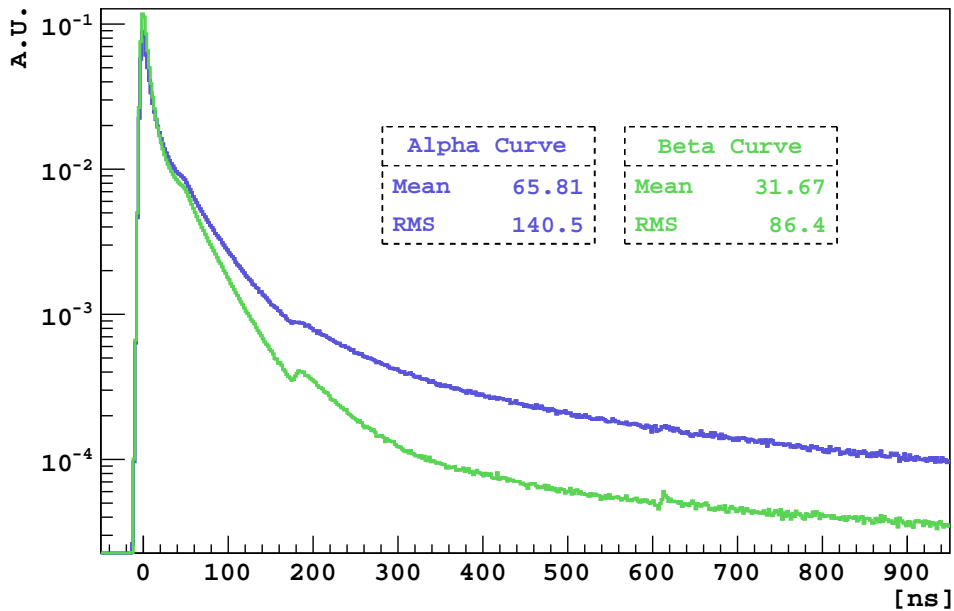


**Figure 3.12:** *Normalized Scintillation Pulse Shape; Generated for  $\alpha$ 's and  $\beta$ 's in the pre-mass-processing stage of Mach4 for the  $^{214}\text{BiPo}$  coincidences. At the time of writing the most recent release of the code was MOE c14.9.8*

## Gatti Parameter

Based on the information obtained from the difference in the hit-time distribution for  $\alpha$  and  $\beta$  particles we can effectively remove the problematic  $\alpha$  background arising mainly from  $^{210}\text{Po}$  decay. In the  $^7\text{Be}$  annual signal variation study, such a strong peak might not only affect the measurement due to its high count but also due to its rate instability in time (studied in Section 4.2). If removed by pulse-shape discrimination, the presence of the  $^{210}\text{Po}$  background will no longer be as important in the spectral-fit analysis; however, due to the Light Yield (LY) changes it might still need attention. On the other hand, the Gatti parameter method

might not be as effective in the peripheries of the detector as it is at the center. Based on the tests performed with the calibration sources, we know that the method guarantees good  $\alpha/\beta$  separation out to 3 m in radius. This could pose possible complications when attempting to increase the available statistics by enlarging the FV. So far, only radii up to 3.291 m have been considered.

The method for separation of the two types of particle interactions in liquid scintillators was first proposed back in 1962 by E. Gatti, F. De Martini in [82]. The Gatti parameter is defined as the following<sup>8</sup> :

$$g_e \equiv \sum_{t=0}^{\infty} e[t] \cdot \frac{r_{\alpha}[t] - r_{\beta}[t]}{r_{\alpha}[t] + r_{\beta}[t]} \quad (3.13)$$

Where  $e[t]$  is the time profile, and  $r_{\alpha,\beta}[t]$  are the reference shapes for the investigated event. As a result, the determined  $g_e$  parameters will be distributed around mean values which are positive for the alpha particles and negative for the beta's.

Reference shapes are normally generated for  $\beta - \alpha$  coincidence events of  $^{214}\text{BiPo}$  from either the data or the  $^{222}\text{Rn}$  calibration source. The tag is completed after satisfying the following conditions for consecutive triggers:

1. Both events must lie within a 4 m radius
2. The first event ( $^{214}\text{Bi}$  candidate) must have an energy in the range of 100 - 1750 `npe_corrected`
3. The second event ( $^{214}\text{Po}$  candidate) must have an energy in the range of 300 - 500 `npe_corrected`
4. The time difference between the two events must be in the range of 20 - 500  $\mu\text{s}$
5. The distance between the two events must be less than 0.6 m

---

<sup>8</sup>Original Gatti parameter determination method was implemented into *Mach4* code by Richard Saldanha of Princeton University.

Based on Equation 3.8, we can calculate the subtracted TOF,  $T_{T_i} - T_{TOF_{i,j}}$  for each tagged event and fill a histogram representing our reference shape (Figure 3.12) that will be used for the determination of the Gatti parameter with 4.2 as shown in Figure 3.13. These Gaussian distributions can also be shown to have the following *mean* and *variance* parameters:

$$\overline{G_\alpha} \equiv \sum_{t=0}^{\infty} r_\alpha[t] \cdot w[t] \quad (3.14)$$

$$\text{var}(G_\alpha) \equiv \frac{1}{N} \sum_{t=0}^{\infty} r_\alpha[t] \cdot w^2[t] - (\overline{G_\alpha})^2 \quad (3.15)$$

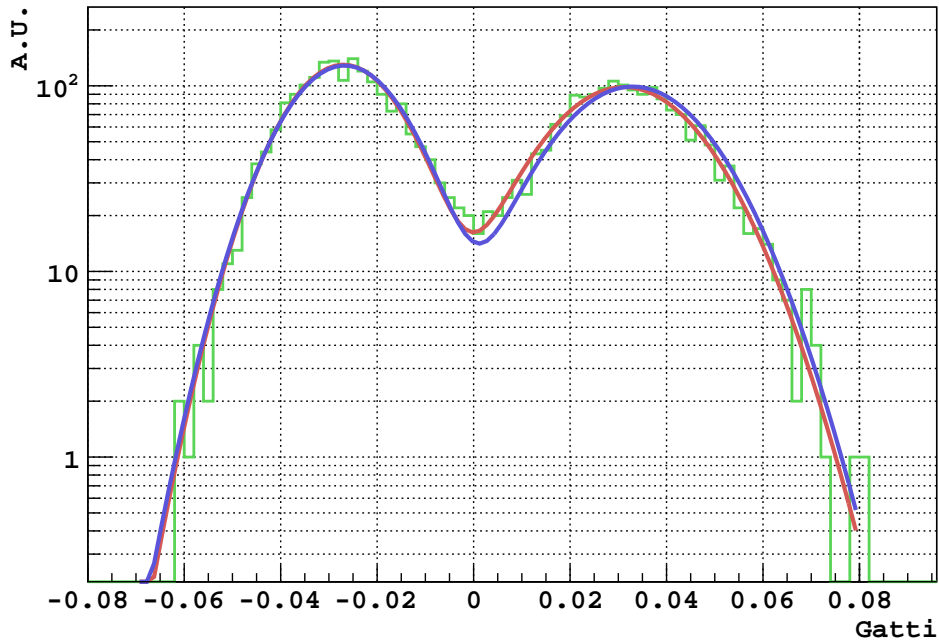


**Figure 3.13:** *Gatti  $\alpha/\beta$  discrimination generated for a fiducial mass of 145 tons in a 5 npe window at 285 npe. The Blue and Red curves also show a bi-Gaussian fit.*

## Statistical Subtraction of $\alpha$ Events

Spectral separation of the  $\alpha$  and  $\beta$  particles is performed in three steps. During each step, the Gatti parameter is calculated in five photo-electron bins; after fitting and re-correcting for possible biases, the original spectrum is split into independent  $\alpha$  and  $\beta$  spectra based on the integral of the distribution in each bin. These three steps were found to be sufficient in correcting for the biases that result from non-Gaussian shapes of the distributions. The observed discrepancy comes from an overwhelming contamination of  $^{210}\text{Po}$ - $\alpha$ 's and an overlap in the shapes' distribution. The three steps of  $\alpha$  statistical subtraction presented are shown also in Figure 3.14 according to the color-code.

### Step I

First, in a single bin, we perform a simple, dual-Gaussian fit to the distribution, leaving the parameters constrained to only reasonable values. Results are saved and sent to step II as initial values of the fitting function.

### Step II

The mean and sigma distributions of the Gatti parameter obtained from the previous step were found to be energy dependent due to the aforementioned high  $\alpha$ -to- $\beta$  ratio in the  $^{210}\text{Po}$  region. As a result of this bias, a linear fit is performed over the -window, excluding the -range, to determine the shape of the dependence that is then used as a  $1\text{-}\sigma$ -constraint to the mean value in step II. With these precautions in mind, the procedure from step I is performed once again.

### Step III

This final step is in principle a Monte-Carlo driven correction for bias in the number of  $\beta$ 's found in the previous steps. Based on a simulated number of events of each species that are determined from the mean Gatti values, the final number of  $\beta$ 's is corrected for the MC result.

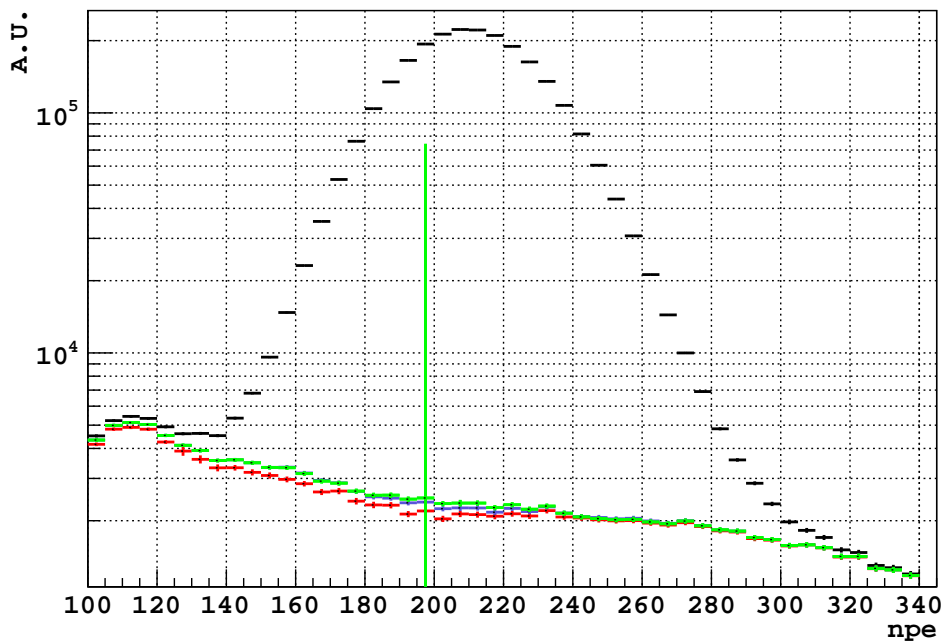


**Figure 3.14:** *Gatti  $\alpha/\beta$  statistical subtraction performed on three two years of data in fiducial mass of 145 tons.*

## 3.3 CCD Positioning System

In Borexino's ultimate goal of achieving the final precision of 3% on the rate measurement, the determination of the target mass becomes one of the most crucial tasks. This in turn, is directly related to how well we can define the software-based fiducial volume cut. Detailed

understanding of the position reconstruction will directly determine the uncertainty on the detected rate of events in the fiducial volume. Moreover, it is worth mentioning that the original design requirements on the calibration system precision were set by the expected flux modulation due to Earth's orbit. At least a 2% accuracy is needed to be able to observe the 7% change in the rate for a 100 ton fiducial volume which was already proven to be satisfied in the initial tests. After many of the successful calibration campaigns that will be discussed in the next section, we can now investigate the precision of the system once again by comparing the physical source position with the reconstructed one. This verification differs from the ones performed before since the system is now tested in the actual scintillator environment rather than air [44].

## The Source Location System

### Introduction

The source location system consists of seven consumer grade digital cameras, six of which are on orthogonal axes, as presented in Figure 3.15. The CCD camera system employs Kodak DC290 2.4 megapixel consumer grade digital cameras, each equipped with a Nikon FC-E8 fish-eye lens. The fish-eye lens allows the entire IV to be viewed by expanding each camera's field of view to 183°.

The camera + lens system is mounted in a housing on the SSS, with a glass underwater photography dome on the front side. There are also four pin-hole LEDs present within each of the camera housings to provide fixed reference points for correcting lens misalignments between pictures. Including the diffuser mounted above the source, there are a total of 29 red light sources that are flashed when a photo is taken. A total of eight 50W halogen lights, split into two independently wired banks, are installed in each camera housing to

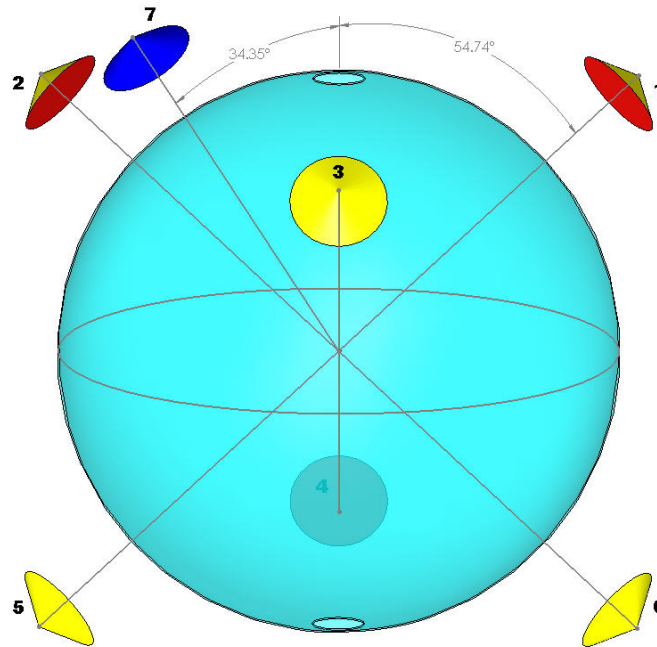


**Figure 3.15:** Positions of the seven cameras as seen from the outside of the Stainless Steel Sphere (SSS). Cameras 1 and 5, 3 and 4, 2 and 6 all face each other, and all 1 through 7 are located at radius of 660 cm w.r. to their pin holes.

illuminate the detector for vessel monitoring or public relations photos. The true location of a calibration source can be determined in the following way: a laser-illuminated diffuser ball, attached close to the source, is flashed while the CCD cameras take pictures simultaneously. The position of the diffuser and of the source is determined via triangulation of all pictures. Although finding a point in three dimensions requires only two cameras, all seven are used to check for self-consistency and to increase the resolution of the system. Before we discuss the methods of source position reconstruction, we will briefly describe how the cameras were calibrated and how the pictures are corrected (tweaked) due to lens' effects.

## Calibration of the Source Location System

A complete calibration of the camera system needs to be performed only once and requires six free parameters and the known PMTs and camera positions in the SSS. They are:

- Pixel Scale- due to non-unitary size of the pixels in the CCD array,
- CCD offset- whenever the CCD is off in x,y with respect to the optical axis,
- Pitch and Yaw- a rotation of cameras with respect to x and y,
- Roll- similarly, a rotation around the z-axis,
- Radial distortions- due to an induced point-symmetric radial bias in the reconstructed positions,
- Distortion due to lenses not being co-axial.

The idea is to take a reference image of the detector with the halogen lights on (as well as LEDs for future 'tweaking'). In our case it was an image from the very beginning of data taking, May 15th 2007. Since we know the physical location of all the light concentrators, we can use the central pixels for these, coupled with the known location of the cameras, to determine well-defined rays in space. Since there are over 2000 PMTs, a simple functional form to correct the optics is over-determined, and a simple fitting routine is used to determine the best parameters for the function. (A pin-hole camera would be a simple direct calculation, but then wouldn't have any light collection efficiency either.)

While angle lenses induce a point-symmetric radial bias in the reconstructed positions. This effect, referred to as 'radial distortions' is corrected for with a ninth-order odd polynomial:

$r' = \sum_{i=1}^9 c_i r^i$  for odd  $i$ , with  $r$ , the uncorrected radial coordinate of the fired pixel ( $\{p_x^2 + p_y^2\}^{1/2}$ ). De-centering distortions are corrected via two de-centering parameters ( $p_1, p_2$ ) shown

in equations 3.16 and 3.17. In the aforementioned equations  $(p_x, p_y)$  are the corrected x and y pixel coordinates of the diffuser,  $\theta$  is the polar angle of the fired pixel,  $r'$  is the radial coordinate of the pixel corrected for radial distortions, and  $r$  is the uncorrected radial coordinate of the fired pixel.

$$p_x = r' \cos \theta + r^2 \{p_1 (1 + 2 \cos^2 \theta) + p_2 \sin (2\theta)\} \quad (3.16)$$

$$p_y = r' \sin \theta + r^2 \{p_2 (1 + 2 \sin^2 \theta) + p_1 \sin (2\theta)\} \quad (3.17)$$

The orientation of the camera is accounted for by three additional free parameters: yaw, pitch and roll. Since the axis of the CCD may not be collinear with the optical axis, we have two free parameters to account for an offset of the CCD with respect to the optical axis. Finally, one free parameter allows for an overall scaling of the pixel size.

The process is to calculate an image, using the above function and known PMT positions, and compare it to the actual image. If the two match, the calibration is good. An uncertainty of one pixel in a camera corresponds to about a 1 cm uncertainty at the center of the detector. The process is iterative, starting with a few identifiable mating points in both the calculated and true images. This is enough to set the x,y offset of the CCD image, as well as an overall scale and rotation (other parameters found from earlier work should be left alone at this point). The calculated image is then regenerated, and a few more identifiable mating points will become apparent. With these added, the function is again fit (minimizing the pixel shifts between the calculated and true-image calibration points), perhaps with a few more parameters active. Repeating this process, one will wind up with perhaps one to two

hundred calibration points. A good fit will result in less than a few pixels difference between any calculated and true image calibration point.

To define a calibration point, the calculated image is overlaid onto the true image, and can be drug around until a calculated light concentrator overlies a true-image light-concentrator. When satisfied, the true image pixel and x,y,z position of this light-concentrator are saved together as a calibration point. One then goes to another region of the image, and repeats the process. If such a 'match' is later seen to be wrong (can't be fit), it can be modified or deleted. The chi-squared used in the fit is the sum of the pixel distances squared for all calibration points between the true-image pixel and the calculated pixel given by the fit function operating on the associated x,y,z position (normalized to the number of points). This approach avoids the problem that the amount of 'drag' will depend upon the function parameters which change between iterations of adding new calibration points.

While the camera's 'pin-hole' is located at the center of the camera housing glass dome, there could still be some lensing effect when the detector is filled with either water or PC. This means that there were in fact three calibrations: air, water, and PC. Each of these required a clear picture where all of the light concentrators were visible. Once calibrated, the halogen lights will never need to be turned on for source work.

### **'Tweak-ing' the Cameras**

Since commercial cameras were used, the lens retracts and returns between each image taken. As a result there can be a slight (several pixel) shift between images. To correct for this, four 'pin-hole' LED light sources in each camera housing can be turned on while taking pictures, red spots in Figure 3.20. Doing this for the 'calibration' image provides fixed reference points for future images. These are then shifted and scaled so the four reference points line

up with those in the calibration images, as it is presented in Figure 3.20, to the left for the 'calibration' image, and to the right for a source picture. The process is fairly automated and it is performed before every image analysis or source location task.

## Determination of the CCD Uncertainty

In this paragraph we will give an estimate of the CCD camera uncertainty on the determination of the source position. In order to do this, we first verify that the detector center, as determined by the cameras, coincides with the nominal center, obtained assuming a perfectly spherical SSS. Second, we obtain an estimate for the uncertainty of the CCD cameras on the z-axis, by using as a reference the physical length of the insertion rods.

### Center of the Detector

The actual center of the detector cannot be determined by any other means than with the cameras. Unfortunately, there is not enough and detailed hardware information to be able to precisely tell where this point is located by measuring from the top-access point. Nevertheless, as it can be seen from Figure 3.15, the center of the detector can be rather easily determined by looking at the intersection point of all the camera rays, where it should be obvious that for a true sphere this is in fact the central point. First of course, the cameras need to be calibrated based on the known positions of the PMT light concentrators as described in details in Section 3.3. Once again, this task was performed at the very beginning of data-taking and needs not be repeated. Before starting work on any picture we do have to 'tweak' it in order to correct for lens-position effects (one click of a button).

By default, the origin of the coordinate frame (0,0,0) is set to where the center of the SSS is expected. What we do next is we send a ray from each camera to the center, and we

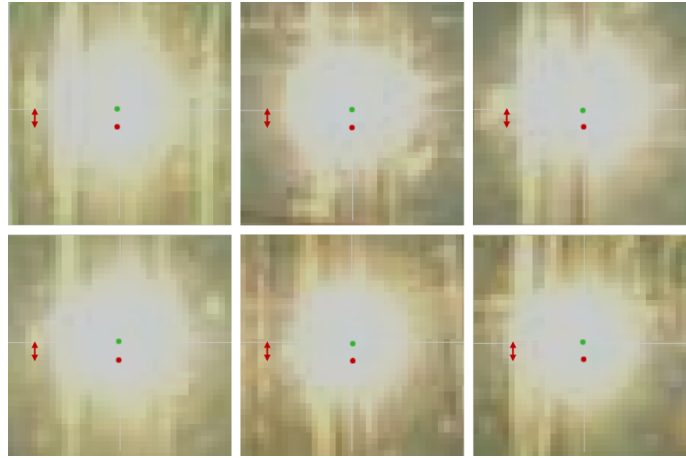


**Figure 3.16:** *Images from each of the 6 cameras except for number 7 that does not have its own, opposite twin. All the rays were set to  $(0,0,0)$  which is indicated with a green dot, a red dot is where a  $(0,0,-4)$  point would have been reconstructed. The shift is rather obvious. 1-pixel corresponds to approximately a distance of 1 cm (The software is designed to be accurate to 0.1-pixels).*

extrapolate the ray across the sphere. If the ‘zero’ was determined correctly, the rays on the opposite side should all be pointing at the centers of the other cameras. Since the pictures are taken with the halogen lights ON, of course the only visible area on the other end will be a bright spot, but this should not affect the determination of the center. In fact, such exercise was performed and in Fig. 3.16 you see the result with an indication of how the image would look like if the center was found to be off by 4 cm. The fact that the camera on the opposite side shows up centered on the fiducial lines is a measure of how good the camera calibration was done. Also, the center point is independent of scale set by SSS radius, and there would be no ‘lensing’ of an inner vessel with a different index material within it.

### Position Uncertainty Estimation

Our insertion rods can be effectively used as a mechanical tape measure from a fixed point in the clean-room-4 glove-box to points on the z-axis. The rods, of course, provide only a differential position determination with respect to a known reference point. However, as it

has been presented in Section 3.3, the center of the detector is the most reliable, and well determined reference in our measurement. Also the position of the rods in the glovebox can be determined to with very high accuracy.

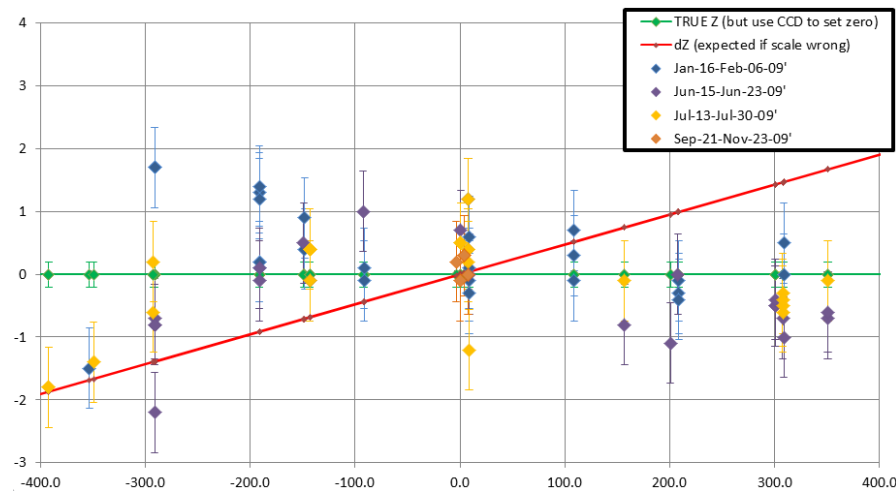


**Figure 3.17:** A comparison of the measured source position using the rods, a mechanical reference, and the CCD reconstruction software. The red line indicates where the position would be expected if the radius of the SSS was smaller by 3 cm. The uncertainty of the distribution is 0.6 cm at  $1\sigma$

Figure 3.17 shows the z-coordinate measured by the CCDs minus the one obtained by a physical measurement of the rod lengths as a function of z. The different colors refer to different calibration campaigns. We see that the points line up along a horizontal line, showing therefore no bias. The maximum and minimum deviation from 0 is  $\sim 2$  cm from which we can estimate an uncertainty of  $\sim 0.6$  cm assuming a flat rectangular distribution. Even though this test was performed only in the z-direction, there is no reason to believe that other orientations would be reconstructing differently. The cameras used in this setup were distributed uniformly around the SSS, as it can be seen in Figure 3.15. Its detailed orientation was obtained from the camera-calibration by relying on the known PMT positions and its reference frame. Furthermore, we had additional piece of information that we used in order to verify the precision of the reconstruction before saving the coordinates. We can look at the distances of the rays from the reconstructed position and try to search for any abnormalities.

```

Range:          8.938
x0, y0, z0:    189.886   -1.130   -189.117
x, y, z:       189.886   -1.130   -189.117
Camera 2 dist = 4.73233032
Camera 3 dist = 3.80692625
Camera 4 dist = 2.38101673
Camera 5 dist = 2.11745572
Camera 6 dist = 1.38304567
Camera 7 dist = 0.411929756

```

**Figure 3.18:** A snapshot of the reconstructed source position and shortest distances to each of the rays.

As it can be seen in Figure 3.18, all the seven cameras identified this source however, cameras 2 and 3 could be eliminated due to higher than expected distance, 4.7 and 3.8 pixels respectively. Such condition has been used elsewhere, throughout the detector. This has additionally provided a check for systematics of the CCD's. There has not been any bias from this rule observed for any of the positions. Rays, from at least 3 cameras, have typically reconstructed to within 2 pixel from the reconstructed source position.

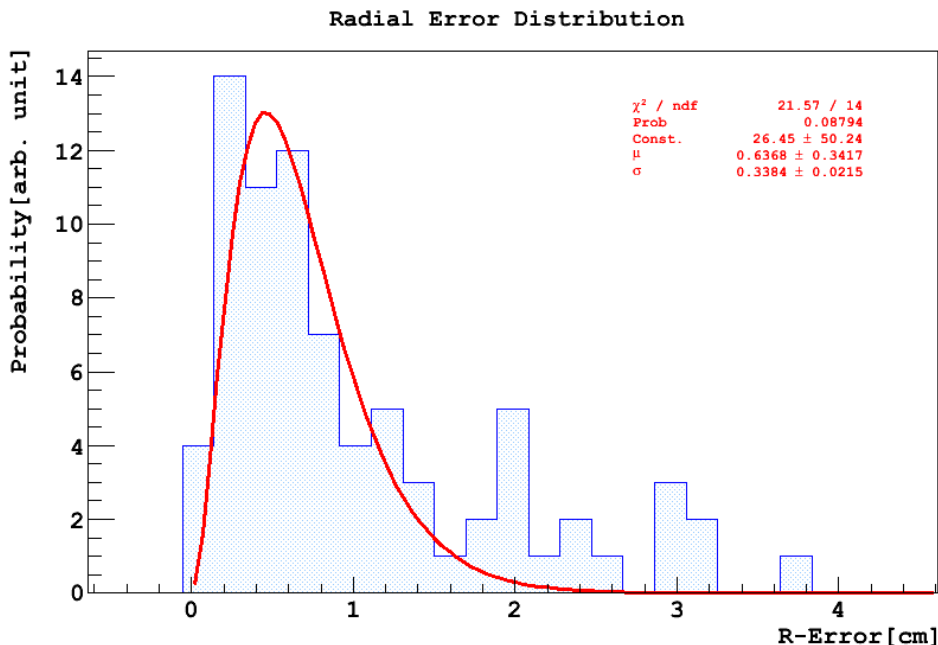


**Figure 3.19:** Histogram of the radial error distribution data from Fig. 3.17. The red line represents fit of the probability density function from Eq. 3.18.

If we assume identical error distributions in all the directions, we obtain the distribution of radial errors shown in Fig. 3.19. We can now fit the distribution of radial errors with function 3.18, and as a result we obtain the best value of  $\mu = 0.64$  cm at  $1\sigma$  confidence level ( $\sim 65.4\%$ ).

$$f(r) = \frac{c}{\sigma\sqrt{2\pi}} e^{-\frac{(r-\mu)^2}{2\sigma^2}} \cdot r^2 \quad (3.18)$$

### Detector Dimensions

As seen in Paragraph 3.3, the calibration of the CCD cameras has been performed by assuming that the PMTs are in their nominal positions. Some issues arose concerning the real radius of the SSS. The radius was actually measured to be on average smaller than the nominal one (682cm instead of 685cm) as can be seen in Table 3.1 and 3.2.

**Table 3.1:** *Dimensions of the SSS, as measured before filling in 2007. All values in mm.*

NORTH-EST	SOUTH-EST	SOUTH-WEST	NORTH-WEST
13643	13634	13660	13657
13650	13624	13654	13660
13642	13625	13638	13646
13642	13632	13634	13638
13644	13640	13632	13633
13641	13631	13630	13648
13644	13642	13638	13660

**Table 3.2:** *Diameter of the SSS. All values in mm.*

Pointing	SOUTH-NORTH
north	13599
east	13595
south	13598
west	13597

From these measurements one can derive that the SSS is not perfectly spherical, being flat-

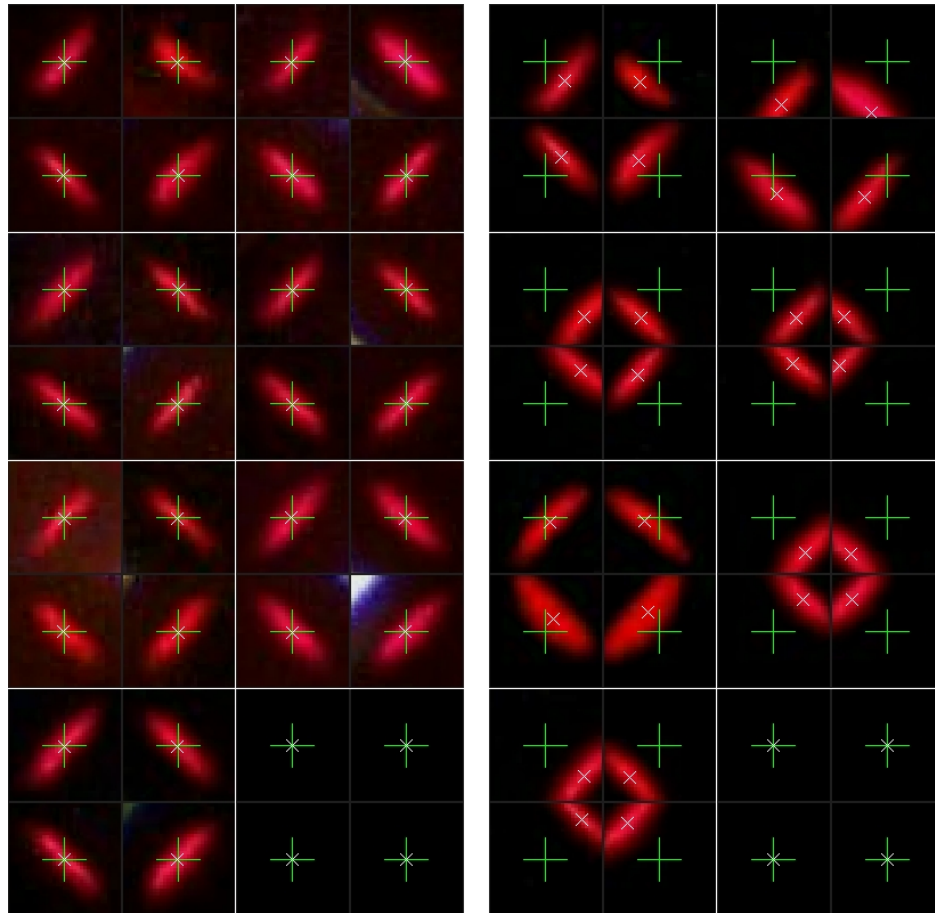


**Figure 3.20:** *This is a composite picture, examining pixels around each of the four 'pin-hole lights' for each of the cameras (1,2,3,4,5,6,7,8 left to right then down) The green 'plus' signs indicate the pixels where the pin-hole lights showed up in the 'calibration' image, while the white 'x's indicate where they are found in the current image. To the left, image number 2875, from before the filling, whereas to the right, image number 3370, from one of the calibration campaigns.*

tened at the poles. We would like to understand whether these points could have introduced a bias in the CCD camera capability of determining the source position. Using the wrong radius for the SSS when calibrating the CCD cameras would not affect the CCD angle determination (and therefore the center determination), but could have an effect on the global scale. Such an effect would show up in Figure 3.17 with points lining up along the red line. This is not the case: the effect is not there and the points correctly line up on the horizontal green line. This means that no systematic effect bias is present due to the geometry.

## The z-shift Issue

We recall that the calibration data provided evidence for a small bias in the z-coordinate: the source position is reconstructed systematically downwards with respect to the nominal position obtained with the CCD camera system by approximately 4 cm. The discussion in paragraph 3.3 proves that the CCD system is not responsible for this offset, since it determines the coordinates, at least on the z-axis, with no bias (see Figure 3.17). A possible reason for the z-shift could be due to a vertical temperature gradient which was observed in the detector's SSS volume. This possibility is discussed in the next paragraph.

## Temperature Gradient

It is hard to describe the history of the Borexino scintillator temperature in one sentence because unfortunately it was affected by many external factors throughout the data-taking period. In Section 4.2 we presented a description of the temperature changes inside of the scintillator buffer. It can be noticed in Figure 4.41 that apart from overall fluctuations<sup>9</sup>, there has always been a temperature gradient with the bottom being cooler than the top by about 4° Celsius on average. This would result in a change in the index of refraction due to the difference in the scintillator density. Since the cameras rely on the visible part of the spectrum, we can imagine light-bending on the distance of about 14 meters across the SSS. One should keep in mind that the biggest observed z-shift with respect to the data was at the center, as it is presented in Figure 3.17, whereas in the case of CCDs the agreement with the rods' reading at this location is the best. It is also important to highlight that the z-shift in the position reconstruction has been observed for all the data points throughout the calibration campaigns, from Oct 2008 to Nov 2009. Over the course

---

<sup>9</sup>Operations of scintillator refilling and water extraction have affected the temperature. The heating of the water tank that started in December 2007 had a major impact on the overall changes.

of time, the temperature difference was changing from  $\sim 4^\circ\text{C}$  in the first, to  $\sim 1.5^\circ\text{C}$  in the last three campaigns. However, there was no correlation in time found with the z-offset, which would provide additional strong argument against the hypothesis of the temperature dependent index of refraction. Even in the very last laser calibration campaign that was performed in September and November of 2009, with a temperature difference of  $\sim 3^\circ\text{C}$ , the location of the source at the center was determined with a very high precision (Orange points in Figure 3.17). In the next section we will discuss what physically the effect of a temperature gradient would be for an even a greater  $\Delta T$  value than observed between the top and bottom of the buffer volume.

### Temperature Dependence

The gradient has not always been that high, but even assuming a more conservative scenario, let us take a 5-degree difference between the top and bottom that would cause about 0.5% change in the index of refraction. A discontinuity in the index of refraction in two dimensions can be assumed for simplicity. Figure 3.21 illustrates such configuration; we assume that points A and C are at known locations. With a continuous line we indicate where the actual light path of ray sent from A to C would be located (lines AB&BC). In the old approach however, this light was travelling along the dashed line and as a result, it was naturally introducing an error (shift) in the reconstructed position. What it means is that now, any light source along the line AB&BC will be observed in the exact same pixel of camera A and C. For the position reconstruction, take the case of two cameras being used to locate position. Clearly, there will be no impact on the x or y coordinate, but the z-coordinate will be falsely reconstructed a bit low.

Consider a realistic case with point A(5.41, 3.78) as camera 1, C(-5.41, -3.78) a camera 5 and the center of the detector for now, as presented in Figure 3.21. Cameras are located

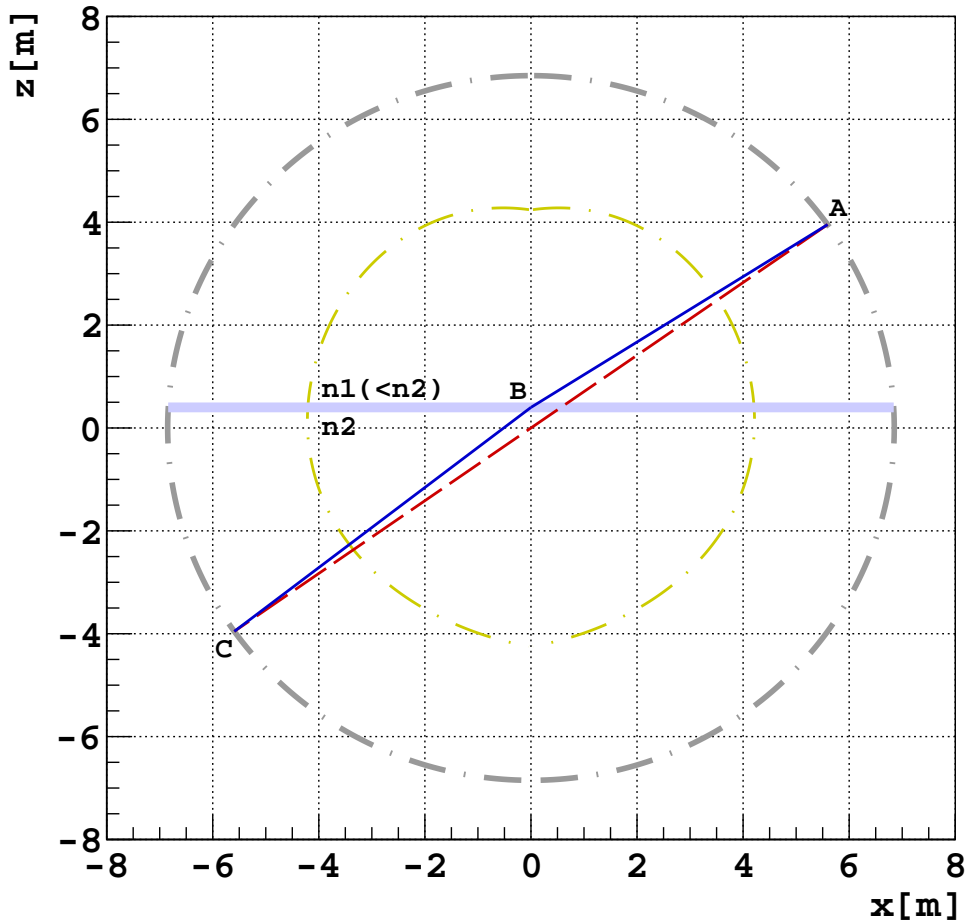


**Figure 3.21:** *The effect of the temperature gradient and, as a result, change in the index of refraction causing a light ray to bend and take longer path at the center of the detector. For better clarity, we scaled the effect in the figure by a factor of 10 at the center.*

at  $\pm 54.74$  degrees from the  $z$ -axis. A straight line towards the center of the detector (Red in Fig. 3.21) will intersect the opposite side of the detector at point A. Now, assume a 0.5% change in the index of refraction between the top and the bottom poles (a distance of 1370 cm). At the bottom we will take an index of  $n=1.50$ . We model this gradient as discrete steps every 11 cm in  $z$ , resulting in uniform-index horizontal plates, with a fixed discontinuity between their indexes. Clearly, any light path between A and C is longer than the straight (unaffected) line across the detector center. In fact, the light ray leaving C in

the same initial direction would intersect the sphere below A by  $dZ = 378 - 373.7 = 4.3$  cm. However, we actually know where A is, and so when the camera at C was calibrated, we used the correct location for A when drawing the straight line from C (the 'pin-hole' of the camera) to A. The pixel on the CCD where A showed up was transformed to be exactly on this line. That is how camera images are 'calibrated'. The calibration is very good at least at the two ends of this line. Any light source along the solid line in Figure 3.21 would have been reconstructed as though it were along the dashed line. Thus, the error in source position due to the index gradient is not 4.3 cm, or even half that, but the deviation of the actual light ray from C to its intersection on the sphere at A, versus a straight line from C to that same intersection. At the center of the detector, this deviation reaches its maximum and is 0.8 cm. This is still well below the  $\sim 3.5$  cm event reconstruction error seen at the center of the detector. The index would have to vary by 2.2% from top to bottom to have a 3.5 cm correction at the center. This, solely, would still not be sufficient in explaining the shift, though. In fact, the temperature gradient effect makes the 'event' z-offsets marginally worse. The only solution would be to imagine that the two light rays, the visible for the cameras, and the UV for the PMTs are affected by the temperature gradient with different magnitudes. This would cause a differential effect that could explain the mismatch between the CCD and reconstructed position. None-the-less, if the index does vary by 0.5% from the top to the bottom pole, then the 0.8 cm correction at the center would be real. At other locations within the detector the corrections are a bit more complicated to determine, and may be larger or smaller. In terms of the event reconstruction code, there is no *a priori* knowledge of the two end-points of the light, and thus the distribution of tubes hit would be affected, with perhaps an impact on event reconstructed z-values larger than that described above for camera calibrations. Exploring these issues may still be important. The magnitude of this effect however, is not known and remains as a subject of another study.

### Laser Ball Calibration and the z-offset

The z-shift has been also tested for a low light intensity and uniform laser run 11195 at a source position (3.1; -3.4; 0.1) cm. Reconstructed with *Echidna* c12 code z-position is shown in Figure 3.22 where one notices a very good agreement with the expected location that was additionally verified with the CCD camera system and the physical length of the insertion rods.

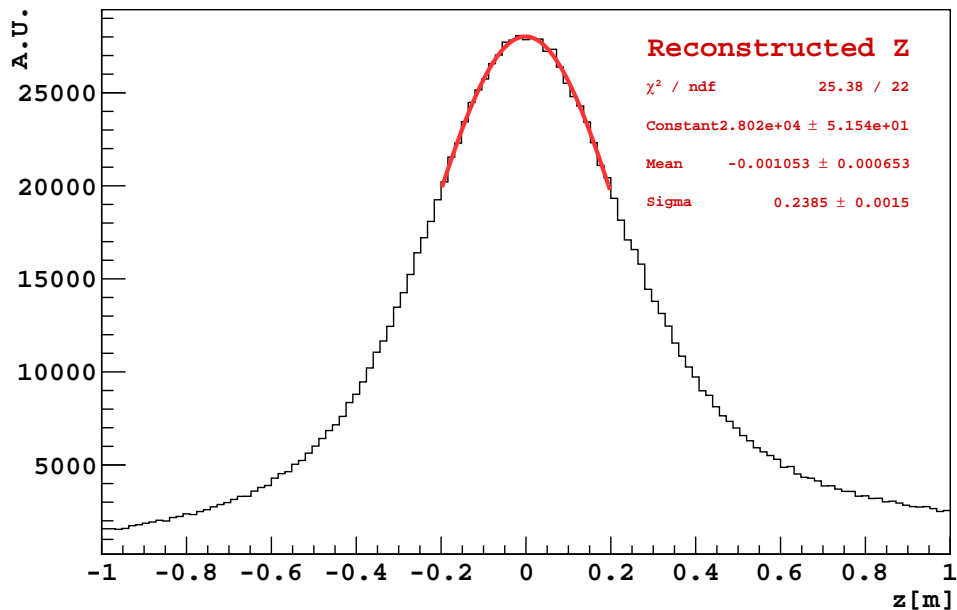


**Figure 3.22:** Reconstructed z coordinate of the laser ball source calibration data with *Echidna* c12 code.

Detailed comparison of the x,y and z coordinates can be found in Table 3.3 where we present the nominal and reconstructed source positions that are in agreement in the vertical direction to within 1.6 cm.

**Table 3.3:** *Comparison of the reconstructed and nominal source position for the laser source calibration data in run 11195.*

Coord. [cm]	x	y	z
nominal	+3.1	-3.4	-0.1
reconstructed	+3.5	-1.8	-0.1

## 3.4 Detector Calibration

Detector calibration is normally considered a mandatory task and is often simply assumed. In the case of the Borexino detector however, its pristine purity was of major concern since source insertion would pose a serious threat to the scintillator’s almost irreplaceable environment. Specifically for this reason, there was no calibration campaign even planned for the first two years of data acquisition. Fortunately, the remaining internal contamination of the scintillator turned out to be critical in this phase. The first Borexino result were available for publication only thanks to the presence of  $^{14}\text{C}$ ,  $^{210}\text{Po}$ ,  $^{222}\text{Rn}$  (for the  $^{214}\text{BiPo}$  coincidence study). Eventually, however, the detector was calibrated extensively, including both internal as well as external sources. The software and hardware components for the internal calibration campaign were designed and prepared at Virginia Tech. The author of this dissertation thesis was extensively involved in the final phase of the preparations and commissioning of the system and later on, in the analysis of the results. This section will discuss the system, sources and results of the performed operations. Details of this work can be found in [67], and [83].

### Internal Source Calibration

Due to the design of the Borexino detector, discussed in Section 3.1 but also presented in Figure 3.24, the only access to the inner vessel volume was through a 4” pipe connecting

the glove-box with the SSS. As a result, the insertion system was composed of a series of interconnecting rods ( $3.8\text{ cm} \times 100\text{ cm}$ ) that would be coupled on-site and lowered into the IV volume with a source attached at the end of the last element. Once the rods were positioned in a desired location, off-axis positions would be reached by pulling the source with a 1/4" teflon tube that additionally was used also as a driver for the fiber optic cable attached to a diffuser ball at the source and laser light at the top of the detector.



**Figure 3.23:** *The special coupler used to attach the insertion rods to a calibration source and tether (entering the coupler midway down its body). A thick collar on the left hand side prevents the coupler from being drawn into the sliding seal. The four spring-steel support wires to which the source is attached are visible at the end of the coupler. Figure from [83].*

It would require normally around 10 to 15 of these metal rods to be able to access most of the locations within the IV. The hinge that allowed them to bend up to  $90^\circ$  was installed in the middle of the bottom rods, whereas at the end there was a source coupler, i.e. a mounting where the operators would place sources after each extraction. The coupler is presented in Figure 3.23.

There is a glove-box on top of the detector where all the calibration components are stored in a class 10 environment, and where the rod insertion actually happens. The box was kept under a constant positive pressure (2-3 mbar) in a Low Argon and Krypton Nitrogen (LAKN) atmosphere (LAKN<sub>2</sub>: 0.01 ppm Ar, 0.02 ppt Kr) in order to avoid the clean-room air from



Specific care was given to the 3 m FV that was used in the  $^7\text{Be}$  analysis (the volume was carefully mapped in full 3-D). Table 3.6 presents a list of sources that were inserted into the active volume over the two years of calibration campaigns.

**Table 3.4:** All radioactive sources used in the Borexino internal calibration campaigns: I (October 2008), II (January 2009), III (June 2009) and IV (Jul 2009), see text for more details.

Source	Type	E [MeV]	Position	Purpose
$^{57}\text{Co}$	$\gamma$	0.122	in IV volume	Energy scale
$^{139}\text{Ce}$	$\gamma$	0.165	in IV volume	Energy scale
$^{203}\text{Hg}$	$\gamma$	0.279	in IV volume	Energy scale
$^{85}\text{Sr}$	$\gamma$	0.514	z-axis + sphere R=3 m	Energy scale + FV
$^{54}\text{Mn}$	$\gamma$	0.834	along z-axis	Energy scale
$^{65}\text{Zn}$	$\gamma$	1.115	along z-axis	Energy scale
$^{60}\text{Co}$	$\gamma$	1.173, 1.332	along z-axis	Energy scale
$^{40}\text{K}$	$\gamma$	1.460	along z-axis	Energy scale
$^{222}\text{Rn}+^{14}\text{C}$	$\beta,\gamma$	0-3.20	in IV volume	FV+uniformity
	$\alpha$	5.5, 6.0, 7.4	in IV volume	FV+uniformity
$^{241}\text{Am}^9\text{Be}$	n	0-9	sphere R=4 m	Energy scale + FV
394 nm laser	light	-	center	PMT equalization

Most of the sources, with an exception for the neutron and laser ones, were enclosed in a 1" diameter quartz vials and sealed at the top. The neck was made of Pyrex glass for easier heat-sealing. The solution used was either Borexino scintillator or water. In the case of the most commonly used and versatile calibration source,  $^{14}\text{C}$ - $^{222}\text{Rn}$  (green in Fig. 3.25), the compound was loaded into the vial in two steps. First, through Radon gas condensation onto the vial's walls and then with an insertion of a  $^{14}\text{C}$ -toluene solution into its volume (normally in the amount of 100 ml). This is a multi-purpose source that provides  $\alpha$ ,  $\beta$ , and  $\gamma$  radiation.

Pure mono-energetic  $\gamma$  sources however, were used to study the energy scale to tune the Monte-Carlo simulation. Their energies spanned from 0-9 MeV, but due to LNGS regulations,

their activities were kept under 2 Bq. Additionally, activities of sources below 1 MeV were carefully measured using  $\gamma$ -ray spectroscopy prior to insertion to study the trigger efficiency in Borexino.

Higher-energy calibration that is needed for such analyses as  ${}^8\text{B}$  ([29]), solar axions ([84]), was achieved by using a  ${}^{241}\text{Am}{}^9\text{Be}$  neutron source. Neutrons are emitted as:  ${}^9\text{Be}(\alpha, n){}^{12}\text{C}_{gs}$  and  ${}^9\text{Be}(\alpha, n){}^{12}\text{C}^*$  (4.44 MeV) with energies up to 11 MeV and 6.5 MeV. The emitted  $\gamma$ -rays form a coincidence tag with the recoil protons. Thermalized neutrons in the hydrogen-rich scintillator are captured either on protons or carbon nuclei emitting characteristic 2.22 MeV and 4.95 MeV  $\gamma$  rays. These characteristic  $\gamma$  rays produce a delayed signal in the scintillator according to the neutron capture time of  $\sim 254 \mu\text{s}$  in pseudocumene [65].

The laser calibration in Borexino was performed using the same diffuser ball that was used for the CCD positioning system. A 394 nm laser was connected to the fiber to provide pulsed light at the center of the detector. The main purpose of this activity was to independently verify the time synchronization of the PMTs. The laser was pulsed at 50 Hz and different light intensities.

## Post-Calibration Cleanliness

The author of this work would like to specifically underline that among the major responsibilities in the early stages of his Ph.D. track at Virginia Tech was cleanliness and quality control of the source insertion hardware components: rods, vials, Viton seals etc. The result of it was that even after placing an enormous total surface into the purest liquid currently available, no long-term contamination has been introduced. This proves how well the meticulous steps were taken to make it work. In the collected post-calibration data, we have searched for the most common coincidence tags,  ${}^{214}\text{BiPo}$  and  ${}^{212}\text{BiPo}$ , that would serve as an indication for the presence of  ${}^{238}\text{U}$  and  ${}^{232}\text{Th}$  respectively. The results were very sat-

isfactory, with concentrations for  $^{238}\text{U}$  determined to be:  $(5.0\pm 0.9)\times 10^{-18}$  g/g before and  $(3.2\pm 0.7)\times 10^{-18}$  g/g after the campaigns, Figure 3.26 shows the count rate evolution for  $^{214}\text{BiPo}$ . Similarly, we have verified the concentration for  $^{232}\text{Th}$  and we estimate it to be from  $(3.0\pm 1.0)\times 10^{-18}$  g/g to  $(5.0\pm 1.5)\times 10^{-18}$  g/g.

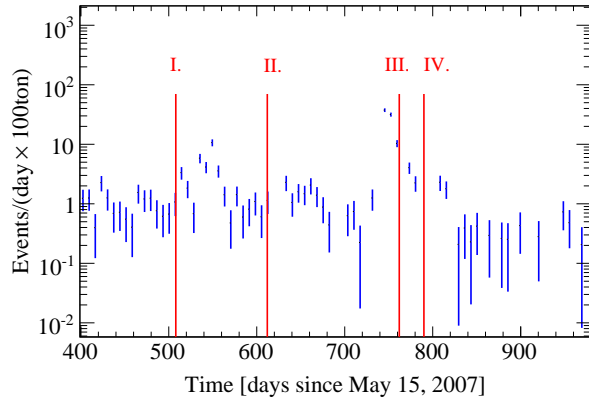


**Figure 3.26:**  $^{214}\text{Bi}^{214}\text{Po}$  coincidences count rates in 100 tons as a function of time. The red lines indicate the internal calibration campaigns.

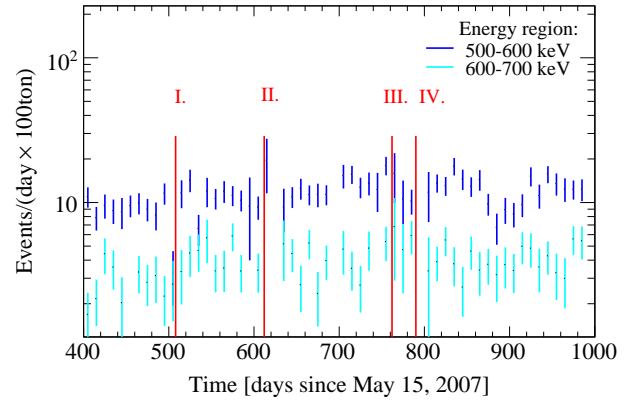


**Figure 3.27:** Count rate in the energy region between (500-600) keV and (600-700) keV as a function of time. As before, the red lines indicate the internal calibration campaigns.

For the overall stability of the backgrounds in the  $^7\text{Be}$  range it was important to check if the valley regions<sup>10</sup> where the signal is negligible, these regions are (500-600) keV and (600-700) keV. Figure 3.27 shows these valleys with no indication of significant, long-term contamination.

## External Source Calibration

This was a non-invasive campaign where all the sources were brought in through reentrant tubes to the SSS, that is to a distance of about  $\sim 635$  cm from the center of the detector. Figure 3.28 shows the geometrical orientation of the ports where the sources were placed.

<sup>10</sup>A ‘valley’ refers to a region to the right of a Compton shoulder of, in this case,  $^7\text{Be}$ .

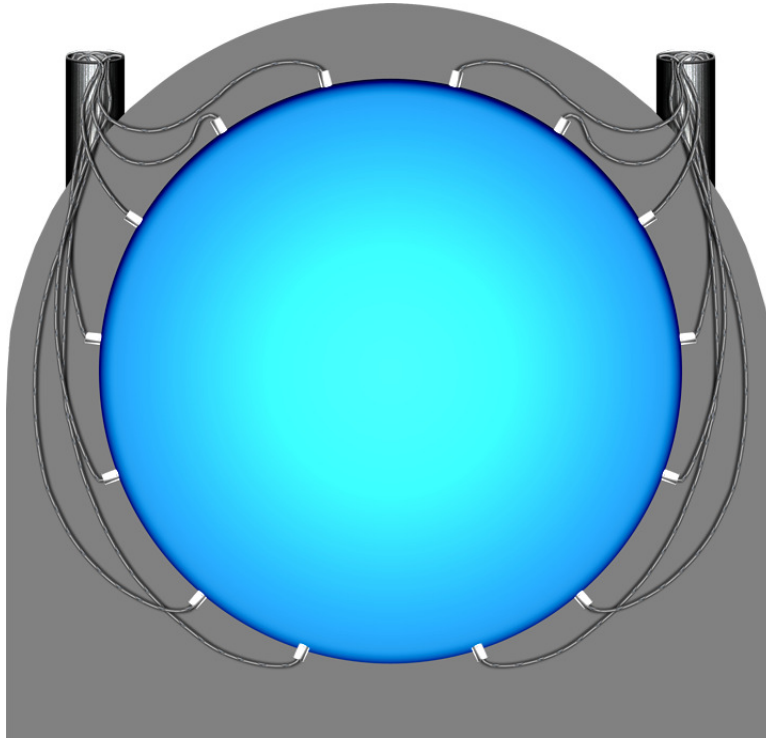


**Figure 3.28:** *Borexino SSS (blue) with indicated polyethylene, reentrant tubes (gray) that were used as guides for the calibration sources to the surface of the PMTs.*

The chosen source for the Borexino external calibration was a custom-made 5.41 MBq  $^{228}\text{Th}$  with a  $\gamma$  line at 2.615 MeV that is emitted 36% of the time from its  $^{208}\text{Tl}$  daughter. The details about this specific kind of source production can be found in [86].

The major goals for the external source calibration can be summarized in the following way:

- Spectral shape determination for the 2.615 MeV  $\gamma$ 's in various spatial cuts;
- Understanding of the peripheral response of the detector, for  $R > 3\text{m}$ ;
- Determination of the radial distribution of the external  $\gamma$  events;
- Along with other techniques, the external  $\gamma$ 's can also be used in the study of the IV shape;
- Tuning and validation of the Monte-Carlo codes;

## Calibration Results and Conclusions

**Energy Scale** The energy reconstruction in Borexino is performed in two modes, the number of collected hits from PMTs and the total collected charge from them. In an ideal case, the scale should be linear, and should directly translate into the deposited energy of a given particle. In the case of the Borexino detector, 500 photoelectrons corresponds to about 1 MeV.

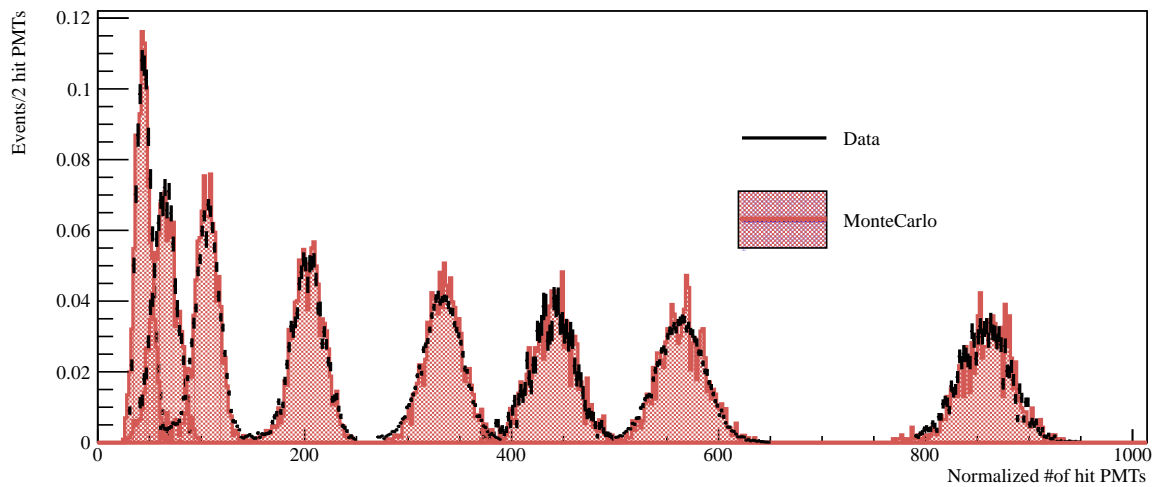


**Figure 3.29:** Energy spectra of  $\gamma$ -lines from eight different calibration sources expressed in terms of the normalized number of hit PMTs. The peaks from left to right belong to the  $^{57}\text{Co}$ ,  $^{139}\text{Ce}$ ,  $^{203}\text{Hg}$ ,  $^{85}\text{Sr}$ ,  $^{54}\text{Mn}$ ,  $^{65}\text{Zn}$ ,  $^{40}\text{K}$ , and  $^{60}\text{Co}$  source. The Monte Carlo simulated spectra are within 0.2% agreement with the measured ones.

Unfortunately, due to various effects, such as light quenching, the low-energy region ( $\sim 1$  MeV and below) becomes non-linear. For this reason, careful tuning of the scale was critical. Figure 3.29 presents a comparison of the reconstructed energies from the calibration  $\gamma$  sources and a Monte-Carlo simulation trying to match these values, with very satisfactory results in this case. Further details regarding this work can be found in [87].

**Position Reconstruction** The reconstruction algorithm considers for each photon: its arrival time  $t_i$  and the position  $\vec{r}_i$  of the PMT which detected it; subtracts its time-of-flight  $T_{flight}^i$ ; and compares the photon time distribution with the reference probability density function (*pdf*) of the Borexino scintillator (Figure 3.30).

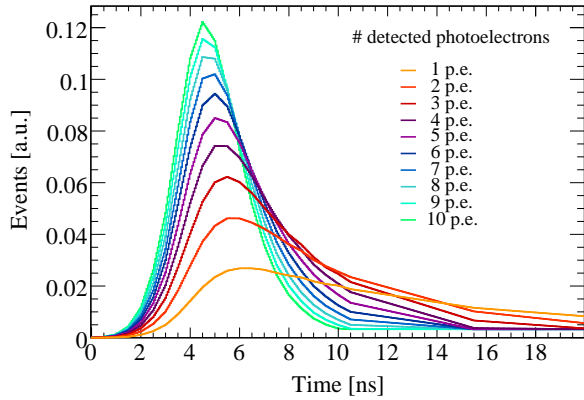


**Figure 3.30:** First photo-electron (*p.e.*) arrival time distribution at a PMT in Borexino. The shapes depend on the collected charge (number of detected *p.e.*). Figure from [67].

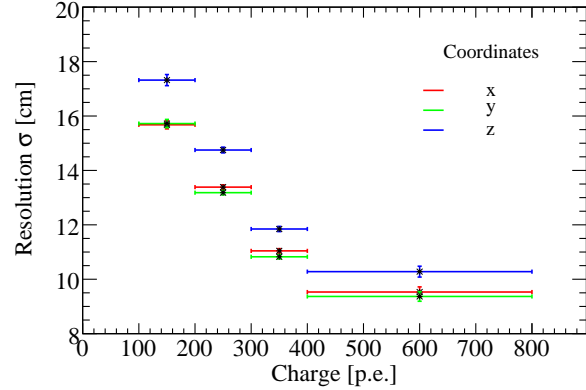


**Figure 3.31:** Resolution  $\sigma$  for the three coordinates  $x$ ,  $y$  and  $z$  as function of the collected charge (unit: number of photoelectrons). Figure from [67].

The  $^{222}\text{Rn}$  and  $^{241}\text{Am}^9\text{Be}$  source data were used to estimate the quality and possible systematics of the position reconstruction performance.

**Trigger Efficiency** Borexino's trigger efficiency is  $>99.999\%$  for energies greater than  $\sim 120$  keV. In this test, pulsed laser light of known intensity was sent simultaneously to all the photomultiplier tubes to check for their timing equalization [88]. The advantage of performing a similar study but with a use of calibration  $\gamma$  sources is that one can then check for better consistency in various locations. Source activities were carefully measured before insertion with a Germanium detector and are reported in the tables below along with a comparison performed in Borexino. The sources were placed in various positions and the study was carried out with two approaches: in Method I, a spherical cut of  $R=1$  m was selected around the source and compared with background count from a spatially identical sphere

but taken for a regular data. Results are shown in Table 3.5. An interesting phenomena can be noticed. Even though there is no significant difference between the positions for various sources, one can observe that the higher the energy used, the more inefficient the trigger. This effect is perhaps associated with the presence of the  $^{210}\text{Po}$  tails (mean around 419 keV) that causes problems in the proper spectral fit and identification of the  $\gamma$  peaks.

**Table 3.5:** Comparison of  $\gamma$  radioactive source count rates for Method I, as described in the text.

Source (En.) BR. Activity ( $z$ )	Activity [Bq] Initial	Activity in Borexino	Ratio Gr/Bx
$^{57}\text{Co}$ (122/136keV) BR(95%)	15:45; 22-JUN	(510h)	
$z=0$ ; $3.45 \pm 0.06$	$3.63 \pm 0.07$	$3.36 \pm 0.06$	$1.03 \pm 0.03$
$z>0$ ; $3.66 \pm 0.08$	$3.63 \pm 0.07$	$3.36 \pm 0.06$	$1.09 \pm 0.03$
$z<0$ ; $3.56 \pm 0.09$	$3.63 \pm 0.07$	$3.36 \pm 0.06$	$1.06 \pm 0.03$
$^{139}\text{Ce}$ (166keV) BR(80%)	15:45; 19-JUN	(627h)	
$z=0$ ; $3.26 \pm 0.07$	$3.56 \pm 0.04$	$2.94 \pm 0.03$	$1.11 \pm 0.03$
$z>0$ ; $3.14 \pm 0.11$	$3.56 \pm 0.04$	$2.94 \pm 0.03$	$1.07 \pm 0.04$
$z<0$ ; $3.74 \pm 0.13$	$3.56 \pm 0.04$	$2.94 \pm 0.03$	$1.27 \pm 0.05$
$^{203}\text{Hg}$ (279keV) BR(81%)	14:45; 17-JUN	(48h)	
$z=0$ ; $3.42 \pm 0.06$	$2.87 \pm 0.06$	$2.75 \pm 0.06$	$1.24 \pm 0.03$
$z>0$ ; $3.21 \pm 0.14$	$2.87 \pm 0.06$	$2.75 \pm 0.06$	$1.17 \pm 0.06$
$z<0$ ; $3.7 \pm 0.11$	$2.87 \pm 0.06$	$2.75 \pm 0.06$	$1.35 \pm 0.05$
$^{85}\text{Sr}$ (514keV) BR(96%)	10:13; 18-JUN	(696h)	
$z=0$ ; $2.77 \pm 0.08$	$3.28 \pm 0.07$	$2.1 \pm 0.04$	$1.32 \pm 0.05$
$z>0$ ; $2.45 \pm 0.13$	$3.28 \pm 0.07$	$2.1 \pm 0.04$	$1.17 \pm 0.07$
$z<0$ ; $2.99 \pm 0.09$	$3.28 \pm 0.07$	$2.1 \pm 0.04$	$1.42 \pm 0.05$

In Method II we perform very similar study, but in this case we use the same DAQ run where a sphere for the background run is shifted with respect to the source sphere and they do not overlap as presented in Figure 3.32. In this way we achieve the same performance of the electronics and detector's condition. Results are listed in Table 3.6. We observe consistent values with Method I, and notice the same tendency for the calculated activity of the source in the detector to be underestimated. This implies another important conclusion, the stability of the detector in time and uniformity in the collection of events within the IV.

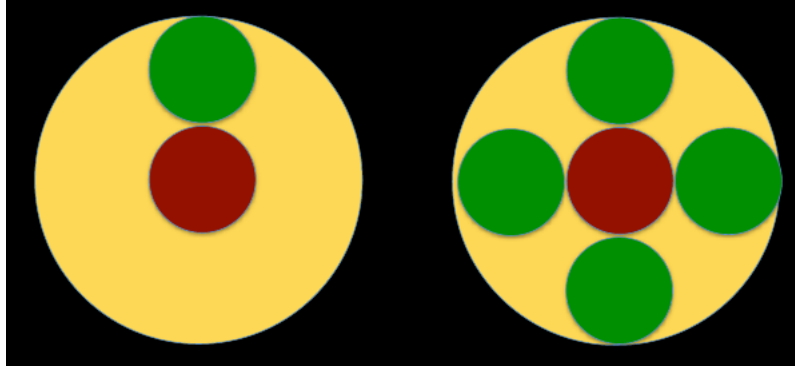


**Figure 3.32:** *Spatial cuts applied in the selection of events from  $\gamma$  sources in Method II. In Red, a sphere around the source is presented, whereas in Yellow, the background sphere for the same DAQ run.*

**Table 3.6:**  *$\gamma$  source activity check in Borexino with Method II where the events were selected for the same DAQ run but from spatially relocated spheres with respect to the initial source position.*

Source (En.) BR. Activity	Activity [Bq] Initial	Activity in Borexino	Ratio Gr/Bx
$^{57}\text{Co}$ (122/136keV) BR(95%) $3.48 \pm 0.02$	15:45; 22-JUN $3.63 \pm 0.07$	(510h) $3.36 \pm 0.06$	$1.04 \pm 0.02$
$^{139}\text{Ce}$ (166keV) BR(80%) $3.53 \pm 0.03$	15:45; 19-JUN $3.56 \pm 0.04$	(627h) $2.94 \pm 0.03$	$1.2 \pm 0.02$
$^{203}\text{Hg}$ (279keV) BR(81%) $3.3 \pm 0.01$	14:45; 17-JUN $2.87 \pm 0.06$	(48h) $2.75 \pm 0.06$	$1.2 \pm 0.03$
$^{85}\text{Sr}$ (514keV) BR(96%) $2.83 \pm 0.02$	10:13; 18-JUN $3.28 \pm 0.07$	(696h) $2.1 \pm 0.04$	$1.35 \pm 0.03$

## 3.5 Physics Potential

Borexino has significantly contributed to the field of neutrino physics since the beginning of data taking in May 2007. In addition to the solar measurements, Borexino has also detected geo-anti-neutrinos thanks to a very convenient location. There are no nuclear reactor power-plants (a strong source of anti-neutrinos) in the proximity of the detector, the closest ones are in France, hundreds of kilometers away from Gran Sasso.

The collaboration's first published result was also the first ever direct detection of the  ${}^7\text{Be}$  neutrinos from the Sun. In the first data release, with only 47.4 live days collected between May and July 2007, we were still struggling with rather high systematics ( $47 \pm 7_{\text{stat}} \pm 12_{\text{sys}}$  counts/(day x 100 ton)) ([25]). Figure 3.33 presents the spectrum obtained after removing the dominant  ${}^{210}\text{Po}$  contribution, easily tagged with the Gatti parameter discussed in Section 3.2.

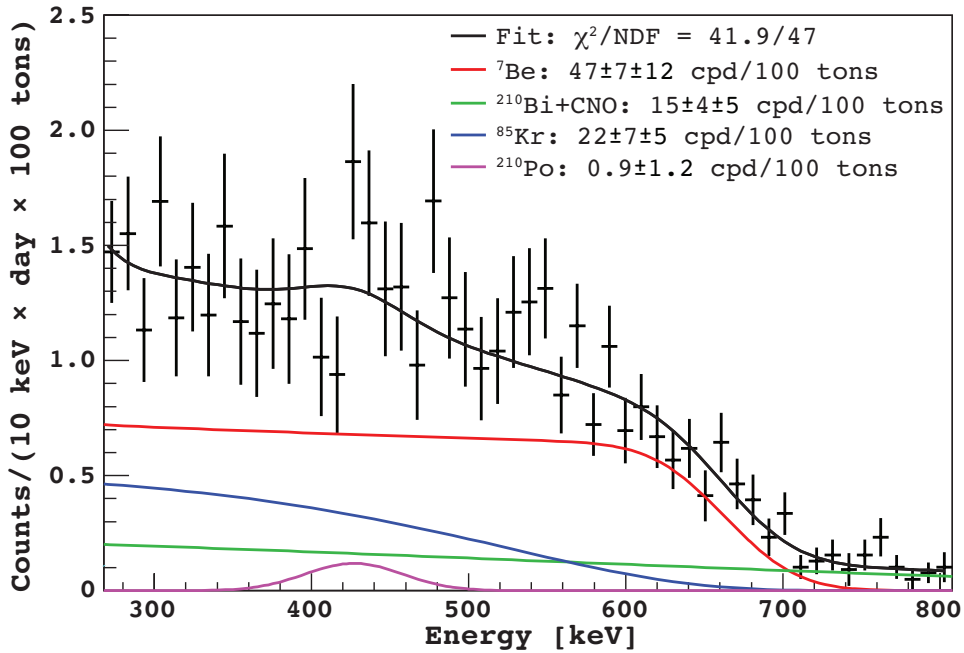


**Figure 3.33:** Borexino spectrum after  $\alpha/\beta$  statistical subtraction, mainly  ${}^{210}\text{Po}$  was eliminated, visible here remaining count in Purple. Fit was performed in the energy region of [270; 800] keV. Figure from [25].

The next years brought further reduction in the systematics, predominantly thanks to the calibration campaigns, and in 2011 the level of uncertainty was at 4%. The most recent results yield interaction rate of  $46 \pm 1.5_{\text{stat}} \pm 1.5_{\text{sys}}$  counts/(day x 100 ton), and the survival probability for the electron-neutrino of  $0.51 \pm 0.07$  at 862 keV ([2]). Based on this result, a measurement looking for any day-night asymmetry of the  ${}^7\text{Be}$  signal was performed in early

2011. Absence of such effect rejects instantly the LOW<sup>11</sup> solution from the SSM at more than  $8.5\sigma$  preserving the restriction on the MSW-LMA scenario at 90% confidence level. Borexino was designed to detect neutrinos via the electron-scattering reaction. However, in the search for geo-anti-neutrinos the reaction of neutron inverse  $\beta$  capture on protons was used instead. Having detected  $9.9_{-3.4}^{+4.1}({}_{-8.2}^{+14.6})$  of these neutrinos with a 252.6 ton-yr fiducial exposure, Borexino alone rejected the hypothesis of a 3 TW geo-reactor in the Earth's core at 95% C.L. [60].

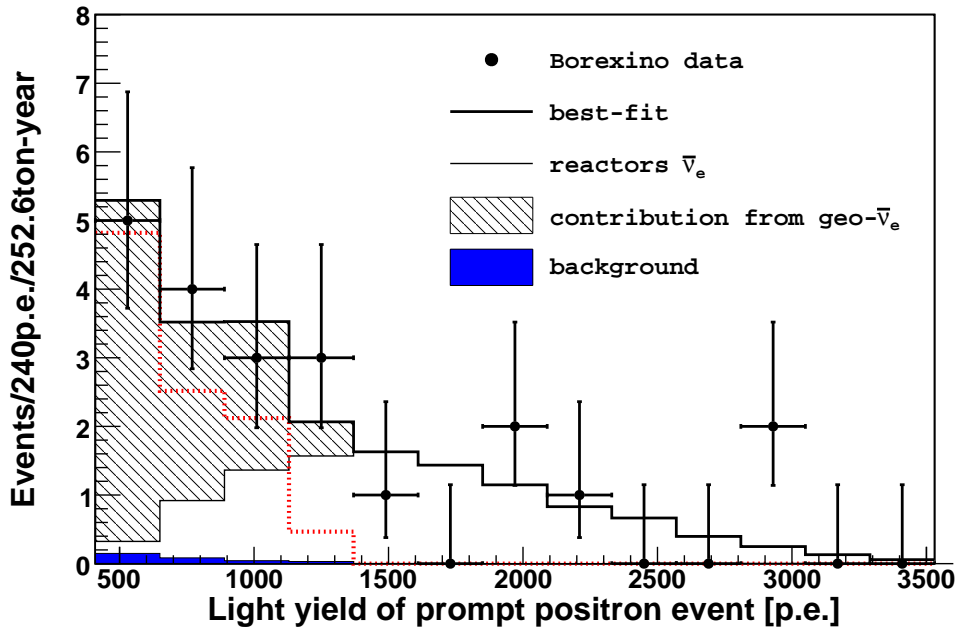


**Figure 3.34:** Anti-neutrino spectrum in Borexino in light yield ( $1 \text{ MeV} \approx 500 \text{ p.e.}$ ) for the 21 selected candidates. Thick black line indicates the best fit value of  $3.9_{-1.3}^{+1.6}({}_{-3.2}^{+5.8})$  events/(100 ton-yr).

At the time of writing, one of our most recent and pioneering measurements was the first evidence of the  $pep$  solar neutrinos with Borexino [30]. The analysis incorporated novel techniques of background rejection, mainly the Three-Fold coincidence (TFC) that resulted in 91% rejection of  $^{11}\text{C}$ . The measured rate of the  $pep$  neutrinos in the energy range of

<sup>11</sup>LOW stands for low-mass-square splitting, and corresponds to a similar angle as the LMA solution but lower  $\Delta m^2$  parameter.

1.0-1.5 MeV is  $(3.1 \pm 0.6_{\text{stat}} \pm 0.3_{\text{syst}})$  counts/(day x 100 ton), the absence of the *pep* was disfavored at 98% C.L. At the same time, this study gave the strongest constraint on the CNO interaction rate of  $<7.9$  counts/(day x 100 ton) [30]. This result filled the missing gap in the transition region of the solar neutrino survival probability,  $P_{ee} = 0.62 \pm 0.17$  at 1.44 MeV. This value is consistent with the High and Low Metallicity Models assuming the MSW-LMA scenario.

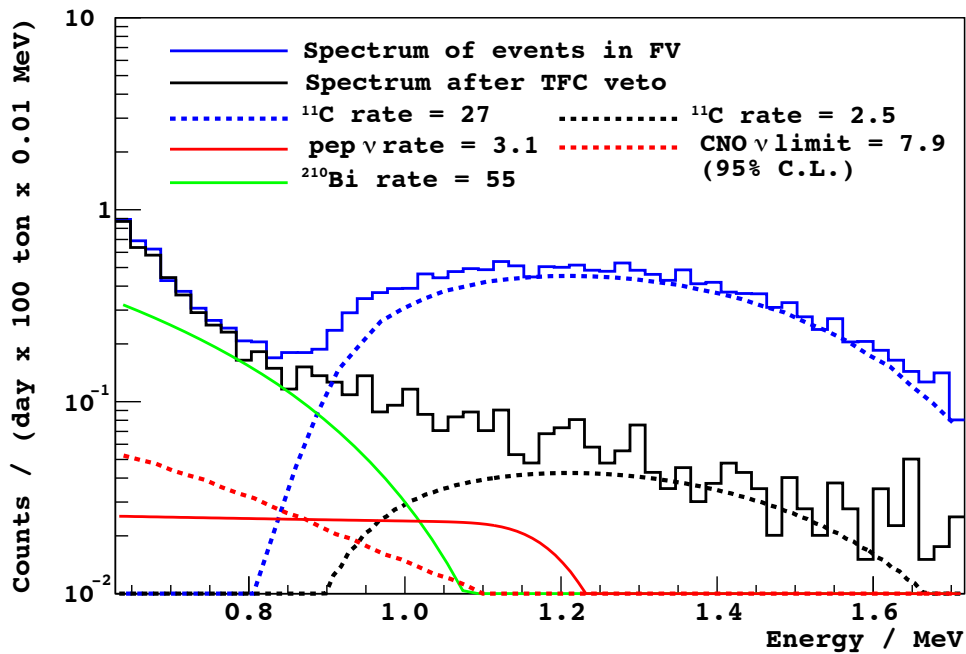


**Figure 3.35:** Energy spectrum for the *pep* candidates (Blue), and after removing  $^{11}\text{C}$ , the dominant background, with a TFC cut (Black). Figure from [30].

Other measurements with Borexino have also been performed, such as the detection of  $^8\text{B}$  neutrinos with a 3 MeV energy threshold [29], and some are still to come. Borexino is an active participant of the supernova program *SuperNova Early Warning System* (SNEWS).

## Current and Future Perspectives

Measuring the  ${}^7\text{Be}$  solar- $\nu$  flux was the original goal for the Borexino collaboration and it was achieved in 2011, with a precision measurement at a remarkable level of 5%. Future improvements are still anticipated; achieving a 3% number could certainly be used in proposed solar experiments such as LENS<sup>12</sup> for its normalization. Additionally, thanks to our deep understanding of the backgrounds, we completed phase I of data-taking with the first direct detection of the *pep* neutrinos. The most significant reduction in the Borexino systematic errors was made possible through a successful calibration campaign with various sources that were carefully studied at multiple energies and positions. The possibility of further improvement in the measurements of the *pep* and CNO neutrinos for instance, was unfortunately limited by the presence of natural radioactive backgrounds in the scintillator, mainly  ${}^{85}\text{Kr}$  and  ${}^{210}\text{Bi}$ . It because their spectral shapes overlap with the signal (*pp*, *pep*, and CNO), and there is no signature that would distinguish them apart, see Figure 4.22 and Section 4.2, for reference. As a result, the detector underwent a series of purification campaigns between 2010 and 2011 (details in [89]), of which the main goal was to reduce the  ${}^{85}\text{Kr}$ <sup>13</sup> and  ${}^{210}\text{Bi}$ <sup>14</sup> contamination. The purification turned out to be very successful,  ${}^{85}\text{Kr}$  was practically eliminated, going down from around  $34.8 \pm 1.7$  counts/(day x 100 ton) to  $4.17 \pm 2.92$ , and in the case of  ${}^{210}\text{Bi}$ , the contamination was reduced by a factor of two, from  $40.6 \pm 2.6$  counts/(day x 100 ton) down to  $17.98 \pm 2.23$  [90]. This would potentially open the door for new measurements, specifically the *pep* and CNO neutrinos, much anticipated for the past years. The first milestones have been reached, but there are still challenges that will have to be resolved, such as the  ${}^{14}\text{C}$ ,  ${}^{14}\text{C}$ -pile-up and  ${}^{210}\text{Bi}$  spectral shapes.

---

<sup>12</sup>Low Energy Neutrino Spectroscopy, a segmented scintillation experiment under the leadership of Virginia Tech [85]

<sup>13</sup>Removal performed via water extraction and  $\text{N}_2$  stripping

<sup>14</sup> In fact it is the  ${}^{210}\text{Pb}$ , higher in the chain, that is removed by Water Extraction

Even though studies of the Z boson decay width strongly indicate the existence of only three active neutrino flavors, some cosmological constraints were placed suggesting the presence of another, *sterile* neutrino. Also, recent years have brought inconsistent results with the SM three-neutrino prediction suggesting mixing with the sterile flavors (LSND [91], MiniBooNE [92], Gallium [93] and reactor experiments [94]). As a consequence, neutrino (anti-neutrino) experiments in the low-MeV range have become a high priority for many collaborations. The Borexino collaboration for instance, received new funding in 2012 for the development of a sterile-neutrino source. At this point of R&D, two neutrino sources are considered, MCi  $^{51}\text{Cr}$  ( $\nu_e$ ) and kCi  $^{144}\text{Ce}$  ( $\bar{\nu}_e$ ). Their decay schemes are presented in Figures 3.36 and 3.37 respectively. If oscillations between sterile and active neutrinos were observed, this would indicate the fourth neutrino, separated by  $\sim 2\text{eV}^2$  mass square difference or more from the other three. Also a new mixing angle could be investigated  $\sin^2(2\theta_{new}) \approx 0.1$ . Exclusion contours for both parameters are presented in Figure 3.38. We notice that for most of the proposed experiments, the Reactor Anomaly region (RAA) is covered at 95% C.L. In the case of Borexino, the  $\bar{\nu}_e$   $^{144}\text{Ce}$  provides very good sensitivity without even a need to place the source inside of the detector.

Nevertheless, certain challenges are strictly fundamental: placing the source at the center of the fiducial volume would require complete rebuilding of the detector, also the political implications of a MCi source production in a foreign country will have to be carefully considered. Without a doubt, Borexino is the perfect place for such a measurement. Very low background levels of about 50 counts/(day x 100 ton) for neutrinos, and only about 10 counts/(day x 100 ton) for anti-neutrino mode, provide a unique setup for this activity.

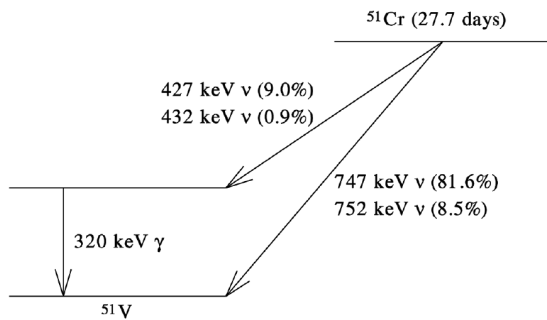


**Figure 3.36:** Decay scheme for the  $^{51}\text{Cr}$  neutrino source. Figure from [95].

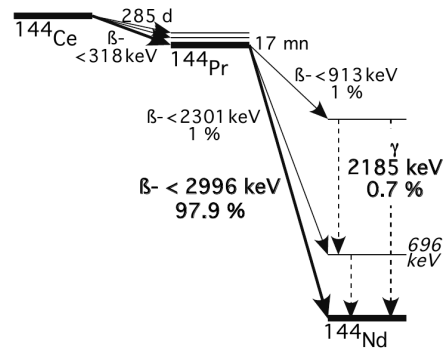


**Figure 3.37:** Decay scheme for the  $^{144}\text{Ce}$  anti-neutrino source. Figure from [95].

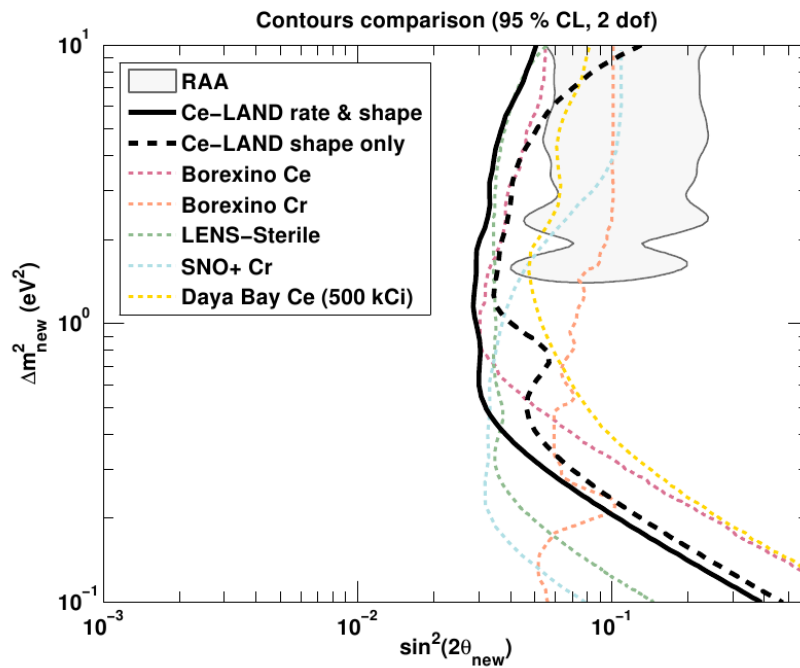


**Figure 3.38:** 95% exclusion plot for the  $\Delta m_{new}^2$  and  $\sin^2(2\theta_{new})$  oscillation parameters. If interpreted as oscillations to sterile neutrinos, the gray-shaded area of Reactor Anomaly (RAA) would be largely covered by most of the proposed experiments. Figure from [95].

# Chapter 4

## Stability Conditions

### Introduction

In this chapter, we will expand our focus beyond the background levels, and study of the scintillator purity. In the search for annual periodicities of the signal, it is equally important to understand whether the response of the detector and the surrounding environment provide sufficiently stable conditions for such a measurement. It is worth underlining that in other Borexino analyses, these conditions were not as critical. For instance, the  ${}^7\text{Be}$  flux measurement relies mainly on the spectral fit and the actual changes in the backgrounds sum over to the total count; the day-night analysis compares conditions on a daily scale which are not expected to vary significantly; the geo-neutrino measurement uses tags of events on a distinct coincidence signal and can neglect many of the problems encountered by other analyses. As a result, investigating signal modulation in Borexino requires detailed understanding of the stability on an annual scale, which became the major challenge for this work, specifically in Phase I of data taking. As we will see in the final chapter, however, the experience gained during the first three years, as well as a very successful purification campaign, resulted in

very promising background levels for this measurement in Phase II of the Borexino program. We will start our discussion at the nylon vessel deformation and later we will focus on the actual conditions of the detector, including the background migration in the IV and spatial asymmetry in the reconstruction and detector response.

## 4.1 The Inner Vessel Shape

Information obtained from the reconstruction of the inner vessel position can be applied not only in the presented analyses, but it can be used to monitor its changing shape and volume conditions. After the first signs of the leak in the IV in April 2008, it became crucial to be able to properly track the evolution of the shape. The leak itself was a result of an increased buoyant force between the buffer<sup>1</sup> and the inner vessel volumes due the density difference. Initially the buffer volume was filled with a light quencher, dimethylphthalate (DMP) [77], at a level of about 5 g/l which was later lowered to  $\sim 2$  g/l, bringing the density closer to the IV level. Additionally, refilling with a warmer batch of PC in the early phase increased this difference and accelerated the dangerous deformation of the IV. As a result, a split in the top of the nylon sphere was observed with an increased count rate in the inner buffer region. In order to visualize these events, we can plot a cross-section view of the entire buffer volume in the energy window of low background and signal count, somewhere in the  ${}^7\text{Be}$ - ${}^{11}\text{C}$  valley, [285; 450] npe. Figures 4.1 and 4.2, show the situation of the events in the buffer before and after the leak was detected, respectively. Throughout this document, we will be referring to the leak events and the deformation to the inner vessel as simply the *leak*.

A campaign of DMP reduction lowered the leak rate significantly over the course of about one month. However, we had experienced a period of about a year when the vessel was strongly

---

<sup>1</sup>A quenched region of scintillator between the inner and outer vessels.

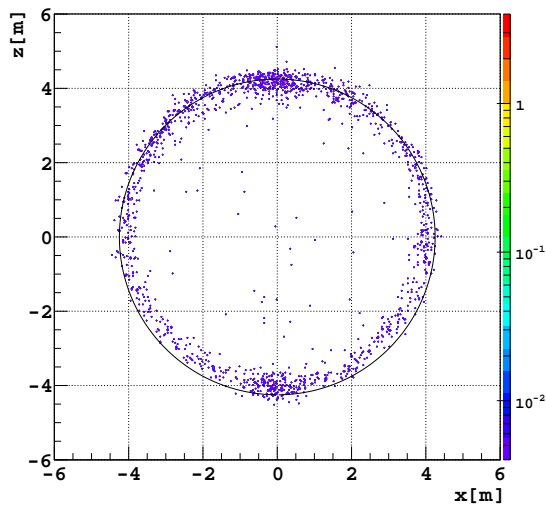


**Figure 4.1:** A cross section view of the buffer in a  $y$ -slice of  $[-1.5; 1.5]$  m. The events were selected for the week of April 06, 2008, at the time when the leak happened.

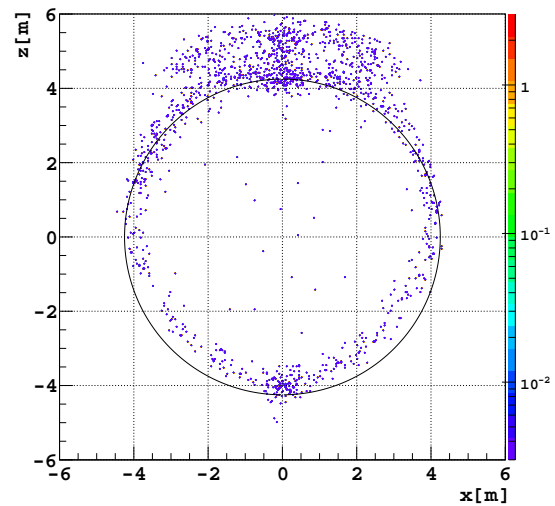


**Figure 4.2:** The same cross section view as on the left-hand-side but this time it was selected in the week of December 28, 2008, six months after the leak was detected.

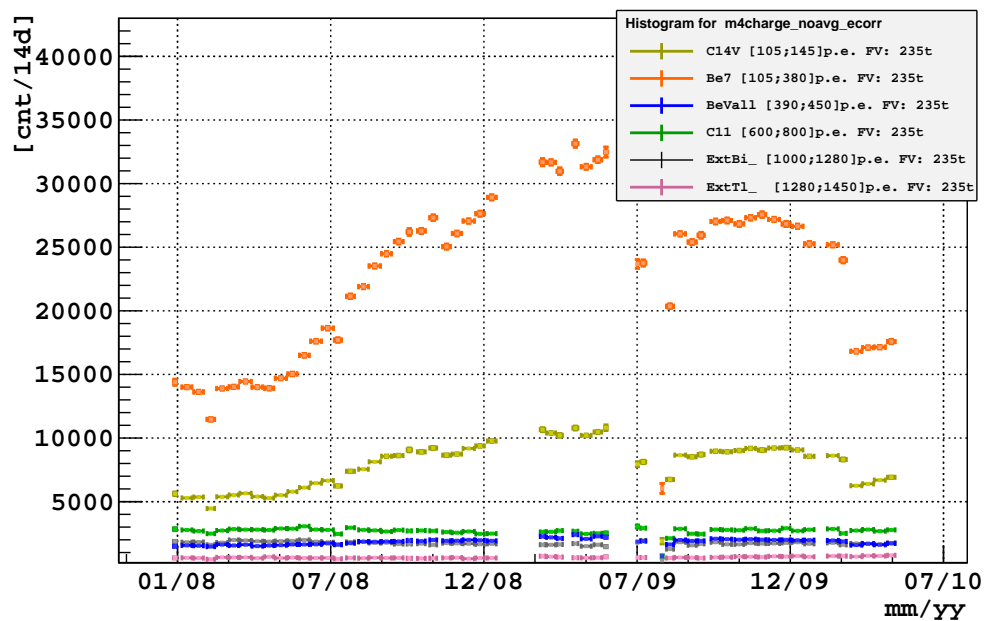


**Figure 4.3:** Rates in different regions of the spectrum for an increased fiducial volume,  $R < 4$  m.

deformed inwards in the bottom of the detector. This became problematic for the analyses with increased fiducial volumes of spherical shapes ( $R \gtrsim 3.75$  m). The dominant backgrounds are those of  $^{210}\text{Bi}$  from the nylon, as well as the external gamma events penetrating the active volume from the outer regions, now also penetrating further in the bottom due to reduced shielding of the active scintillator. An example of the increased count rates is presented in Figure 4.3, where we observe how the count rate goes up rapidly around the middle of 2008, specifically in the  $^{210}\text{Bi}$  window (Orange markers in the plot).

It is thus desirable to perform a scan of the position of the inner vessel as it fluctuates in time.  $^{210}\text{Bi}$  which is present in the nylon will be used as a tag; and due to the convenience of weekly DST ROOT-files (short for ‘Data Storage and Transfer’, defined in Section 5.2) as well as the need for increased statistics, steps of three week will be considered in the reconstruction.

## Selection of Events

Initially, it was believed that the  $^{14}\text{C}$  background would prove more than sufficient in terms of the potential of available statistics, which would in fact, allow for a run-by-run shape determination. Spatial distribution of the  $^{14}\text{C}$  events for one week is shown in Fig. 4.4.

However, it turns out that these events were energetically too low and unsuitable for this analysis due to the poor position resolution, significantly affecting the precision below 100 npe. Thus, in the next step, a much higher energetically region in the external gamma range was considered. While perfect in terms of the position reconstruction, the available statistics in that part of the spectrum were significantly lower, and would require much longer than one-month periods to be included. This, in normal circumstances, would be perfectly acceptable, but the IV shape was changing on a much shorter scale. As a result, focus was put on the

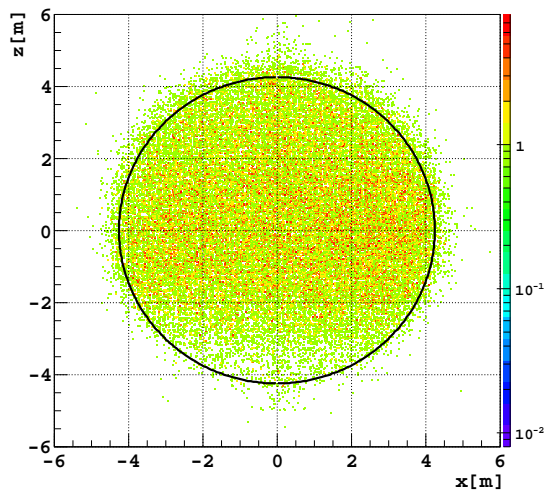


**Figure 4.4:** *Spatial distribution of the  $^{14}\text{C}$  background taken for one week of data. A cross section of events in a  $y$ -slice of  $[-0.5; 0.5]$  m, is included.*

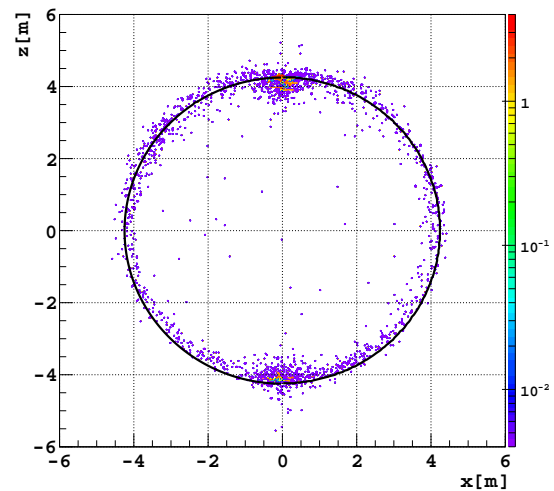


**Figure 4.5:** *Spatial distribution of the  $^{210}\text{Bi}$  in the  $^7\text{Be}$ -valley,  $[385; 450]$  npe. Similar to the plot on the left, the black circle represents nominal radius of 4.25 m.*

$^7\text{Be}$ -valley. The amount of  $^{210}\text{Bi}$  events and the vessel contamination itself turned to be perfectly sufficient in this energy window. An example of a  $-0.5 < y < 0.5$  m slice from the  $[385; 450]$  npe window is plotted in Figure 4.5, where we can see how precisely they reflect the actual vessel shape indicated as a black circle of 4.25 m radius.

As stated before, the energy region selected for further analysis was not fully covering the valley region. Rather it was adjusted, and corrected for a small influence of the external background that was causing a miss-reconstruction of the fitted vessel shape.

## Reconstruction of the Shape: $\mathbf{R}(\theta)$

We have already discussed the spatial distribution of the events and the energy window in photoelectrons where the cut results in the best possible representation of the IV shape. For additional ‘cosmetic’ cuts, we need to impose the following requirements that will clean our sample from invalid triggers and muon events:

- `m4s.laben__recon__valid == 1`
- `m4s.muon_num_events < 25`

It has also been noticed by Jingke Xu of Princeton University that the best agreement with the CCD reconstructed profiles was achieved in the position independent variable `m4s.laben_hitdist_npe_aver_corrected`. The details of this reconstruction algorithm can be found in [80].

In order to collect a sufficient number of points for the shape determination, scanning from 0 to  $\pi$  in theta is performed in six-degree steps. The IV shape is assumed to be azimuthally symmetric, which we will prove in the next sections to be the case. At each step, the distribution of the events is fit with a Gaussian function, as long as the radius reconstructed under 5 m. However, due to a proximity of the outer vessel and an increase in the leak events in certain periods, a Bi-Gaussian fit was performed instead. The fit result to a distribution of the IV events in one of the slices is shown in Figure 4.6.

The Bi-Gaussian correction had to be implemented only for the significantly deformed periods around November 2008 - February 2009. In terms of the necessary statistics, it was asserted that even a full week would be sufficient for an accurate IV shape reconstruction. Nevertheless, due to the varying duty-cycle and, in some periods, missing data due to external operations, it has been decided that three overlapping weeks will always be analyzed.

## Determination of the Shape

The data for consecutive bins was stored in a graph of radius  $R$  [m] vs  $\theta$  angle [radians]. In the next, and last step of this process, the input points are used in a global fit representing the shape of the vessel. Originally, a sixth-order polynomial was used in the code: however, it was quickly discovered that in the case of a possible mis-reconstruction in one of the

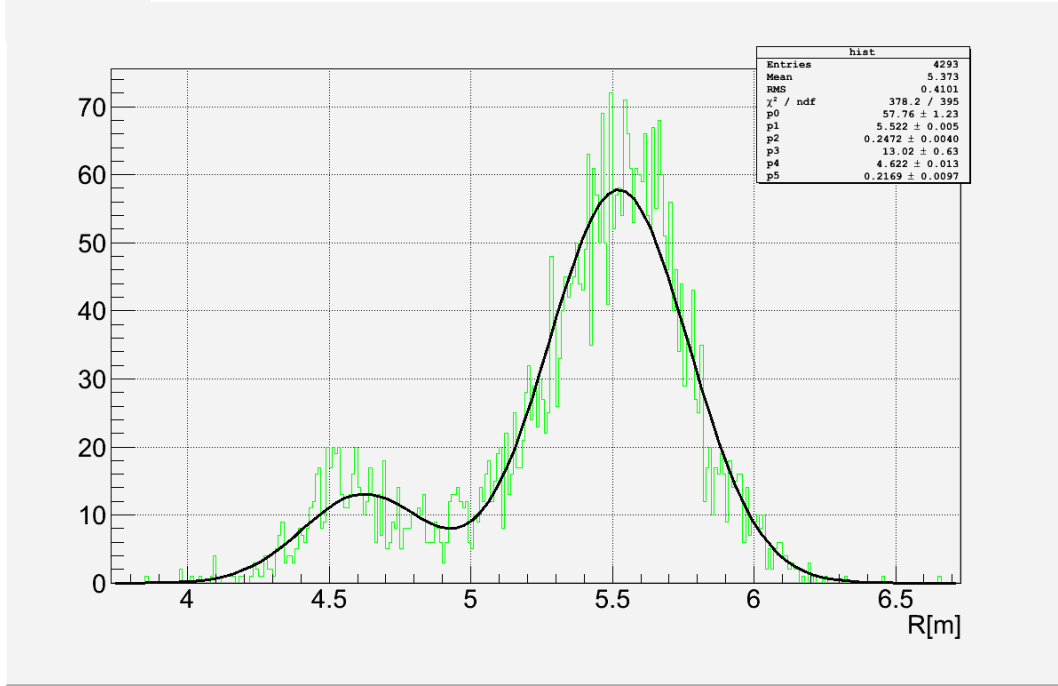


**Figure 4.6:** Correction for the leak events with a Bi-Gaussian fit to the radial distribution of  $^{210}\text{Bi}$  background in a six-degree slice. Suggested and implemented by F. Lombardi of LNGS.

slices, the functional fit would fail rather completely. As a result, a new functional form was developed and implemented for the analysis. With very good accuracy, the shape of the deformed vessel<sup>2</sup> represents a rotated fraction of an ellipse. In polar coordinates, such a function is defined as the following:

$$R(\theta) = \frac{ab}{\sqrt{(b\cos(c + d\theta))^2 + (a\sin(e + f\theta))^2}} \quad (4.1)$$

Where,  $a$  and  $b$  define the semimajor-, and semiminor- axes, and  $c$ ,  $d$ ,  $e$  and  $f$  represent the coordinate system rotation such as:

$$x' = a\cos(c + d\theta) \quad y' = b\sin(e + f\theta) \quad (4.2)$$

---

<sup>2</sup>For a deformation < 40 cm.

Such an interpretation of the new coordinate system is mathematically incorrect, but we will still use it for a better understanding of the problem.

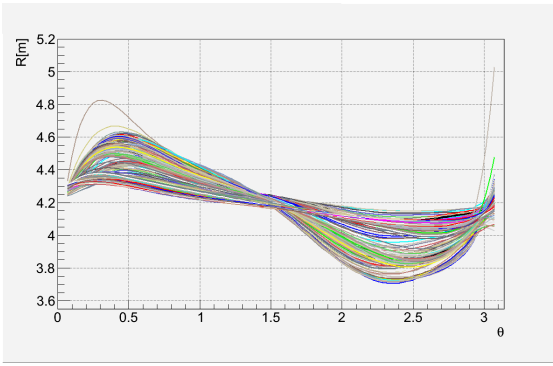


**Figure 4.7:** *Eight order polynomial fit to the data points obtained from the DST years of 2007 through 2011.*

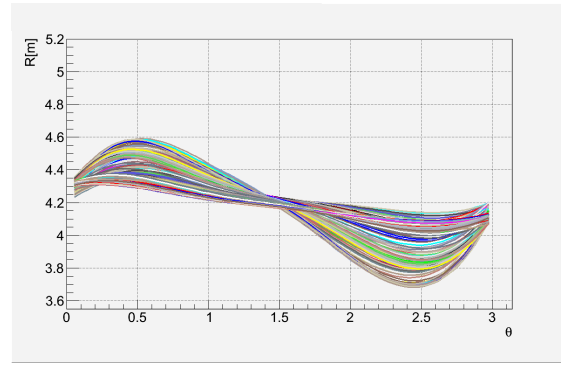


**Figure 4.8:** *Elliptical fit, defined in 4.3, on the same data set from the DST years of 2007-2011*

For better efficiency control, we can look at the fit function parameters in order to determine whether they remain stable within a reasonable range from week to week. The interpretation of the polynomial is rather difficult, because the parameters might be arbitrary and fluctuate significantly due to a high order of the function. However, in the case of the ellipse, the representation of  $a$  and  $b$  as the semi-major axis within  $[4.25; 6]$  m, and semi-minor axis in the limits of  $[3; 4.25]$  m refers to the actual vessel geometry. Parameters  $c$ ,  $d$ ,  $e$ , and  $f$ , responsible for the rotation of the coordinate frame, are expected to change slightly as the shape evolves. Nine parameters for the polynomial and six for the ellipse are plotted in Figures 4.9, and 4.10 respectively.

It is advantageous for the ellipse that due to its naturally realistic shape, the fit is not sensitive to spontaneous changes in the data points. A full comparison of the two functions with the data points from the DAQ and CCD is presented in the Figures below:

Within error bars, both the reconstructions are in good agreement with the true shape coming from the digital cameras. The IV shape determination from the CCD's is performed

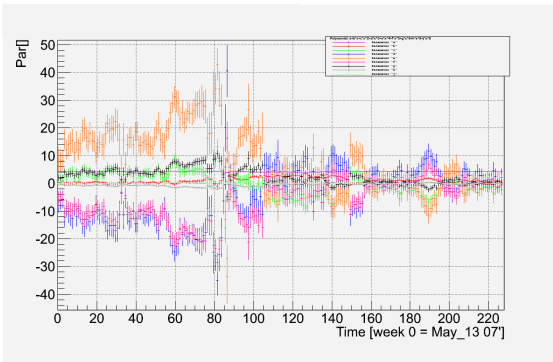


**Figure 4.9:** Time evolution of the nine fit parameters for the eighth order polynomial function.

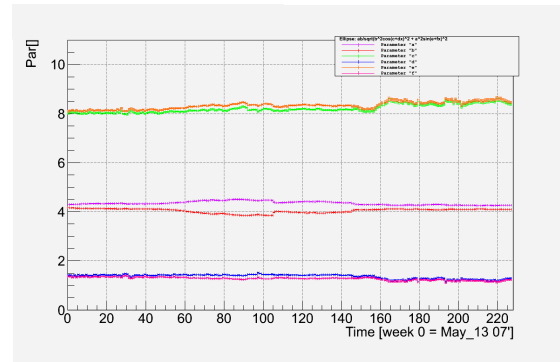


**Figure 4.10:** Time evolution as in Fig. 4.9, but of the six fit parameters for the elliptical function.

by eye. This procedure was the original one and performed on a regular basis, particularly during the initial filling phase and stage of the detector's operation. The principle of the reconstruction is the same as in the case of the calibration source position determination. Once the operator visually identifies the edge of the IV, the software finds a sphere centered at  $(0,0,0)$  for which a ray from the particular camera becomes its tangent.

## Shortest Distance to the IV

It certainly would have been much easier to carry out this calculation if the design of the Borexino detector was left with the originally planned, rigid, acrylic vessel. Although the solution of a thin, nylon sphere resulted in greater performance in the search for the  ${}^7\text{Be}$  neutrinos, the majority of the analysis tasks suffer from the unstable shape that has been changing in time due to multiple factors, such as: the density difference, temperature gradient and volume variations. Knowing exactly how the shape of the inner vessel has been changing over time becomes critical when selecting physics events for analyses requiring increased fiducial volume. These additional statistical data are especially important in the search for geo-neutrinos, as well as other anti-neutrinos that by nature leave in our experiment only a few

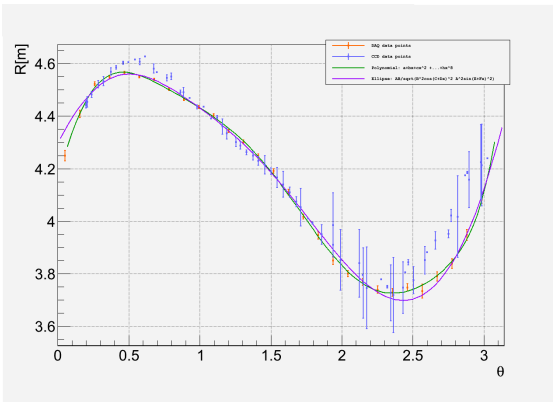


**Figure 4.11:** Comparison of the polynomial and elliptical fit functions with the data as well as the CCD camera information in the month of February 2009 when the deformation of the vessel was significant.

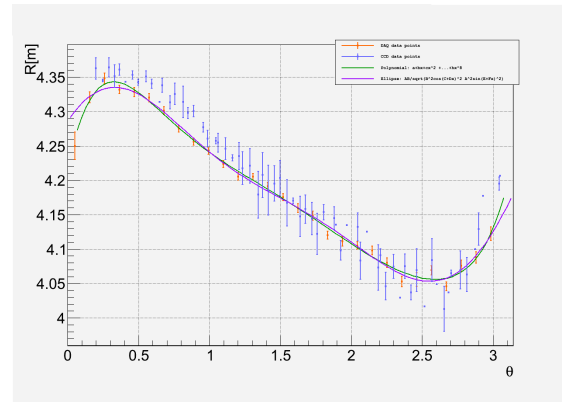


**Figure 4.12:** Similar comparison to the one presented in Fig. 4.11, but this time obtained for the data from November 2010 which is a representative shape for normal conditions of the vessel.

times per year<sup>3</sup>. In the following section, we will present how the obtained shape information can be used in the determination of the event position with respect to the vessel.

## Methodology and Geometry

The pre-processed Borexino data is grouped into single DST-weeks and so we can choose the most representative week, in this case the most deformed one of May 2009, and perform the geometrical scan on it. The method uses a simple numerical algorithm implemented in ROOT for a point of intersection search between two functions:

```
TF1 *f1, *f2;
Double_t inter(double *x, double *par){
    return TMath::Abs(f1->EvalPar(x,par) - f2->EvalPar(x,par));
}
```

<sup>3</sup>It has to be kept in mind however, that also the nature of a triple-coincidence tag available in the inverse-beta decay allows for a much efficient identification of the candidate events than a pure fiducial volume cut

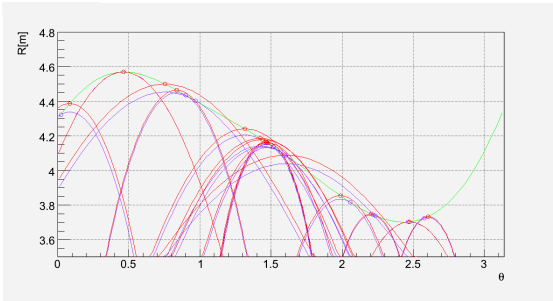


**Figure 4.13:** Vessel shape [green] and the determined circles for the distances to the vessel along the radii [red], and the shortest distance, *dsv* [violet].

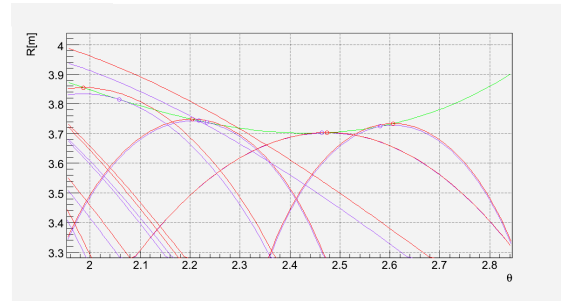


**Figure 4.14:** A zoomed view on the bottom of the detector,  $\theta$ : [140;150], presenting in detail how the shortest distance is being determined.

If the functions do not intersect, the returned value is the shortest distance between them. In the case of the IV, we search for an intersection point of a circle with a center at the origin of the event, and the shape function, but in an equivalent form in polar coordinates. After plotting, the program searches for the closest distance between the two curves, as long as that distance is not equal to zero<sup>4</sup>. When this condition is satisfied, the radius of the drawn circle determines the closest distance to the vessel. Presented in Figures 4.13 and 4.14, are the distances determined for the week of May 17, 2009. It can be seen how the shortest distance to the vessel (DSV) values approach the distance of the radii along the event for a perfectly spherical shape as expected, since for a sphere this radius becomes perpendicular to the curve at the closest point.

A more user-friendly representation of the results can be seen in Figure 4.15, in which the data were transformed into Cartesian coordinates. For clarity, only the events within a small radii of 3.021 m were plotted due to the enhanced effect of the difference between the DSV, and the distance determined by extrapolating the radius for a given event. It can be seen how the two lines (Violet and Red) overlap in the case when the shape becomes spherical. The full effect of the overlapping is shown in Figure 4.16, where the original shape was replaced

<sup>4</sup>Within a 0.0001 m precision

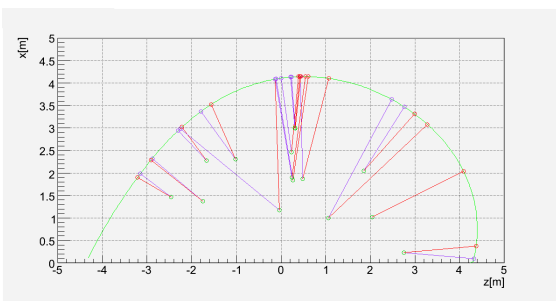


**Figure 4.15:** The vessel shape function for May 17 2009 [green] with reconstructed position of the events within a 3.021 m radius [green circles], and the distances, shortest in [violet] and along the radii in [red].

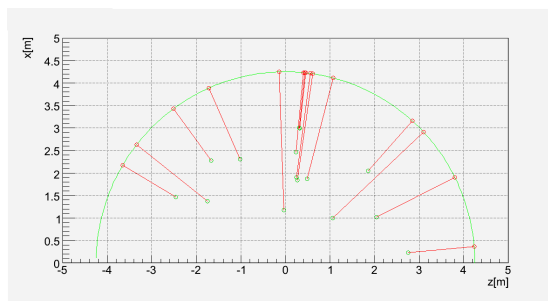


**Figure 4.16:** An identical set of events, and conditions as in Fig. 4.15, however implemented into a hypothetical sphere of radius 4.25 m. As expected,  $dsv = \text{distance along the radii}$ .

with a perfectly spherical vessel of radius 4.25 m. We also tested the reconstructed shortest distance by drawing circles of that radii. We notice in Figures 4.17 (15 selected events) and 4.18 (all the events in one DST), that the circles are contained within the boundary of the IV, which confirms the found distance to be the shortest.

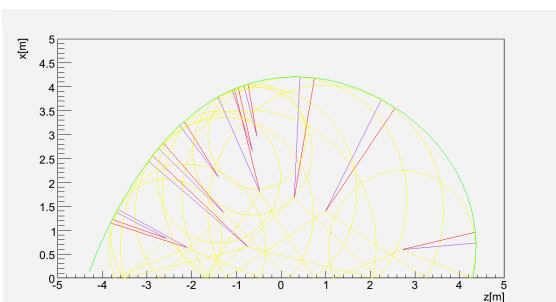


**Figure 4.17:** The vessel shape function from Aug 2009 [green] showing about fifteen events, and the calculated DSV values using the second method with yellow circles of  $R = DSV$ .

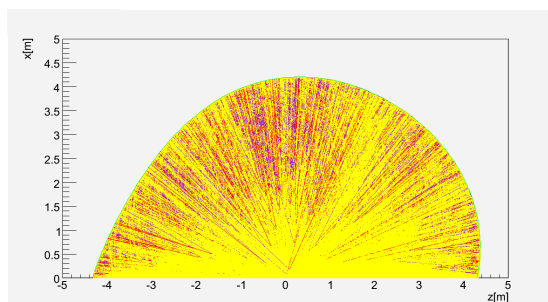


**Figure 4.18:** An identical representation of the shape and distances, but this time for all the 800k events within that DST file. The yellow circles fully, and with no leaks, fill the IV.

This is a faster version of the algorithm that was implemented, since for the DST root files that contain in some cases over two million events, the numerical calculation becomes too inefficient. This method takes a shape of the vessel in polar coordinates and it calculates only a differential function with a circle of  $R = (1/2)(R_{IV} - R_{event})$ . The angle for a minimum of this function is assumed to converge to the point of the closest distance to the event.

## Further Modifications to the Code

Even though the original proposal and implementation of the vessel reconstruction code was done by the author of this work, we naturally developed other versions later on. One of the most popular, and the one used in this analysis, was performed by F. Lombardi and N. Rossi of LNGS. In this approach, selection of the events remained the same, but the method of functional fitting and the definition of the shape-function itself were changed. First, all the events were plotted on a 2-D plane of  $R$ - $\theta$ , then the fit was performed using a two-dimensional function. Figure 4.19 shows the mean value in *Blue* that corresponds to the IV profile as of November 04, 2007. The function itself is a combination of a higher-order polynomial, a Fourier series, and a Gaussian distribution, but it will not be discussed here.

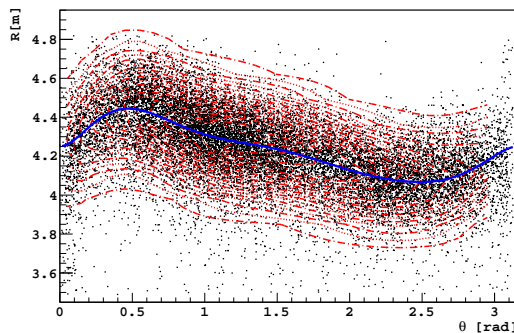


**Figure 4.19:** *Two-dimensional distribution of the vessel-events used for the shape fit (Red). The IV position is shown in blue.*

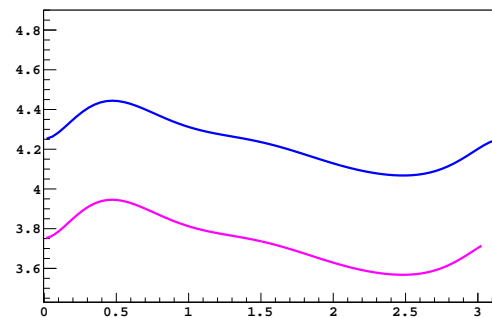


**Figure 4.20:** *In Blue, the mean value of the 2-D fit function from Fig. 4.19, and in Pink, the shortest to the IV at 0.50 m.*

A fundamental difference was made in the way the events were selected for further analysis. In this case, we define a new function that is of certain distance to the IV, and we require all the events to be within its range. Figure 4.19 presents two profiles, in *Blue* we see the IV and in *Pink*, a similar profile but in this case shifted by 0.50 m inwards. The biggest advantage of this technique is that it provides much faster event selection since there is no need for an event-by-event distance to the vessel determination anymore.

## Determination of the Volumes

### The IV Volume

We have so far collected all the necessary information in order to perform the final step required for the implementation of the shapes into analysis. A correct determination of the FV will be one of the most critical steps accounting for the systematics of the results and it will be discussed later. The total volume of the inner vessel can be calculated in two ways:

- With a trapezoid integration of the x-z shape obtained from the elliptic fit, in principle

$$\int_a^b f(x) dx \approx (b - a) \frac{f(a) + f(b)}{2}, \text{ or} \quad (4.3)$$

- Or by finding the volume of a solid through a revolution around the z-axis

$$V_{IV} = \frac{2}{3}\pi \int_0^\pi R(\theta)^3 \text{Sin}(\theta) d\theta \quad (4.4)$$

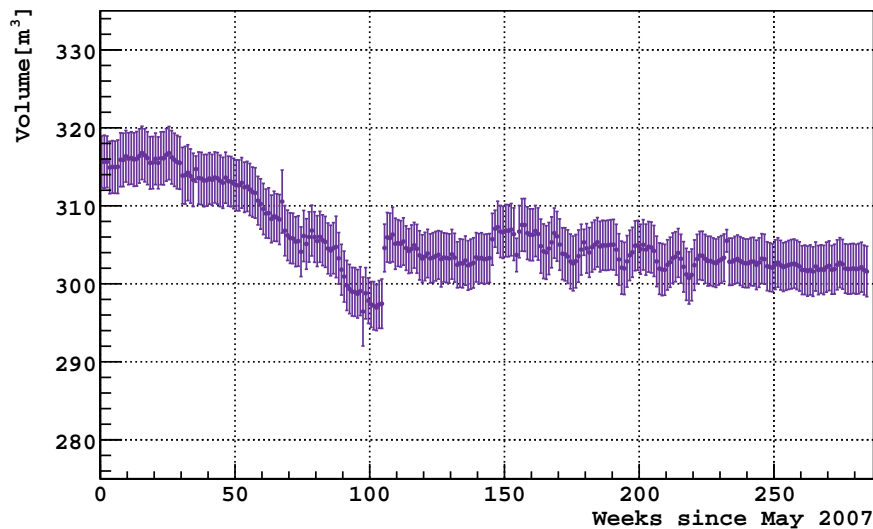


**Figure 4.21:** *Rotational integration of the vessel profile function obtained for the DST years of 2007 through 2011.*

The error bars have been estimated based on the distribution of the reconstructed shapes ( $\sigma_r$ ). After applying the standard propagation of errors, we obtain the following relationship:

$$\frac{\sigma_V}{V} = \frac{1}{V} \sqrt{\left(\frac{\partial V}{\partial r}\right)^2 \sigma_r^2} = \frac{3\sigma_r}{r} \Rightarrow \sigma_V = 2\pi\sigma_r \int_0^\pi R(\theta)^2 \sin(\theta) d\theta \quad (4.5)$$

There is an additional error in the trapezoidal integration due to a concave-down shape of the function that yields an underestimation of the volume. It becomes insignificant for an increased number of the integration points.

The inner vessel volumes determined on a weekly basis are presented in Figure 4.21. One of the goals of the total IV volume calculation is to monitor the status of the inner vessel. It is not only important from a maintenance point of view, but also critical in determination of the leak rate, which even though significantly reduced after the DMP removal, still contributes to a slow reduction in the active volume mass. Based on the data between August 2010 and August 2011, it can be concluded that the volume has decreased by about 1.4 m<sup>3</sup> in the past year.

### The FV Volume

For simplicity of analysis, the fiducial volume events were selected using a size-reduced shape of the inner vessel, as presented in Pink in Figure 4.20. As a result, the calculation of the fiducial mass was based on this shape and did not required any other tools than the standard rotational integration as in Equation 4.4, and its error in Eq. 4.5.

## 4.2 Backgrounds Stability

The results presented in this work strongly depend on the study of the backgrounds, specifically their stability over the course of the first three years of data taking. In fact, as long as the ratio of signal-to-noise remains high enough to reveal the modulation (as discussed in the next chapter) the stability checks narrow down only to stability control. In the following sections we will present some of the most important factors that had a significant impact on the event count rates that fall into the energy window of our interest,  $[105;380]$  npe. The figure below presents spectral functions for the  ${}^7\text{Be}$ , neutrinos and two major contaminants in this region,  ${}^{210}\text{Bi}$  and  ${}^{85}\text{Kr}$ .

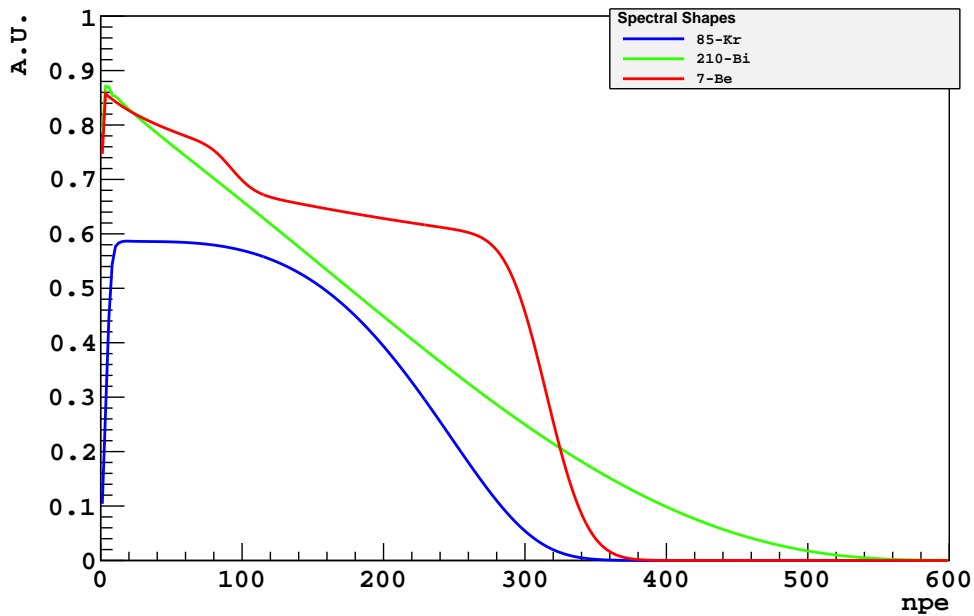


**Figure 4.22:** Spectral shapes of  ${}^{85}\text{Kr}$  and  ${}^{210}\text{Bi}$  overlapped on a linear scale with the  ${}^7\text{Be}$  line. The similarity in shapes and equivalent count rates pose the biggest difficulty in the analysis.

**$^{210}\text{Bi}$  Contribution**

The dominant and most difficult to eliminate background comes from a  $\beta$ -decaying isotope of  $^{210}\text{Bi}$  whose spectral shape overlaps with our signal, the Q-value of  $^{210}\text{Bi}$ =1162.1 keV (see Figure 4.22 for reference). Due to the changing environment inside of the inner vessel, and release of surface contamination, the contribution of  $^{210}\text{Bi}$  started to change in late 2007 and resulted in a continuous increase over the course of Phase I.

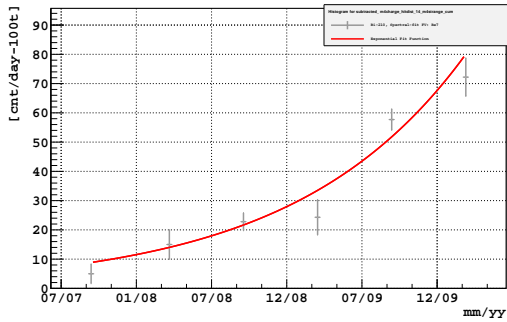


**Figure 4.23:**  $^{210}\text{Bi}$  count rate in the  $^7\text{Be}$ -valley in three years between 2007 and 2010. Fiducial mass: 100 tons.

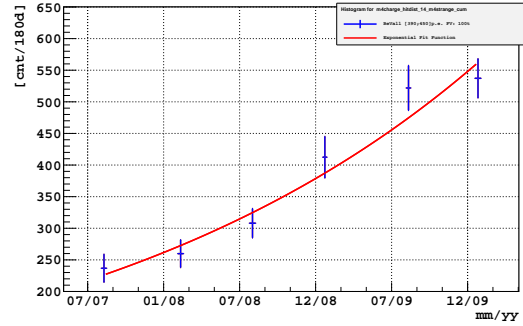


**Figure 4.24:**  $^{210}\text{Bi}$  count rate from spectral fit in periods as listed in Table 4.1. Fiducial mass: 100 tons.

$$B = C + e^{St}; \quad (4.6)$$

**Table 4.1:** Division of the official Borexino Phase I periods into six, approximately even in terms of live time groups.

Period	Start Week	End Week	Livetime (days)
1	13 May 2007	9 Dec 2007	138.334
2	13 Jan 2008	1 June 2008	127.604
3-4	15 Jun 2008	11 Jan 2009	74.671
5	8 Feb 2008	14 Jun 2009	85.169
6-7	26 Jul 2009	24 Jan 2010	72.705
8	14 Feb 2010	2 May 2010	69.218

In Figure 4.23, we illustrate the evidence for increasing count rate in the so-called  $^7\text{Be}$ -valley,

a narrow window between [390;450] npe, where  $^{210}\text{Bi}$  dominates over the neutrino signal. We can also reproduce the same plot by using a spectral fit in six individual periods as listed in Table 4.1, and plotted in Figure 4.24 for comparison. In this procedure, we fixed all other spectral components to their best known values; both the figures were generated for a standard  $^7\text{Be}$ -FV. We have also performed a similar exercise on the increased FV of 145 tons and we have found very similar shape of the building up of background as shown in Figure 4.25. Unfortunately, due to high contribution of the external backgrounds, we were not able to perform a successful spectral fit for the increased fiducial mass, but we do not expect any inconsistency based on the results shown in Figures 4.23 and 4.24.

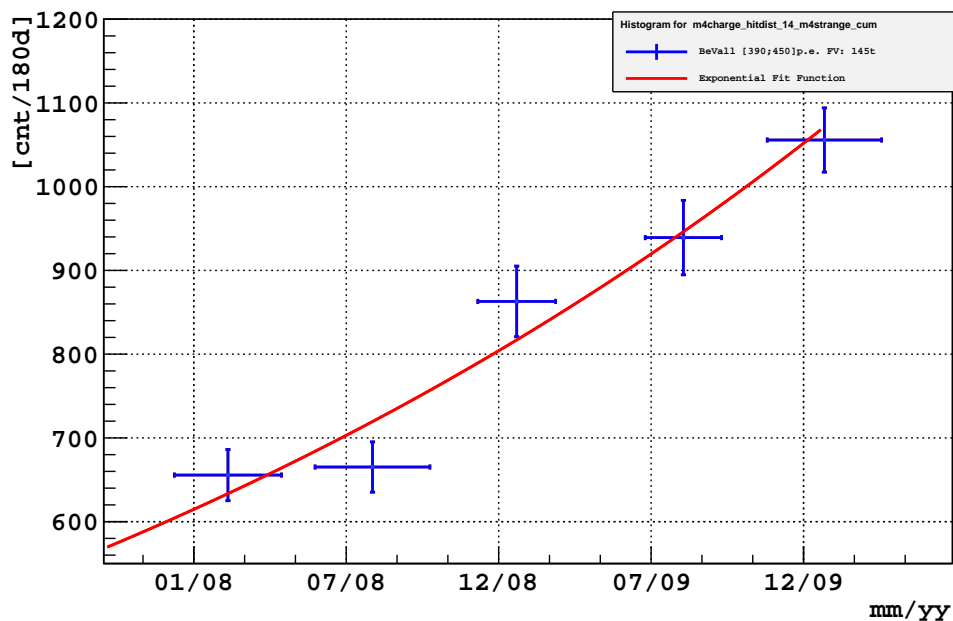


**Figure 4.25:**  $^{210}\text{Bi}$  count rate in the  $^7\text{Be}$ -valley for the fiducial mass as it was in the actual analysis, i.e. 145 tons and between Jan 2008 and May 2012. Bins are six months long.

It is important to notice that the overall trend from the fit agrees with the one obtained from the count-rate analysis and that the exponential, best fit function from Equation 4.6, shown in both figures in Red, is a reasonable choice. Later on, it will become important to be able

to eliminate this trend from the data by subtracting it from the count rate. This is because while performing Fourier analysis in the search for significant periodicities, our technique misidentifies the trend as an actual significant modulation and returns false Spectral Power Density (SPD) for the  $\nu$  periodicity. As an example, we present a comparison of the un-subtracted and subtracted exponential function in Figure 4.26, notice a higher SPD peak at 1-year in the left figure. In the analytical fit on the other hand, we will perform it in two steps, first by fitting only the trend and then using the result as a slope parameter of the background.

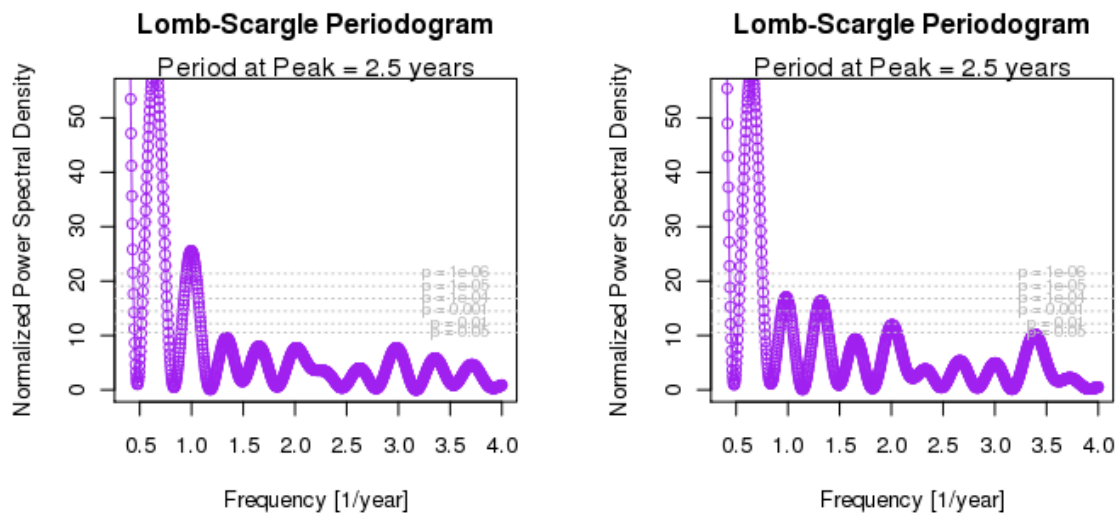


**Figure 4.26:** An illustration of the effect of exponential background component on the mis-identification of the Lomb-Scargle peak at around 1 year Left: un-subtracted, Right: subtracted exponential  $^{210}\text{Bi}$  shape from the  $^7\text{Be}$  window. Higher SPD visible on the left-hand side.

### $^{210}\text{Po}$ Concentration

By far the most dominant background in Borexino is the daughter of  $^{210}\text{Bi}$ ,  $^{210}\text{Po}$ . However, in our case it is unfortunately out of equilibrium due to contamination related to the purification plants, specifically the metal pipes used to transport water.  $^{210}\text{Po}$  is an  $\alpha$  emitter with a peak at 5.3 MeV, but to due strong quenching of alpha particles in organic scintillators, its

energy reconstructs eight to ten times lower, which in our case happens to be around 210 npe, certainly below the Compton edge of the  ${}^7\text{Be}$   $\nu$  line.

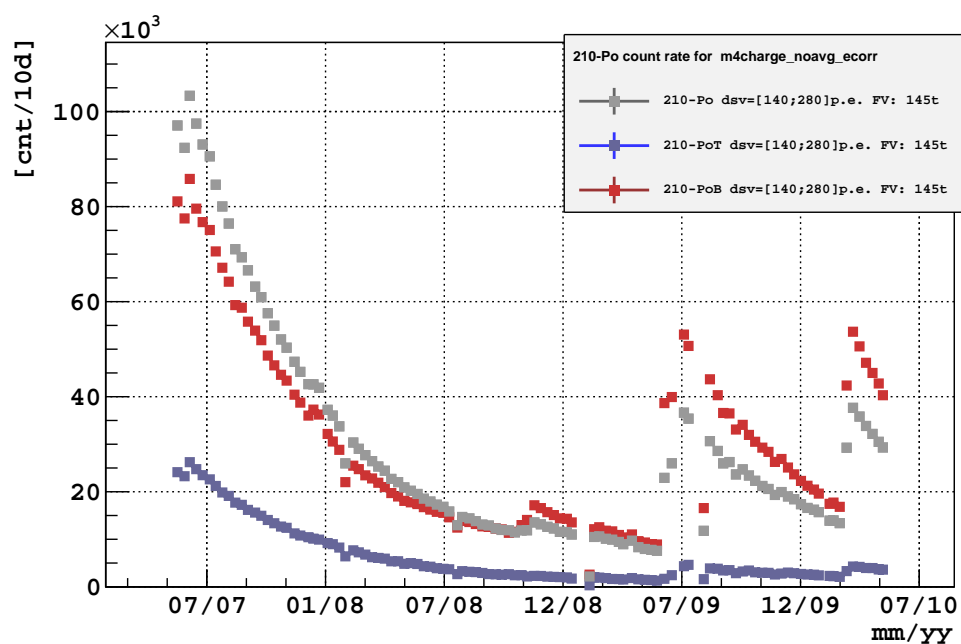


**Figure 4.27:**  ${}^{210}\text{Po}$  count rate in the FV used in this analysis. Each rapid increase in concentration corresponds to a refilling campaign or other activity, as listed in Table 4.2. The count rates were normalized according to live time but not mass in the individual hemispheres.

**Table 4.2:** Major operations on the Borexino scintillator that are responsible for the increase in  ${}^{210}\text{Po}$  count rate.

Date	Weeks since May 13, 2007	Operation
2008-Jan-04	(35)	Water Loop ON
2008-Oct-24	(77)	PC+PPO added at bottom (4kl in 2 weeks)
2009-Feb-12	(92)	Buffer purification (DMP from 5 to 3 g/l)
2009-Jun-01	(108)	PC+PPO added at bottom (9kl over 5 days)
2009-Dec-02	(134)	Buffer purification (DMP reduced to 2 g/l)
2010-Mar-13	(149)	added $4.5\text{ m}^3$ at top
2010-Mar-25	(150)	added $4.5\text{ m}^3$ at top

Nevertheless, the Gatti parameter (defined in the previous sections) can be effectively used in reduction of the  ${}^{210}\text{Po}$  background which will be discussed in the next chapter, along with

other details regarding selection of the events for this analysis. At this point, we would only like to mention its time dependence. Even though  $^{210}\text{Po}$  decays away with a half-life of 138.376 days, which theoretically should lead to a significantly reduced concentration after about a year, the actual amount was increasing. Unfortunately, additional refilling campaigns that were necessary due to the leak in the inner vessel, introduced  $^{210}\text{Po}$  every time the operation was performed. Changes in concentration of Polonium presented in Figure 4.27 should be compared with Table 4.2; it is clear how these events are correlated.

### $^{85}\text{Kr}$ Concentration

**Spectral Shape** Potentially,  $^{85}\text{Kr}$  poses similar problems for the annual modulation study as  $^{210}\text{Bi}$ ; this is because its spectral shape is almost identical to the one of  $^7\text{Be}$  (Blue in Fig. 4.22), its  $Q_v=687.1\text{ keV}$ . Even though the design requirements and the PC purity strived for no initial concentration of  $^{85}\text{Kr}$  ( $\sim 1\text{ counts}/(\text{day} \times 100\text{ ton})$ ), its count rate in Borexino was found to be at the level of  $\sim 30\text{ counts}/(\text{day} \times 100\text{ ton})$  in phase I.

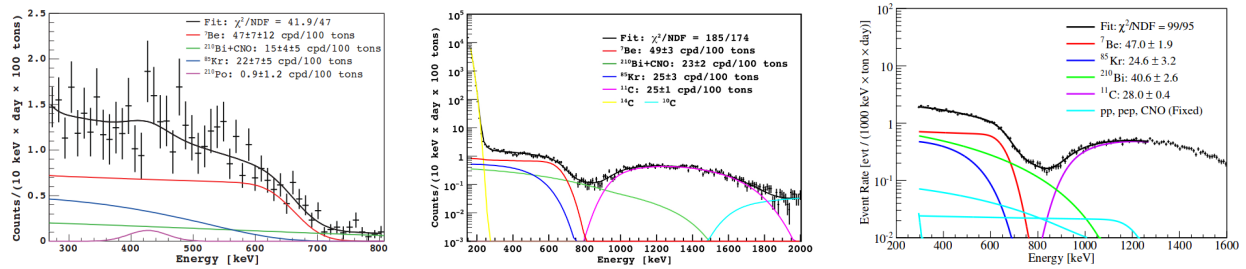


**Figure 4.28:** Spectral fit results for the Borexino data after 90, 192, and 740 days from left to right. Determined  $^{85}\text{Kr}$  rate was the following:  $22 \pm 7$ ,  $25 \pm 3$ , and  $24.6 \pm 3.2\text{ counts}/(\text{day} \times 100\text{ ton})$ .

The presence of  $^{85}\text{Kr}$  in the Borexino scintillator is a result of external factors, specifically the natural concentration of this isotope in the atmosphere, which means that the initial contamination should not change throughout the data-taking period (as opposed to  $^{210}\text{Bi}$ , whose origin is in the surface contamination of  $^{210}\text{Pb}$ ). As a first order check, we can simply

look at the spectral fit results from the Borexino published measurement of the  ${}^7\text{Be}$  line. Figure 4.28 shows the spectra with statistically removed  ${}^{210}\text{Po}$  for 90, 190, and 740 live days. The counts determined for  ${}^{85}\text{Kr}$  are consistent within error bars around the value of 24 counts/(day x 100 ton). An additional check was done using separate periods as defined in Table 4.1. Also in this case, no fluctuation was found in the determined rates.

**Coincidence Tag** Even though spectral fit is the most straightforward way of obtaining the  ${}^{85}\text{Kr}$  count in Borexino, we have one more tool available that is a result of the decay scheme of this isotope. About 0.43% of the time,  ${}^{85}\text{Kr}$   $\beta^-$ -decays with a  $Q_\nu=176$  keV into a meta-stable state of  ${}^{85m}\text{Rb}$ . After a mean-life of about  $1.46 \mu\text{s}$ ,  ${}^{85m}\text{Rb}$  then decays into  ${}^{85}\text{Rb}$  emitting a  $\gamma$  at 514 keV. This coincidence can be tagged in a similar way to how we tag  ${}^{214}\text{BiPo}$ . Unfortunately, the rare decay, combined with low trigger efficiency and massive  ${}^{14}\text{C}$  background, make this technique very inefficient. Nevertheless, using 750 days in Phase I, we were able to determine the  ${}^{85}\text{Kr}$  rate accurately enough to find a good agreement with the spectral fit.

### ${}^{222}\text{Rn}$ Tagging

The second most important source of contamination is related to the fact that the active volume has been frequently exposed to effects of external operations. Calibrations, refillings and exposure to air from the outside, resulted in an increased count rate of  ${}^{222}\text{Rn}$  background. Fortunately though, its short decay time did not pose any long-term danger on the overall purity of the detector.

We present in Figure 4.29 the result of Radon-tagging in the whole volume of the inner vessel. Its most significant contribution in correlation with a changing count rate in the  ${}^7\text{Be}$ -window was observed for the period of initial filling. For this reason, along with a

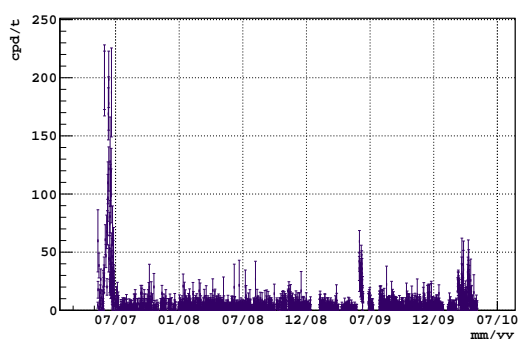


**Figure 4.29:**  $^{222}\text{Rn}$  coincidence tagged on in the whole inner vessel between May 2007 and May 2010. FM: 278 t.

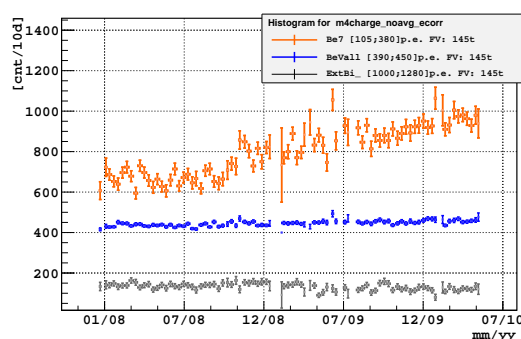


**Figure 4.30:**  $^7\text{Be}$  count rate without  $^{214}\text{Pb}$  reduction.  $^7\text{Be}$ -Valley count-rate was scaled by a const. number. FM: 145 t.

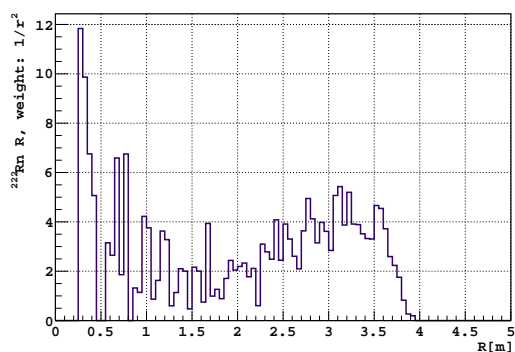


**Figure 4.31:**  $^{222}\text{Rn}$  events radial distribution, weighted by  $1/r^2$ . Events shown correspond to the high count from the beginning data taking, between May and July 2007.

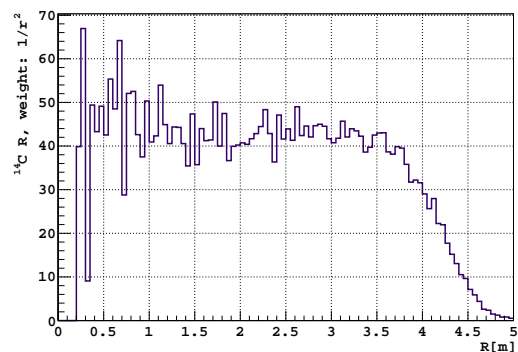


**Figure 4.32:** For comparison, weighted radial distribution of the  $^{14}\text{C}$  event within the inner vessel. It's clear how uniform it is with respect to  $^{222}\text{Rn}$  in Fig. 4.31.

problematic trigger in the first few months of data taking, we will exclude period 1 from further analysis. As an additional check for the  $^{222}\text{Rn}$  contamination being related only to the filling phase, we plot radial distribution of the tagged events from Figure 4.29, and we weigh it by the volumetric factor of  $1/r^2$ . In Figure 4.31, we show only the events from the period of high count rate between May and July 2007. It is clear how the distribution is biased towards the outer regions of the inner vessel volume. For comparison, a perfectly uniform distribution is shown on a similar plot, but in this case for the  $^{14}\text{C}$  events which are

believed to be the most uniformly distributed background in the scintillator.

## External Gamma Background

In order to be able to safely increase the fiducial volume, it was necessary to study the contribution of the external gamma background coming from the SSS and the PMTs. The majority of it is in a form of the 2.6 MeV  $\gamma$ 's from  $^{208}\text{Tl}$ . Using calibration data from the campaign in 2011, we were able to plot radial distribution of events in the energy region of interest, [95; 380] npe, as well as the high energy window, [1000; 1280] npe. Results from cross-sections of the fiducial volume are shown in Figures 4.33 and 4.34 respectively.

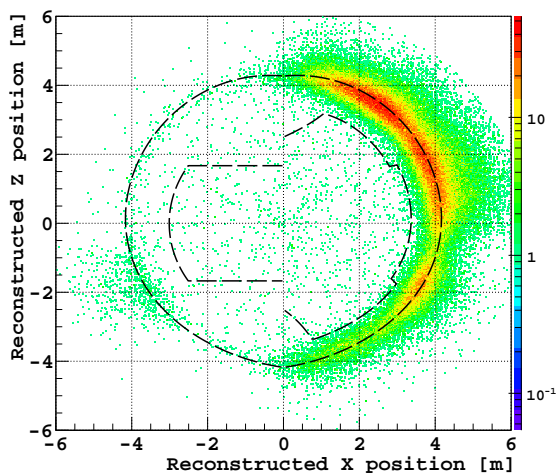


**Figure 4.33:** Cross section of the external calibration source impact in [95; 380] npe window. FV: 75 tons (inner left-shape), 145 tons (inner right-shape).

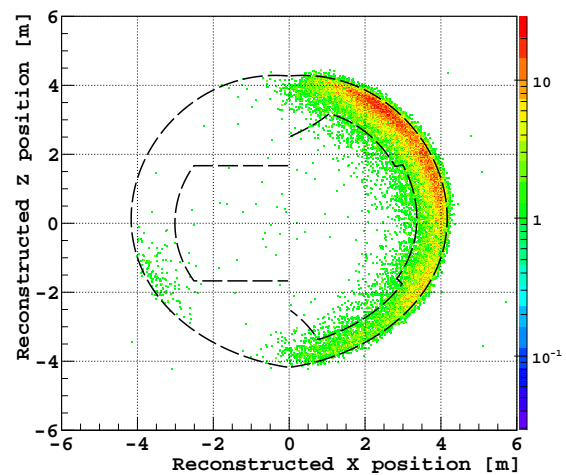


**Figure 4.34:** Cross section of the external calibration source impact in [1000; 1280] npe window. FV: 75 tons (inner left-shape), 145 tons (inner right-shape).

## Long Term Stability: Gatti, Energy and Position Resolution

Due to the fact that in the rate analysis we have to rely on raw counts in the desired energy window, we need to keep in mind that the dominant (but at the same time easily distin-

guishable) background comes from the element of  $^{210}\text{Po}$ . These and other  $\alpha$  events in the [95; 380] npe window can be identified using the Gatti parameter and statistical subtraction that was originally developed for the precision measurement of the  $^7\text{Be}$  flux in Borexino, details of which can be found in [96]. In order to verify whether the procedure that was adapted in Section 5.2 could introduce an artificial fluctuation, we looked at the time stability of both  $\alpha$ - and  $\beta$ -like events by fitting a dual Gaussian function in the Gatti space for every week and three energy regions independently: [95; 380], [380; 665] and [665; 950] npe.

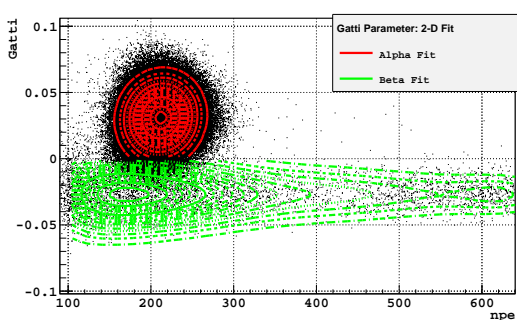


**Figure 4.35:** 2-D fit in the energy-to-Gatti space. Data divided into weekly bins and collected from the whole IV.

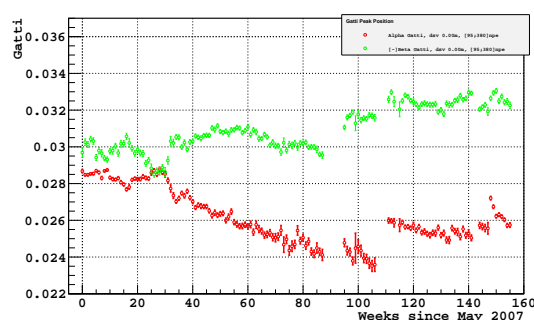


**Figure 4.36:** Peak positions in the Gatti parameter space in [95; 380] npe. From the fit presented in Fig. 4.35

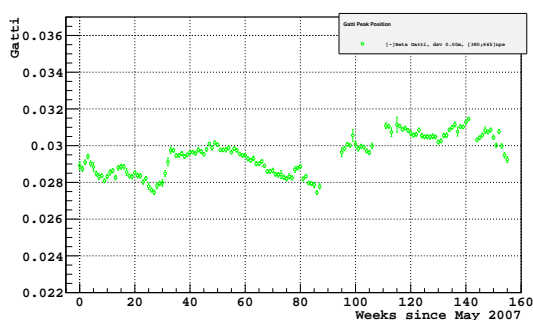


**Figure 4.37:** Peak positions in the Gatti parameter space in [380; 665] npe. From the fit presented in Fig. 4.35

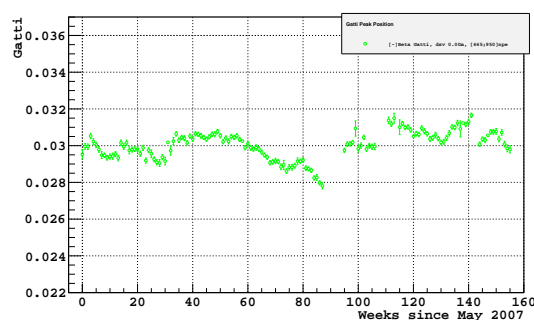


**Figure 4.38:** Peak positions in the Gatti parameter space in [665; 950] npe. From the fit presented in Fig. 4.35

Results are presented in Figure 4.36 for the first region<sup>5</sup>. It can be seen that after January

<sup>5</sup>The Gatti parameter for  $\beta$  particles (green) is in fact negative but here, it was multiplied by (-1).

2008, the distribution stabilizes for the  $\beta$ 's with a visible kink due to refilling of the IV and a change in both the amount and location of  $^{210}\text{Po}$  within the detector. Figures 4.37 and 4.38 indicate that the Gatti parameter for  $\beta$ 's is slightly dependent on the presence of the  $\alpha$  events. Additionally, after performing a similar check in the actual, reduced fiducial volumes, we consider the effect negligible and not correlated with the annual periodicity.

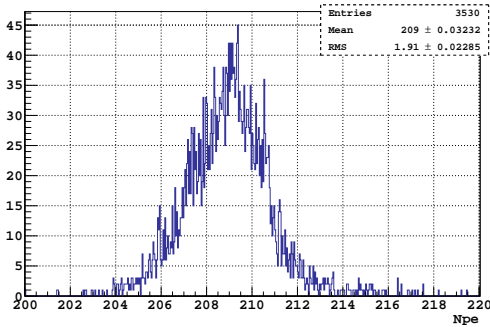


**Figure 4.39:**  $^{210}\text{Po}$  npe peak position distribution in weekly bins. Selected data contains events within the whole IV.

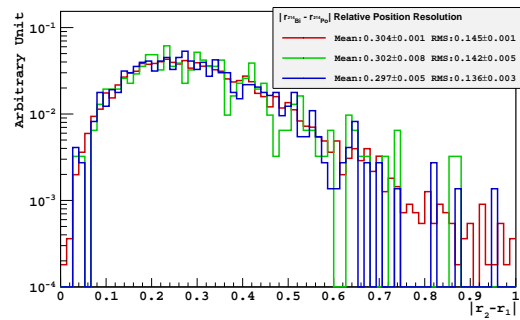


**Figure 4.40:** Absolute distance between  $^{214}\text{BiPo}$  in three periods, Red: May'07, Green: Jul'09, Blue: Apr'10.

In order to verify the stability of energy reconstruction, we looked at the position of  $^{210}\text{Po}$  peak w.r. to time in the whole IV. It's clear from Figure 4.39 that we can trust the energy scale on a long term to within 2 npe. It should be kept in mind also that alpha-events tend to misreconstruct when close to the nylon vessel and this could be causing further fluctuations present in Figure 4.39 that disappear when fiducial volume cuts are used for the analysis.

Another important check was performed on the events' reconstructed position resolution. For this purpose, we used the easily-tagged, space-time coincidences of  $^{214}\text{BiPo}$  that are present in the  $^{222}\text{Rn}$  chain. We selected three periods for the sample that were temporarily high in Radon: 1) the initial filling in 2007, 2) the first off-axis calibration campaign in 2009 and 3) another refilling in 2010. Next, we plotted the absolute distance between  $^{214}\text{Bi}$  and  $^{214}\text{Po}$ , and normalized histograms for each period to their total integrals. Results are shown

in Figure 4.40 where it is clear how well the three histograms align.

### Top-Bottom Asymmetry

**IV-OV Temperature** It is also worth noticing that such a small effect as a changing temperature of the air surrounding detector, different tasks performed in the water buffer or the scintillator itself, could affect the internal temperature, which in turn would result in a release of surface contamination present in the nylon vessels. We were able to identify a periodic signal in the rate of change of temperature in the top buffer itself, but it is difficult to estimate how this could be translated directly into the surface contamination release. For this reason, we selected data from a shell of only 0.25 m from the inner vessel and tried to study the count rate distribution of events in the energy window of interest, but the signal was overwhelmed by the external  $\gamma$ 's. Plots of the temperature data and its significant periodicities for the top OV are presented in Figures 4.41 and 4.42 respectively.

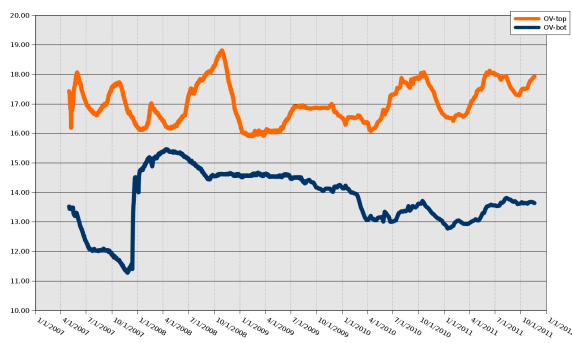


**Figure 4.41:** Temperature readings from the top and bottom regions of detector buffer. Units are degrees Celsius.

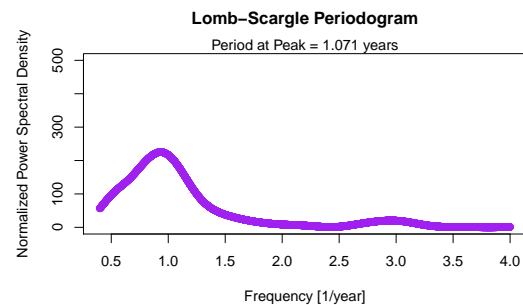


**Figure 4.42:** Lomb-Scargle periodogram for the temperature distribution in the top of the outer detector.

**$^{210}\text{Bi}$  Mixing** We have identified an interesting effect related to the spatial distribution of the  $^{210}\text{Bi}$  background while studying the asymmetry of the detector. Figure 4.45 shows count rates in each hemisphere for the  $^7\text{Be}$ -valley events in a small FM of 33 tons. In order

to clarify the graph, we plotted deviations of the rates with respect to the total count rate (top+bottom). What we have found, is a periodic modulation of the  $^{210}\text{Bi}$  background between the two halves. This could be related to a changing temperature outside of the detector (Hall C) and as a result, generation of convective currents within the volume of the volume. This is why the oscillating background is visible only in a reduced FV.

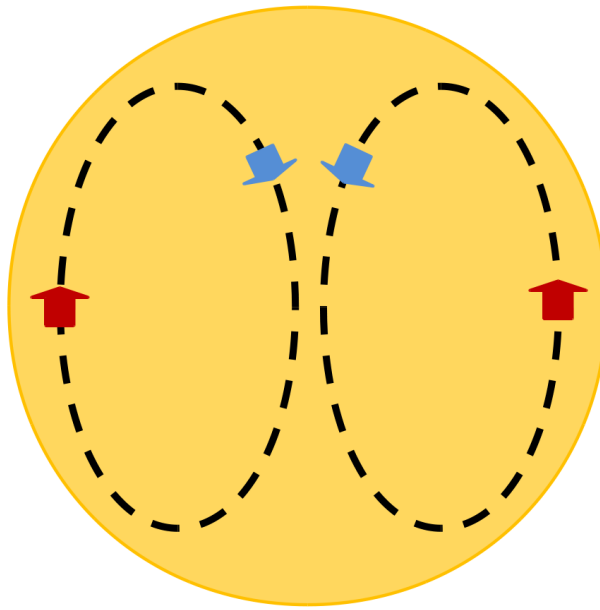


**Figure 4.43:** An idea of the PC mixing in the active volume due to temperature gradient.

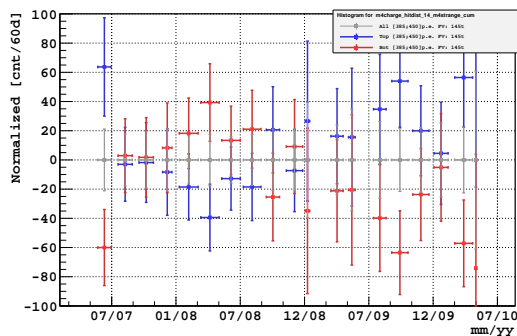


**Figure 4.44:** Asymmetry of the  $^{210}\text{Bi}$  count rate between the top and bottom hemispheres in the  $^7\text{Be}$ -valley for FM: 145 tons.

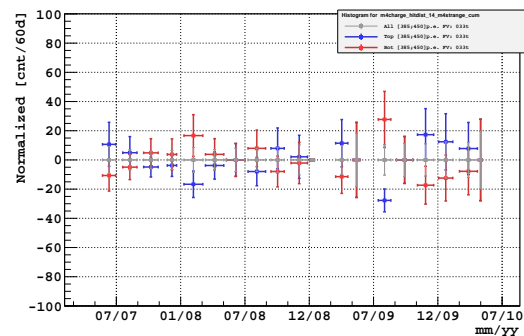


**Figure 4.45:** Count rates in the  $^7\text{Be}$ -valley for the top and bottom hemispheres. Rates are shifted such that  $T_{ob}+B_{ot} = 0$ . FM: 33 tons.

**Energy Scale Correction** Another effect related to the vertical asymmetry in the detector was already identified by the external calibration group while studying higher energy gamma events in the FV with  $R > 3$  m. It was observed that the energy scale for these events was shifted in the top with respect to the bottom of the detector. As a result, a geometrical correction was proposed in the following form:

$$Q_{corr} = Q_{rec} \cdot \frac{1}{(1 + A \cdot Z \cdot |Z|^n + B \cdot |Z|^k)} \cdot \frac{1}{1 + C \cdot \left(\frac{d}{1+|Z|}\right)}; \quad (4.7)$$

where  $d$  is the distance from the  $z$  axis,  $d = \sqrt{(x^2 + y^2)}$ , and  $A=8.6510^{-3}$ ,  $B=4.9310^{-5}$ ,  $C=2.110^{-3}$ ,  $n=0.58$ ,  $k=5.75$ . Further details regarding the correction and its derivation can be found in [97]. Even though this effect is mainly relevant for higher energies, we have found that it significantly also improves the energy scale in the lower energy region.

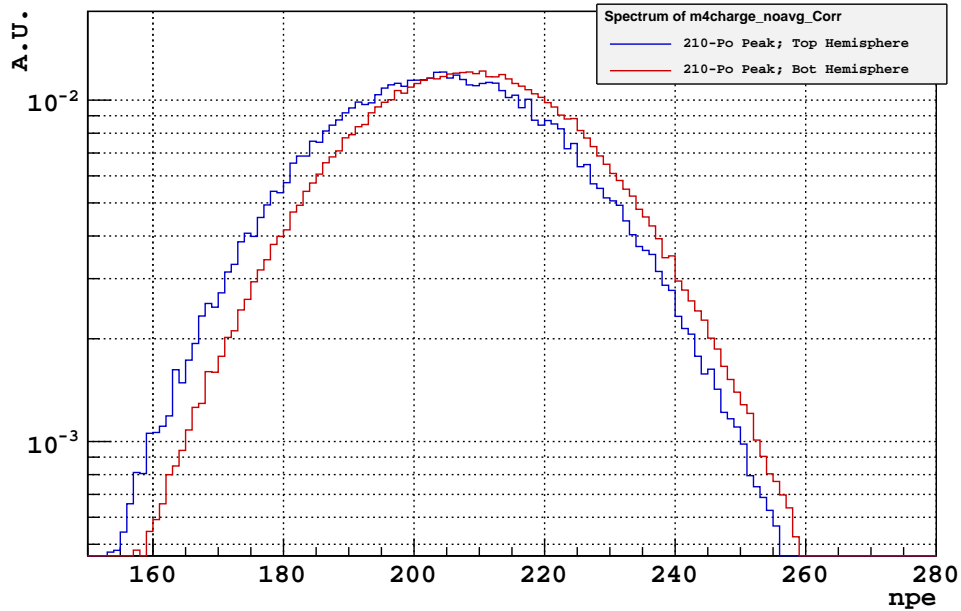


**Figure 4.46:** Comparison of the energy scale in the top and bottom hemispheres in number of photoelectrons. FM: 145 tons.

In Figure 4.46, we show a  $^{210}\text{Po}$  peak for top and bottom after applying the geometrical correction. It's clear that the normalized histograms are still not perfectly aligned but the improvement with respect to uncorrected spectra is non-negligible.

**Top-Bottom IV Asymmetry** It is worth noticing that not only the fluctuating volume and shape of the inner vessel could affect our measurement, but also its asymmetry between the top and bottom of the detector. This asymmetry could result in a different detector response not only because of the higher count rate in the upper hemisphere, but also because the mass of the scintillator acting as shielding from the external gamma rays. In the two plots below, Figures 4.47 and 4.48, we show how large the asymmetry was in certain periods, both in terms of the shape change as well as the volume differential.

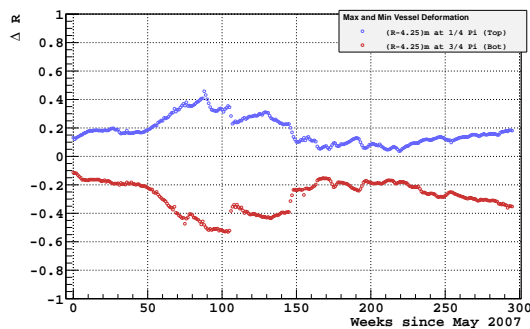


**Figure 4.47:** *Asymmetry plot of radius for the further most point in the top of the vessel, and the closest in the bottom.*

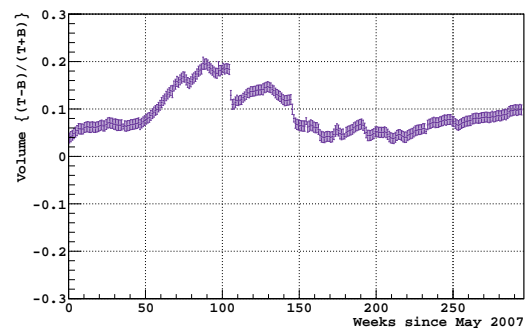


**Figure 4.48:** *Asymmetry plot for a fraction of the volumes between the top and bottom hemispheres.*

**Top-Bottom External  $\gamma$  Rates** Directly related to the asymmetry and shape changes of the inner vessel is the contribution of the external background that we can observe by looking at the count rates in the higher energy region of the spectrum. What corresponds to the gamma scattered part is around [1000; 1280] npe, with the full energy peak at [1280; 1450] npe, this contribution coming from external  $^{214}\text{Bi}$  and  $^{208}\text{Tl}$ . When selecting the in-

creased fiducial volume for analysis, we addressed this issue carefully by studying various spatial cuts with respect to the position of the inner vessel. The external background of course is not as dominant in the  ${}^7\text{Be}$  window, but its contribution is not negligible. As expected, the closer the cut was to the IV the more significant contribution was observed in those energy regions. In Figures 4.51 and 4.52, we show the first FV we studied. One notices quite easily where the increase of the count rate is located, and how closely correlated in time it is with the deformation of the vessel. Compare it with Figures 4.47 and 4.48, for further reference.

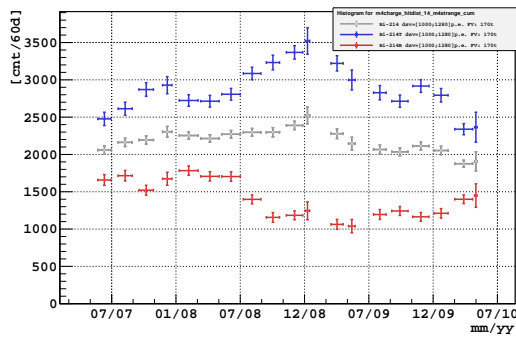


**Figure 4.49:** Top-to-bottom comparison in the window of  $[1000; 1280]$  npe for a  $DSV=0.50$  m cut; FM: 170 tons.

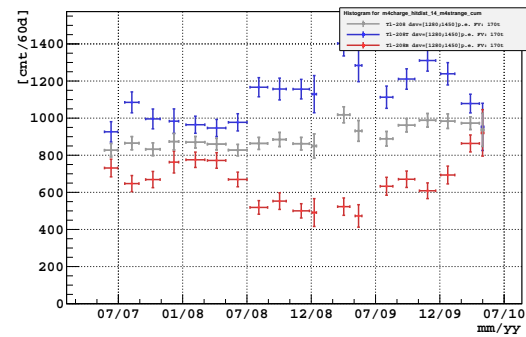


**Figure 4.50:** Top-to-bottom comparison in the window of  $[1280; 1450]$  npe for a  $DSV=0.50$  m cut; FM: 170 tons.

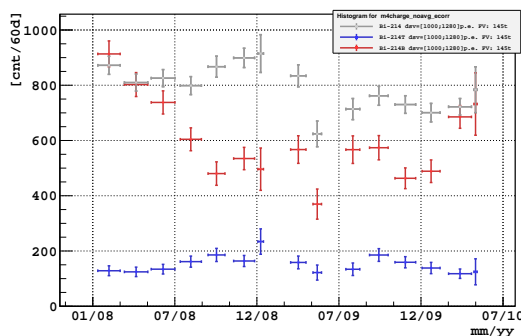


**Figure 4.51:** Top-to-bottom comparison in the window of  $[1000; 1280]$  npe; FM: 145 tons.

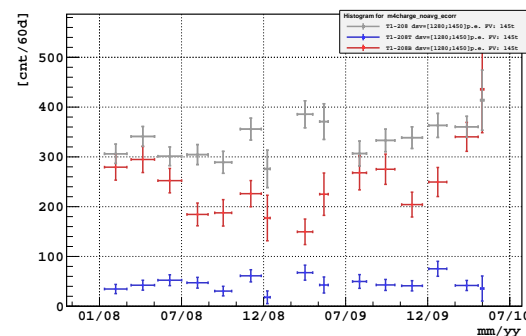


**Figure 4.52:** Top-to-bottom comparison in the window of  $[1280; 1450]$  npe; FM: 145 tons.

The last two figures show the same count rate plots, but this time for a fiducial volume selected for the annual modulation study. We can still notice fluctuation of the background but we no longer see the correlation with the vessel shape. Additionally, the overall count per bin is a factor of three lower in this case. We have also tested a cut of 0.75 m from the vessel, but the results were almost identical with the DSV=0.50 m case. This indicates that we have successfully maximized statistics in the neutrino window (for FM of 145 tons) with the lowest possible contribution from the external background.

### Azimuthal Asymmetry

**The Inner Vessel** In the discussion on the IV shape reconstruction in the previous chapters, we have assumed a symmetry in the azimuthal direction ( $\theta$  angle), which we expect since the effect of deformation was a result of a uniform buoyant force. Nevertheless, we would like to present a study of this symmetry that could be used to verify the actual error on the reconstructed radius of the IV. It is important to keep in mind that the vessel itself is supported by nylon ropes that cause a natural tessellation of the surface, especially in the top part of the volume where the upward force is the greatest. We perform the scan in the following geometry:

- Vertically: We divide the vessel into three regions every  $60^\circ$
- Horizontally: We take a step every  $5^\circ$  where we reconstruct the radius

The division into these regions is presented on a diagram in [Figure 4.53](#).

This choice in the azimuthal direction was mainly driven by the fact that there are 18 ropes supporting the IV (20 for the OV), meaning a rope every  $20^\circ$ . As a result, we would like to see whether there is any deformation related to the ropes and if possible, their pushing against the inner vessel which could result in additional damage to the nylon vessel.

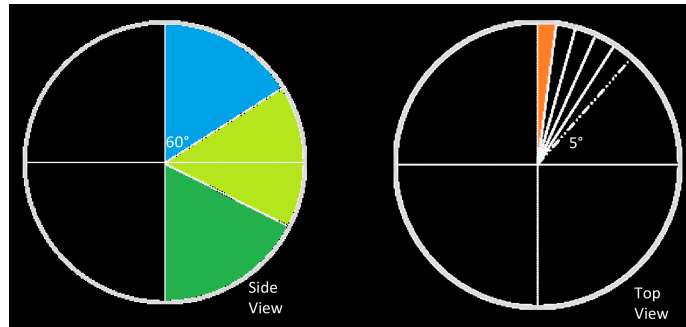


**Figure 4.53:** Visual representation of the inner vessel division into 3 vertical and 72 horizontal regions.

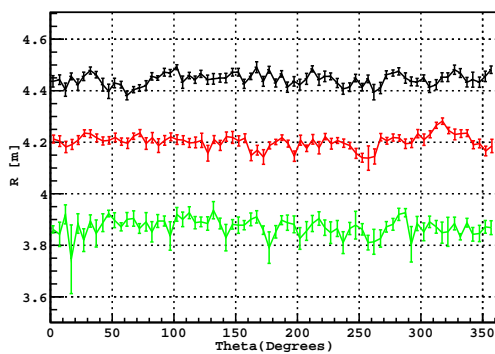


**Figure 4.54:** Reconstructed position of the vessel in the 3 vertical regions: Top (Black), Middle (Red), Bottom (Green).

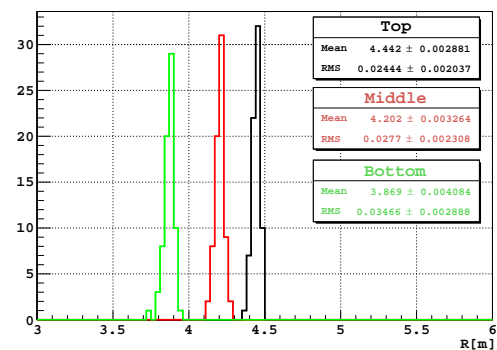


**Figure 4.55:** RMS of the reconstructed vessel position in the three regions shows no indication of big variation in  $\theta$ .

The conclusions of this test are satisfactory and confirm symmetry in the azimuthal direction of the vessel position. In Figure 4.54, we observe a slight oscillation of the reconstructed radius that could be associated with the mentioned tessellation of the vessel. The deformation appears to be, however, within the error of each reconstructed step. Additionally, we plot the RMS for each step in each of the three vertical regions in Figure 4.55. First, there seems to be no significant deviation in distribution (none greater than 2.5 cm). Second, the RMS for the Top, Bottom, and Middle are consistent for all individual regions.

## Radial Asymmetry

**IV Shells** In this scan we look at radial distribution of count rates with spatially separated regions (shells) with respect to the position of the inner vessel. The goal here is to identify whether the backgrounds are related to the distance from the nylon or if the convective currents of the mixing scintillator could be tracked. Shells are defined in Figure 4.56.

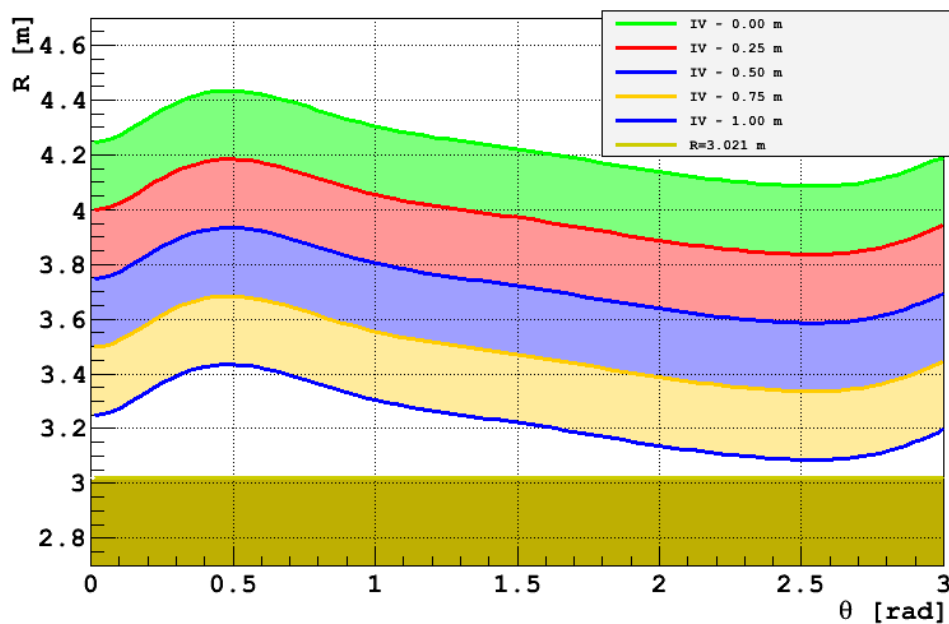


**Figure 4.56:** Definition of shell regions, I through V, based on the original IV shape function.

In the first step we defined, based on a given inner vessel shape function, all the other functions of reduced distance with respect to the original one. As a result, we had five different regions with one of fixed radius at  $R=3.021$  m, which is the radius of the  ${}^7\text{Be}$  FV. Finally, we looked at count-rates in each of the shells.

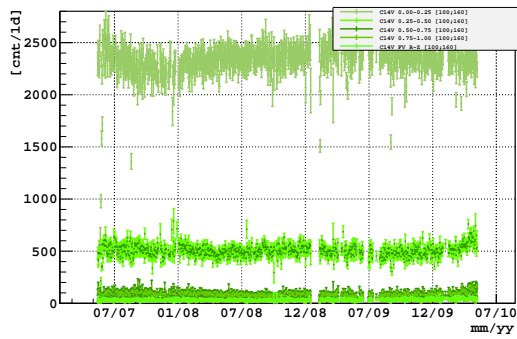


**Figure 4.57:**  $^{14}\text{C}$ -valley region; [100; 160] npe; Shells I-V are shown.

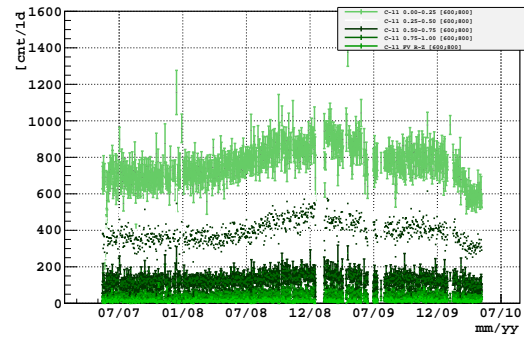


**Figure 4.58:**  $^{11}\text{C}$ -dominated region; [600; 800] npe; Shells I-V are shown.

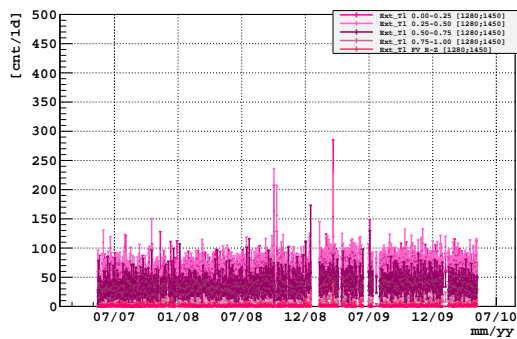


**Figure 4.59:** External background region of  $^{208}\text{Tl}$  [1280; 1450] npe; Shells I-V are shown.

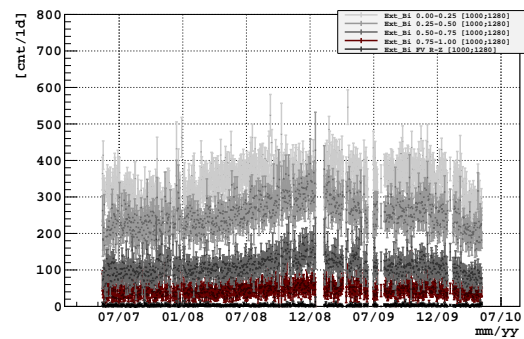


**Figure 4.60:** External background region of  $^{214}\text{Bi}$  [1000; 1280] npe; Shells I-V are shown.

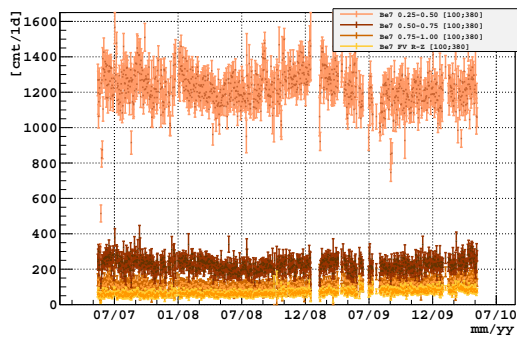


**Figure 4.61:**  $^7\text{Be}$ -dominated region; [100; 380] npe; Shells I-IV are shown.

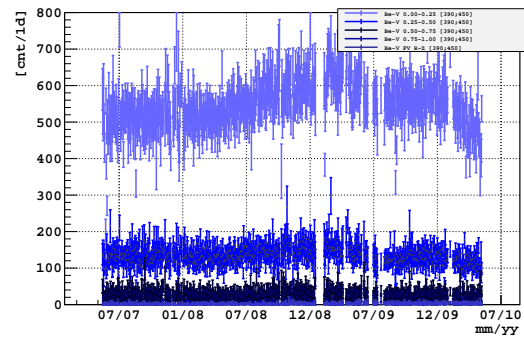


**Figure 4.62:**  $^7\text{Be}$ -valley region; [390; 450] npe;  $^{210}\text{Bi}$ -dominated; Shells I-V are shown.

In general, we observe in each of the cases that the spatial region closest to the inner vessel, between 0.00 and 0.25 m, will always be dominated by the external background contribution that should be compared with its exact shape from Figure 4.60. For this reason, we will not consider this contribution as important for the later results of the analysis since it is outside of the fiducial volume cut. The effect of increasing count with consecutive shell number is related only to the fact that the shells were not normalized to the volume; they cover the same area enclosed between the two surfaces so the effect is purely volumetric. In the first step, we looked at count rates in the two regions of backgrounds dominated by  $^{14}\text{C}$  and  $^{11}\text{C}$  that are presented in Figures 4.57 and 4.58, respectively. The rates behave as expected and we also notice that the external backgrounds are more dominant in the higher energy region of  $^{11}\text{C}$ , which agrees with the spectral shape distribution of external gammas. Their detailed rates are presented in Figures 4.59 and 4.60, where we observe that the region of the full-energy peak is not penetrating the volume as expected since its contribution is only dominant in the initial region, closest to the IV, of the active scintillator. The most important part of the check was related to the distribution in our energy region of interest, the  $^7\text{Be}$  and  $^7\text{Be}$ -valley dominated by  $^{210}\text{Bi}$ . In Figure 4.61, we do not show the contribution from the outer-most shell since its rate was too high due to the presence of the surface contamination of the inner vessel. We can observe a small oscillation of background in Shell II (0.25-0.50 m), with a peak around December 2008. In order to determine whether it is coming from the neutrino signal, we compared it with the same shell of a signal-free range in Figure 4.62- the patterns are very similar. Additionally, we notice that the increasing count rate of  $^{210}\text{Bi}$  concentration, verified also with the spectral fit, can be observed only in the inner-most shell (V), indicated in Yellow in Figure 4.61. This could confirm that the contamination was in fact coming from the outer regions of the IV to the center, originally free of  $^{210}\text{Bi}$ .

### 4.3 Spectral Fit Stability

In this section we will show that the spectral fit results agree with the count rates for backgrounds and remain stable over the course of three years of Phase I. At this point, we are not interested in the external factors, and we would like to avoid the impact of the changing vessel or other operations as much as possible. For this reason, we concentrate on analyzing only the bulk volume of the detector, using the standard  ${}^7\text{Be}$  fiducial volume as used for the flux analysis ( $R=3.021\text{ m}$ ,  $|z|=1.67\text{ m}$ ). In the tables below, we present the fit results on merged six- and twelve-month long sub-periods in a way that any expected annual modulation of the solar neutrino signal would cancel out.

**Table 4.3:** *Table for one-year long periods, presenting comparison of the spectral fit with rates for  ${}^7\text{Be}$ ,  ${}^{85}\text{Kr}$ , and  ${}^{210}\text{Bi}$ . Total values for the fit are shown in the last column. Additionally, the component count rates were normalized with respect to the last row in the table (Total) of the spectral sum.*

Period	counts/(day x 100 ton)	${}^7\text{Be}$	${}^{85}\text{Kr}$	${}^{210}\text{Bi}$	Total
I	84.3	52.1±3	26.7±4.1	11.7±2.8	90.5
II	112.1	45.2±3.3	27.5±5.6	34.6±4.3	107.3
III	134.8	49.7±3.7	20±7.5	61.3±6.5	131
All	110.5	48.7±2	24.1±3.1	37.7±2.4	110.5

**Table 4.4:** *Similar table to 4.3, however presenting the results in a finer binning of six-months.*

Period	counts/(day x 100 ton)	${}^7\text{Be}$	${}^{85}\text{Kr}$	${}^{210}\text{Bi}$	Total
I	78.7	52.2±4.1	29.5±5.8	7.5±3.2	89.2
II	91.1	48.4±4.1	29.3±6	15.4±4.4	93.1
III	108.7	46.2±4.2	17.4±6.8	39±6.1	102.6
IV	132.1	43.5±4.9	31.2±8	44.3±6.7	119
V	130.7	44.6±5.7	37±10	52.1±8.3	133.7
VI	140.3	56.8±5.5	11±12	69.3±8.5	137.1
All	110.5	48.7±2	24.1±3.1	37.7±2.4	110.5

From Tables 4.3, and 4.4, it is clear that the values achieved from the fit are in good agreement with the count rates. Stable  ${}^7\text{Be}$ , and exponentially building up  ${}^{210}\text{Bi}$ , starting at zero, are

observed within the limits of uncertainty according to the expectations. We note that for an easier comparison, the component count rates in the above tables were normalized to the total number from the spectral fit. It is because the raw spectral rates contain additional background components that could not be eliminated. This however, does not affect the result of the overall trend of the dominant contributors.

Finally, we also show the results for other fit parameters that can be used to investigate the overall stability and performance of the detector that would not be revealed with the background scan. We take the same one-year- and six-month-long periods as before, and we look at the Light-Yield,  $^{11}\text{C}$ ,  $q\text{-}^{11}\text{C}$ : the  $^{11}\text{C}$  starting point, and  $\chi^2$  that this time were the only parameters left free in the fit.

**Table 4.5:** *Table for one-year long periods with a comparison of the stability fit parameters.*

Period	Light Yield	$^{11}\text{C}$	$q\text{-}^{11}\text{C}$	$\chi^2/\text{NDF}$
I	499.2 $\pm$ 3.5	26.87 $\pm$ 0.67	0.8877	81/94
II	506.8 $\pm$ 5.2	27.58 $\pm$ 0.69	0.877	129/94
III	500.6 $\pm$ 6.5	28.35 $\pm$ 0.72	0.882	128/94
All	501.7 $\pm$ 2.8	27.88 $\pm$ 0.4	0.8831	93/94

**Table 4.6:** *Similar table to 4.5 but in six-month binning.*

Period	Light Yield	$^{11}\text{C}$	$q\text{-}^{11}\text{C}$	$\chi^2/\text{NDF}$
I	498.7 $\pm$ 4.5	26.06 $\pm$ 0.85	0.887	100/94
II	503.4 $\pm$ 5.8	26.65 $\pm$ 0.86	0.876	89/94
III	499.4 $\pm$ 6.9	29.5 $\pm$ 1	0.898	105/94
IV	509.1 $\pm$ 7.1	24.9 $\pm$ 0.97	0.88	120/94
V	510.6 $\pm$ 9.4	31.6 $\pm$ 1.1	0.856	120/94
VI	491.6 $\pm$ 7.4	23.9 $\pm$ 1	0.899	5200/94
ALL	501.7 $\pm$ 2.8	27.88 $\pm$ 0.4	0.8831	93/94

In this case the results were satisfactory, all the parameters are in very good agreement. This information was important to obtain since in the final step of the signal modulation analysis, we will once again use the spectral fit to verify merged data into sub-periods around January and December.

# Chapter 5

## Methodology and Approach

### 5.1 Analysis Approach

#### Lomb-Scargle

Spectral-fit analysis is one way of determining the overall rate of the spectral components. However, when searching for the annual signal modulation we are constrained by a minimal length of a sub-period for the fit. Having only three-years of data available leaves a non-sufficient amount of statistics for independent spectral-fitting. On the other hand if we can only use spectral-fitting to determine the overall composition and confirm the stability of, in this case, background components of the spectrum, there is in fact no need for the spectral-fit anymore. In an ideal case of an oscillating signal, when all the present backgrounds are stable in time, spectral-fit only introduces unnecessary additional uncertainty into the measurement. We proceed with rate analysis by dividing the data into 10-day-long bins in the energy regions as listed in Table 5.1 and presented in Figure 5.1. Such choice of binning was justified with a Monte-Carlo simulation where we have checked that the significance of

a Lomb-Scargle peak does not change drastically with a bin size between 1-14 days.

**Table 5.1:** *Spectral regions of interest (also indicated with various colored regions in Fig. 5.1).*

Region	Window [charge]
${}^7\text{Be}$ -Line	[105; 380]
${}^7\text{Be}$ -Valley	[390; 450]
${}^{11}\text{C}$	[600; 800]
Ext- ${}^{214}\text{Bi}$	[1000; 1280]
Ext- ${}^{208}\text{Tl}$	[1280; 1450]

In the case of the  ${}^7\text{Be}$  events, we are already experiencing low statistics due to the natural interaction rate in Borexino, thus it is desirable to try to increase the signal coverage range to as broad a window as possible. The first step was obviously to remove the  $\alpha$  particles mainly from  ${}^{210}\text{Po}$  which normally would give a tail extending to even 250 npe, significantly limiting the available data in the  ${}^7\text{Be}$  shoulder (below 15 counts/(day x 100 ton) for a [280;380] npe window). With the Polonium peak removed, we were able to go as low as to 105 npe resulting in an average count rate of about 26.84 counts/(day x 100 ton), accounting for the efficiency of cuts and DAQ threshold.

Continuous functional forms or, as in this case, discrete time signal variations can be analyzed in a variety of ways. Mathematics gives us tools that allow one to either study the evolution of the signal in time, assuming all the real values are known, or in the frequency space after certain transformations (Fourier series, Fourier, Laplace, Wavelet, and Z transforms). A typical discrete signal is depicted in Figure 5.2. Its periodicity can be easily transformed and interpreted into the frequency domain, as shown in Figure 5.3. There are also multiple tools available for analysis in a 2-dimensional space, the so called Time-Frequency Representation, studying time and frequency domains simultaneously with short-time Fourier transform (STFT), being the basic available transform. Nevertheless, no matter how sophisticated the tools, the detector's stable response will still need to be taken into account.

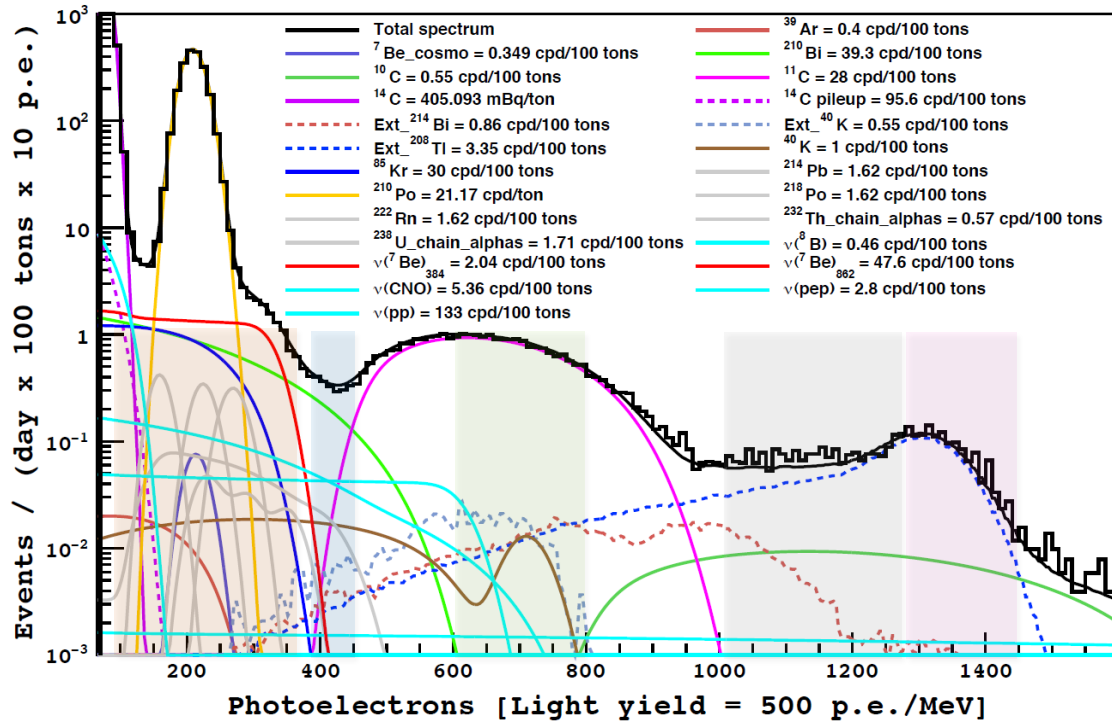


**Figure 5.1:** Selection of the Spectral Regions<sup>1</sup> according to Table 5.1. Three significant points of interest are shown: -Annual Signal Variation, -Valley, Major Backgrounds, -Muon-Induced Seasonal Variation. Figure from [96].

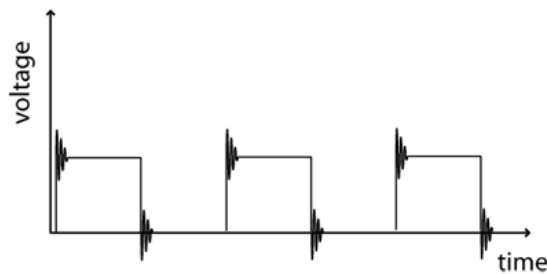


**Figure 5.2:** An electrical signal in the Time-domain. Because it is periodic, its Frequency transformation can be plotted on the power spectrum.

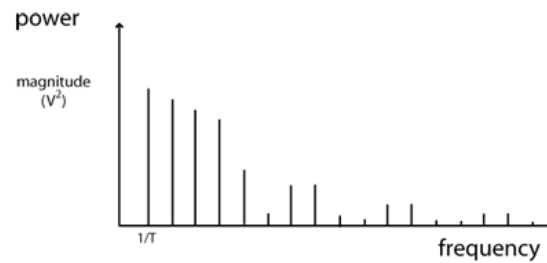


**Figure 5.3:** Classic Power Spectrum after transformation from the Time-domain. Representation of the periodic signal in the Frequency-domain.

**Table 5.2:** Fraction of  $\beta$  spectra in the  ${}^7\text{Be}$  window according to Fig. 5.1 in the units of photoelectrons and counts/day-100t.

$\beta$ -source <sub>(cpd/100t)</sub>	105-380	210-360	390-450	600-800
${}^{14}\text{C}_{(3.5E06)}$	0.00	0.00	0.00	0.00
${}^{14}\text{C-pileup}_{(95)}$	1.14	0.00	0.00	0.00
${}^{210}\text{Bi}_{(42)}$	23.12	8.27	0.37	0.00
${}^{85}\text{Kr}_{(29)}$	16.22	4.13	0.00	0.00
${}^{11}\text{C}_{(28)}$	0.00	0.00	5.15	5.75
${}^{210}\text{Po}_{(2100)}$	2099.97	662.09	0.00	0.00
${}^7\text{Be}^*_{(2.04)}$	0.00	0.00	0.00	0.00
${}^7\text{Be}_{(46)}$	30.57	14.82	0.00	0.00
${}^{13}\text{N}_{(2.36)}$	1.02	0.34	0.00	0.00
${}^{15}\text{O}_{(3.36)}$	1.48	0.69	0.12	0.00
$pp_{(133)}$	5.17	0.00	0.00	0.00
$pep_{(2.8)}$	1.60	0.86	0.32	0.00
${}^8\text{B}_{(0.46)}$	0.09	0.05	0.02	0.06
S/B	39.93 / 2141.70	16.76 / 675.03	0.47 / 5.52	0.06 / 5.75

A problem making the above listed tools unsuitable for our analysis is the fact that Borexino data is distributed irregularly and contains gaps. Even though we tried to keep the duty cycle as high as possible, it was never going to be 100%. Even if using considered data being taken on a daily basis, its collection is scattered around the day randomly. Some days need to be completely excluded due to maintenance or other operations. The erratic data acquisition requires use of a weighted-lifetime of the detector. Further details regarding unstable background and data selection and its quality will be discussed in Section 5.2.

## Time-Domain

The time domain is the most commonly used representation of signal evolution, for instance in electronics. Oscilloscopes for example, use plots of either voltage or current as a function of time. In the case of our modulated signal, its time dependence would appear as a sinusoidal variation as described in detail in Section 2.4. For this approach we use as input, data

divided into time bins for various species as defined in Table 5.1 with associated horizontal as well as vertical error bars. By the means of an analytical fit we attempted to determine the oscillation parameters, such as the amplitude  $\epsilon$ , period  $T$ , and phase  $\phi$ . Such an approach, even though revealing a convincing signature of the expected seasonal variation, might actually be coming from a non-physical source. However, by a transformation into the frequency domain we could also perform further studies of the significance of any oscillatory patterns identified in the signal.

### Frequency-Domain

Often applied in other fields of statistics or engineering, transformation from time to the frequency domain is a method of studying mathematical functions or signals with respect to frequency, rather than time. It becomes helpful when searching for periodicities since it represents the density evolution of the signal in a given frequency band. The Fast Fourier Transform (FFT) is the most popular and efficient algorithm for calculating the Discrete Fourier Transform (DFT), considered by some the most important numerical algorithm of mathematics. In principle, the mechanism of any transformation is based on decomposition of the signal in time into constituent frequencies. Normally, the periodicities would be determined by searching for any prominent peaks in the FFT periodograms. But in case of the Fourier Transform only complete, and evenly distributed data samples can be analyzed. FFT also lacks the possibility to determine the statistical significance of the identified periodicities. A standard method to analyze non-uniformly spaced data samples, extracting the statistical significance of each frequency component was developed by Nicholas R. Lomb and Jeffrey D. Scargle [98], [99]. The method was later referred to as the Lomb-Scargle frequency study. It is based on a least-square fit of sinusoids to data samples in order to identify the probability distribution of the height of the highest peak in a periodogram. Such probability

distribution can be shown to follow an exponential shape, when properly normalized through a division over the total variance of the data. As a result, the smaller the p-value the more probable it is that the identified peak was physical. An example of an ideal sinusoidal oscillation of the solar neutrino signal is presented in Figure 5.4 for which the derived p-value for the identified period of 1 year, equals "0" as expected.

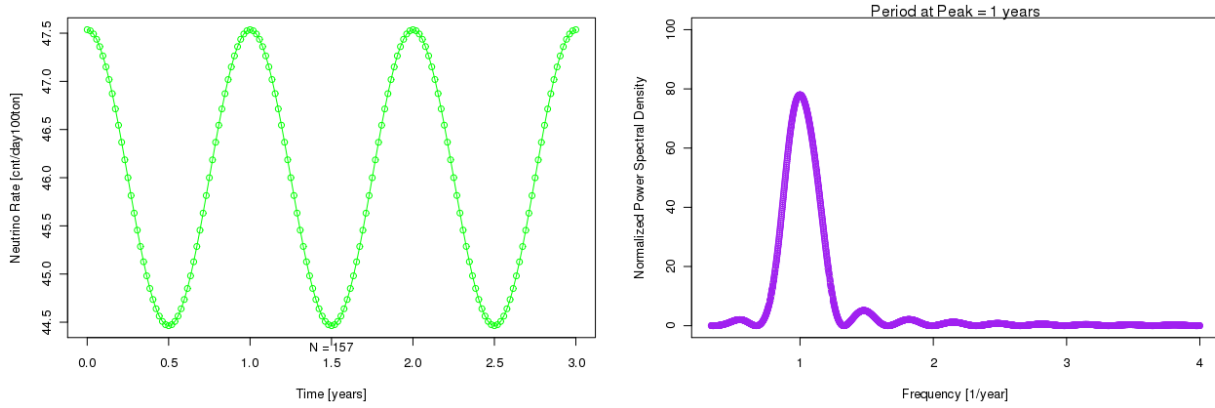


**Figure 5.4:** *Lomb-Scargle Periodogram for an ideal, evenly distributed data-set with a signal variation as defined in Eq. 6.1 Sec. 2.4*

Here we present the Lomb-Scargle formalism, with the Normalized Spectral Power Density (SPD), also known as the L-S periodogram derived for  $N$  data points ( $X_1 \dots X_j \dots X_N$ ) at specific times  $t_j$ . SPD is evaluated for  $M$  test angular frequencies  $\omega$  and plotted with respect to frequencies  $f$ .

$$SPD(f) = \frac{1}{2\sigma^2} \left\{ \frac{\left[ \sum_j (X_j - \bar{X}) \cos \omega(t_j - \tau) \right]^2}{\sum_j \cos^2 \omega(t_j - \tau)} + \frac{\left[ \sum_j (X_j - \bar{X}) \sin \omega(t_j - \tau) \right]^2}{\sum_j \sin^2 \omega(t_j - \tau)} \right\}; \quad (5.1)$$

Where  $\bar{X}$ , and  $\sigma$  are respectively *mean*, and *variance* of the data, and  $\tau$  is the frequency-dependent time offset:

$$\bar{X} = \frac{X_1 + X_2 + X_3 + X_N}{N} = \frac{1}{N} \sum_{j=1}^N X_j, \quad (5.2)$$

$$\sigma^2 = \frac{1}{N-1} \sum_{j=1}^N (X_j - \bar{X})^2; \quad (5.3)$$

$$\tan 2\omega\tau = \frac{\sum_j \sin 2\omega t_j}{\sum_j \cos 2\omega t_j}. \quad (5.4)$$

Estimation of the peak's statistical significance based on the calculated periodograms is mainly dependent on the number of the scanned test frequencies  $M$ . We need to be able to predict this number first, since scanning for  $M > N_{independent}$  does not give us any new information on the statistical significance of the result, where  $N_{independent}$  is the number of independent frequencies that we scan. From Horne and Baliunas [100] we take the least-square root based estimation on  $N_{independent}$ :  $N_{independent} \approx -6.362 + 1.193N + 0098N^2$ . Now, the probability for a given SPD, that there is no other peak of greater value is given by:

$$[1e^{-z}]^{N_{independent}} \quad (5.5)$$

And accordingly, the dashed lines of the significance levels  $z$  depicted in each L-S periodogram of this analysis are defined as

$$z = -\ln \left[ 1 - (1 - p)^{1/N_{independent}} \right], p = P(> z) = 1 - [1e^{-z}]^{N_{independent}}; \quad (5.6)$$

It is reasonable to expect that in many cases the data will be corrupted or missing due to external operations, maintenance or regular activities. Should the data collected from such periods eventually be proven to satisfy our quality requirements and contribute to the overall statistics, its resulting time variation might in a significant manner affect our sensitivity to signal variations that we are trying to identify. It was thus decided that certain runs or

periods would be removed from analysis, and the resulting benefit of stability overwhelms the loss of statistics by a couple factors. Further details on data selection will be outlined in the next section. However, we have shown using an artificially reduced data sample with unevenly distributed runs that the Long-Scargle transformation remains a powerful tool in identification of a simulated periodic signal. For this exercise, not only the standard runs<sup>2</sup>, but also 65% of the rest of the data were randomly excluded from a sample for this exercise. Results are presented in Figure 5.5. Of course, the situation will not be so good in the case of Borexino data since we will not only analyze a non-ideal oscillation but also the signal will be hidden in a background higher by a factor of two or three. In the ideal case, the peak at 1-year was still identified however, with a lower by a factor of four SPD.

In this analysis we also use the unweighted version of Lomb-Scargle which does take into account asymmetries in error bars. In the case of Borexino data the effect is insignificant. Based on Monte-Carlo simulations the results of weighted and unweighted LS are consistent to within 5% in terms of identified period and below 0.5% for significance of the highest peak in the periodogram.

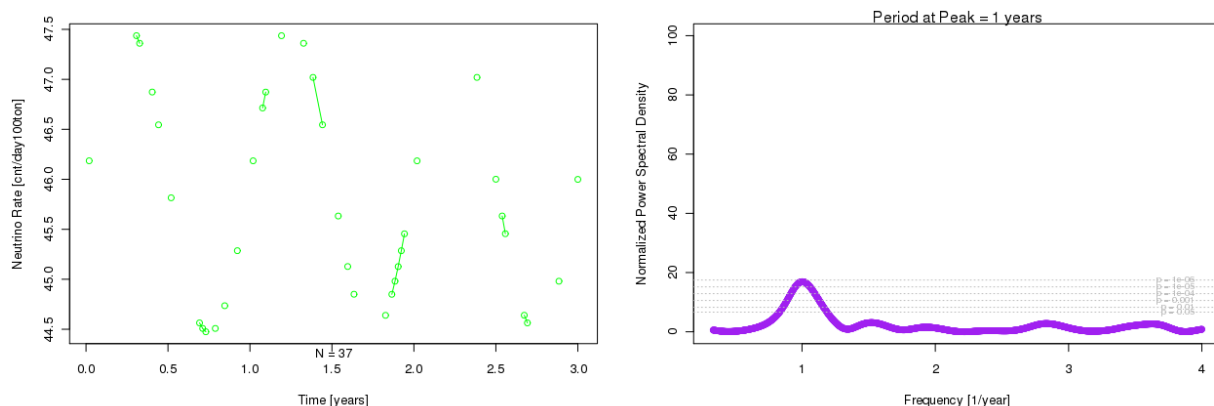


**Figure 5.5:** *Lomb-Scargle Periodogram from Fig. 5.4 after randomly removing 75% of data points. As a result, the periodogram still indicates a significant peak at 1-year period.*

<sup>2</sup>13 weeks out of 3 years of short, noisy, or corrupted runs were decided to be excluded

## LS Monte-Carlo

For the Monte-Carlo estimation of the Lomb-Scargle sensitivity, we performed a simulation of  $10^4$  sample modulations in order to test whether the amplitude is pronounced enough on top of the realistic Borexino background. For each of the simulations, we calculated the SPD periodograms and extracted the power at the expected period of one year. In the next step, we simulated the same number of white-noise samples, i.e. containing no sinusoidal modulation. If, for example, we set the detection threshold to 99.7%, which corresponds to a  $3\sigma$  level of discovery potential, and we find that the whole signal SPD spectrum falls into this region, we would claim a 100% probability of a  $3\sigma$  discovery. An example of such a situation is presented in Figure 5.6.

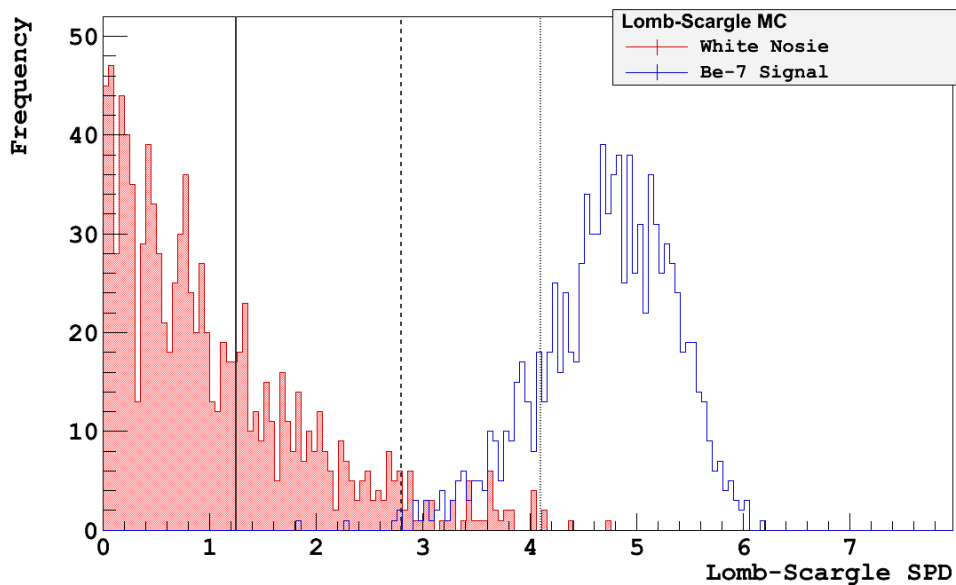


**Figure 5.6:** A Monte-Carlo simulation for an ideal sample of  $10^4$  Lomb-Scargle periodograms with a 100% of the detected signal in the  $1\sigma$ , 99.7% in  $2\sigma$ , and 85.3% in the  $3\sigma$  confidence level region.

We have also tested the sensitivity of the Lomb-Scargle method to the binning size. We

ran a more realistic sample than in the case of Figure 5.6, where the level of backgrounds is comparable to Phase I of the Borexino data taking period. In Figures 5.7 and 5.8, we show a comparison between two very different binning, 1- and 60-day accordingly. The results of detection sensitivity are shown in Table 5.3. We conclude that the choice of binning does not have as drastic an impact on the sensitivity as we had originally anticipated. As a result, we will select 10-day binning for the final study of the Borexino data with Lomb-Scargle and 60-day binning for the sinusoidal fitting. The longer binning for the fit is a reasonable guess rather than a calculated value. Such a choice will guarantee a balance between reasonable statistics per bin, and visible modulation, so that  $\text{bin-size} < \text{period}$ .

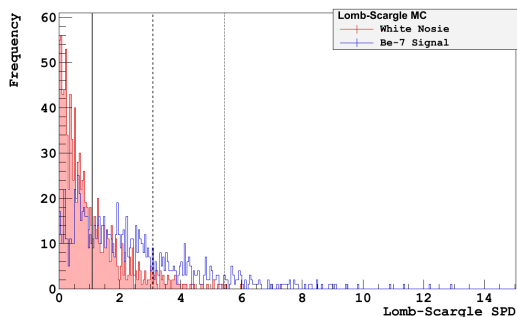


**Figure 5.7:** *Lomb-Scargle Monte-Carlo simulation for the 1-day binning.*

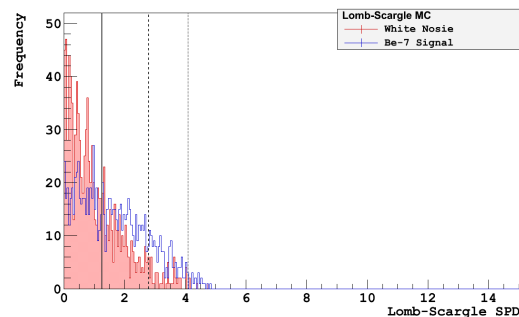


**Figure 5.8:** *Lomb-Scargle Monte-Carlo simulation for the 60-day binning.*

**Table 5.3:** *Detection efficiency with a Lomb-Scargle method for the two extreme binning cases, 1-day and 60-day, assuming realistic background levels in Borexino.*

Confidence Level	Det. Eff. 1-day bin	Det. Eff. 60-day bin
$1\sigma$	69.00%	58.00%
$2\sigma$	26.10%	17.30%
$3\sigma$	7.60%	1.90%

Further sensitivity study with Monte-Carlo simulations, appropriate to each presented result, will be demonstrated in the next section along with the Lomb-Scargle analysis for the data in Phase I and II (Phase II covers the data collected up to the last week of September, 2012).

## 5.2 Event Selection

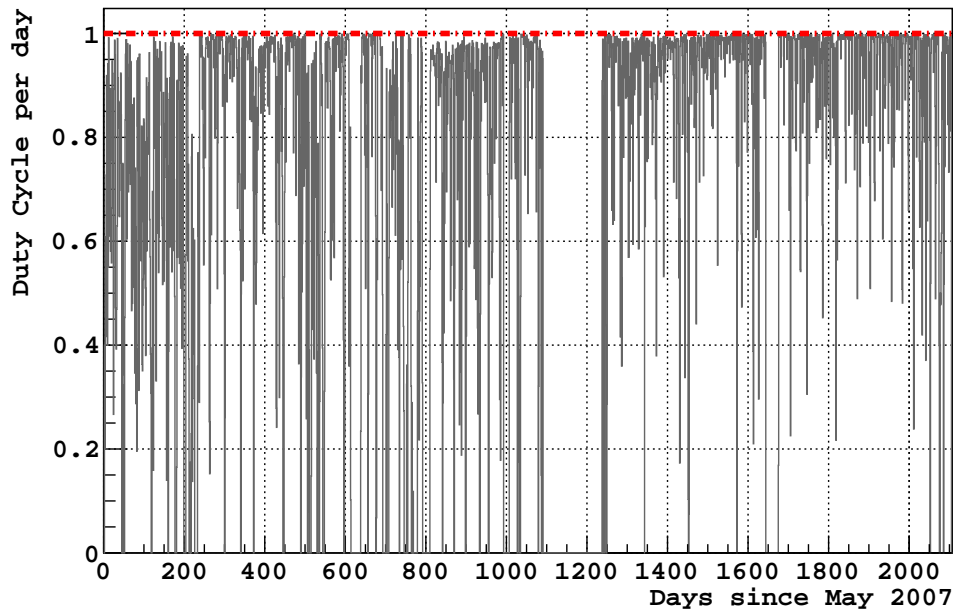


**Figure 5.9:** *Duty cycle per day in the data taking phase of Borexino between May 13, 2007 and Feb 17, 2010. As anticipated, the efficiency was gradually increasing and reached a stable level of about 90% after first year of operation.*

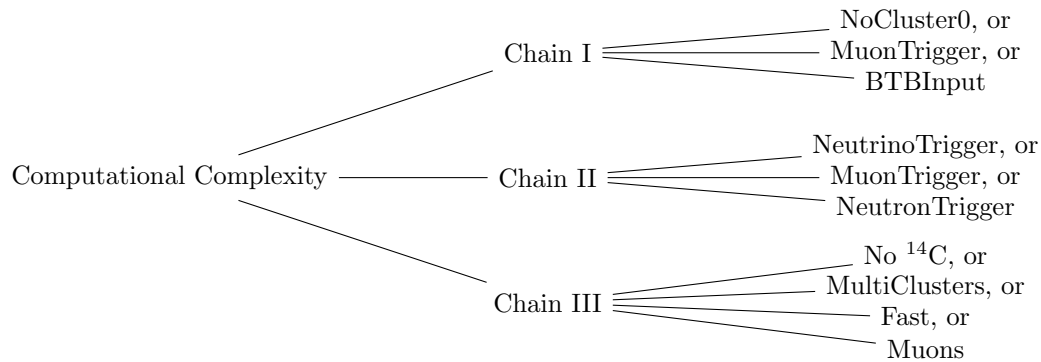
The analysis presented in this work relies heavily on the identical collection of software cuts as used for the  ${}^7\text{Be}$  flux measurement ([2], [25], [26]). Specific differences that could affect these cuts in the enlarged fiducial volume have already been studied in the previous chapter, regarding the stability conditions. In this section, we will present the original cuts as well as modifications that were necessary for the annual flux modulation study, namely, the new fiducial volume and the new method of eliminating the  $\alpha$  events based on statistical subtraction.

Figure 5.9 shows the duty cycle in Borexino, i.e. simply the efficiency of data collection on a daily basis. Notice how in the initial phase the data taking was suffering from multiple operations and unexpected crashes of the DAQ software. The true improvement can only be

seen in the second phase of data-taking; starting around day 1200, when the average daily duty cycle reaches over 90% efficiency.

## Low Level Cuts

We begin by listing the three fundamental filtering chains used in the generation of the DST files that are later implemented into the filtering program that performs a refined selection of events for a given topic.



Only those events that satisfy these chain cuts will be written to the output ROOT file. DST's are grouped into one-week long sets of runs, and usually take less disk space (by a factor of three to five) than the raw files would. An example of a spectrum from one of the DST files in comparison with the original data is plotted in Fig. 5.10.

It is clear how significantly the number of events was reduced, making the file very lightweight. The region of  $\sim 100$  npe (about 200 keV) and below was affected the most, but the fine noise reduction in the higher energy region is also present but not as noticeable. Presented below is a list of DST chains with a detailed definition of the cuts:

**Chain I**, events identified either in the inner or outer detectors:

- NoCluster0: empty clusters are removed

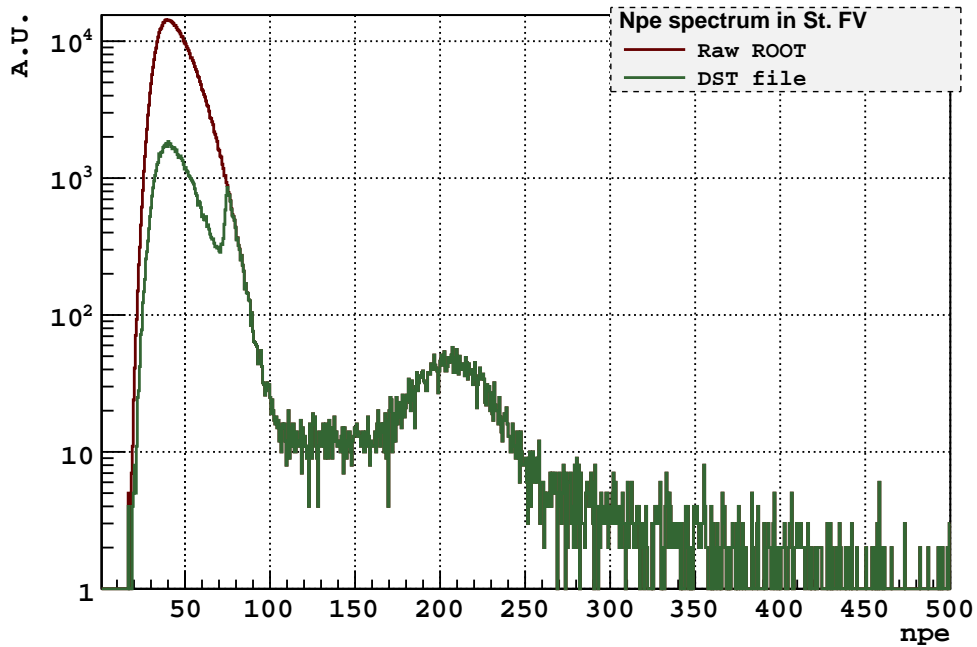


**Figure 5.10:** Comparison of a raw ROOT-file, run 13992, with low-level cuts in a DST-file for the week of Aug-08 2010. Standard mach4 charge variable was used. The reduction is visible in the  $^{14}\text{C}$  region.

- MuonTrigger: only events with `trigger type = 2` are kept
- BTBInput: only events with `btb_inputs & 4` are kept

**Chain II**, even with inner, outer or neutron triggers (`trigger type 1,2 or 128`):

- NeutrinoTrigger: only events with `trigger type = 1` are kept
- NeutronTrigger: only events with `trigger type = 128` are kept

**Chain III**, an event is valid if it passes at least one of the three:

- No  $^{14}\text{C}$ : only events with `charge > 75` or `nhits > 75` are kept
- MultiClusters: only events with  $\geq 1$  clusters are kept
- Fast: keeps sequence of events with `dt` between events of  $< 2$  ms

The muon filter has been applied to the internal muon identification in order to use the most updated muon selection criteria, as well as external muons, and CNGS muons. For every muon, every event in the subsequent 300 ms is identified as a daughter muon and kept for future analysis (if not empty).

## High Level Cuts

In most of the Borexino analyses, e.g.  ${}^7\text{Be}$   $\nu$ ,  ${}^7\text{Be}$  day–night, about fifteen standard cuts are used to tune the spectrum, removing muons, all electronic noise, and any kind of removable background in the  ${}^7\text{Be}$  window. Two of the most effective cuts applied in order to achieve a satisfactory signal-to-background ratio are cuts #8 and #9, as listed below. For the precision measurement of the  ${}^7\text{Be}$  flux, the radial reduction of the FV down to  $R=3.021$  m eliminates almost all of the background related to the nylon vessel as well as the external Gammas (see Figure 5.11). The additional  $z$ -cut at  $\pm 1.67$  m, on the other hand, was applied in a more conservative manner, and it was driven by the presence of the  ${}^{40}\text{K}$  background in the nylon end-caps that support the inner vessel of the Borexino internal structure. Optionally, a statistical subtraction of  $\alpha$  events may be applied. Complete results of both procedures can be seen in Figure 5.11, and here we list the basic set of the analysis cuts, a more detailed description can be found in [96] (page 211).

As one notices, for the consecutive reduction of background events presented in Figure 5.11 (cuts 1, 8, 16 and additionally the statistical subtraction of  $\alpha$  events), the effect is most significant in the  ${}^7\text{Be}$  shoulder region and above. Almost no change in the  ${}^{14}\text{C}$  range is visible,  $\lesssim 145$  npe. There is, in fact, no evident technique for tagging the  ${}^{14}\text{C}$  and pile-up background events. The only solution for a potential study of the  $pp$  neutrinos in this region, is a calibration with a dissolved  ${}^{14}\text{CO}_2$  gas that is planned after the end of Phase II of the solar campaign in Borexino.

1. Empty cluster events and *Mach4* vs *Echidna* consistency
2. Search for sequences of fast coincidences (2 ms) in 1.5 m radius
3. Selection of only trigger type = 1 (the neutrino trigger)
4. Removal of multi cluster events
5. Verification of the cluster start-time in a trigger
6. Drop crate noise events, i.e. with more than 75% of their hits in one electronics rack
7. Radial cut at  $R=3.021$  m, in this work changed to a vessel-shape dependent cut
8. Z cut at  $|1.67|$  m, here changed a narrow cut only around the end-caps
9. Geometrical uniformity check of the scintillation light emission (using *Mach4*'s variables)
10. Spherical harmonics check of the scintillation light emission using an *Echidna* variable
11. Number of peaks in the hit-time profile, used in the reduction of the pile-up events
12. Verification of the reconstructed charge variable by comparing it with the number of hit PMTs
13. Removal of *Mach4*'s strange events, events that in *Echidna* are very close to zero
14.  $^{214}\text{Pb}$  subtraction for 3 h and within 80 cm of  $^{214}\text{BiPo}$  coincidence (later referred to as simply the *Radon* cut)
15. Reduction of  $^{11}\text{C}$ , tagged with an independent filter<sup>3</sup>

---

<sup>3</sup>This cut will not be presented in this work as its application is mainly for the *pep* and *CNO* analysis, a detailed discussion on this subject can be found in [101].

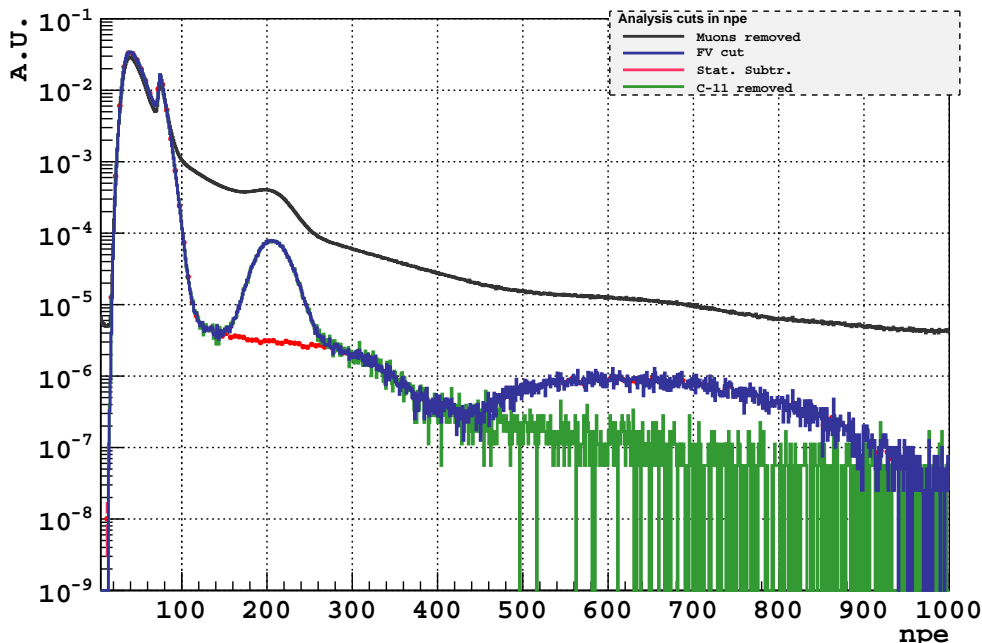


**Figure 5.11:** Comparison of the raw photoelectron spectrum (Gray), after applying the fiducial volume cut at  $R=3.021$  m (dark Blue), statistical subtraction (Red), and finally the 91% reduction in  $^{11}\text{C}$  count-rate (Green).

## New Analysis Cuts

**Fiducial Volume** The number of neutrino events collected per day per 100 tons in Borexino is already relatively low, on the order of 50<sup>4</sup>. As a result, in the study of the annual modulation signal, we will increase the collected statistics by enlarging the fiducial volume. For the first time in the Borexino analysis, we will also use the inner vessel shape information obtained from the weekly scans of the nylon background. This information was critical since for a pure count-rate study as presented here, this gave us the opportunity to multiply the statistics by a factor of  $\sim 2$ . We would also like to underline, that in the most recent results published with the Borexino data, the *pep* and *CNO* measurement ([30]), the fiducial

<sup>4</sup>Excluding the *pp* events in the low energy region.

volume cut was fixed due to the background contribution of the changing vessel shape, and was set to only 71.30 tons of the target scintillator mass. As we will show in this section, the average mass achieved with the new approach will deliver  $141.83 \pm 0.55$  tons on average, Table 5.4 summarizes different fiducial volumes used in the Borexino solar neutrino analyses in Phase I.

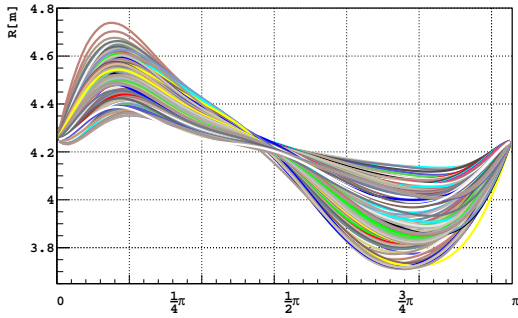


**Figure 5.12:** Shapes of the inner vessel obtained from an elliptical fit to background events in the nylon during Phase I.

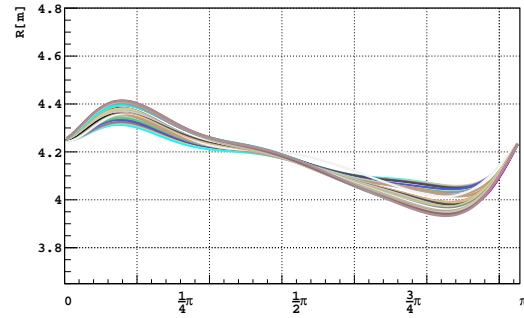


**Figure 5.13:** Shapes of the IV in Phase II can be compared with Phase I; the improvement in stability is very clear.

**Table 5.4:** Definition of the fiducial volumes used in the different solar neutrino analyses.

Analysis	$R_{\max}$ [m]	$z_{\min}$ [m]	$z_{\max}$ [m]	Volume [ $m^3$ ]	Mass [ton]	$N_e$ $\times 10^{31}$
${}^7\text{Be}$	3.021	-1.67	1.67	86.01	75.47	2.835
<i>pep-CNO</i>	2.8	-1.8	2.2	81.26	71.30	2.679
${}^7\text{Be}$ day-night <sub>asymmetry</sub>	3.3	-3.3	3.3	151.01	132.50	4.978
${}^7\text{Be}$ annual modulation (mean)				161.64	141.83	5.329

The mechanically unstable inner vessel was changing its position with respect to the detector as a result of difference in scintillator densities between the active volume and the buffer. The graphs of the radius vs  $\theta$  angle are presented in Figure 5.12 for the period of May 2007 to May 2010, and in Figure 5.13 for the second phase, the period between December 2011 and September 2012. For an increased and fixed fiducial volume this would result in a fluctuation of surface background coming from the nylon. As we introduced in Section

4.1, the information from the vessel position was used to define a  $\theta$ -dependent cut for the selection of events. Since the contribution of the external background during the period of the leak was becoming significant, we have chosen to use a larger distance from the vessel at the top, gradually decreasing towards the bottom of the IV. As a result, we divided the FV into three vertical regions of DVS values, as listed in Table 5.5 for Phase I and II.

**Table 5.5:** Definition of the fiducial volumes for the annual modulation study in Phase I and II.

$\theta$ [degrees]	DVS <sub>PhaseI</sub> [cm]	DVS <sub>PhaseII</sub> [cm]
0-60	100	75
60-120	80	75
120-180	60	75

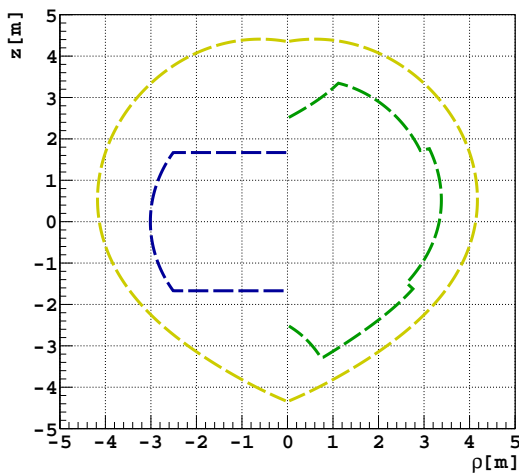


**Figure 5.14:** Phase I, Fiducial Volume cuts. Presented shape of the inner vessel as of May 03 2009. Yellow- the inner vessel shape, Blue- 75 tons, Green- 145 tons.

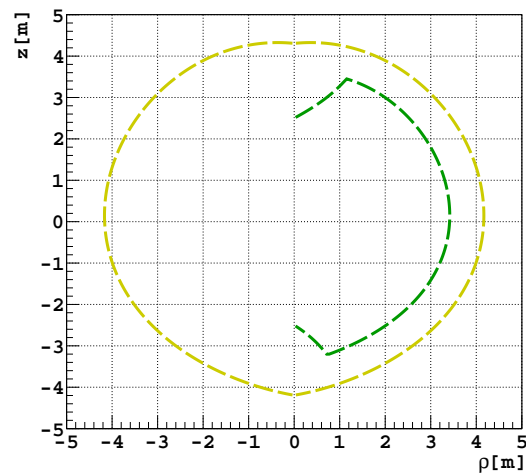


**Figure 5.15:** Phase II, Fiducial Volume cut. Presented shape of the inner vessel as of June 17 2012. Yellow- the inner vessel shape, Green- 145 tons.

Figures 5.14 and 5.15 graphically present the concept of the fiducial volume cuts in the two phases. The removal of the end-cap regions was a little more difficult to describe geometrically, as it was tuned visually using the cross-section plots of the  $^{40}\text{K}$  background. Since the contamination was more significant in the top, due to the presence of the nylon insertion

tube, the cut there is more conservative than in the bottom. Both the shapes and position of these cuts were chosen to be the same in Phase I and II. Figure 5.14 also includes the standard  ${}^7\text{Be}$  fiducial volume for comparison (marked in Blue).

**Reduction of  $\alpha$  Events** As mentioned in Section 5.2, the events were selected using all cuts required for the  ${}^7\text{Be}$  flux measurement with an exception for the statistical alpha-subtraction (or the soft-alpha cut- not discussed here) that was replaced by a stringent Gatti cut, removing all the alpha-like events at a cost of less than half of betas in the window of interest. The cut was defined in the Gatti space using statistical  $\alpha/\beta$  subtraction tools discussed in detail in [96]. The tools were applied in a similar way, taking the whole data set in the old and new FV. We performed a scan in 5 npe bins, defining the  $\alpha/\beta$  separation by fitting the Gatti parameter with a bi-Gaussian function. In the next step, for each bin we took the alpha fit to find cut  $3.4\sigma$  from its mean. The resulting cut as a function of npe was fit with an eighth-order polynomial function to obtain the shapes presented as Red lines in Figures 5.16 and 5.17. Such a conservative selection of the separation line guarantees no presence of  $\alpha$  events to better than 99.9%.

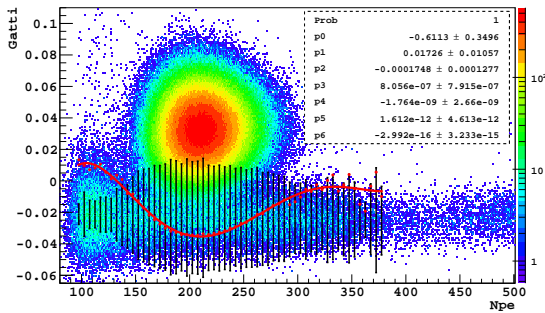


**Figure 5.16:** *Gatti parameter vs number of p.e in 75 tons. Red markers and a line indicate where the Gatti-cut was placed. Blue markers represent the mean position of the Beta-Gatti peak with bars of 99.9% beta count.*

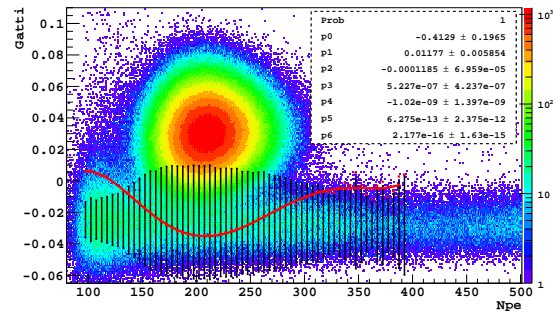


**Figure 5.17:** *Gatti parameter in 170 tons. Red markers and a line indicate where the Gatti-cut was placed. Black markers represent the mean position of the Beta-Gatti peak with bars of 99.9% beta count.*

As a test for the performance of the newly implemented cut, we plotted the charge energy spectra of the removed  $\alpha$ -dominated events, i.e. the positive, or the upper fraction of the Gatti parameter, shown in Figure 5.18 for the standard FV and in Figure 5.19 for the enlarged volume of 145 tons. As we can see, the peaks are very clean in both cases with a bit of imperfection in the  $^{14}\text{C}$ - $^{210}\text{Po}$  valley in Fig. 5.19. This effect might be related to some of the mis-reconstructed  $\alpha$ -events in the peripheral region of the active volume or close to the nylon vessel, but it does not pose any threat to the overall performance of the technique.

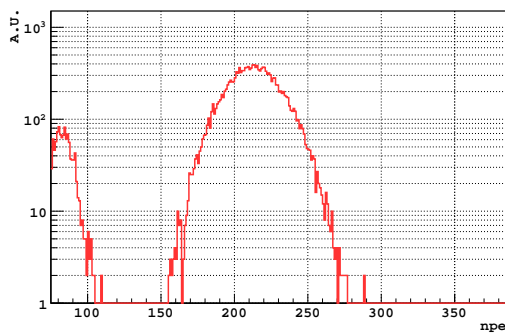


**Figure 5.18:** Energy spectrum of the removed  $\alpha$  events with the presented in Fig. 5.16 Gatti-cut.; FM: 75 tons.

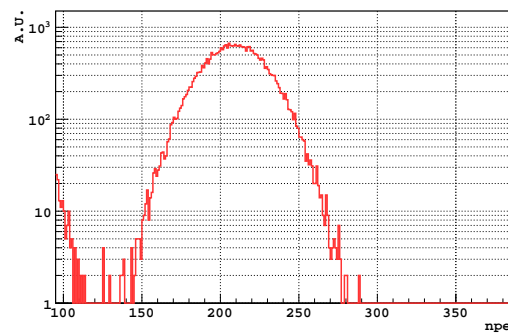


**Figure 5.19:** Energy spectrum of the removed  $\alpha$  events with the presented in Fig. 5.17 Gatti-cut.; FM: 145 tons.

Table 5.6 shows the resulting reduction in count-rates for specific species in 145 tons after applying the Gatti cut onto the Monte-Carlo simulated spectra. The loss of  $\beta$  events was estimated to be around 34% of the original concentration in the energy window of [95; 380] npe.

The Gatti cut defined and presented above was applied to all the data prepared in different phases, fiducial volumes and binning, whether 10- or 60-day long. This cut was taken into account in the Monte-Carlo simulations<sup>5</sup> for the Lomb-Scargle sensitivity study.

<sup>5</sup>A complete list of spectral fractions that survive our cuts is presented in Table 5.2 for all species and in Table 5.6 after the Gatti cut and only those species that were simulated with Monte-Carlo for the Borexino detector.

**Table 5.6:** Fractions of  $\beta$  events in the energy regions affected by the Gatti cut (FM: 145 tons.). Species available from a Monte-Carlo simulation in Borexino.

$\beta$ -line <sub>(cpd/145t)</sub>	105-380	210-360	390-450	600-800
$^{14}\text{C}$	0.00	0.00	0.00	0.00
$^{14}\text{C}_{pileup}$	0.12	0.00	0.00	0.00
$^{210}\text{Bi}$	21.84	7.39	0.54	0.00
$^{85}\text{Kr}$	14.08	2.70	0.00	0.00
$^{11}\text{C}$	0.00	0.00	7.46	8.34
$^{210}\text{Po}$	0.13	0.00	0.00	0.00
$^7\text{Be}^*$	0.01	0.00	0.00	0.00
$^7\text{Be}$	27.38	13.28	0.00	0.00
$^{13}\text{N}$	0.95	0.29	0.00	0.00
$^{15}\text{O}$	1.45	0.69	0.18	0.00
$pp$	7.40	0.00	0.00	0.00
$pep$	1.65	0.91	0.47	0.00
$^8\text{B}$	0.07	0.04	0.03	0.09
S/B	38.92 / 37.95	15.21 / 10.85	0.68 / 8.00	0.09 / 8.34

**Excluded Periods** All the standard and validated runs were considered for this analysis. However, due to stability requirements presented in the previous chapter, we were forced to additionally exclude three individual periods. They are all related to the increased concentration of  $^{222}\text{Rn}$  due to either initial filling or other operations, even though the applied  $^{214}\text{BiPo}$  tagging method was highly effective. Rejected periods are listed in Table 5.7.

**Table 5.7:** List of rejected periods from the analysis in both Phase I and II.

Date	Days since May 13, 2007	Reason
May 13 - Dec 16, 2007	0 - 217	$^{222}\text{Rn}$ , 16 ms gate
Feb 10 - Mar 8, 2009	639 - 665	DMP reduced from 5 to 3 g/l
Jun 1, - Jun 21, 2009	750 - 770	9000 l of PC+PPO added
May 8, '10 - Nov 9, '11	1091 - 1639	Maintenance and purification

We would like to underline that the longest period excluded from the analysis covered the first six initial months of the detector's operation. We notice in the plot presented earlier that the increased level of  $^{222}\text{Rn}$  after the initial filling was a few orders of magnitude higher than the average. All calibration campaigns have been excluded, as listed in Appendix B.

# Chapter 6

## Results

### 6.1 Phase I and II

After careful investigation of the most important backgrounds and verification of the stability of the detector in both phases, we can concentrate on the solar neutrino signal itself. Even though Phase I was rich in statistics, it also experienced difficult stages related to the calibration campaigns and scintillator refillings, that were affecting the conditions, not always in a predictable manner. A pause in the solar neutrino program was imposed by the purification campaign throughout the second half of 2010, the entirety of 2011 and most of 2012. Nevertheless, the investment of time and effort during these periods resulted in a magnificent reduction of the dominant backgrounds, namely,  $^{85}\text{Kr}$  and  $^{210}\text{Bi}$ .

In the following chapter we present results of the annual modulation investigation in Phase I using three techniques: the Lomb-Scargle search for periodicities, a sinusoidal fit to the rate distribution, and finally, the spectral fit results for the merged data into maximum, and minimum-flux sets. We will also present current analysis of Phase II, and we will draw a prediction for the sensitivity to the modulation for the planned running period of 28 months.

## Phase I

### Lomb-Scargle

**Monte-Carlo** We begin by a study of the sensitivity in Borexino to the annual modulation. Similarly to Section 5.1, we prepare a set of Monte-Carlo simulations for the 75- and 145-ton fiducial volumes. The data is represented realistically, i.e. the period, excluded runs, and binning was taken as in the final sample. Results of the count-rates are shown in Fig. 6.1 and 6.3, where the green curve corresponds to a sinusoidal modulation of  $\sim 7\%$  and a period of one year. The neutrino signal in each bin was simulated based on Table 5.6, following the trend with a Poissonian distribution. We would like to point out that only the signal was simulated based on the previously determined Monte-Carlo prediction of the data. The background events were assumed to be the remaining fraction of the total count. This is because some of the components were difficult to be accurately predicted for an enlarged fiducial cut, specifically the external gamma's. As one can observe, we have simulated flat-background distribution, corrected for any known trends. In order to preserve the actual statistical uncertainty in each bin, we performed the correction after the simulation of the events itself<sup>1</sup> Having prepared  $\sim 10^4$  of these samples, we applied Lomb-Scargle in order to determine the Spectral-Power-Density at 1 year. In Figures 6.6 and 6.8, for 75 and 145 tons respectively, the blue distribution corresponds to a white-noise case, whereas the red, to the expected annual modulation. Because of the increased statistics for the enlarged FV, our sensitivity almost doubles, but it is still not sufficient for a significant measurement. As we can read from the figures, the probability to obtain a  $3\sigma$  result in 75 and 145 tons is at the level of 3.85 and 11.68%, respectively. There is however, a reasonable ability to perform a consistency check at the level of  $1\sigma$  with 65.33 and 81.62%.

---

<sup>1</sup>This became important for the data analysis as we had identified an increasing  $^{210}\text{Bi}$  background that was subtracted from the sample.

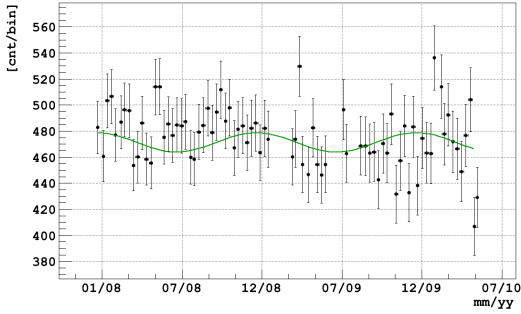


**Figure 6.1:** MC simulation of rate distribution with 10-day binning. Green curve represents the simulated signal. FM: 75 t.

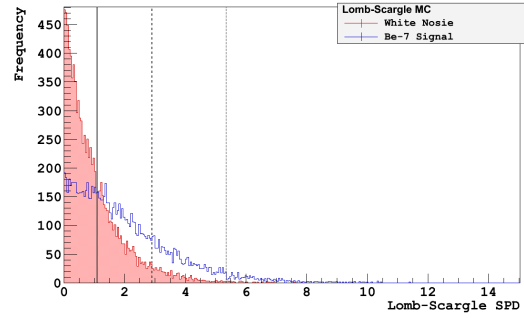


**Figure 6.2:** Lomb-Scargle power spectral sensitivity at 1, 2, 3 sigma with corresponding probability of 65.33, 23.42 and 3.85%.

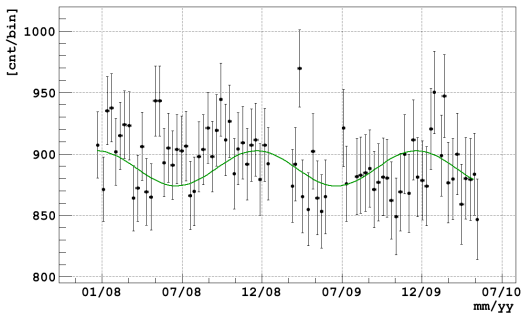


**Figure 6.3:** MC simulation of rate distribution with 10-day binning. Green curve represents the simulated signal. FM: 145 t.

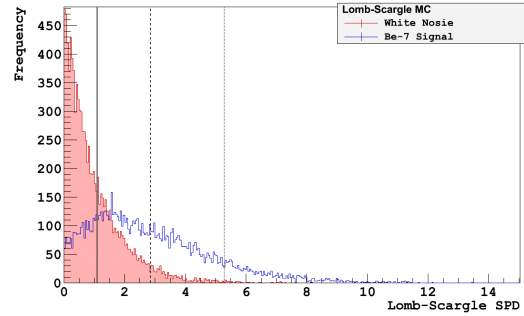


**Figure 6.4:** Lomb-Scargle power spectral sensitivity at 1, 2, 3 sigma with corresponding probability of 81.62, 43.54 and 11.68%.

**Data** In this paragraph we look again at the two fiducial volumes and the data divided into 10-day bins. The obtained count-rates are presented in Figures 6.5 and 6.7, where in orange we show the window of interest ([105; 380] npe), in blue, the  ${}^7\text{Be}$ -valley dominated by  ${}^{210}\text{Bi}$  (shifted up by a constant number in the plots for clarity), and finally in gray, the time distribution of high-energy gamma's (the so-called, external background). As expected, the count-rates for the fiducial mass of 145 tons increased, but by far the biggest increase can be seen for external events. We would like to note however, that even though the high-energy contribution is dominating now, the  ${}^7\text{Be}$ -window was not affected, reflecting a very precise definition of the fiducial volume. By comparing the two orange rates from Figures

6.5 and 6.7, we see that doubling the target mass; resulted in doubling the signal without a non-linear increase in the backgrounds. In the next step we focused on eliminating the exponential contribution from  $^{210}\text{Bi}$ .

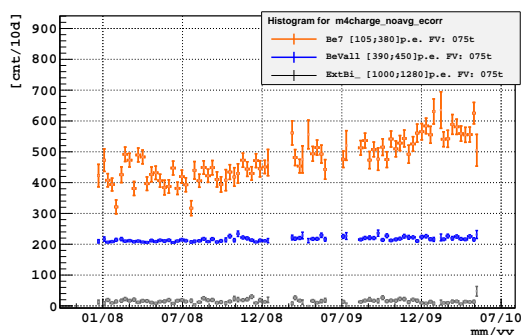


**Figure 6.5:** Rates distribution with 10-day binning.  $^7\text{Be}$ -valley count-rate was shifted by a const. number. FM: 75t.

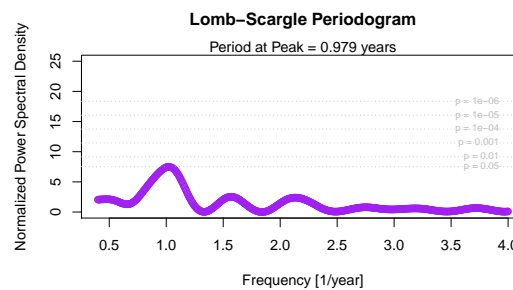


**Figure 6.6:** Lomb-Scargle periodogram from Fig. 6.5. A significant peak close to 1-year period was identified at SPD of 7.411.

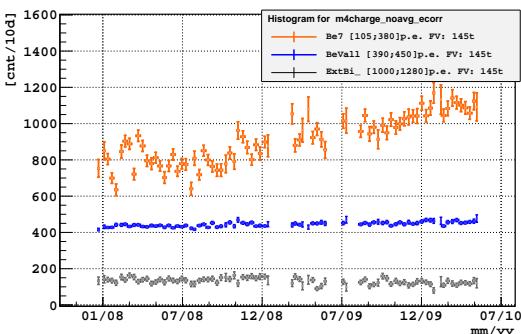


**Figure 6.7:** Rates distribution with 10-day binning.  $^7\text{Be}$ -valley count-rate was shifted by a const. number. FM: 145t.

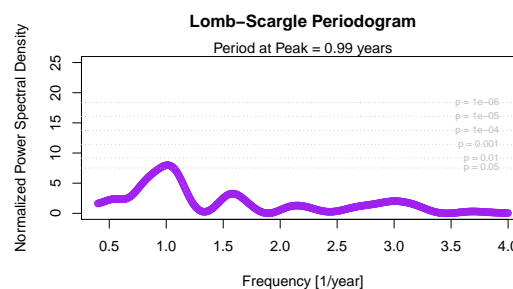


**Figure 6.8:** Lomb-Scargle periodogram from Fig. 6.7. A similar peak close to 1-year period was identified at SPD of 7.961.

This exponential trend, present in the figures above, poses a significant complication to our analysis since it not only causes Lomb-Scargle to misidentify the annual peak (as it was shown in Section 4.2) but, due to its unknown origin, leaves the exponential shape used upon to further debate. Nevertheless, we continue our analysis by implementing a background model of a pure exponential function. We would like to underline, however, that various functional

forms have been studied, of sinusoidal, step and combined shapes, leaving the exponential function the simplest, and in fact, giving the best results solution. Once we determine its shape by a standard,  $\chi^2$ -minimized fit, we subtracted it from from the actual data-set, bin by bin. One side effect of such operation on the future sinusoidal fitting routine, could be revealed in the  $\chi^2$  minimization where the number of events in the numerator would be reduced due to the implemented correction. This would result in an underestimation of the minimization and certainly not wrong, but an inaccurate fit-probability parameters. As a result, we have decided to perform the subtraction only for the Lomb-Scargle analysis, whereas in the fitting procedure we will implement the predetermined shape and fix its parameters to the best values.

Finally, in Figures 6.6 and 6.8, we present Lomb-Scargle periodograms for the two fiducial masses. We notice the most significant peaks at 0.98 and 0.99 years, for which the corresponding Spectral-Power-Densities are: 7.411 and 7.611, respectively. These densities correspond to p-values of 0.05 for 75 tons, and 0.04 for 145 tons. Based on the exponential probability distribution for the periodograms, derived in Section 5.1, we determined that there are no other, more significant peaks in the two distributions with probability of 95 and 96%, respectively. In the case of the 145 t-mass, the SPD value at 1-year corresponds to a significance of detection of  $2.35\sigma$ ; a comparison with the expected distribution when the signal is present shows consistency of 11.68%. In the case of the smaller mass however, even though the detection significance was found to be  $2.71\sigma$  with SPD at 7.411, the probability of it is much smaller, on the order of 3.85%.

As a final remark, we notice that in both cases the peaks are rather broad which additionally reduces the confidence of the obtained result, suggesting additionally, that there may be other periodicities contributing to the peak around 1 year.

## Sinusoidal Fit

In this section we present the most straight-forward approach, that is a sinusoidal fit to the rates obtain with standard cuts and divided into 60-day bins. If the backgrounds were stable over the course of three years, we would be able to merge the periods into 1 year, and perform a similar study to SNO and Super-K collaborations ([4], [5]). In such approach, the statistical uncertainties would be significantly reduced, but unfortunately, due to the already mentioned instabilities in Borexino, especially regarding the  $^{210}\text{Bi}$  background, this is not possible here. In Figure 6.9 we present the rates distribution for the selected data in 75 tons. Due to small statistics, we will perform the fit only using the enlarged fiducial volume of 145 tons. One can already notice however, the modulation trend in the presented data, even though the shown error bars (statistics only) are rather large and in this case, could even agree with a linear function.

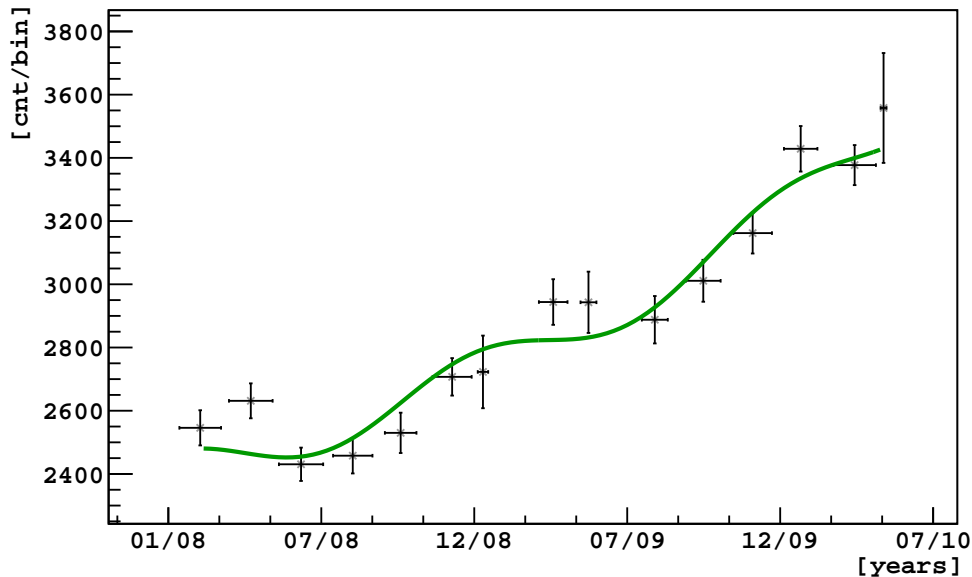


**Figure 6.9:** Best fit result using Equation 6.1. Green curve represents the expected signal whereas the red one is a fitted function. FM: 75 t.

The green function on the figure above, is the expected modulation based on the equation derived in Section 2.4:

$$R(t) = (C + e^{St}) + \bar{R} \left[ 1 + 2\epsilon \cos \left( \frac{2\pi t}{T} - \phi \right) \right]; \quad (6.1)$$

where the background part, is an exponential with C being a constant. The same function  $R(t)$  will be then used in the fit for the enlarged fiducial volume, but we will leave all the parameters free, instead of fixing them to their expected values, as in Fig. 6.9. The statistics in each bin is high enough so we can use reduced- $\chi^2$  as a check for the goodness-of-the fit. In our case, we applied the MIGRAND minimizer from the Minuit package of ROOT. Equation 6.2 presents the definition of our  $\chi^2$ , where we have added a penalty factor (Eq. 6.3) on the available phase offset with respect to the perihelion. It allows for a fluctuation of 21 days around 0, as defined in Equation 6.3.

$$\chi^2 = \sum_{i=1}^n \left[ \frac{(y_i - f(x_i))^2}{\sigma_{y_i}^2 + \left( \frac{\partial f}{\partial x} \sigma_{x_i} \right)^2} \right], \quad (6.2)$$

$$\chi_\phi^2 = \left( \frac{\phi - 0}{21} \right)^2; \quad (6.3)$$

The expected number of neutrinos,  $\bar{R}$  in Eq. 6.1, was calculated from Table 5.6 for the [105; 380] npe energy window, and equals 26.84 counts/(day x 100 ton) ( $\sim 2335$  counts/60-days per 145 tons). Additionally, the slope of the exponential function was predetermined in a fit that leaves out any other parameters.

In Figure 6.10, we present the fit results for the fiducial mass of 145 tons. The fitted function is in good agreement with the expectation and it is worth noticing again, that only thanks to a meticulous selection of events with respect to the known position of the vessel we can observe not only undisturbed shape but also almost doubled signal without a noticeable

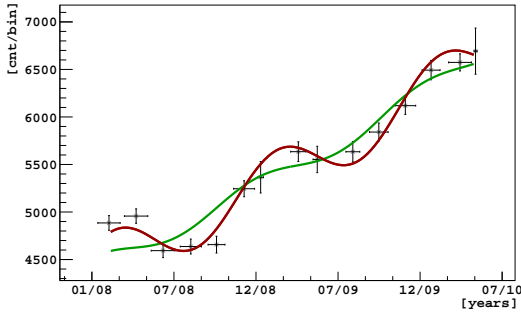


**Figure 6.10:** Best fit result using Equation 6.1. Amplitude  $15.93 \pm 4.07\%$ ,  $\bar{R}$   $3222.34 \pm 427.09$  cnt/bin,  $T$   $1.01 \pm 0.07$  y,  $\phi$   $11.00 \pm 4.01$  d, Fit  $\chi^2 = 1.27$ . FM: 145 t.

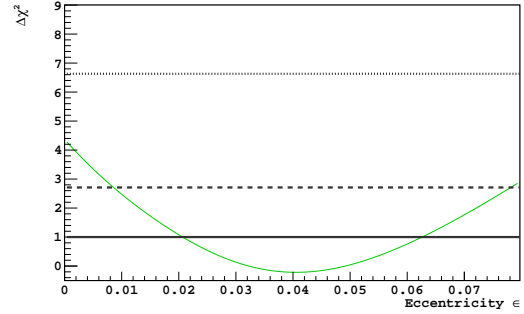


**Figure 6.11:** 1 d.o.f.  $\chi^2$  profile for eccentricity as in the fit in Fig. 6.10. Horizontal lines indicate the confidence levels of 68, 90, and 99%, from bottom to top, respectively.

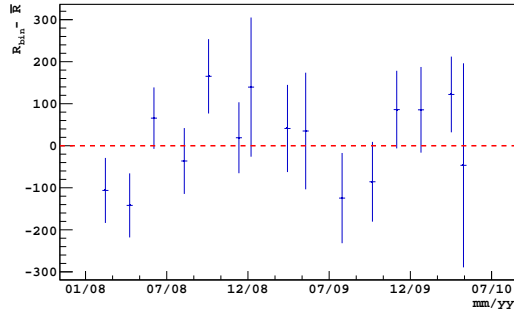


**Figure 6.12:** Residuals distribution from Fig. 6.10. Red-dashed line indicates the zero level.

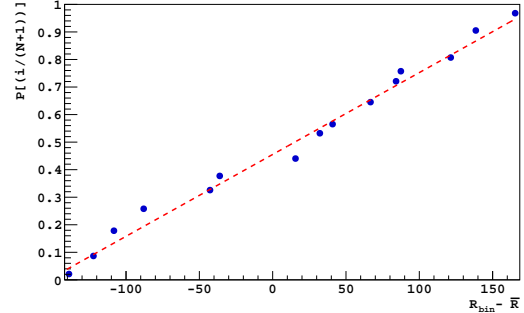


**Figure 6.13:** Residuals normal probability distribution. Red-dashed line shows a linear regression line.

increase in the background to signal ratio. Even though the amplitude and average neutrino rates are larger than expected, 15.93% and 3222.34 cnt/bin, the agreement is within  $2\sigma$ . Figure 6.14 shows the reduced- $\chi^2$  profile for the modulation amplitude (the eccentricity), where 0.0167 is the expected value. The period and the phase are close to the theoretical values of 1.01 year  $\pm 0.07$  and 11.00 days  $\pm 4.01$  respectively, achieved mainly thanks to the applied penalty factor. The quality of the fit is verified by very good  $\chi^2 = 1.27$ , as well as plots of residuals with respect to the best fit function presented in Figures 6.12 and 6.13. A full correlation matrix for the fit parameters was included at the end of this section.

Finally, we present the 2 d.o.f.  $\chi^2$  contour plots of allowed regions for the three fit parameters: eccentricity, period and neutrino rate; at 1,2, and 3  $\sigma$  C.L. What we show in Figures 6.14 and 6.15 is a rate of change of reduced chi-square with respect to the minimal value, i.e.  $\Delta\chi_R^2 = \chi_{R_{min}}^2 - \chi_{R_{xy}}^2$ . In both cases our results are within 2  $\sigma$  from the expected values (indicated with a black star for the expectation, and a yellow star for the minimal value in the plots).

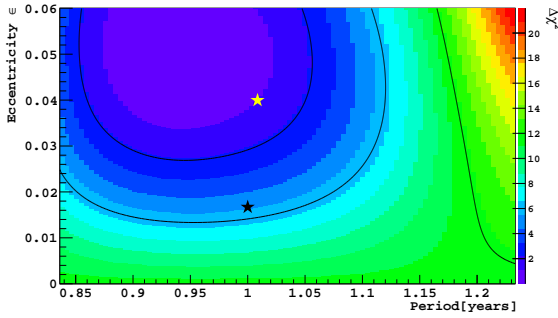


**Figure 6.14:** A  $\chi^2$  profile for eccentricity with respect to period. Confidence contours of 1,2,3  $\sigma$  are indicated.

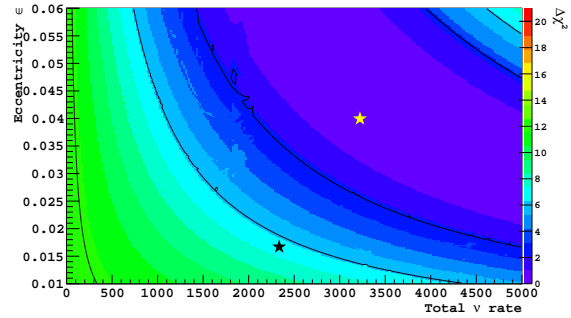


**Figure 6.15:** A  $\chi^2$  profile for eccentricity with respect to  $\nu$ -rate. Confidence contours of 1,2,3  $\sigma$  are indicated.

**Table 6.1:** Correlation matrix for the fit parameters in Fig. 6.10.

	Eccentricity	Period	Avg. Rate	Phase	Const.	Slope
$\epsilon$	1.0000	-0.0268	0.1459	0.0265	-0.1675	-0.0065
T	-0.0268	1.0000	-0.1239	0.0102	0.0871	0.1110
$\bar{R}$	0.1459	-0.1239	1.0000	0.1355	-0.9844	-0.2197
$\phi$	0.0265	0.0102	0.1355	1.0000	-0.1299	-0.0420
C	-0.1675	0.0871	-0.9844	-0.1299	1.0000	0.0611
S	-0.0065	0.1110	-0.2197	-0.0420	0.0611	1.0000

The method presented here, reveals the total  ${}^7\text{Be}$  count rate. If the backgrounds in Borexino were too high, the annual modulation would be the only technique to achieve this measurement. It was determined with a Monte-Carlo simulation, that for the observed  $\nu$ -rate, which dominates the sensitivity, and current signal-to-background ratio, the best precision on the  ${}^7\text{Be}$  number would be on the order of 20%. The number from the spectral fit however, was achieved with a statistical error of 2.5% ([2]), a result of pristine purity of the target.

## Spectral Fit

As it was mentioned in previous chapters, the statistical uncertainty of spectral fitting is not sufficiently good in order to reveal the expected  $\sim 7\%$  amplitude ( $\sim 4\%$  for average rates). The data-set has to be divided into two sub-periods with about a  $3.5\%$  error on each  ${}^7\text{Be}$  number that would overlap with the modulation. We can however, try to use it for the actually observed modulation in Phase I. The determined amplitude from rate analysis in the previous section, was found to be on the order of  $15\%$ . If this was the case, then we would be able to investigate it with better chances even with the available precision of the spectral fit; the difference between Winter and Summer times would be on the order of  $\sim 8\%$ . In the next two sections, we will present results of such comparison performed on two data sets:

- the whole available statistics in Phase I, Figure 6.16
- the statistics chosen for this analysis, Figure 6.17

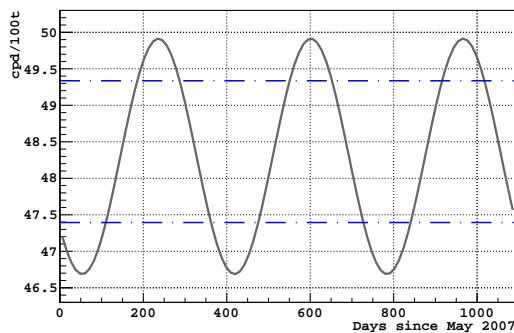


**Figure 6.16:** The expected annual modulation of  $48.30$  cpd of  ${}^7\text{Be}$   $\nu$ . Total average count for the maxima =  $49.34$  cpd (top Blue line), and the minima =  $47.39$  cpd (bottom Blue line).

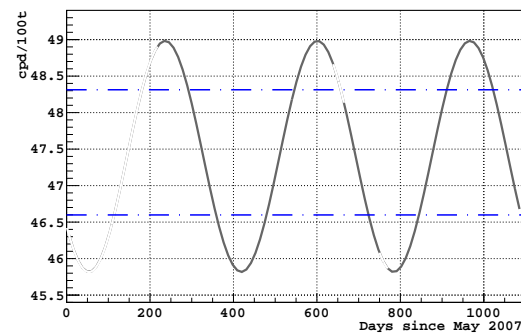


**Figure 6.17:** The expected annual modulation of  $47.40$  cpd for the removed data. Total average count for the maxima =  $48.31$  cpd (top Blue), and the minima =  $46.60$  cpd (bottom Blue).

Throughout this presentation, we will refer to the merged data over all the periods for which the Earth-Sun distance is less than 1 A-U (increased  $\nu$ -flux) as *Maximum*, and greater than 1 A-U (decreased  $\nu$ -flux) as *Minimum*. The blue lines in Figures 6.16 and 6.17, represent

the expected integrated count rates for  ${}^7\text{Be}$   $\nu$  with respect to the total count determined from the spectral fit, 47.4 and 48.3 counts/(day x 100 ton) respectively. As it can be noticed, since Earth's orbit is not a step-function, but in fact a continuous ellipse, the maximum and minimum rates are less than the peaks of the amplitude ( $47.40 \pm 1.64$  and  $48.30 \pm 1.67$  counts/(day x 100 ton)). In both cases presented here, we use the exact same analysis cuts as were used for the annual modulation study however, we constrain the fit only to the 75 ton-fiducial volume ( $R=3.021$  m,  $|z|=1.67$  m).

**${}^7\text{Be}$  Data-Set** In the first step we discuss the whole available data set as it was used also in the official release of the  ${}^7\text{Be}$  flux measurement ([2]), May 13, 2007 - May 08, 2010. Figure 6.18 shows how the distance between Earth and Sun was changing over that period of time in Astronomical Units (A-U). We notice once again that the observed seasons correspond to the tilt of Earth's axis and not the distance to the Sun (the distance is the greatest during Summer in the Northern hemisphere). In Figure 6.19 we present the corresponding total spectra in Borexino for the merged periods of maximum (Blue) and minimum (Magenta) expected  $\nu$ -fluxes, normalized to live time.

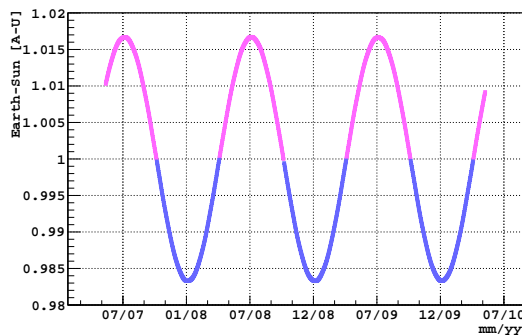


**Figure 6.18:** Earth-Sun distance between May 13, 2007 and May 8, 2010. Data from [103]. Magenta:  $> 1$  A-U, Blue:  $< 1$  A-U.

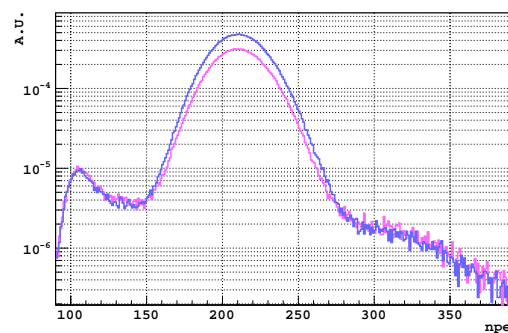


**Figure 6.19:** Comparison of normalized spectra between the maximum and minimum distance according to Fig. 6.18.

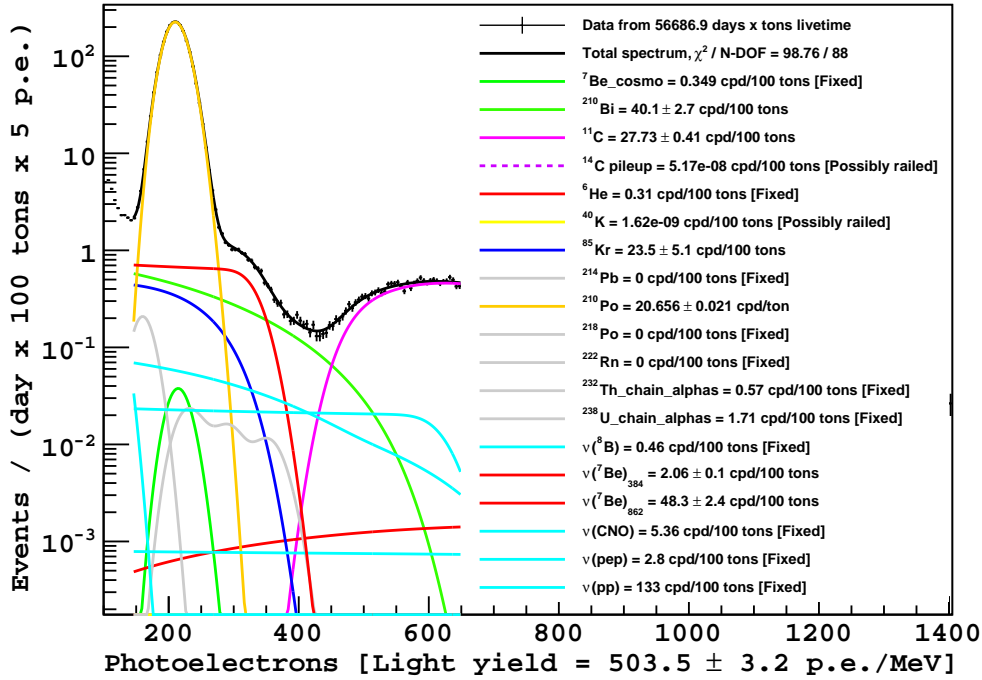


Figure 6.20: Spectral fit results for the whole data-set and standard  $^7\text{Be}$  fiducial volume, 75 tons.

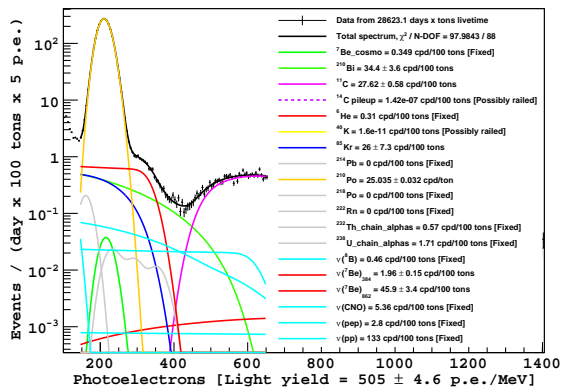


Figure 6.21: Spectral fit results for the whole data-set and only the minimal Earth-Sun distance.

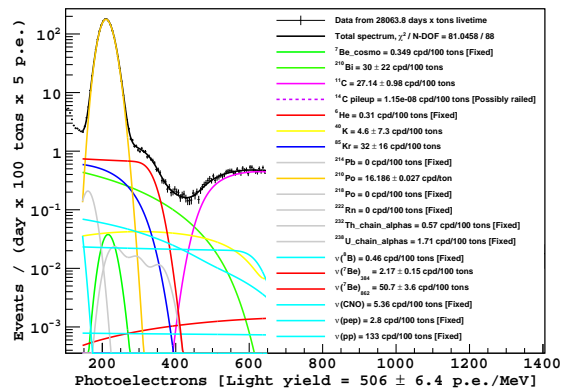


Figure 6.22: Spectral fit results for the whole data-set and only the maximal Earth-Sun distance.

Next, we perform spectral fitting in three cases, 1) for the whole data set, 2) the *Magenta* and 3) the *Blue* periods, individually. The fit is performed with all the neutrino species fixed to their expected values of the MSW-LMA solution, except for the  ${}^7\text{Be } \nu$ . Results for are shown in Figures 6.20, 6.21 and 6.22, respectively. Additionally, table 6.2 contains a collection of all the determined values making the comparison very clear. We observe very consistent results for the fit parameters, such as Light Yield, and backgrounds, stable  ${}^{210}\text{Bi}$ ,  ${}^{11}\text{C}$  and  ${}^{85}\text{Kr}$ . The count rate of  ${}^{210}\text{Po}$  changes significantly since its greatest contamination was observed only in the very beginning of data-taking (compare Figure 4.27 for reference). As for the  ${}^7\text{Be } \nu$ , we determined  $45.9 \pm 3.4$  (47.4 expected), and  $50.7 \pm 3.6$  (49.3 expected). If however, the annual modulation was, as observed in the rate analysis, on the order of 15% peak-to-peak, we would expect, 46.35 and 50.53 counts/(day x 100 ton) respectively, i.e. a difference of  $\sim 8.6\%$ .

**Table 6.2:** Collection of the spectral fit results from Figures: 6.20, 6.21 and 6.22.

Parameter	All	Min	Max
L.Y. [p.e./MeV]	$503.5 \pm 3.2$	$505 \pm 4.6$	$506 \pm 6.4$
${}^{210}\text{Bi}$ [cpd/100t]	$40.1 \pm 2.7$	$34.4 \pm 3.6$	$30 \pm 22$
${}^{11}\text{C}$ [cpd/100t]	$27.73 \pm 0.41$	$27.62 \pm 0.58$	$27.14 \pm 0.98$
${}^{85}\text{Kr}$ [cpd/100t]	$23.5 \pm 5.1$	$26 \pm 7.3$	$32 \pm 16$
${}^{210}\text{Po}$ [cpd/t]	$20.66 \pm 0.02$	$25.04 \pm 0.03$	$16.19 \pm 0.03$
${}^7\text{Be}_{384}$ [cpd/100t]	$2.06 \pm 0.1$	$1.96 \pm 0.15$	$2.17 \pm 0.15$
${}^7\text{Be}_{862}$ [cpd/100t]	$48.3 \pm 2.4$	$45.9 \pm 3.4$	$50.7 \pm 3.6$
Mass-time [days x tons]	56686.93	28623.1	28063.83
$\chi^2/\text{N-DOF}$	1.12	1.11	0.92

**A-M Data-Set** Similarly to the presented results in the previous paragraph, we concentrate on the data-set that was used in this analysis. As a reminder, we excluded the first 219 days due to high Radon concentration and about four weeks total after the two calibration campaigns in the Summer of 2009. Figures 6.23 and 6.24 show again the Earth-Sun distance for the selected period with the corresponding spectra. This time, the  $^{210}\text{Po}$  concentration is evenly distributed among the merged sets due to the excluded first half-a-year of data with high Polonium, as mentioned before. The spectral fit results are shown in Figures 6.25, 6.26 and 6.27. As we would expect, the uncertainty on the determined parameters is slightly lower than in the previous case due to limited statistics.

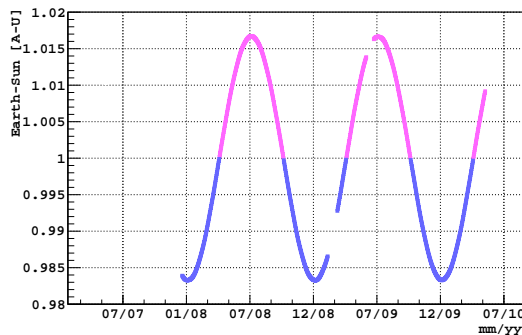


**Figure 6.23:** *Earth-Sun distance for the periods considered in this analysis. Data from [103]. Magenta:  $> 1$  A-U, Blue:  $< 1$  A-U.*

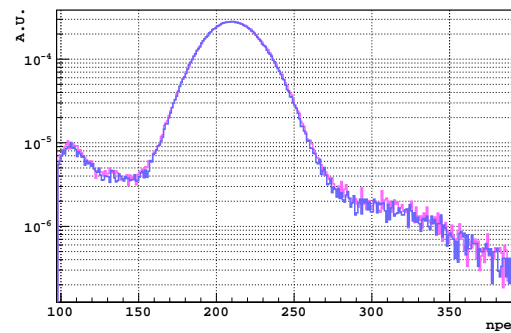


**Figure 6.24:** *Comparison of normalized spectra between the maximum and minimum distance according to Fig. 6.18.*

Nevertheless, we find consistent results in all the cases, specifically, we notice that  $^{210}\text{Bi}$  concentration is currently higher because of its increasing trend and exclusion of the first period, and that  $^{210}\text{Po}$  is now flat. This time, for the  $^7\text{Be}$   $\nu$ , we determined  $43.0 \pm 4.0$  (46.6 expected), and  $51.6 \pm 3.9$  (48.3 expected). In the case of the inspected 15% annual modulation, we would expect 45.7 and 49.4 counts/(day x 100 ton), respectively; i.e. a difference on the order of  $\sim 7.8\%$ . All the results and are presented collectively in Table 6.3.

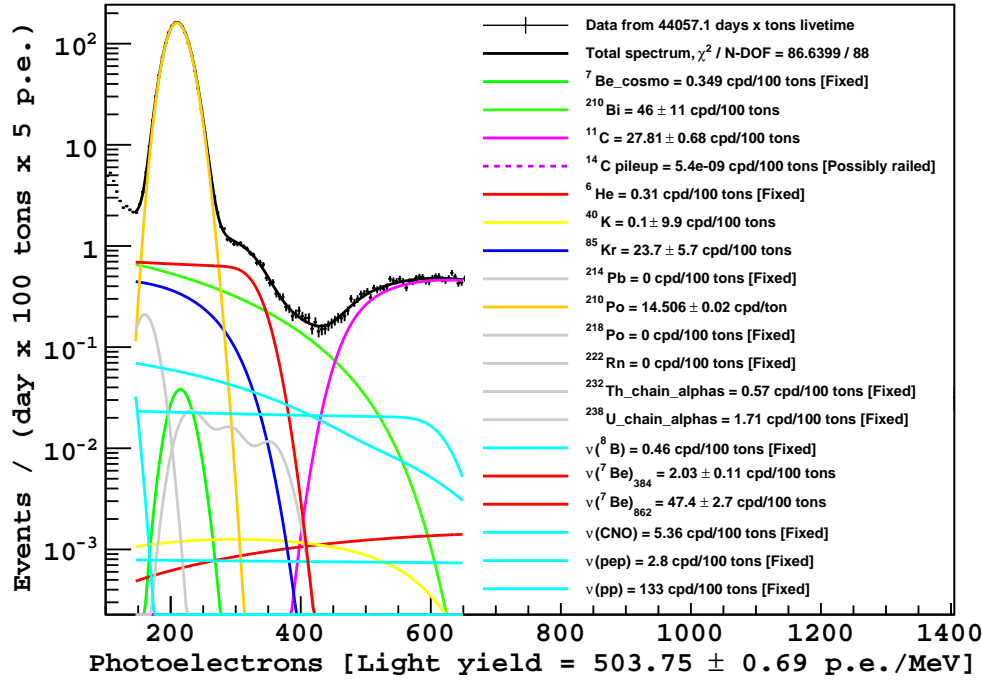


Figure 6.25: Spectral fit results for the selected data-set and standard  ${}^7\text{Be}$  fiducial volume, 75 tons.

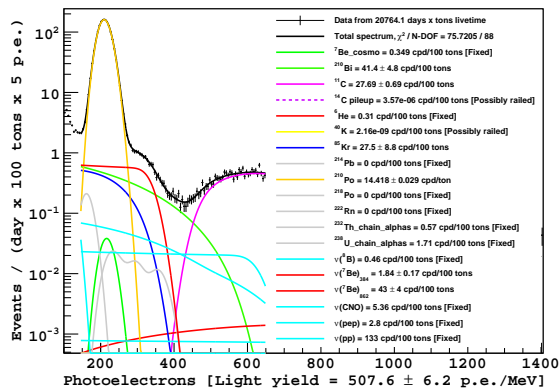


Figure 6.26: Spectral fit results for the selected data-set and only the minimal Earth-Sun distance.

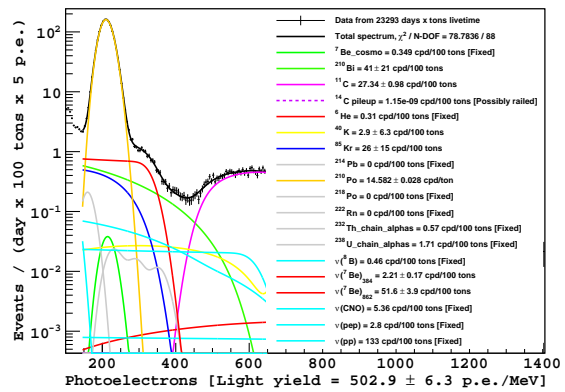


Figure 6.27: Spectral fit results for the selected data-set and only the maximal Earth-Sun distance.

**Table 6.3:** *Collection of the spectral fit results from Figures: 6.25, 6.26 and 6.27*

Parameter	All	Min	Max
L.Y. [p.e./MeV]	$503.75 \pm 0.69$	$507.6 \pm 6.2$	$502.9 \pm 6.3$
$^{210}\text{Bi}$ [cpd/100t]	$46 \pm 11$	$41.4 \pm 4.8$	$41 \pm 21$
$^{11}\text{C}$ [cpd/100t]	$27.81 \pm 0.68$	$27.69 \pm 0.69$	$27.34 \pm 0.98$
$^{85}\text{Kr}$ [cpd/100t]	$23.7 \pm 5.7$	$27.5 \pm 8.8$	$26 \pm 15$
$^{210}\text{Po}$ [cpd/t]	$14.51 \pm 0.02$	$14.42 \pm 0.03$	$14.58 \pm 0.03$
$^7\text{Be}_{384}$ [cpd/100t]	$2.03 \pm 0.11$	$1.84 \pm 0.17$	$2.21 \pm 0.17$
$^7\text{Be}_{862}$ [cpd/100t]	$47.4 \pm 2.7$	$43 \pm 4$	$51.6 \pm 3.9$
Mass-time [days $\times$ tons]	44057.14	20764.09	23293.04
$\chi^2/\text{N-DOF}$	0.98	0.86	0.90

In conclusion, we have performed a spectral fit on two data sets in the standard  $^7\text{Be}$  fiducial volume. The first one, with the full statistics available in Phase I, and the second sample, with statistics chosen for the annual modulation study. Even though, we eliminated the first six months of data from the rate analysis, this period does contain perfectly valid data, with no impact on the spectroscopic properties. We have determined the following results for the  $^7\text{Be}$  neutrino rate, presented in Table 6.4.

**Table 6.4:** *Summary of the spectral fit results, based on the full and limited data-samples, in comparison with the expected 7% and observed 15% annual modulation.*

Data Set	Spectral All	Spectral Min	7% Min	15% Min	Spectral Max	7% Max	15% Max
$^7\text{Be}$ Def.	$48.3 \pm 2.4$	$45.9 \pm 3.4$	47.4	46.4	$50.7 \pm 3.6$	49.3	50.5
A-M Set	$47.4 \pm 2.7$	$43.0 \pm 4.0$	46.6	45.7	$51.6 \pm 3.9$	48.3	49.4

Even though there is a tendency of the determined fit parameters to follow the larger-than-expected modulation, we need to take into account the uncertainties on the central values. In both cases, they are on the order of  $\sim 3.5$ - $4.0$  counts, which in the end, gives an agreement between the measured minimum and the expected minimum and also the maximum rates, even in the case of 15% peak-to-peak modulation. We also need to keep in mind that the systematic uncertainties account for additional 3% error that was considered here.

## Phase II

Even though the second phase of Borexino data-taking has almost just begun, we would like to present the preliminary results from only a little over a year of statistics. After a very successful purification campaign, see [89] for details, with reduced  $^{85}\text{Kr}$  to the level of ‘a few’ counts/(day x 100 ton), and  $^{210}\text{Bi}$  by a factor of two with respect to Phase I, we have very good reason to believe that even with limited data, the results would be quite promising. Additionally, Phase II was scheduled to last for about 28 months total, and we would like to present a similar study of sensitivity as presented earlier for the Lomb-Scargle periodograms, but in this case, using the new levels of backgrounds. In Phase II, we are also much more comfortable with the inner vessel shape, as at this point, it has been over two years from the time of the DMP removal and the vessel has had enough time to stabilize. As a result, we only remind that this imposes a new FV cut defined for this period, details below.

## Current and Future Potential

### Oct 2011 - Sep 2012

After applying the identical analysis cuts as for the data in Phase I, we look at the  $^7\text{Be}$  count-rate in our standard energy window [105; 380] npe, but this time unfortunately for only the available, a little over, a year of data. Naturally, we would not expect any sensitivity from the Fourier search for periodicities, as applied earlier Lomb-Scargle, due to limited statistics. In particular, because the period that we are searching for is in this case on the order of the length of the sample itself. As a result, we will present only the count-rates in comparison to the expected shape of the annual modulation. At the time of writing, the end of data

was taken to be on the last day of the validated DST-week of September the 23rd, 2012.

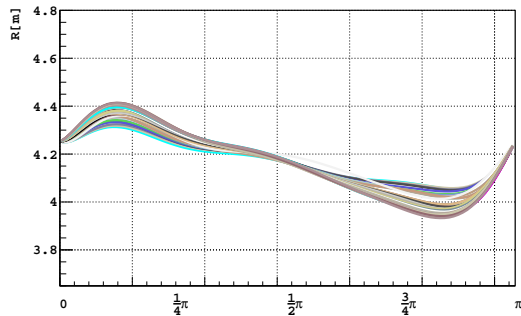


**Figure 6.28:** A history of the IV shapes obtained from an elliptical fit to background events reconstructed on the surface of the nylon.

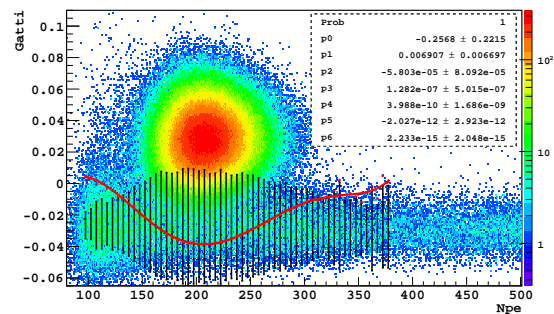
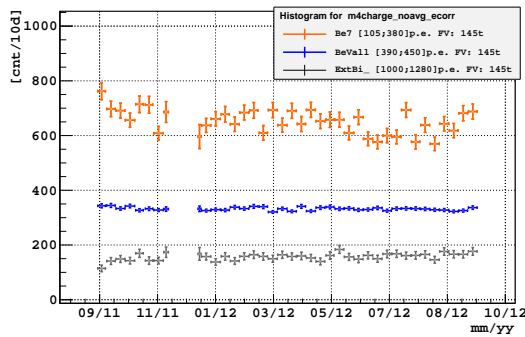


**Figure 6.29:** Gatti parameter cut definition in Phase II. Fiducial Volume cut:  $DSV=0.75$  m. Fiducial Mass: 145 tons.

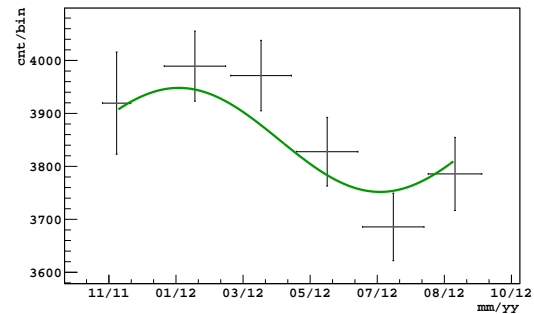
There is no apparent reason to believe that the stability checks presented in Section 4.2 could not be extrapolated to Phase II, since neither the electronics, nor properties of the scintillator were changed or affected during the purification period. It is obvious however, that verification of the vessel shape stability is necessary due to potential fluctuations in the liquids' density and temperature. An interesting report speculating the correlation between the temperature gradient and the vessel deformation can be found in [104]. Figure 6.28 presents again a full scan of the inner vessel shape profile, week by week; we notice that apart from about a 10 cm shift in the vertical direction, the position of the vessel was very stable. As before, we verify it by looking at the high-energy external Gamma-events, the distribution in time presented in Figure 6.30, confirms that the choice of the DSV cut at 0.75 m was in this case correct. Full count-rates with 10-day binning for other energy regions ( ${}^7\text{Be}$ ,  ${}^7\text{Be}$ -valley), are also presented in Figure 6.30.

As before, we have applied a fixed Gatti cut in order to eliminate the  $\alpha$  events from  ${}^{210}\text{Po}$  but also potential  ${}^{222}\text{Rn}$  daughters<sup>2</sup> We also perform an exercise with the new data and in

<sup>2</sup>Water extraction campaigns always carry a risk of additional contamination with  ${}^{222}\text{Rn}$ , and the first weeks of August 2011 could be still showing signs of its presence.



**Figure 6.30:**  ${}^7\text{Be}$  rate distribution.  ${}^7\text{Be}$ -valley count-rate was scaled by a const. number. FM: 145t.



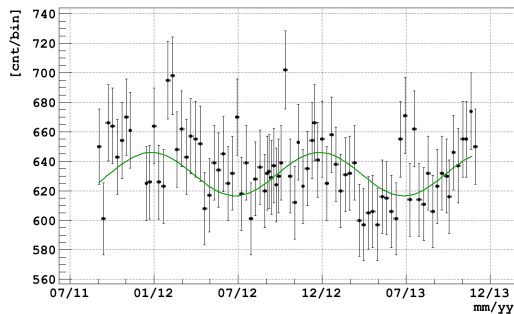
**Figure 6.31:** Count rate in 60-day binning in comparison with the expected modulation (green curve).

Figure 6.31 we show count rates for the window in 60-day bins and along with it a curve that represent annual modulation of solar neutrinos for this period of time. As you may notice, not all the data points were included. The first month after the end of purification campaign was very unpredictable in terms of background mixing throughout the inner vessel. Mainly responsible for it was the remaining  ${}^{222}\text{Rn}$  but predominantly,  ${}^{210}\text{Bi}$ . An increase in count rates in the first weeks of phase II can be seen in Figure 6.30 in (Blue) and (Orange). As a result, we were forced to remove these two bins, and instead of in August, start phase II officially in November of 2011. The data however looks very promising and also based on the simulation in the next section we anticipate very satisfactory results from this period of data-taking.

### Aug 2011 - Dec 2013

We perform now a similar evaluation of our sensitivity to the one presented in Section 6.1. This time however, we will artificially expand the sample's size to a total of twenty-eight months assuming that all the backgrounds will stabilize at the current level. We believe that the process of internal mixing due to convection and further settling down of  ${}^{210}\text{Bi}$  is

responsible for what we are observing with respect to the clearly visible in Figure 6.30 steady slope in the window. We present in Figure 6.32 what would the rate distribution look like assuming 10-day-long binning and 145 tons of fiducial mass.



**Figure 6.32:** Simulation of 28 months of data in Phase II. Rate distribution with 10-day binning and 145 t fiducial mass. The expected modulation is shown in green.

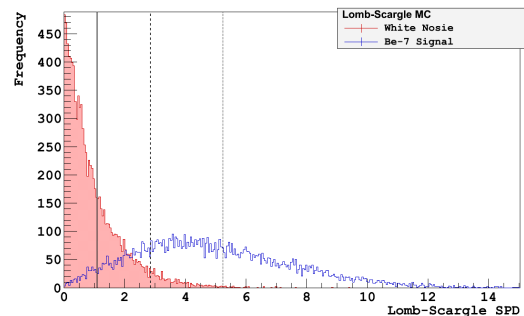


**Figure 6.33:** Detection sensitivity. The vertical lines indicate  $1\sigma$  (continuous),  $2\sigma$  (dashed), and  $3\sigma$  (dotted) confidence level above white-noise (shown in blue).

As show in Figure 6.33, for 28 months of data taking with current assumption of the background levels, Borexino will reach potential of a  $1\sigma$  measurement with 96.03% probability,  $2\sigma$  with 77.85% and  $3\sigma$  with 41.12%. For comparison, the corresponding probabilities in phase I would be at the level of 81.62, 43.54 and 11.68% respectively. It has to be kept in mind however, that the first phase lasted not only longer by about 30% but also due to rather easily reproducible shape of the changing background we were able to eliminate it effectively. Such a simple correction usually results in a significant improvement in Lomb-Scargle detection sensitivity. On the other hand, if we were to extrapolate the shape of the background in the second phase and continue with its steady drop we would be able to perform a similar exercise to reduce the trend. This would again help improve the sensitivity above the presented here level. Unfortunately, since we cannot predict precisely what is going to happen we assumed a more conservative scenario. The offset in the red-shaded region w.r. to the signal in Figure 6.33 is in fact a result of the decreasing trend in the simulation.

# Chapter 7

## Conclusion

In the following summary we would like to bring together some of the most important aspects of this analysis, specifically regarding the stability checks that provided the critical understanding of the count-rates in Borexino throughout the two phases of data-taking. We also underline, that the performed Monte-Carlo simulations have revealed rather poor sensitivity of our neutrino signal to the expected 7% change in amplitude, even though the backgrounds were assumed to be well known and stable in time. This fact however, is naturally caused by the low rate of neutrinos collected in the detector. It is interesting to compare results for the Borexino count-rate of  $\sim 50$  counts/(day x 100 ton) of  ${}^7\text{Be}$  (SPD-MC shown again in Figure 7.1), with a future mega-ton scale facility, such as LENA for instance, with  $\sim 10^4$  counts/day (analysis from [105]). Even if we assume only a 2% peak-to-peak modulation, and a period of 0.1 years, we can show how the sensitivity drastically improves with this kind of statistics. Figure 7.2 presents a similar Monte-Carlo simulation as we have prepared for Borexino, i.e. a Lomb-Scargle Spectral-Power-Density plot for white-noise and the given amplitude and period. In this case, the sensitivity threshold was set to 99.7% (red-dashed line in the figure), and as we can see, all the signal is contained above the threshold.

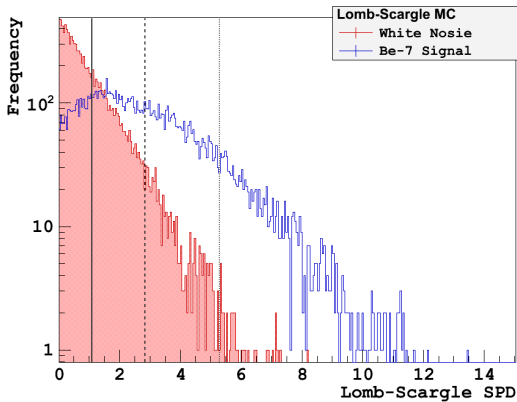


**Figure 7.1:** A Monte-Carlo simulation of  $\sim 10^4$  events in Borexino. Phase I, FM: 145 t.

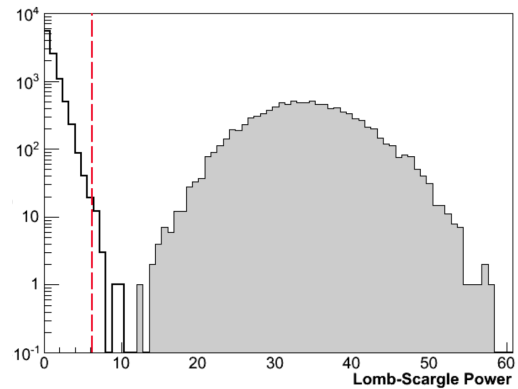


**Figure 7.2:** A Monte-Carlo simulation of  $\sim 10^4$  events in LENA. Figure from [105].

Nevertheless, we begin our summary by presenting once again, the results obtained in Sections 4.1 and 4.2 that were devoted to a discussion on the stability conditions. By far, the two most important factors affecting our final results were:

- the changing shape of the vessel, shown in Figure 7.3
- the increasing  $^{210}\text{Bi}$  rate over time, shown in Figure 7.4

In the first case, we have successfully avoided the impact of the IV shape by a careful study of the external backgrounds. We were able to extrapolate the Gamma events' tail into the  $^7\text{Be}$ -window-of-interest and select such FV cut so that the contribution would be negligible, at the same time, maximizing the target mass. Unfortunately however, the internal  $^{210}\text{Bi}$  concentration turned out to be the most problematic, not only because of its impact on the Signal-to-Background ratio, but mainly due to its increasing trend. We have carried out several steps in order to reveal the origin of this behaviour, but we were only able to determine the shape of the trend to be exponential, which was assumed to be the case throughout the rest of the analysis.

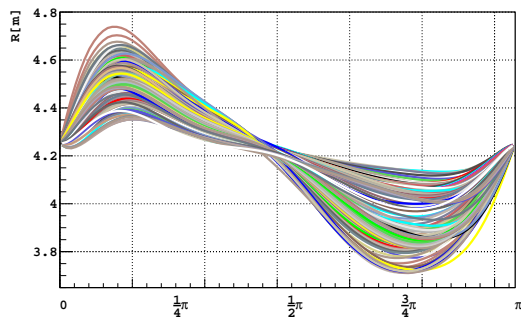


**Figure 7.3:** The evolution of the inner vessel shapes during Phase I.

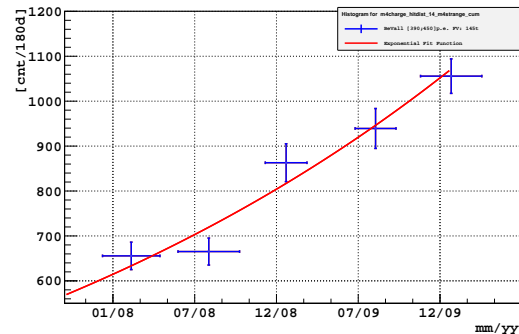


**Figure 7.4:**  $^{210}\text{Bi}$  background count-rates throughout Phase I, FM: 145 tons.

Finally, we present the two major results, and even though we have also performed a Lomb-Scargle search for periodicities, the actual count-rate along with a sinusoidal function of the expected modulation, gives the most representative conclusion.

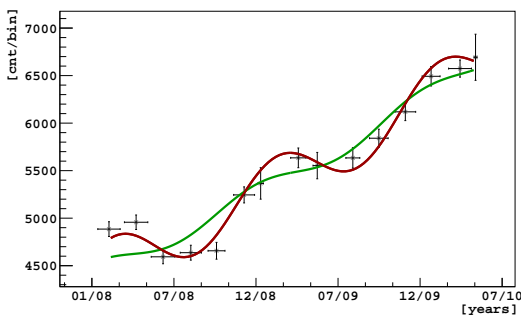


**Figure 7.5:** Count-rates in the energy window of interest in Phase I, FM:145 tons, Binning:60 days.

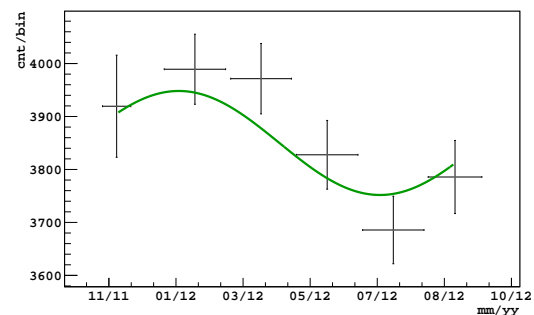


**Figure 7.6:** Count-rates in the energy window of interest in Phase II, FM:145 tons, Binning:60 days.

The count-rates for two phases, Phase I and II, are shown in Figures 7.5 and 7.6, respectively. A full study was carried out only in the first case, including the sinusoidal fit shown above; nevertheless, the preliminary results in Phase II are very promising and will be up-dated as soon as additional data is collected and validated for analysis. Table 7.1 summarizes all the results obtained in Phase I in comparis with the expected values for the eccentricity ( $\epsilon$ ),

period ( $T$ ), average- $\nu$ -rate ( $\bar{R}$ ), and finally, phase ( $\phi$ ). We also add to the table a consistency check performed with the spectral fit to two megred periods of minimum- and maximum-flux, respectively.

**Table 7.1:** Comparison of the results presented in Section 6.1 for the FM of 145 tons and energy window between [105; 380] npe. The expected number of neutrinos was calculated based on Table 5.6.

	Expected	Lomb-Scargle	Sin-Fit	Spectral-Fit
$\epsilon$	7%	X	$15.93 \pm 4.07$	X
$T$	1-year	0.99	$1.01 \pm 0.91$	X
$\bar{R}$	38.92 cpd/145-t	X	$53.71 \pm 7.12$	X
$\phi$	0 d	X	$11.00 \pm 4.01$	X
Min-count	46.6 cpd/100-t	X	X	$43.0 \pm 4.0$
Max-count	48.3 cpd/100-t	X	X	$51.6 \pm 3.9$

# Appendix A

## Table of Abbreviations

**Table A.1:** *Table of Abbreviations.*

Abbreviation	Meaning
<b>ATLAS</b>	A Toroidal LHC Apparatus
<b>A-U</b>	Astronomical Unit = 149 597 870 700 km
<b>A.U.</b>	Arbitrary Unit
<b>BTB</b>	Borexino Trigger Board
<b>CKM</b>	Cabibbo-Kobayashi-Maskawa
<b>CC</b>	Charged Current
<b>CMS</b>	Compact Muon Spectrometer
<b>CNGS</b>	CERN Neutrinos to Gran Sasso
<b>CTF</b>	Counting Test Facility
<b>DAQ</b>	Data Acquisition
<b>DONuT</b>	Direct Observation of the NU Tau
<b>DST</b>	Data Storage and Transfer
<b>DSV</b>	DiStance to the inner Vessel
<b>EU</b>	European Union
<b>FV</b>	Fiducial Volume
<b>GUT</b>	Great Unification Theory
<b>ID</b>	Inner Detector
<b>LAKN</b>	Low Argon Krypton Nitrogen
<b>LHC</b>	Large Hadron Collider
<b>LNGS</b>	Laboratori Nazionali del Gran Sasso
<b>LY</b>	Light Yield
<b>NC</b>	Neutral Current

Abbreviation	Meaning
<b>OB</b>	Outer Detector
<b>OV</b>	Outer Vessel
<b>PDF</b>	Probability Distribution Function
<b>PMT</b>	Photomultiplier Tube
<b>PC</b>	Pseudocumene
<b>R&amp;D</b>	Research and Development
<b>SSS</b>	Stainless-Steel Sphere
<b>SLAC</b>	Stanford Linear Accelerator Center
<b>SM</b>	Standard Solar
<b>SSM</b>	Standard Solar Model
<b>SVM</b>	Support Vector Machines
<b>TMB</b>	Trimethylborate
<b>TFC</b>	Three Fold Coincidence
<b>WL</b>	Water-Loop
<b>WT</b>	Water Tank

# Appendix B

## List of Operations

**Table B.1:** *Table of operations and maintenance of the Borexino detector.*

Date	DAQ Run	Operation
15. May. 2007	5000	The end of initial filling
01. Jun. 2007	5224	Refilling from the top
15. Jun. 2007	5279	Changed firmware against retrigg. BTB 200
23. Jun. 2007		Settling of triple veto against muons
05. Jul. 2007	5470	Trg 128 introduced
09. Jul. 2007	5494	801 of PC + DMP in inner buffer
13. Jul. 2007	5516	Noisy channels removed. BTB 40
19. Jul. 2007	5541	Changed DAQ profile
23. Jul. 2007	5565	Threshold of ref. channels lowered from 60 to 53 mV
30. Jul. 2007	5602-5653	Trigger window moved from 55 to 99 ns
01. Aug. 2007		Lot of oscillating FEB
06. Aug. 2007	5657	Trigger window moved back to 60 ns
Sep. 2007		Maintenance of oscillating FEB
24. Sep. 2007	5972	CNGS beam ON
28. Sep. 2007	5796	Rack #10 dismounted, repaired and recabled
19. Oct. 2007	5796	CNGS beam OFF
20. Oct. 2007		Rack #10 back into trigger
28. Nov. 2007	6396	Trigger gate moved to 99 ns, first test of 16 ms gate
04. Dec. 2007		Changed PPC software: gate back to 6 ms
10. Dec. 2007		PMT gain equalization (130 channels changed)
12. Dec. 2007		Start of the first waterloop

Date	DAQ Run	Operation
23. Dec. 2007		Stop of the first waterloop
16. Dec. 2007	6562	16 ms gate
04. Jan. 2008		WL ON
21. Jan. 2008		Channels back into trigger (except dead PMTs)
12. Feb. 2008		WL temperature decreased
19. Feb. 2008		Maynteinance of several FEB
18. Jun. 2008	8013	CNGS beam ON
09. Apr. 2008		Possible start of the leak
10. Jun. 2008		Patch for the 6:25 am DAQ crash
04. Oct. 2008	8768-8892	First calibration campaign
24. Oct. 2008		5001 PC added (bottom)
29. Oct. 2008		5001 PC+PPO added (bottom)
03. Nov. 2008	9052	CNGS beam OFF
07. Nov. 2008		10001 PC added (bottom)
10. Nov. 2008		20001 PC+PPO added (bottom)
16. Jan. 2009	9458-9711	Second calibration campaign
12. Feb. 2009		Buffer purifications (DMP reduced from 5 to 3 g/l) start
03. Apr. 2009		Buffer purifications (DMP reduced from 5 to 3 g/l) stop
27. May. 2009	10201	CNGS beam ON
06. Apr. 2009	9986	The Earthquake
14. Apr. 2009		Restart (the very first runs were noisy)
01. Jun. 2009		30001 PC+PPO added (bottom)
03. Jun. 2009		30011 PC+PPO added (bottom)
05. Jun. 2009		30021 PC+PPO added (bottom)
15. Jun. 2009	10301-10493	III calibration campaign start
29. Jun. 2009	10301-10493	III calibration campaign stop
13. Jul. 2009	10546-10727	IV calibration campaign start
29. Jul. 2009	10546-10727	IV calibration campaign stop
23. Nov. 2009	11685	CNGS beam OFF
02. Dec. 2009		Start of buffer purifications (DMP reduced to 2 g/l)
03. Dec. 2009	12000	Rack #14 removed, cable reshuffling, new profile #18
21. Jan. 2010		End of Buffer purifications (DMP reduced to 2 g/l)
02. Feb. 2010	12422	New laben firmware (first hit time moved very close to the beginning of the gate)
19. Feb. 2010		Several FEB and LB replaced for maintenance
13. Mar. 2010	12626	4.5 m <sup>3</sup> of pure PC added from top
25. Mar. 2010		4.5 m <sup>3</sup> of pure distilled PC added from top
20. Apr. 2010	12833	CNGS beam ON
16. Jun. 2010	13412-13433	The first test of WE (50 m <sup>3</sup> ), start
18. Jun. 2010	13412-13433	The first test of WE (50 m <sup>3</sup> ), stop
05. Jul. 2010	13560-13756	Start of the external source ( <sup>228</sup> Th) calibration

Date	DAQ Run	Operation
13. Jul. 2010	13728	Start of first WE cycle (the external source calibration was still running)
31. Jul. 2010	13912	Stop of first WE cycle (315+50 m <sup>3</sup> from the first trial)
30. Aug. 2010	14084	Start of second WE cycle
04. Sep. 2010		Boards replaced
12. Sep. 2010	14160	Stop of second WE cycle because of a pump failure
21. Sep. 2010	14210	Start of third WE cycle
25. Sep. 2010	14232	Many HV channels in different HV boards broken
13. Oct. 2010		Boards replaced, HV tuning
16. Oct. 2010	14373	Stop of third WE cycle (315 m <sup>3</sup> )
29. Oct. 2010	14450	PMT gain equalization
22. Nov. 2010	14620	CNGS beam OFF
24. Nov. 2010	14634	PMT gain equalization
18. Jan. 2011	14977	1001 of PC added (top)
26. Jun. 2011	15029-15036	Restart of WE (immediately stopped because of a broken disk in the skids, ~12 m <sup>3</sup> processed)
01. Feb. 2011	15091	Start of fourth WE cycle
19. Feb. 2011	15295	Stop of fourth WE cycle
10. Apr. 2011	15637	Some HV channels in different HV boards broken, high rate
19. Mar. 2010	15509	CNGS beam ON
06. May. 2011	15765	24 broken PMTs disconnected
10. May. 2011	15791	Start of fifth WE cycle
12. May. 2011	15807	PMT gain equalization
17. May. 2011	15849	PMT gain equalization
19. May. 2011	15868	PMT gain equalization
24. May. 2011	15915	HV board exchange, 24 PMTs back in DAQ
31. May. 2011	15988	PMT gain equalization
08. Jun. 2011		Stop of the fifth WE cycle
29. Jun. 2011	16192	PMT gain equalization
06. Jul. 2011	16239	Modification of the initialization procedure of the laben boards
19. Jul. 2011	16296	Start of 6th WE cycle
11. Aug. 2011	16483	Stop of 6th WE cycle
Sep. 2011	16654-16669	Changed five HV Boards and recovered 53 PMTs
Sep. 2011	16704	Exchange of 5 FE Boards (begin of a larger maintenance campaign)
28. Sep. 2011	16737	PMT gain equalization
09. Nov. 2011	17030	Change Front End boards: CR 12 FE 3,12,13; CR 13 FE7,13
14. Nov. 2011	17057	Start of external source ( <sup>228</sup> Th) calibration campaign

Date	DAQ Run	Operation
12. Dec. 2011	17315	End of external source ( $^{228}\text{Th}$ ) calibration campaign
12. Jan. 2012	17461	replaced the OD TDCs
20. Mar. 2012	18000	Added new reference channels for CNGS trigger. New channel profile (#19, Mar 12)
21. Jan. 2013	19764	HV of crate 6-13 suddenly OFF for a short circuit
22. Jan. 2013	19773	borexino laser substitution
08. Feb. 2013	19685-19871	BTB threshold at 20
09. Feb. 2013	19872-19905	BTB threshold at 22
15. Feb. 2013	19907	BTB threshold at 20

# Bibliography

- [1] F. Lombardi. Measurement of Seasonal Variation of  ${}^7\text{Be}$  flux with Borexino Experiment and New Observables Sensitive to Matter Effect from Updated Solar Neutrino Global Fit, Ph.D. thesis, LNGS, 2013.
- [2] G. Bellini et al., Precision measurement of the  ${}^7\text{Be}$  solar neutrino interaction rate in a Borexino, Phys. Rev. Lett. 107:141302, 2011.
- [3] C. Arpesella et al., Absence of a day-night asymmetry in the  ${}^7\text{Be}$  solar neutrino rate in Borexino, Phys. Lett. B 707:22, 2012.
- [4] Precise measurement of the solar neutrino day-night and seasonal variation in Super-Kamiokande-I, Phys. Rev. D. 69:011104, 2004.
- [5] SNO Collaboration, Search for periodicities in the  ${}^8\text{B}$  solar neutrino ux measured by the Sudbury Neutrino Observatory, Phys. Rev D. 72:052010, 2005.
- [6] Tentativo di una teoria dei raggi  $\beta$ , Ricerca Scientifica, 1933.
- [7] G. Danby, J.-M. Gaillard, K. Goulianos, L. M. Lederman, N. B. Mistry, M. Schwartz, J. Steinberge, Observation of high-energy neutrino reactions and the existence of two kinds of neutrinos, Phys. Rev. Lett. 9:36, 1962.

- [8] M. L. Perl et al.; G. Abrams, A. Boyarski, M. Breidenbach, D. Briggs, F. Bulos, W. Chinowsky, J. Dakin, et al., Evidence for Anomalous lepton production in  $e^+e^-$  annihilation, *Phys. Rev. Lett.* 35:1489, 1975.
- [9] K. Kodama et al. (DONuT Collaboration), Observation of tau neutrino interactions". *Physics Letters B* 504 (3): 218. arXiv:hep-ex/0012035. Bibcode:2001PhLB..504..218D. doi:10.1016/S0370-2693(01)00307-0.
- [10] P. Dirac, A theory of electrons and protons, *Proceedings of the Royal Society A* 126:801, 1930.
- [11] P. Higgs, Broken symmetries and the masses of gauge bosons, *Physical Review Letters* 13:16, p508509, 1964.
- [12] CMS Collaboration, Observation of a new boson at a mass of 125 GeV with the CMS experiment at the LHC, arXiv:1207.7235, 2012.
- [13] Atlas Publications, Observation of a new particle in the search for the Standard Model Higgs boson with the ATLAS detector at the LHC, arXiv:1207.7214, 2012.
- [14] K. Nakamura et al., Particle Data Group Collaboration, *J. Phys. G* 37:075021, 2010.
- [15] J. Christensen-Dalsgaard, Helioseismology, *Rev. Mod. Phys.* 74:1073, 2002.
- [16] N. Grevesse, A. J. Sauval, Standard solar composition, *Space Sci. Rev.* 85:161, 1998.
- [17] J.N. Bahcall, A.M. Serenelli, S. Basu, New solar opacities, abundances, helioseismology, and neutrinos, *Astrophys. J.* 621, 2005.
- [18] C. Pena-Garay, A.M. Serenelli, Solar neutrinos and the solar composition problem, arXiv:astro-ph/0811.2424, 2008.

- [19] M. Asplund, N. Grevesse, A. J. Sauval, The solar chemical composition, review presented at “Cosmic abundances as records of stellar evolution and nucleosynthesis”, F.N. Bash and T.G. Barnes eds., ASP conf. series, Nucl. Phys. A 777, 2006.
- [20] N. Grevesse et al., The chemical composition of the Sun, *Astrophys. Space Sci.* 328, 2010.
- [21] A. Serenelli et al., New Solar Composition: The Problem With Solar Models Revisited, *Astrophys. J.* 705, 2009.
- [22] H. A. Bethe, Energy Production in Stars, *Phys. Rev.* 55:434, 1939.
- [23] J. N. Bahcall, The luminosity constraint on solar neutrino fluxes. *Phys. Rev. C* 65:025801, 2002.
- [24] J. N. Bahcall and A. M. Serenelli, New solar opacities, abundances, helioseismology, and neutrino fluxes. *The Astrophysical Journal*, 621:L85L88, 2005.
- [25] C. Arpesella et al., First real time detection of  $^7\text{Be}$  solar neutrinos by Borexino, *Phys. Lett. B* 658, p.101-108, 2008.
- [26] C. Arpesella et al., Direct measurement of the  $^7\text{Be}$  Solar Neutrino Flux with 192 Days of Borexino Data, *Phys. Rev. Lett.* 101:091302, 2008.
- [27] Y. Fukuda et al., Measurements of the solar neutrino flux from Super-Kamiokande’s first 300 Days, *Phys. Rev. Lett.* 81:4279, 1998.
- [28] Q.R. Ahmad et al., Direct evidence for neutrino flavor transformation from Neutral-Current interactions in the Sudbury Neutrino Observatory, *Phys. Rev. Lett.* 89:011301, 2002.

- [29] G. Bellini et al., Measurement of the solar  $^8\text{B}$  neutrino rate with a liquid scintillator target and 3 MeV energy threshold in the Borexino detector, *Phys. Rev. D* 82: 033006, 2010.
- [30] G. Bellini et al., First evidence of pep solar neutrinos by direct detection in Borexino, *Phys. Rev. Lett.* 108:051302, 2012.
- [31] A. M. Serenelli, New results on Standard Solar Models, *astro-ph.SR/0910.3690*, 2009.
- [32] B. Pontecorvo, Inverse beta processes and nonconservation of lepton charge, *Sov. Phys. JETP*, 7:172173, 1958.
- [33] B. Pontecorvo, Neutrino experiments and the question of leptonic-charge conservation, *Sov. Phys. JETP*, 26:984988, 1968.
- [34] Z. Maki, M. Nakagawa, and S. Sakata, *Prog. Theor. Phys.* 28:870, 1962.
- [35] M. C. Gonzalez-Garcia, M. Maltoni, and J. Salvado, Updated global fit to three neutrino mixing: status of the hints of  $\theta_{13} > 0$ , *JHEP* 04:056, 2010.
- [36] G. Fogli, E. Lisi, A. Marrone, D. Montanino, A. Palazzo, Global analysis of neutrino masses, mixings and phases: entering the era of leptonic CP violation searches, 2012, [arXiv:1205.5254](https://arxiv.org/abs/1205.5254).
- [37] D. Forero, M. Tortola, and J. Valle, Global status of neutrino oscillation parameters after recent reactor measurements, 2012, [arXiv:1205.4018](https://arxiv.org/abs/1205.4018).
- [38] T2K collaboration, Indication of electron neutrino appearance from an accelerator-produced off-axis muon neutrino beam, *Phys. Rev. Lett.* 107, 2011.
- [39] F. P. An, et al., Observation of electron-antineutrino disappearance at Daya Bay, *Phys. Rev. Lett.* 108:171803, 2012.

- [40] S. Mikheyev, A. Y. Smirnov, Resonant amplification of  $\nu$  oscillations in matter and solar-neutrino spectroscopy, *Il Nuovo Cimento*, 9C:1:17-26, 1986.
- [41] L. Wolfenstein, Neutrino oscillations in matter, *Phys. Rev. D* 17:2369-2374, 1978.
- [42] J. N. Bahcall, M. C. Gonzalez-Garcia, C. Pena-Garay, Robust signatures of solar neutrino oscillation solutions, *JHEP* 079:0054, 2002; P.C. de Holanda A. Yu. Smirnov, Solar neutrinos: Global analysis with day and night spectra from SNO, *Phys. Rev. D* 66:113005, 2002.
- [43] K. Eguchi et al., (KamLAND collaboration), First results from KamLAND: Evidence for reactor anti-neutrino disappearance, *Phys. Rev. Lett.* 90:021802, 2003.
- [44] H. O. Back, Internal radioactive source calibration of the Borexino solar neutrino detector, Ph.D. thesis, Virginia Polytechnic Institute and State University, 2004.
- [45] A. Y. Smirnov, The MSW effect and solar neutrinos, hep-ph/0305106, 2003.
- [46] K. S. Hirata et al. (KamiokaNDE Coll.), *Phys. Rev. Lett.* 63:16, 1989;
- [47] J. Hosaka et al. (Super-Kamiokande Coll.), *Phys. Rev. D* 73:112001, 2006;
- [48] J. P. Cravens et al. (Super-Kamiokande Coll.), *Phys. Rev. D* 78:032002 (2008);
- [49] K. Abe et al. (Super-Kamiokande Coll.), arXiv:1010.0118 [hep-ex].
- [50] Q. R. Ahmad et al. (SNO Coll.), *Phys. Rev. Lett.* 87:071301, 2001;
- [51] Q. R. Ahmad et al. (SNO Coll.), *Phys. Rev. Lett.* 89:011301, 2002;
- [52] B. Aharmim et al. (SNO Coll.), *Phys. Rev. Lett.* 101:111301, 2008;
- [53] B. Aharmim et al. (SNO Coll.), *Phys. Rev. C* 81:055504, 2010.

- [54] Resolution No. 10 of the XVIth General Assembly of the International Astronomical Union, Grenoble, 1976.
- [55] A. de Gouvea, A. Friedland, H. Murayama, Seasonal Variations of the  $7\text{Be}$  Solar Neutrino Flux, *Phys. Rev. D* 60:093011, 1999.
- [56] U.F. Katza, Ch. Spieringb, High-energy neutrino astrophysics: Status and perspectives, *Progress in Particle and Nuclear Physics* 67:3:651704, 2012.
- [57] Neutrinos as Dark Matter, astro.ucla.edu, 1998, [www.astro.ucla.edu](http://www.astro.ucla.edu).
- [58] Hirata, K. and Kajita, T. and Koshiba et al., Observation of a neutrino burst from the supernova SN1987A, *Phys. Rev. Lett.* 58:1490, 1987.
- [59] Fukuda et al., Evidence for oscillation of atmospheric neutrinos, *Phys. Rev. Lett.* 81:15621567, 1998.
- [60] The Borexino Collaboration, Observation of Geo-Neutrinos, *Physics Letters B* 687:299, 2010.
- [61] J. Cao, Observation of electron-antineutrino disappearance at Daya Bay, *Phys. Rev. Lett.* 108:171803, 2012.
- [62] J. Benziger, F. P. Calaprice, et al., Borexino: a Real Time Detector for Low Energy Solar Neutrinos, Princeton University, CTF proposal submitted to the National Science Foundation, 1992.
- [63] DarkSide Collaboration, DArkSide-50 Proposal, 2008, "[DarkSide50.DOE.Project.Narrative.FNAL.pdf](#)".
- [64] Particle Data Group, Section 26. Cosmic rays, Revised in 2011.

- [65] G. Bellini et al., Muon and Cosmogenic Neutron Detection in Borexino, JINST 6:P05005, 2011.
- [66] G. Bellini, M. Campanella, D. Giugni, R.S. Raghavan (Eds.), A Real Time Detector for Low Energy Solar Neutrinos, Milano, 1991.
- [67] B. Caccianiga et al., Borexino calibrations: hardware, methods, and results, JINST 7:P10018, 2012.
- [68] K. B. McCarty. The Borexino Nylon Film and the Third Counting Test Facility, Ph.D. thesis, Princeton University, 2006.
- [69] J. B. Birks, The theory and practice of scintillation counting, Pergamon Press, 1964.
- [70] O. Smirnov, Determination of PC quenching in the Borexino detector, Borexino Internal Report, 2009.
- [71] National Institute of Standards and Technology. TRC Tables-Hydrocarbons. U.S. Dept. of Commerce, Technology Administration, 2000.
- [72] A. Pocar. Low Background Techniques and Experimental Challenges for Borexino and its Nylon Vessels, Ph.D. thesis, Princeton University, 2003.
- [73] LSND Collaboration, Measurement of electron-neutrino electron elastic scattering, arXiv:hep-ex/0101039, 2001.
- [74] D. D'Angelo et al., Seasonal modulation in the Borexino cosmic muon signal, arXiv:1109.3901 [hep-ex], 2011.
- [75] M. Selvi, Analysis of the seasonal modulation of the cosmic muon flux in the LVD detector during 2001-2008, PROCEEDINGS OF THE 31st ICRC, 2009.

- [76] K. Blum, DAMA vs. the annually modulated muon background, arXiv:1110.0857, 2011.
- [77] G. Alimonti et al., The Borexino detector at the Laboratori Nazionali del Gran Sasso, Nucl. Instr. and Meth. A 600 p.568-593, 2009.
- [78] A. Razeto, Events Readout for a Real-Time Neutrino Detector, Ph.D. thesis, Universita Degli Studi Di Genova, 2002.
- [79] R. Saldanha, Reduction of Background in Borexino- Internal Report, January, 2009, "[C11\\_Background\\_Borexino.pdf](#)".
- [80] J. Xu, Position indepedent change variable, Mach4 Internal Report, 2010.
- [81] Mach4 on top of Echidna, The MOE Source Code, "[argus.princeton.edu/cvs/bx/](#)".
- [82] E. Gatti, F. De Martini, A new linear method of discrimination between elementary particles in scintillation counters, Nuclear Electronics, 2:265-276, 1962.
- [83] S. Hardy, Measuring the  ${}^7\text{Be}$  neutrino flux from the sun: Calibration of the Borexino solar neutrino detector, Ph.D. thesis, Virginia Polytechnic Institute and State University, 2010.
- [84] G. Bellini et al., Search for Solar Axions Produced in  $p(d, {}^3\text{He})\alpha$  Reaction with Borexino Detector, Phys. Rev. D 85:092003, 2012.
- [85] R. S. Raghavan, "Inverse beta decay of  ${}^{115}\text{In} \rightarrow {}^{115}\text{Sn}^*$ : A new possibility for detecting solar neutrinos from the proton-proton reaction, Phys. Rev. Lett. 37:259, 1976.
- [86] W. Maneschg et al., Production and characterization of a custom-made  ${}^{228}\text{Th}$  source with reduced neutron source strength for the Borexino experiment, Nucl. Instr. and Meth. A 680 p.161-167, 2012.

- [87] G. Bellini et al., The Borexino detector response and its full simulation, *in preparation*, Expected in 2013.
- [88] B. Caccianiga et al., A multiplexed optical fiber system for the PMT calibration of the Borexino experiment, *Nucl. Instr. and Meth. A* 496 p.353-361, 2003.
- [89] F. Calaprice, Purification Campaign, Borexino internal report presented at the Collaborative Meeting in December, 2012.
- [90] S. Zavatarelli, The status of the Borexino backgrounds, Presentation at the Borexino Collaborative Meeting in December, 2012.
- [91] C. Athanassopoulos et al., *Phys. Rev. Lett.* 75 2650, 1995). C. Athanassopoulos et al., *Phys. Rev. C* 54, 2685, 1996.
- [92] A. Aguilar-Arevalo et al., *Phys. Rev. Lett.* 105:181801, 2010.
- [93] J. Bahcall, P. Krastev, E. Lisi, *Phys. Lett. B* 348:121, 1995. M. Laveder, P. Anselman et al., *Phys. Lett. B* 342:440, 1995.
- [94] G. Mention et al., *Phys. Rev. D* 83:073006, 2011.
- [95] Testing the Reactor and Gallium Anomalies with Intense (Anti)Neutrino Emitters, Proceedings of the Neutrino 2012 Conference, Kyoto, Japan, arXiv:1209.5090, 2012.
- [96] R. Saldanha, Precision Measurement of the  ${}^7\text{Be}$  Solar Neutrino Interaction Rate in Borexino, Ph.D. thesis, Princeton University, 2012.
- [97] W. Maneschg, Low-energy solar neutrino spectroscopy with Borexino: Towards the detection of the solar pep and CNO neutrino flux, Ph.D. thesis, University of Heidelberg, 2011.

- [98] N. R. Lomb, Least-squares frequency analysis of unequally spaced data, *Astrophysics and Space Science*, 39:447-462, 1976.
- [99] J. D. Scargle, Studies in astronomical time series analysis. II - Statistical aspects of spectral analysis of unevenly spaced data, *Astrophysical Journal* 263:835, 1982.
- [100] Horne, J.H and Baliunas, S.L. A Prescription for Period Analysis of Unevenly Sampled Time Series, *Astrophysical Journal*, 302:757-763, 1986.
- [101] S. Davini. Measurement of the *pep* and CNO solar neutrino interaction rates in Borexino, Ph.D. thesis, Universit degli studi di Genova, 2012.
- [102] J. Hosaka et al., Solar neutrino measurements in SuperKamiokandeI, *Phys. Rev. D.* 73:112001, 2006.
- [103] NASA Jet Propulsion Laboratory HORIZONS Web-Interface,  
<http://ssd.jpl.nasa.gov/horizons.cgi>.
- [104] L. Cadonati, J. Howard, MOE Rate Trends (2007-2012), Borexino Internal Report, February 2013.
- [105] M. Wurn et al., Search for modulations of the solar  ${}^7\text{Be}$  flux in the next-generation neutrino observatory LENA, *Physical Review D* 83:032010, 2011.

# VITA

Szymon Manecki was born in Kraków, Poland in 1984. He earned his B.Sc. in Solid-State Physics from Akademia Górniczo-Hutnicza in 2007. He earned his first M.Sc. in General Physics from Virginia Tech in 2009 and the second M.Sc. in Particle Physics from Akademia Górniczo-Hutnicza in 2011. His Ph.D. thesis focused on the measurement of the annual flux modulation of solar neutrinos with the Borexino detector. He earned the Ph.D. in Physics from Virginia Tech in 2013 under the supervision of Prof. R. Bruce Vogelaar.